

Investigation of the Effect of Oxides on the Critical Impact Velocity during the Cold Spray Process of High Purity Aluminum Powder

Thesis by: Victor K. Champagne, Jr.

Committee Members: Dr. Richard Sisson (Advisor), Dr. Diran Apelian and Dr. Danielle Cote, Worcester Polytechnic Institute
Dr. Tim Eden, Pennsylvania State University
Dr. Christian Widener, South Dakota School of Mines

Name	Signature	Date
Victor K. Champagne, Jr.		12/13/18
Dr. Rick Sisson		12/13/2018

Executive Summary

The objective of the thesis is to understand the particle/substrate interaction of micron-sized High Purity (HP) aluminum (Al) powder particles with varying surface oxide/hydroxide layers, during single particle impact and determine the critical impact velocity (CIV). Advancements in analytical techniques enable in-situ supersonic impact of individual metallic micro-particles on substrates with micro-scale and nanosecond-level resolution. This novel capability allowed direct observation and measurement of a material-dependent threshold velocity, above which the particle underwent impact-induced material ejection and adhered to the substrate, (critical impact velocity). The data was then compared to empirical, as well as predicted values of the CIV from published data that were based upon theoretical iso-entropic fluid dynamics models. A major emphasis of this research was to perform, in-depth characterization of the Al powder in the as-received, gas atomized state and subsequent to controlled temperature and humidity exposure (designed to form a prescribed oxide and/or hydroxide surface layer) and finally after single particle impact. Analytical techniques including XPS, ICP, IGF, TEM and SEM were performed to determine the species of oxide and/or hydroxide, bulk chemical composition, oxygen content and thickness of the surface oxide/hydroxide layer. Finally, bulk samples of material were produced by the cold spray process, from powder representing select test groups and subsequently characterized to determine tensile and hardness properties, chemistry, microstructure and conductivity. A fundamental understanding of the role of surface oxidization in relationship to particle deformation during impact and the bonding mechanism will be applicable toward the development of optimized parameters for the cold spray (CS) process. Results from this study will aid in the development of industrial practices for producing, packaging and storing Al powders.

ETD Approval Form - etd-103018-143442

Return completed form along with a copy of the signed title page to the Graduate Coordinator, Registrar's Office, or fax to 508-831-5931.

Student name: **Victor K Champagne, Jr.** ID#: **575996289** Department: **Manufacturing Engineering**

Advisor: **Dr. Rick Sisson** Degree: **Doctor of Philosophy** Document type: **Dissertation** Initials: **RDS**

Title: **Investigation of the Effect of Oxides on the Critical Impact Velocity during the Cold Spray Process of High Purity Aluminum Powder**

Student Agreement

I hereby certify that, if appropriate, I have obtained and attached hereto a written permission statement from the owner(s) of each third party copyrighted matter to be included in my dissertation, allowing distribution as specified below. I certify that the version I submitted is the same as that approved by my advisory committee.

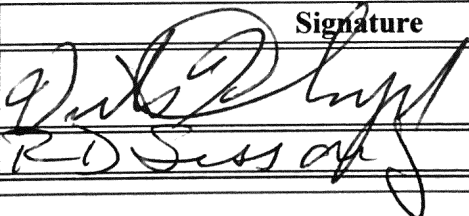
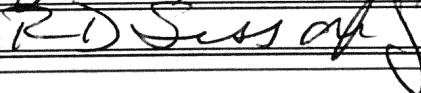
I hereby grant to WPI and its agents the non-exclusive license to archive and make accessible, under the conditions specified below, the aforementioned document in whole or in part in all forms of media, now or hereafter known. I retain all other ownership rights to the copyright of this document, except those which have been handed to a third party through a separate intellectual property agreement. I also retain the right to use in future works (such as articles or books) all or part of this document.

Student and Advisor Agreement

We, the student and advisor, agree that the aforementioned document be restricted to WPI access for 3 years. After 2021-10-30 it will be released for worldwide access in the ETD archive unless another approval form is submitted.

Review and Acceptance

The aforementioned document has been reviewed and accepted by the student's dissertation committee. The undersigned agree to abide by the statements above. **(Please include a copy of the signed title page)**

Name	Signature	Date
Victor K Champagne, Jr.		12/13/18
Dr. Rick Sisson		12/13/2018

-- To be completed by faculty advisor --

I authorize all outstanding grades (SP/I/Q/?) in previous Dissertation credits to be changed to a letter grade by the Registrar's Office.

Grade: Signature:



Investigation of the Effect of Oxides on the Critical Impact Velocity during the Cold Spray Process of High Purity Aluminum Powder

Thesis by: Victor K. Champagne, Jr.

Committee Members: Dr. Richard Sisson (Advisor), Dr. Diran Apelian and Dr. Danielle Cote, Worcester Polytechnic Institute
Dr. Tim Eden, Pennsylvania State University
Dr. Christian Widener, South Dakota School of Mines

Executive Summary

The objective of the thesis is to understand the particle/substrate interaction of micron-sized High Purity (HP) aluminum (Al) powder particles with varying surface oxide/hydroxide layers, during single particle impact and determine the critical impact velocity (CIV). Advancements in analytical techniques enable in-situ supersonic impact of individual metallic micro-particles on substrates with micro-scale and nanosecond-level resolution. This novel capability allowed direct observation and measurement of a material-dependent threshold velocity, above which the particle underwent impact-induced material ejection and adhered to the substrate, (critical impact velocity). The data was then compared to empirical, as well as predicted values of the CIV from published data that were based upon theoretical iso-entropic fluid dynamics models. A major emphasis of this research was to perform, in-depth characterization of the Al powder in the as-received, gas atomized state and subsequent to controlled temperature and humidity exposure (designed to form a prescribed oxide and/or hydroxide surface layer) and finally after single particle impact. Analytical techniques including XPS, ICP, IGF, TEM and SEM were performed to determine the species of oxide and/or hydroxide, bulk chemical composition, oxygen content and thickness of the surface oxide/hydroxide layer. Finally, bulk samples of material were produced by the cold spray process, from powder representing select test groups and subsequently characterized to determine tensile and hardness properties, chemistry, microstructure and conductivity. A fundamental understanding of the role of surface oxidization in relationship to particle deformation during impact and the bonding mechanism will be applicable toward the development of optimized parameters for the cold spray (CS) process. Results from this study will aid in the development of industrial practices for producing, packaging and storing Al powders.

Contents

1.0 Introduction.....	5
1.1 Project Need.....	6
1.2 Project Goals.....	7
1.3 Background.....	8
1.4 Powder Selection	9
1.4.1 Chemistry.....	9
1.4.2 Particle Size and Morphology.....	10
2.0 Literature Review.....	12
2.1 Summary.....	12
2.2 The Cold Spray Process Literature Review	17
2.3 Gas Atomization Literature Review	20
2.4 Aluminum Oxide/Hydroxide Formation Literature Review.....	21
2.5 Cold Spray Bonding Mechanism Literature Review	24
2.6 Critical Impact Velocity Literature Review.....	27
2.7 Single Particle Impact Literature Review	30
3.0 Experimental Approach	35
3.1 Design of Experiment	35
3.2 Test Procedure	37
3.2.1 Sequence of Tests Performed.....	43
3.2.2 Analytical Testing Roles and Facilities	43
4.0 Experimental Results	47
4.1 Characterization of HP Aluminum Powder Groups	47
4.1.1 Particle Size Distribution	47
4.1.2 Inert Gas Fusion (LECO Elementrac ONH-p).....	49
4.1.3 Inert Gas Fusion (LECO ONH836).....	50
4.1.4 Differential Scanning Calorimetry.....	51
4.1.5 Thermogravimetric Analysis	55
4.1.6 Fourier Transform Infrared Spectroscopy	57
4.1.7 X-ray Photoelectron Spectroscopy	59
4.1.8 Transmission and Scanning Transmission Electron Microscopy	60
4.1.9 Scanning Electron Microscopy	66
4.1.10 Raman Spectroscopy.....	67

4.1.11 Dynamic Nanoindentation	70
4.2 Single Particle Impact and Critical Impact Velocity	78
4.2.1 Substrate Preparation	78
4.2.2 Single Particle Impact Test-UMass	80
4.2.3 Single Particle Impact Test-MIT	84
4.3 Characterization of Bulk Cold Spray Samples	88
4.3.1. Mechanical tests.....	91
4.3.2. Fractography	94
4.3.3 X-ray Mapping of Fracture Surfaces	98
.....	100
4.4 TEM and EDS Analysis of Single Particle Impact “Splats”.....	102
4.4.1 Analysis of RH-95% Splats	106
5.0 Analysis.....	116
5.1 Previous Research.....	116
5.2 Results of Characterization of the HP-Al Powder Groups	121
5.2.1 IGF, DSC and TGA	122
5.2.2 FTIR, XPS, SEM, TEM and Raman Spectroscopy	125
5.2.3 Dynamic Nanoindentation	127
5.2.4 Single Particle Impact and Critical Impact Velocity	127
5.2.5 Bulk Cold Spray Samples	129
5.2.6 Single Particle Impact Splats	131
5.3 Summary of Analysis.....	131
6.0 Conclusions.....	132
7.0 Recommendations for Future Research	132
8.0 Technology Transfer Plan.....	132
9.0 References.....	133
10.0 Relevant Papers and Presentations.....	151
10.1 Published Papers (refereed journals)	151
10.2 Publications (other).....	152
10.3 Technical Briefings and Conference Presentations	153
10.4 Book Chapters.....	153
10.5 Books	154
10.6 Patents.....	154
11.0 Acknowledgements.....	155

12.0 Appendix A: List of Tables..... 156
13.0 Appendix B: List of Figures 157

1.0 Introduction

A thorough understanding of the cold spray bonding mechanism is essential toward the development of process parameters leading to advanced cold spray materials, coatings and applications. Without such knowledge, the advancement of cold spray technology would consist of a trial and error approach. This research was undertaken to study the interaction of aluminum powder particles (consisting of various surface oxide/hydroxide layers) with the substrate, during single particle impact and determine the critical impact velocity (CIV).

An advanced laser induced projectile impact test (α -LIPIT) [1] was incorporated to achieve a highly-controlled microscopic single particle collision event to accelerate Al particles. Supersonic velocities comparable to the cold spray process and impact of individual metallic micro-particles on substrates with micro-scale and nanosecond-level resolution were employed. This apparatus allows direct observation of the collision dynamics and nonlinear material characteristics [2].

High purity (HP) aluminum powder particles were chosen in this research, specifically to minimize the variables associated with alloying elements, in terms of the formation and controlled growth of multiple oxides and/or hydroxides and phases [3]. Since the objective of this research was to study the effect of an oxide/hydroxide surface layer on the CIV, it was essential to control as many variables as possible, and minimize extraneous microstructural variations from alloying elements. This aided in the interpretation and prediction of microstructural phases and the processing required to facilitate the formation of an oxide/hydroxide layer on the surface of micron sized aluminum particles.

It was also important to control the growth of the layer to represent that which would be associated with usage under three general scenarios; (1) as a result of variations in the passivation step during gas-atomization, (2) while in storage and handling at manufacturing facilities, where powders may be subjected to high humidity and (3) during the cold spray process, where aluminum powders are exposed to temperatures in the range of 300°C-450°C. Such considerations make this research practical and of interest, not only to the research community but also to companies where aluminum powders are an integral part of a manufacturing process. Aluminum (Al) powders are used extensively throughout the powder metallurgy industry, as well as the thermal and cold spray industries and in numerous additive manufacturing (AM) processes to produce coatings, provide dimensional restoration or to produce near net shaped parts [4]. Therefore, the results of this research has significant impact throughout various sectors of industry.

An important aspect of this research was to fully characterize the starting HP aluminum powders in their as-gas atomized state, and after being subjected to various heat treatments and high humidity conditions at room temperature, which were designed to promote controlled oxide/hydroxide growth. Precise measurements and characterization of the type of surface film along each stage of the test plan allowed accurate interpretation of post particle impact results. Extensive characterization was performed prior and subsequent to single particle impact experimentation. Analytical techniques including X-ray photoelectron spectroscopy (XPS), inductively coupled plasma mass spectrometry (ICP-MS), inductively coupled plasma optical emission spectrometry (ICP-OES), inert gas fusion (IGF), direct current plasma emission spectroscopy, transmission electron microscopy (TEM) and scanning electron microscopy (SEM)

were performed to determine the species of oxide and/or hydroxide, bulk chemical composition, oxygen content and thickness of the surface oxide/hydroxide layer. Samples of impacted particles bonded to a commercially pure (CP) Al substrate were also be studied and the deformation characteristics recorded. Microprobe analysis was conducted at areas of interest along the particle/substrate bond line to determine the chemical composition and contrasted against that of the substrate and HP Al particle. Microstructural features influencing bonding were identified and characterized.

Bulk samples of material were produced from each powder group by the cold spray process. The main gas temperature used to cold spray Al, under standard industrial operating conditions, was in the range of 300°C-450°C, and its influence on oxide formation was incorporated into the design of experiment (DOE). The tensile properties from the bulk material were measured and used as an indicator of the influence of the surface film on the mechanical properties, especially the ductility. The bulk samples were produced from powder representing select test groups and also characterized to determine hardness, chemistry, microstructure and conductivity.

In conclusion, the data generated provided insight and a fundamental understanding of the role of surface oxide/hydroxide layers on particle deformation and bonding during supersonic impact, which directly related to the cold spray critical impact velocity.

1.1 Project Need

The fundamental understanding of the behavior of aluminum particles with varying degrees of surface oxide/hydroxide layers on the CIV is not fully developed. Researchers have predicted through numerical simulations, that during cold spray deposition the activation of the particle/substrate interface by the removal of surface oxides is a necessary prerequisite for bonding [5,6] and that these oxides have a significant effect on the bonding behavior [7-11].

The powder metallurgy industry has expanded the use of aluminum in the form of powder production by gas atomization and powder consolidation into billets to be used as forgings, extrusions or rolled into plate or sheet stock [12,13]. Near net shaped components are produced from aluminum powder for use in the automotive, aerospace, appliance, power tool and heavy equipment industries. Aluminum powder is the most widely used metal fuel additive to propellants, explosives, and rocket fuel and it is also used in paints and chemicals, printing inks, abrasives and ceramics [14-19]. Al powders are used extensively in the thermal and cold spray industry and the global aluminum powder market was approximately 602,800 Tons in 2017 and is expected to reach a volume of around 670 Thousand Tons by 2022 [20].

One of the most important issues associated with the consolidation of aluminum powders, during PM processing, is the inherent oxide layer that forms of the external surface of the powder particles, as a result of air gas atomization [21]. The problem was addressed in the early to mid-1980s, by incorporating the use of inert gas atomization which reduced the thickness of the oxide layer [21]. However, the growth of oxide/hydroxides on Al powder can also be caused by the adsorption of water, as a result of improper packaging, storage and handling of aluminum powders. The natural oxide formed on the Al powder also contains adsorbed water [22,23]. When water reacts with aluminum, in addition to the formation of aluminum oxides and hydroxides, there can

be a release of hydrogen which can form porosity at the grain boundaries leading to blistering and/or cracking in consolidated material [24]. Blistering and cracking as a result of hydrogen has been observed in consolidated Al powders produced from various PM techniques; including cold spray, and the higher the oxide content, the greater the amount of hydrogen released [22,24].

The oxide that forms on the surface of the Al powder is not converted back to the metal state during sintering and can adversely affect the properties of the PM product [22]. The bonding of Al powder particles during the cold spray process is also influenced by the surface oxide/hydroxide layer. The entrapped oxide film between the particle/particle and particle/substrate interfaces prohibits a uniform metallurgical bond that requires a clean metal surface [25,26].

A fundamental comprehension of the role of surface oxides in relationship to particle deformation during impact and the bonding mechanism is essential for all sectors of the powder metallurgy (PM) industry and will be directly applicable toward the development of optimized parameters for the cold spray (CS) process. The results from this study will also aid in the development of industrial practices for producing, packaging and storing aluminum powders. In fact, the results of this thesis have been transitioned toward the introduction of the first cold spray aluminum powders that are specially prepared and packaged in an inert gas to prevent moisture uptake and the formation of surface films with a company called Solvus Global, Worcester MA.

1.2 Project Goals

The objective of the thesis research “Investigation of the Effect of Surface Oxide on the Critical Impact Velocity during the Cold Spray Process of High Purity Aluminum Powder” was designed to enable the analysis of the influence of surface oxide/hydroxide layers on micron-sized HP aluminum particles on the critical impact velocity. This study is relevant to the scientific community by advancing the state-of-the-art of cold spray technology and to industry, by providing valuable insight regarding the adsorption of water by Al powders and the deleterious effects on the consolidation of powders during AM processes. The adverse effects are more pronounced for the cold spray process because powder consolidation takes place without melting, in the solid state. It was the intent that the results and recommendations of this study, will form the basis of a practical solution to the production, packaging, storage and handling of Al powders which are extremely important for the AM industry [27]. Solvus Global is the first company to commercialize the results of this thesis, on a long term basis.

Specifically, this research will incorporate a unique and innovative approach for the determination of extreme single particle impact behavior using the advanced laser induced projectile impact test (α -LIPIT). For the first time, the actual critical impact velocity were measured with unprecedented precision to enable in-depth analysis of the particle/substrate bond interface and particle deformation characteristics. The data generated from this study was compared to published values of the CIV from literature that were either (1) based upon theoretical iso-entropic fluid dynamics models [28,29], or (2) derived from rudimentary cold spray experiments [30], where accurate tracking of specific single particles was not accomplished.

Additionally, this study provided the means to establish cold spray process parameters through direct correlation of the CIV to particle deformation behavior and particle/substrate bonding. This

proved to save time in the development of optimal cold spray processing parameters, by eliminating trial and error. Table 1 summarizes the general project goals that include scientific contributions to the advancement of cold spray technology, as well as practical insight regarding the importance of controlling aluminum feedstock powders for use in cold spray and other AM processes.

Table 1. Summary of Project Goals

Project Goals	
Fundamental Understanding	Practical Insight
Oxide formation on HP-Al powder	Adsorption of moisture by HP-Al powder
Influence of oxide/hydroxide on CIV	Development of cold spray process parameters
Bonding mechanism	Production, packaging, storage & handling Al powders
High strain-rate particle deformation	Effects of oxides on HP-Al cold sprayed bulk material

1.3 Background

The additive manufacturing industry is expected to transform the way parts are produced and/or repaired. Currently, there are various AM techniques commercially available including; the powder-bed, powder-fed, and wire-fed processes incorporating laser, electron beam, accelerated gas or plasma melting [31]. Powder, wire and sheet materials are forms of feedstock for metal AM processes [32]. A technical challenge that exists today is the production of AM parts with uniform and predictable properties [27]. In order to achieve consistent and repeatable properties in materials produced by AM methods, there must be control of the quality of the raw feedstock [33].

The thesis research was of special significance because it involved topics (AM, feedstock powder and cold spray) that have gained international attention from industry, academia and the military, as evidenced by the large number of publications, funded programs and heavy commercial investment [33]. This study investigated HP Al feedstock powder and the cold spray process, which is an AM technique that makes use of an accelerating gas as the means to consolidate powder by ballistic impact.

The properties of aluminum feedstock powder differ depending on the processing method, in terms of particle size and distribution, morphology, chemical composition and the formation of surface oxides/hydroxides [34]. The process most widely used for the production of cold spray aluminum powders is gas atomization (GA). Initially, the feedstock is melted in a furnace before being transferred to a tundish, which is a crucible that regulates the flow rate of the melt into the atomizer [33]. An inert gas such as nitrogen or argon is piped into the atomization chamber and symmetrically positioned around the stream of liquid metal, atomizing and solidifying the particles from above, producing a relatively spherical shaped particle [33]. The use of an inert gas decreases the formation of surface oxides but later air is introduced to passivate the powder to make it safe for handling, since aluminum metal can be highly reactive when exposed to oxygen. The solidified powder drops to the bottom of the chamber, where it is collected. GA aluminum powders generally have good flowability and a high packing ratio, which are important attributes for producing materials of high density and low porosity, regardless of the PM process employed [34].

The Cold Spray (CS) process was proposed in this study because it is an emerging AM technology of high interest internationally, with many technology gaps that are not fully developed nor

understood; including the CIV and bonding mechanism. Cold spray also has significant potential as an ‘enabling technology’ because it is a solid state consolidation process with unique characteristics and is the focus of research and development for the US Department of Defense and many large manufacturers across the globe. It also spans across numerous industries including; aerospace, automotive, petrochemical, nuclear, ship building and even the medical field to produce anti-microbial coatings [35].

The gas atomization processing conditions directly contributes to the formation of surface oxide/hydroxide layers, which influence the resultant powders response to PM consolidation [21]. As part of the GA process, cooling air is introduced into the spray chamber, from ambient atmospheric conditions in order to passivate the surface of the powder [21,36]. This practice is performed as a safety precaution due to the explosive nature of aluminum. Al powders are high explosive (HE) materials, which are characterized by the release of intense heat and gaseous decomposition products by violent exothermic chemical reactions [37]. These types of reactions can occur when the powder forms a cloud or comes into contact with an electrical discharge, high impact or high temperatures [21,24,37]. When Al powder is exposed to water at room temperature, highly flammable hydrogen can also form [24,38].

Al powders can form additional hydroxides/oxides after gas atomization during packaging, storage, handling and while in use, when the powders are exposed to humid air. Flumerfelt [21] has shown that the rate of oxidation of GA pure aluminum powders is directly proportional to relative humidity of the handling and storage atmospheres, which accentuates one of the main tenants of this research topic. Exposure temperatures, as well as alloying elements contribute to the continued growth of the oxide film after gas atomization [24]. High temperature exposure of powder that has adsorbed moisture after gas atomization, is a real concern for the cold spray industry and is an important aspect of this study.

1.4 Powder Selection

The choice of HP Al gas atomized powder for this study was driven by several important factors: (1) chemistry, (2) particle size and morphology, and (3) representative of industry practice.

1.4.1 Chemistry

The control of chemical composition assists in the unambiguous interpretation of the test results without consideration of the effects of alloying elements. This aided in the characterization of the oxide/hydroxide surface layers, [21] at each stage of the study. One of the important aspects of this research was to provide a fundamental understanding of the effects of these surface layers on the CIV. Therefore, the study of pure metals, for which the formation of the surface oxide layers is less complex, allows a basis for comparison upon which to build. Future research efforts could concentrate on generating data obtained from aluminum alloys and other materials. Table 2. Chemical Composition of High Purity Al Powder-Valimet (9-40 μm dia.) [39] lists the chemical composition of HP-Al obtained from Valimet Corporation, CA [39] while Table 3. Chemical Composition of High Purity Al Powder- FLP12 (5-25 μm dia.) [40] lists the chemical composition of HP-Al from Henan Yuanyang Aluminum Industry Company [40]. Table 2.

Chemical Composition of High Purity Al Powder-Valimet (9-40 μm dia.) [39] contains the weight percentage of water, which can be the result of atomization.

Table 2. Chemical Composition of High Purity Al Powder-Valimet (9-40 μm dia.) [39]

CHEMICAL COMPOSITION WT.%						
Al	Cu	Fe	Si	Mg <0.01	Mn	Zn
Balance	<0.01	0.01	0.01	<0.01	<0.01	<0.01

Table 3. Chemical Composition of High Purity Al Powder- FLPG12 (5-25 μm dia.) [40]

CHEMICAL COMPOSITION WT.%				
Al	Cu	Fe	Si	H ₂ O
99.9 min	0.005	0.015	0.015	0.02

1.4.2 Particle Size and Morphology

The size and particle morphology of the HP aluminum powder are important considerations for the single particle impact experiment and for purposes of impact modeling.

Aluminum is now produced by atomization techniques and in some instances, ball milling to form powder of different sizes and morphologies, some of which are not conducive for the cold spray process, as shown in Figure 1. The most predominate methods are: (1) Gas-atomization, (2) Water-atomization, (3) Plasma-atomization and (4) Ball milling [33,41,42]. The morphology of aluminum powders produced by these methods can differ considerably as shown in Figure 1.

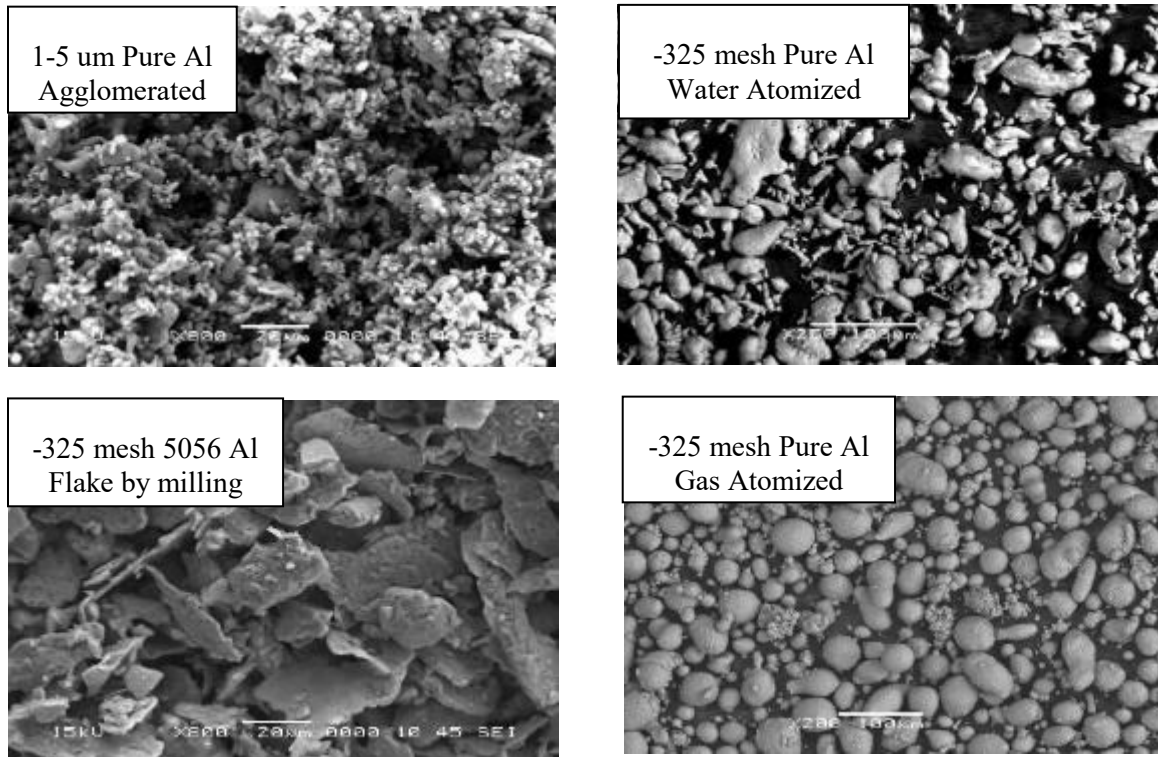


Figure 1. The morphology of aluminum powders produced by different processes.

The cold spray process utilizes particles typically ranging in diameter from about 5 to 100 μm , and are accelerated at velocities from 300 to 1,500 m/sec by injection into a high-velocity stream of gas (typically nitrogen or helium) [35]. Particles that are $<5 \mu\text{m}$ do not have enough momentum to leave the gas stream and impact the substrate. Hence, submicron and nanoparticles cannot be deposited using high pressure cold spray under standard operating conditions and feedstock.

In this work, the advanced laser induced projectile impact test (α -LIPIT) [1] was used as a highly controlled means to accelerate a single particle against an aluminum substrate to study its impact behavior and was designed to simulate the cold spray process. The α -LIPIT has limitations on the size and density of the particle it can accommodate for this type of experiment. The approximate particle size range that can be accelerated to the required velocities ($\sim 700\text{-}900 \text{ m/sec}$) is 10-40 μm . Additionally, the geometry of the particle is important for aerodynamic considerations. To minimize the complexity of particle flow modeling and favorable gas-particle dynamics, a spherical shaped particle is desirable, as shown in *Figure 2*.

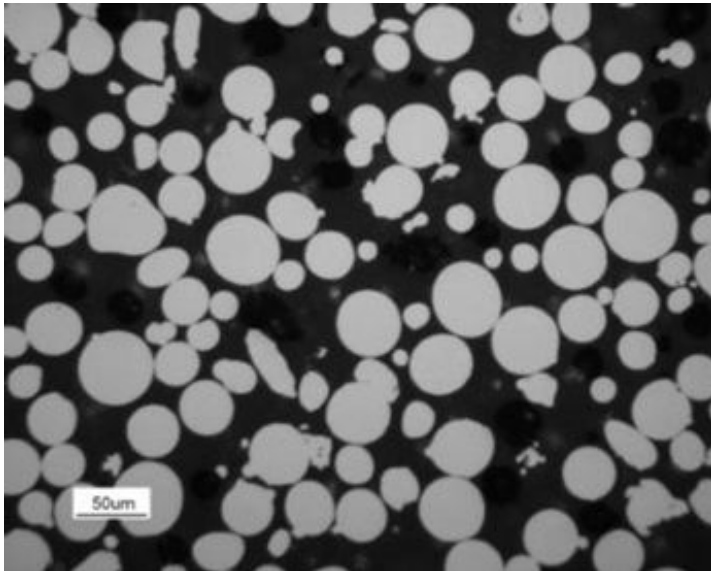


Figure 2. Cross-section of gas atomized aluminum powder showing spheroidal shape.

Figure 3 illustrates the deformation characteristics of a spherical shaped (Figure 3a) powder particle as compared to a particle having an acicular shape (Figure 3b) during cold spray. The spheroidal particle offers a more favorable geometry to allow plastic deformation and bonding to occur.

To determine a minimum particle size for this study, the particle velocity and subsequent impact has been modeled through the application of conventional rocket nozzle flow equations and by an empirical materials driven impact relationship [43]. Particle velocities and temperatures can be predicted at the nozzle exit, downstream of the bow shock and at the substrate surface [44]. These conditions were subsequently used to predict the deposition efficiency (DE). In other words, the prediction that a particle having certain characteristics will bond upon impact.

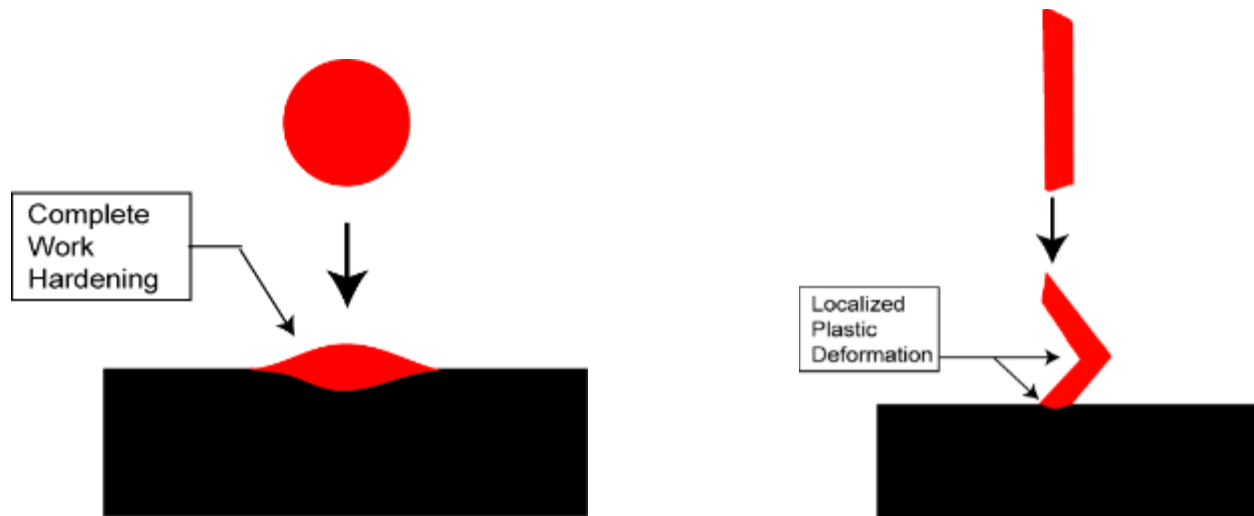


Figure 3. Deformation characteristics of a spheroidal shaped particle (a) as compared to an acicular shaped particle (b).

Previously, it was thought that because the smallest particles attain the highest velocities during the cold spray process they would bond together and consolidate. While it is true that small particles exit the nozzle at high velocity, their velocity at impact can be significantly lower. Modeling efforts revealed that the low gas velocity following the bow shock wave decreases particle velocities, especially for the smallest particles [45]. It was shown that impact velocity increases as the particle diameter decreases until a diameter of 4 to 8 μm is reached [45]. Therefore, particles having a diameter less than 8 μm were not used in this study. Deng et al., has shown that particle size of aluminum powder also affects the rate of the aluminum water reaction and is related to surface area [46].

2.0 Literature Review

2.1 Summary

An extensive literature review was conducted on the main topic of the thesis research topic, as well as the technical areas that supported the study. Specifically, the current state of the art was summarized for the following: (1) the industrial process to produce HP Al powder, (2) the cold spray process, (3) the formation of oxide/hydroxide on HP Al powder, (4) the cold spray bonding mechanism, (5) the critical impact velocity and (6) the advanced laser induced projectile impact test (α -LIPIT). These topics have been reviewed and relevant information summarized to provide the basis for conducting the study, performing the necessary characterization and analyzing the results. The information consists of published research and industrial practices, as well as hands on experience by the author, obtained over a thirty-four year time period, of which approximately eighteen were devoted towards cold spray research and development.

Published literature investigating the effect of oxides on the critical impact velocity of high purity aluminum powder, as presented in this study, was lacking. There has been published research concerning the influence of surface oxidation of cold spray powders in regards to deposit efficiency and bonding but many of these studies used a theoretical approach, incorporating finite elemental analysis (FEA). From these studies, researchers have made predictions based upon numerical simulations about the effect of surface oxides on the critical impact velocity but controlled single particle impact experiments that isolate specific aluminum particles that have been hydrolyzed, have not been conducted to date.

R.C. Dykhuizen et al., [30] were some of the first important researchers who studied particle impact of copper particles onto stainless steel, during the cold spray process, using both numerical and experimental methods. The authors used the Steinberg-Guinan-Lund viscoplastic model [47] and a computer code generated by The Sandia National Laboratories CTH [48] that was developed to model a wide range of solid dynamics problems involving shock wave propagation and material motion in one, two, or three dimensions [30]. The focus of their research involved the examination of individual particle impacts or ‘splats’ at various velocities to determine the extent of particle and substrate deformation and to study the bonding mechanism. The resultant craters were of interest to Dykhuizen et al., and they concluded that higher velocities formed deeper craters but the radius of the resultant splats was insensitive to the impact velocity, except for particles with very low velocities, which did not adequately deposit. The authors observed material jetting at the impact interface, which they concluded promoted bonding, similar to that of explosive welding. They hypothesized that plastic deformation resulted in material jetting, which acted to break apart surface films. This provided clean metal surfaces between particles and/or the substrate that are in intimate contact, under high local pressure, providing the conditions conducive to bonding. Dykhuizen et al., also determined that the numerical simulation of copper over predicted penetration of the splat and attributed this to possible improper modeling of the large strain rates or incorrect material properties, which substantiates the concern over the limitations of these types of theoretical models [30].

Grujicic et al. in their research, use a dynamic finite element analysis and ABAQUS/Explicit, Version 6.3, a commercially available finite element program, to study the interaction of a single particle impacting a surface [49]. The critical velocity for Al particles generated by numerical simulation by researchers, Schmidt et al. [50] and Grujicic et al. [49] reported the results of the critical impact velocity of Al particles on Al substrates as approximately 760 m/s but the effect of surface oxides was not considered. W.-Y. Li, et al., determined that such simulation results were very dependent on the meshing sizes replicated with the Lagrangian algorithm. This was an indication that the critical impact velocity was dependent on the mesh size and the accuracy of the FEA simulation was significantly compromised [51,52]. The concern originated from the fact that certain features depicted in these simulations of numerically-generated behavior may be a numerical artifact, rather than a physical fact due to limitations of a Lagrangian finite element simulation. Gangaraj has further explained that when the frame of reference for the simulation is changed from Lagrangian to Eulerian (to avoid distortion) the material behavior changes, [53] as determined from calculating the stress distribution at critical velocity in the jet region and in the particle.

Assadi et al., provided a hypothesis for the bonding observed in the cold spray process, by numerical modeling of the deformation during particle impact. The authors demonstrated that bonding can be attributed to adiabatic shear instabilities, which occurred at the particle surface at or beyond the critical velocity [54]. Assadi et al., predicted the critical velocity to be 660 m/s for inert-gas-atomized 99.93% aluminum powder with particle size below 45 μm , when deposited onto an Al substrate. Depending on the researcher and the simulation used, the values of the CIV for an Al-particle/Al-substrate combination are as much as 100 m/s apart, [55,56].

The Grujicic [49] study extended the work of both Dykhuizen [30] and Assadi et al., and in addition to the critique of the computational aspect already provided, there are other considerations which are of significant importance, that relate to the lack of characterization of feedstock powder, as well as a lack of empirical data associated with microstructural analysis of the interfacial bond region between particles and of the particle/substrate. Finally, there is an inadequate determination of the criteria constituting a cold spray bond. This has led to inaccurate assumptions on the part of researchers, who have set out to determine the CIV either through empirical means or by mathematical models. There are serious shortcomings associated with the various models, including the J-C as previously discussed and even Assadi et al., admit that “... *this experimental method could not give an unambiguous correlation between particle sizes and velocities...*” in regards to the use of the J-C model [54]. In these studies the effects of surface oxidation were not taken into consideration.

Wen-Ya Li et al., have used an Arbitrary Lagrangian Eulerian (ALE) method to investigate the deformation characteristics of Al powder and the effect of surface oxide films during cold spray [52]. The authors modeled the impact behavior of an Al particle impact on an Al substrate using LS-DYNA and concluded that with increasing oxide thickness, the particle deformation was restrained and that oxide fragments could become entrapped at the interfaces and adversely affect the bond strength of the deposition [52]. Wen-Ya Li et al., [52] also pointed out in their study that the particle conditions, such as oxide film, prior to impact, have significant effect on the critical velocity, but was not considered in the previous studies [30, 49,50,51,54,57,58].

Other researchers have taken an empirical approach and have performed actual cold spray trials using powders of varying oxide thickness and measured deposit efficiency. C.-J. Li et al., studied the effects of varying oxide thickness of copper, 316L stainless steel, and a Monel alloy on the critical impact velocity by conducting spray trials and measuring the weight gain of each specimen after deposition [59]. The powders used in this study were received at the lowest oxygen content level and then oxidized under ambient conditions at high temperatures to produce powders with varying oxygen content. An inert gas fusion (IGF) techniques was used to measure oxygen by exposing the samples to elevated temperatures and measuring the oxygen gas release. The results indicated that the CIV was significantly higher for those powders that were severely oxidized. For example, C.-J. Li et al., reported that the critical velocity of copper powder changed from about 310 m/s at an oxygen content of 0.02 wt.% to 610 m/s at an oxygen content of 0.38 wt.%. Figure 4 shows the linear relationship of oxygen content and CIV for 316 stainless steel [59]. This data corresponded well with those reported by previous researchers, who also showed a similar trend in the CIV [60-62].

The effects of an oxide coating on the deposit characteristic and bond strength have been investigated by several other researchers. W-A Li et al [63] revealed the manner in which particle impact causes the surface oxide layer to break up along the contact area, leaving behind a clean metal surface, which promotes bonding but also random patches of oxide (Figure 5) which inhibit bonding. The authors further explain that the presence of this captured oxide at the interface causes reduced adhesion to the mating surface and to previously deposited material. W-A Li et al., reported the adhesion strengths of cold sprayed copper powder with different levels of initial oxidation and found that the adhesive strength of the coating was significantly decreased when increasing the oxygen content in the feedstock.

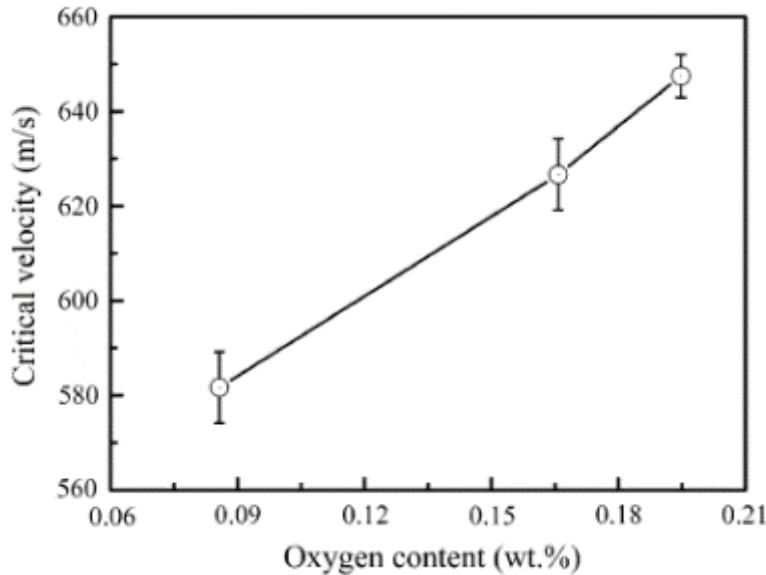


Figure 4. Effect of oxygen content on CIV of 316L stainless steel powder [59].

Figure 5 shows the manner in which the surface oxide film on particles are disrupted and can become trapped at the interface of the impact regions. The surface oxides can inhibit the jet formation and decrease the adhesive strength of the deposit. The authors revealed that the cold spray bond strength decreases, as the oxygen content in the feedstock increases [63].

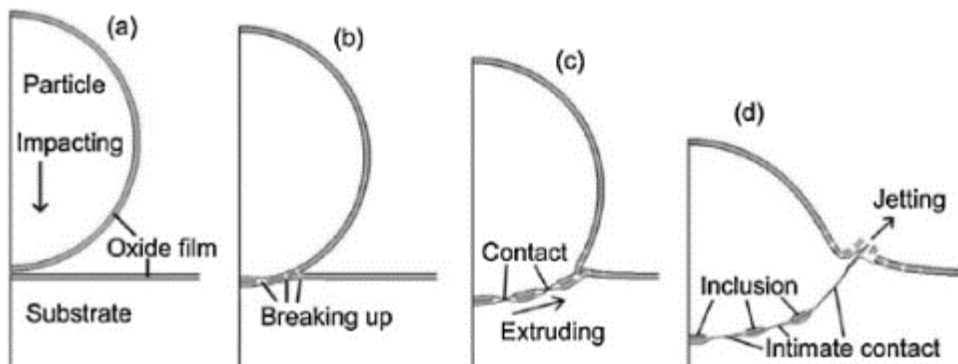


Figure 5. Schematic of the cold spray bonding process showing the break-up and entrapment of surface oxides and the formation of jetting [63].

Yin et al., [64] model the break-up of the oxide layer as depicted in Figure 6 using a Johnson–Holmquist plasticity damage model. Figure 6 shows the time (nanoseconds) sequence of particle deformation and break-up and ejection of the surface oxide layer of an Al 6061-T6 particle impacting on an Al 6061-T6 substrate, at an impact velocity of 700 m/s [64]. The authors explain that the oxide is crushed immediately upon impact (a) and the central portion begins to flatten. In (b) the particle base material, at the outermost edges of the impact interface begins to flow and form a jet which extends further in (c-f) pushing the fractured oxides out into space leaving behind a clean metal surface that promotes bonding. However, cracked oxides at the center can become trapped interfering with metallic bonding. The same phenomenon is also reported by others through experimental observations including the following particle/substrate combinations: Al–Al [59,65] , Ti–Al [66], Cu–Cu [67,68] and Cu–Q235 mild steel [63].

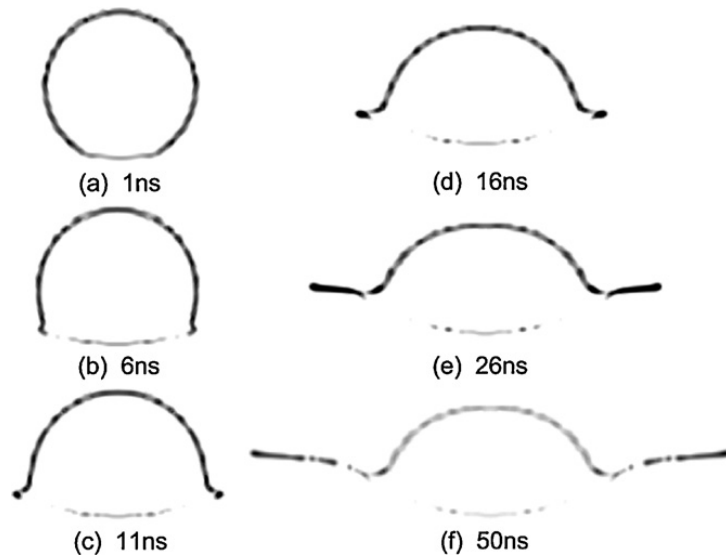


Figure 6. Simulation of the break-up of the surface oxide layer during cold spray, of an Al 6061-T6 particle, at an impact velocity of 700 m/s.

The work of Kang et al. [69] combined with that of Yin et al., [64] serve as a basis of close comparison to this thesis study because both researchers set out to determine the effect of the surface oxide layer on the CIV of commercially pure (CP) aluminum. Yin et al., uses an FEA approach while Kang et al., attempt to study individual impact behavior and examine the microstructure at the impact interface. In the work performed by Kang et al., the oxygen content of CP aluminum was varied by chemical etching and temperature exposure, to produce four different groups of powder, which were then used in the cold spray process to produce samples for examination. High raster rates in combination with low powder feed rates were incorporated into the DOE, in an attempt to isolate individual particles whose in-flight velocities were measured with a SprayWatch system that includes a high power pulsed laser diode (Hiwatch) to illuminate

the in-flight particles and a high speed camera (SprayWatch camera unit) to monitor in-flight particles.

Kang et al., made some important observations and deductions associated with particle deformation characteristics and bonding. Specifically, more impact energy is expended to remove the oxide from the surface leaving less available energy for particle deformation, adversely affecting bonding [69]. The authors found a slight decrease in the flattening ratio with an increase in oxygen content (Figure 7). Oxides were broken up and pushed out from the interface and ejected by the action of shear stress but some oxides are trapped and remain, especially at the center and prohibit metallic bonding

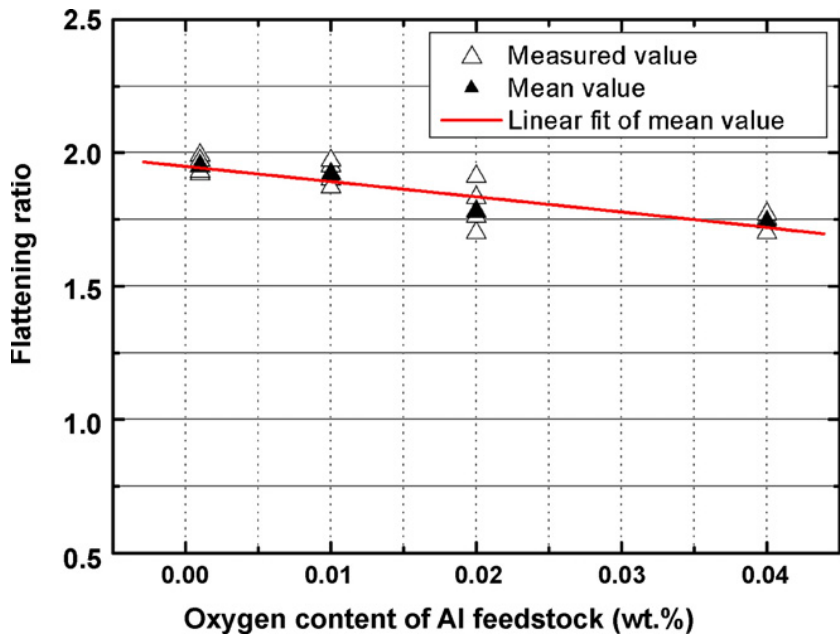


Figure 7. Flattening ratio of deposited aluminum particles with different oxygen content for the same process condition [69].

Therefore, it can be deduced that the amount of surface oxidation has a direct correlation to deformation characteristics and the ratio of bonded surfaces. Kang et al., calculated the CIV from the analysis of the deposition rates and particle velocity and concluded that as the oxygen content of aluminum feedstock increased, critical velocity increased significantly [69].

The importance of all the cited research is that the CIV can be more significantly influenced by surface oxidation than by the material properties.

2.2 The Cold Spray Process Literature Review

Cold Spray (CS) is a solid state AM process whereby micron sized particles of a metal, ceramic and/or polymer are accelerated through a spray gun fitted with a De Laval rocket nozzle using a

heated high-pressure gas such that the particles exit at supersonic velocities and consolidate upon impacting a suitable surface, (Figure 8) to form a coating or a near-net shaped part, by means of ballistic impingement [70-75]. There is a classification of cold spray that uses a sonic nozzle which has a converging section followed by a section that maintains the flow at sonic conditions. Both versions of the CS nozzle work on the main principle of expanding the gas to higher velocities by controlling the cross-sectional area of the nozzle. The particles utilized are typically in the form of commercially available powders, ranging in diameter from about 5 to 100 μm , and are accelerated at velocities from 300 to 1,500 m/sec by injection into a high-velocity stream of gas (typically nitrogen or helium). Particles that are $<5 \mu\text{m}$ do not have enough momentum to leave the gas stream and impact the substrate.

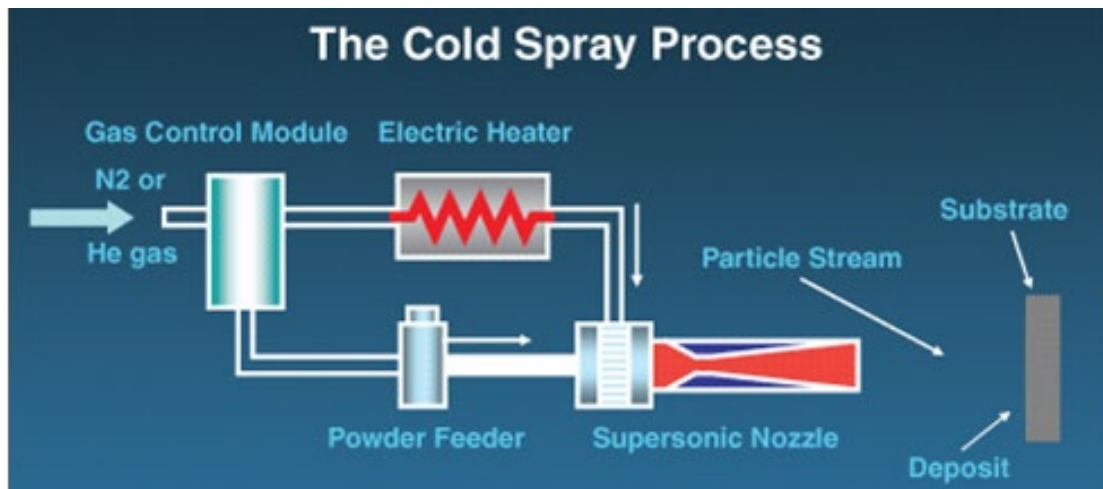


Figure 8. Schematic of the cold spray process.

The cold spray process incorporates a high velocity gas stream that is generated via the expansion of a pressurized, preheated, gas through a converging-diverging de Laval rocket nozzle. The pressurized gas is expanded to supersonic velocities, with an accompanying decrease in pressure and temperature [76-78]. The particles, which can be carried from the pressurized powder feeder through a separate line or in the same line as the gas stream, are injected into the nozzle either prior to the throat of the nozzle or downstream of the throat. The particles are subsequently accelerated by the main nozzle gas flow and impact onto a substrate after exiting the nozzle. If the critical impact velocity of the accelerating particles is attained upon impact, the solid particles deform and create a bond with the substrate [79-81]. Adequate velocity is necessary for optimal particle consolidation and coating density, and several important CS process parameters, including gas conditions, particle characteristics, and nozzle geometry, affect the particle velocity. It has been well established that impacting particles must exceed the critical velocity to deposit otherwise they may rebound off of the substrate. The magnitude of the critical velocity can be estimated through the use of empirical relationships, which generally depend on particle material characteristics, such as density, ultimate strength, yield and melting point, as well as the particle temperature [81].

As the process continues, particles collide with the substrate and form bonds with the underlying consolidated material resulting in an adherent, uniform deposit with very little porosity and high

adhesive and cohesive bond strength. The term cold spray has been used to describe this process due to the fact that the temperatures are typically well below that of the melting temperature of the feedstock powders. The heated gas stream cools significantly as it expands through the de Laval rocket nozzle. This is illustrated in (Figure 9), which uses a cold spray model developed by Helfritch et al. [82] to calculate the temperature of the gas as it expands from the nozzle as a function of inlet temperature and pressure.

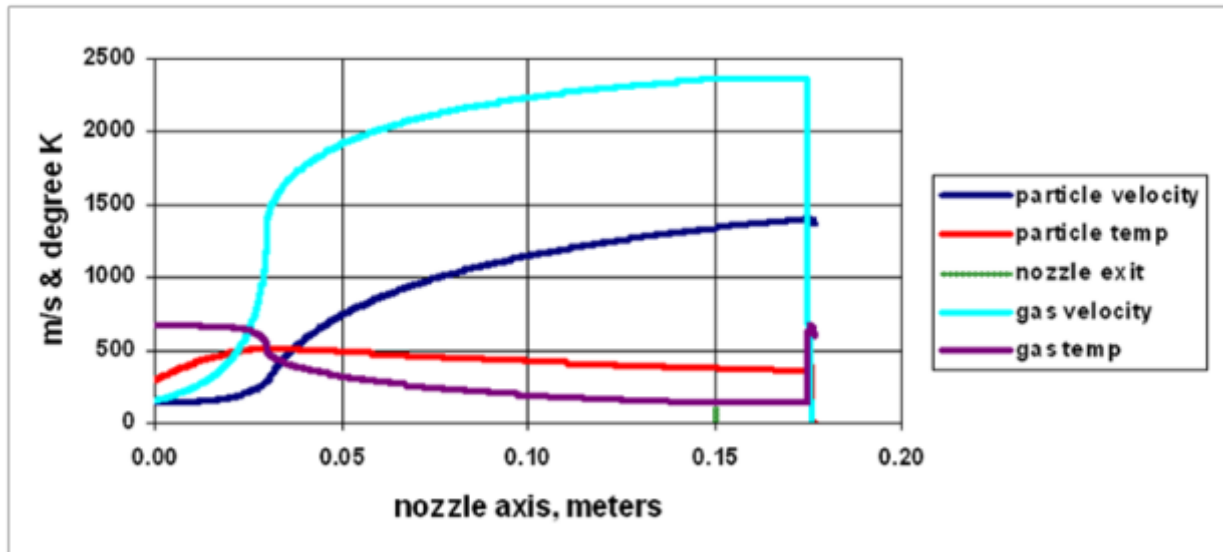


Figure 9. Cold spray model developed by Helfritch et al. [59] to calculate the temperature of the gas as it expands from the nozzle as a function of inlet temperature and pressure.

Since the temperature of the gas stream is always below the melting point of the particulate material during cold spray, the resultant consolidated material is formed in the solid state. Since the adhesion of the impacted particles to the substrate, as well as the cohesion of the subsequent layers of CS deposit, is accomplished in the solid state, at low temperatures, the characteristics of the cold spray material are quite unique in many regards. The low temperatures associated with the cold spray process are desirable when attempting to maintain the microstructure, grain size and elemental composition of the starting feedstock powder. Such is the case with nanostructured powders because the risk of grain growth and phase transformation is minimal or nonexistent. In addition, particle oxidation is avoided, as well as deleterious tensile stresses that occur during solidification and the accompanying thermal contraction associated with conventional thermal spray processes. The cold spray process has been developed as of late, to deposit a wide variety of engineering materials, as shown in Figure 10, including; steels, titanium, aluminum, nickel, zinc, tin, copper, brass, zirconium, silver, Inconel, Peek, cermets, polymers and/or combinations of these materials and many more with near theoretical density. The strength and modulus values of the cold spray material often exceed those of wrought materials and the hardness of Al and Al-alloy cold spray is generally higher than for wrought alloys because of the extreme work hardening induced by the spray process but the ductility can be lower.

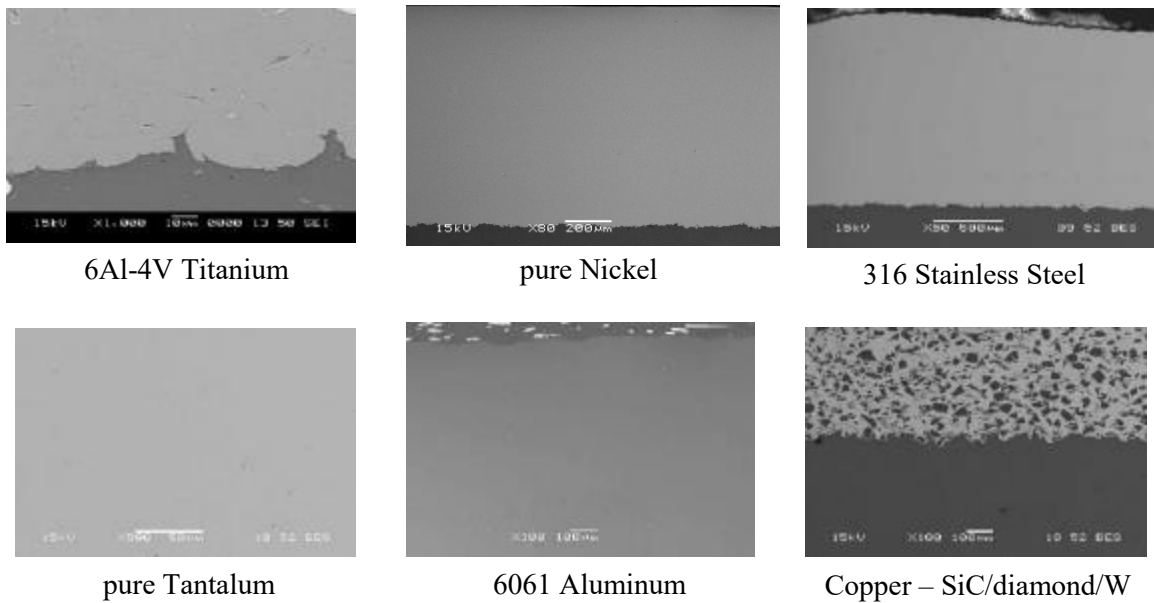


Figure 10. CS is capable of depositing various engineering materials with near theoretical density.

2.3 Gas Atomization Literature Review

Gas atomization (GA) represents the most widely used process for the production of aluminum powder and begins with the melting of the raw material in a furnace. The molten aluminum is then transferred into a type of crucible, called a ‘tundish’, whose function is to regulate the flow rate of the melt into the atomizer [33,83]. Vacuum induction melting (VIM) furnaces can be employed to control interstitial elements [33]. To prevent contamination from the ceramic lining of the tundish, two types of inert-gas atomization are used today; electrode-induction melting in combination with inert-gas atomization (EIGA) and plasma melting in combination with inert-gas atomization (PIGA)[84,85]. The melt is fed through the atomizer and is broken up into fine liquid metal droplets by the action of high pressure gas jets, as depicted in Figure 11 [86,87]. The molten droplets solidify in flight and fall down into a collection chamber. Cooling air is introduced into the spray chamber, from ambient atmospheric conditions in order to passivate the surface of the powder and may not have a low enough dew point to minimize hydration of the oxide film [21,36]. In addition, it has been reported that the inert purge gas doesn’t completely remove all traces of oxygen and water vapor from the atomization chamber [21,91]. These residual gases are the cause of the incorporation of oxygen and water into the oxide layer on aluminum during gas atomization [21, 91].

The properties of the powders produced by the various atomization techniques differ as a result in cooling rate and heat capacity of the quenching media, [34] in terms of particle size and distribution, morphology and localized chemical composition, (i.e. segregation).

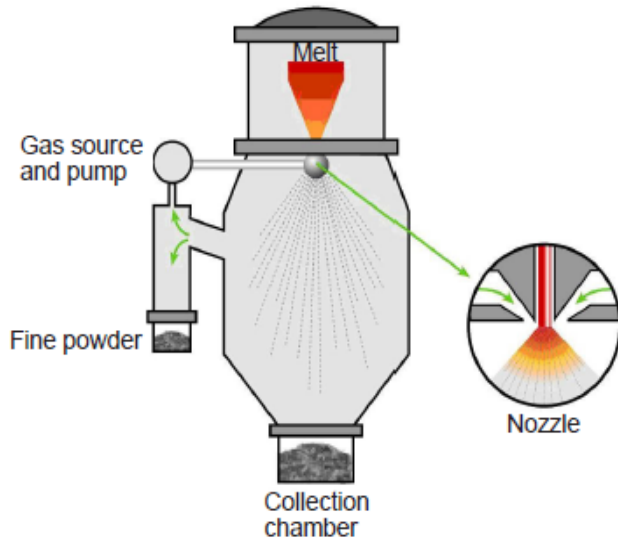


Figure 11. Schematic of the gas atomization process for production of AM powders (Courtesy of LPW Technology, UK). [33]

The type of gas and melt phase, as well as gas injection pressures, affect the size and morphology of the resultant powder [88-90]. Gas atomized powders have a more spheroidal shape due to differences in solidification rates as compared to water atomized powders, which tend to have an irregular morphology and high oxygen content [33,34]. Flowability and packing density are important powder characteristics for cold spray and AM processes. Spherical or regular, equiaxed particles are likely to arrange and pack more efficiently than irregular acicular shaped particles [33].

The rapid formation of an oxide layer during gas atomization and other thermal processes along with the high solubility limits of hydrogen are a concern during the production and AM processing of Al powders [92].

2.4 Aluminum Oxide/Hydroxide Formation Literature Review

The production of AM parts with consistent and predictable properties requires that the feedstock powders used to produce them have predictable and repeatable characteristics [27]. It has been reported that limiting the thickness of the surface oxide film is desirable on feedstock powders to enhance interparticle bonding during AM consolidation, especially during the cold spray process [21,30,49,50,51,55-58, 60, 62-70]. Therefore, the mechanics involved in the formation of the surface oxide layer during (1) gas atomization, (2) powder packaging, storage and handling, (3) powder post-processing, such degassing, (4) during cold spray consolidation are important [93,94].

The oxidation of aluminum is a very complex process [95]. The surface reactions are complicated by exposure of powders to humid air where water vapor can bind at the surface of the powder, either as $\text{Al}_2\text{O}_3 \cdot (\text{H}_2\text{O})$, or as physically adsorbed water [95].

Hayden et al. [96] identified two stages of oxidation of aluminum at temperatures between 20°C and 550°C and oxygen pressures of 10^{-9} - 10^{-2} torr. In summary, the authors described a fast initial

stage consisting of a thin amorphous oxide layer (0.3nm) formed by nucleation and growth by chemisorption and amalgamation of oxygen in the metal surface that is rate dependent on temperature and oxygen pressure [96].

The second stage was characterized by slow thickening growth of a closed amorphous oxide layer until at temperatures above 450°C and extended oxidation times, a crystalline Al₂O₃ was formed at the aluminum metal surface, beneath the amorphous oxide layer, by a nucleation and growth process [96].

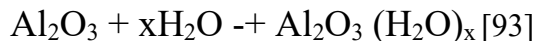
The premise of the thesis research was that aluminum powders continue to oxidize after gas atomization, during post atomization powder handling and in use during cold spray and other AM processes [21,36,92,95]. Previous work has shown that the processing conditions during gas atomization contribute to the formation of undesirable surface oxide/hydroxides that adversely affect the properties of AM consolidated material [21,30,49,55-58]. The extent of surface oxidation of powders during gas atomization is directly related to the partial pressures of oxygen and water vapor [21, 97]. Even though an inert gas, such as argon, may be used during gas atomization, oxidation of Al powders will always take place because in the aluminum-oxygen system, the partial pressure of oxygen in equilibrium with Al₂O₃ is very small and far below what can be achieved in conventional GA systems [95]. The thickness of the surface layer is dictated by oxidation kinetics and the conditions in each stage of the GA process, such as the available water vapor and oxygen, solidification rate and time of flight during atomization [98]. The rate of oxidation is directly proportional to the relative humidity and oxygen concentration in the air of the GA, the collection chamber and the handling and storage atmospheres [21, 97].

Camey et al. [98] investigated the oxide formation of gas-atomized powder and the oxidation process was divided into three stages: (1) in-flight solidification, (2) powder in the collection box and (3) exposure of powder to air.

During in-flight solidification, the atomized droplets having a diameter less than 200 μm were rapidly cooled by the atomizing gas as shown in Figure 12 by Flumerfelt [21, 95]. Estrada et al. [93] estimated the cooling time for particle diameters of 5 - 100 μm and a gas velocity of 100 m/s to be 10⁻⁵ – 10⁻³ s [95]. Since the cooling rates of the molten droplets are so high, the growth of the oxide at these temperatures is much below 0.1 nm, and only the first stage of the amorphous layer takes place, contrary to what thermodynamics may dictate [93]. This is consistent with Hayden et al.,[96] and the natural oxide formed on gas atomized powder is in the order of 100 x 10⁻¹⁰m thick, and is amorphous in nature, containing adsorbed water [22,100].

Upon heating at high temperature the oxide crystallizes first to η(Al₂O₃), then to χ(Al₂O₃) or γ'(Al₂O₃) and finally to the stable γ(Al₂O₃) [22].

These reactions represent gas atomization using argon or nitrogen gas in which the partial pressure of oxygen is only about 10⁻⁴ – 10⁻⁵ atm. At temperatures below - 350 °C the thermodynamic conditions for the reaction of aluminum oxide with water vapor become favorable [93, 99,101]



Therefore, this reaction may be expected to take place during atomization in a (humid) air stream.

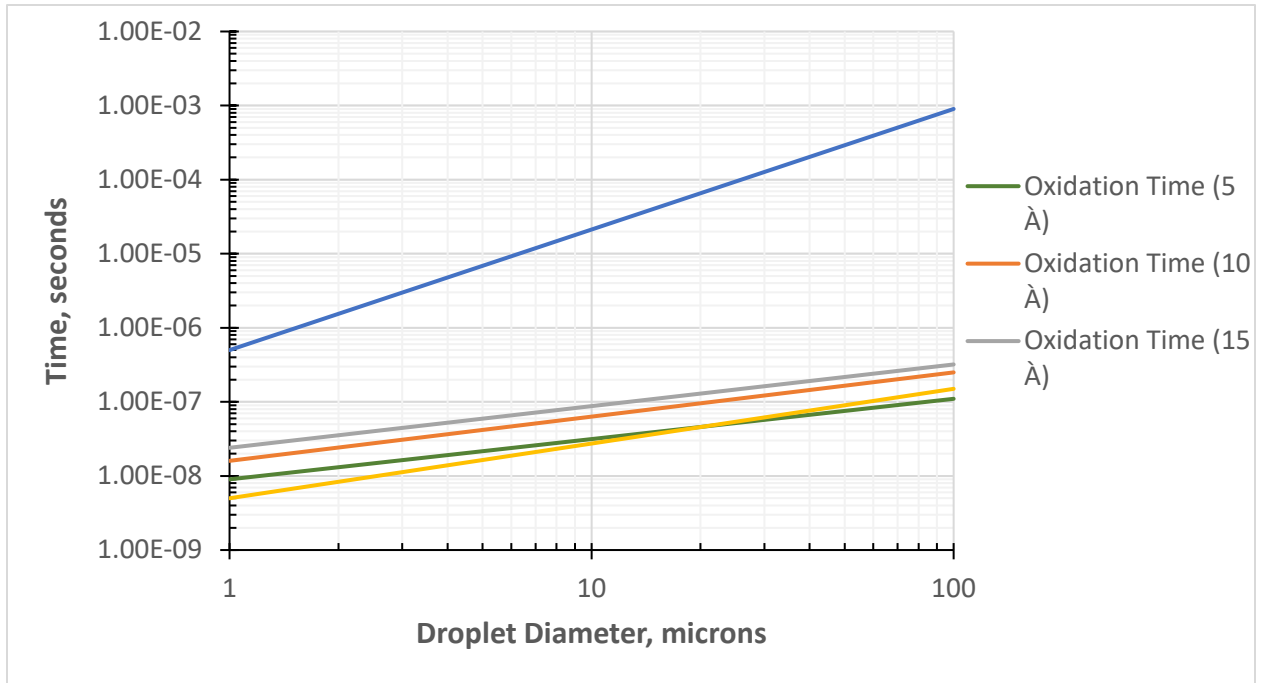


Figure 12. Time evolution for aluminum powder oxidation during helium gas atomization with 2.0 volume percent oxygen in the atomization gas [21].

Individual particles may exhibit variation in the oxide layer, which may result in the formation of thick islands of oxide during solidification of the molten droplet, due to temperature gradients in the droplet and the compressive stresses in the vicinity of the oxide islands [102-107]. Additionally, as Flumerfelt and other researchers point out, the in-flight oxidation reaction products are aluminum oxide and varying concentrations of hydrated aluminum oxide incorporated into an amorphous oxide surface film [21,93,99,101].

Another important consideration regarding oxide film thickness is in relation to particle diameter. Figure 13 shows a plot of the oxide film on commercially pure aluminum (CP-Al) as a function of particle diameter and oxide film thickness, formed during gas atomization [21]. The results indicate that the percentage of oxide on smaller diameter particles is greater than that contained on particles with larger diameters. Therefore, when powders are consolidated by AM methods, (including cold spray), more oxide content can be anticipated when using powder with smaller diameters, unless the partial pressure of available oxygen is reduced during atomization.

The oxidation of Al powders begins within the first milliseconds of the gas atomization process and continues during all stages of gas atomization [21,30,49,55-58, 93,97, 99,102-107]. The oxidation reaction products are aluminum oxide and varying concentrations of hydrated Al oxide incorporated into an amorphous oxide surface film [21,30,49,55-58, 93-107]. Residual oxygen and water vapor serve as the oxidation source and are found in the all stages of gas atomization. During handling, storage and use of the Al powder, oxidation will continue depending on the oxygen content and the relative humidity of the atmosphere [21,93,99,101].

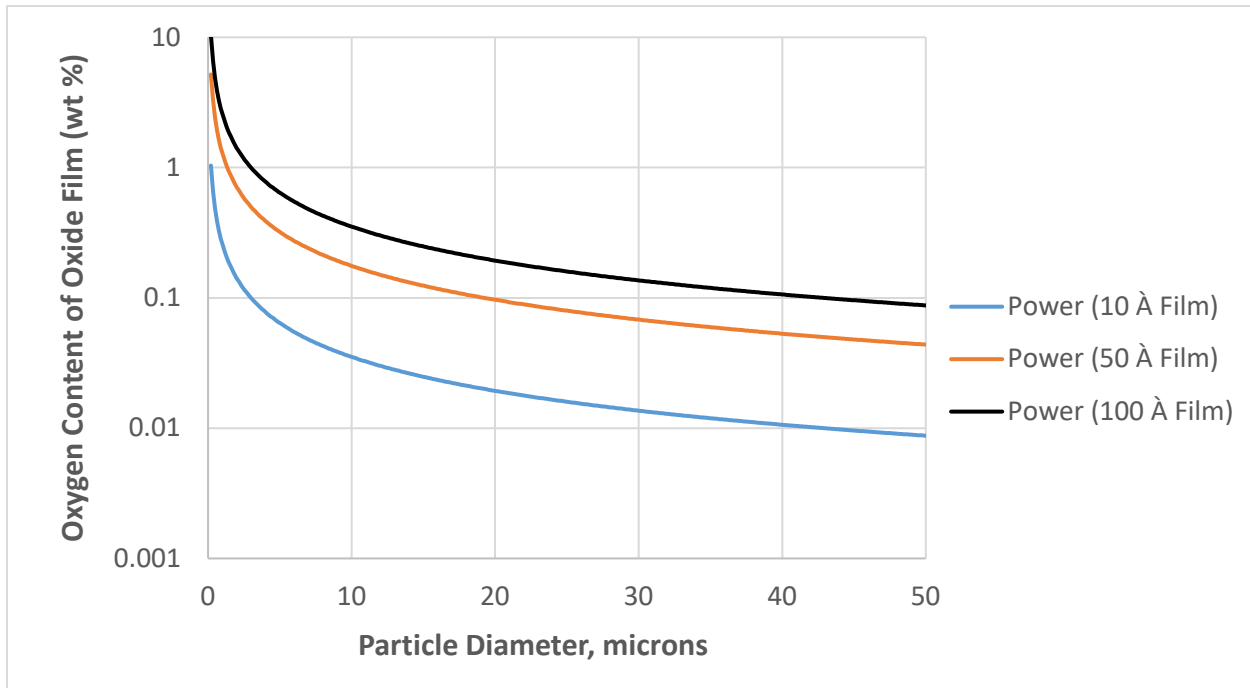


Figure 13. Graph of oxygen content of the oxide layer on CP-Al powder as a function of particle diameter and oxide film thickness [21].

In summary, the formation and continued growth of the surface oxide/hydroxide layer can occur during (1) gas atomization, (2) powder packaging, storage and handling, (3) powder post-processing, and (4) during cold spray consolidation [21,93,94,99,101].

2.5 Cold Spray Bonding Mechanism Literature Review

The Cold Spray (CS) process involves the acceleration of micron-sized particles (~5-75 μm) in the form of commercially available powders that are carried in a high pressure (6.8 bar/100psi -69 bar/1,000 psi) and sometimes heated gas stream (R.T. – 1,200°C) in the solid state toward a suitable substrate upon which the particle undergoes tremendous plastic deformation. Upon impact the plastic deformation can disrupt and break down surface oxide layers on both the powder and substrate leading to a metallurgical bond, as well as mechanical interlocking and in some instances melting, if the temperature of the main gas and pressure are too high. Since the feedstock powder is deposited in the solid state, the microstructure is retained after deposition with the exception of dynamic recrystallization due to high strain levels. During the cold spray process, both the particles and/or substrate undergo physical transformation in the form of particle rotation, grain deformation and refinement, work hardening, strain, generation of heat and formation of residual stress [35].

The CS process is conducive to materials that can undergo high levels of strain with low energy input but also work harden sufficiently to obtain the desired strength. It has been reported that

localized temperature increases and strain concentration play a major role in the high speed deformation of the particles upon impact, as a result of adiabatic shear. Approximately 90% of the work of plastic deformation is converted to heat [108], and the flow stress of most metals is sensitive to temperature, decreasing as temperature increases. During impact of the solid feed stock powder particles, the oxide layers on both the powder and the substrate surface are disrupted and partially removed along with other impurities at the particle substrate interface causing the exposure of highly reactive “virgin” metal and subsequent metallic bonding between particle and substrate material. [109] The feedstock powder is in intimate contact with the exposed substrate forming an adherent metallurgical bond as a result of the severe plastic deformation during particle impact [110]. Thermal softening due to the presence of severe plastic deformation (SPD) can enhance particle deformation and interlocking of adjacent particles resulting in the intimate contact at the interface and consequently pancaked structures in the deposited material [108]. Deformation of these particles can at times result in recrystallization or intermetallic phase formation [111]. It is evident in Figure 14 that some of the particles have experienced sufficient deformation and heat during the impact that they have completely recrystallized at the interface, resulting in the formation of an ultra-fined grained (UFG) structure [108].

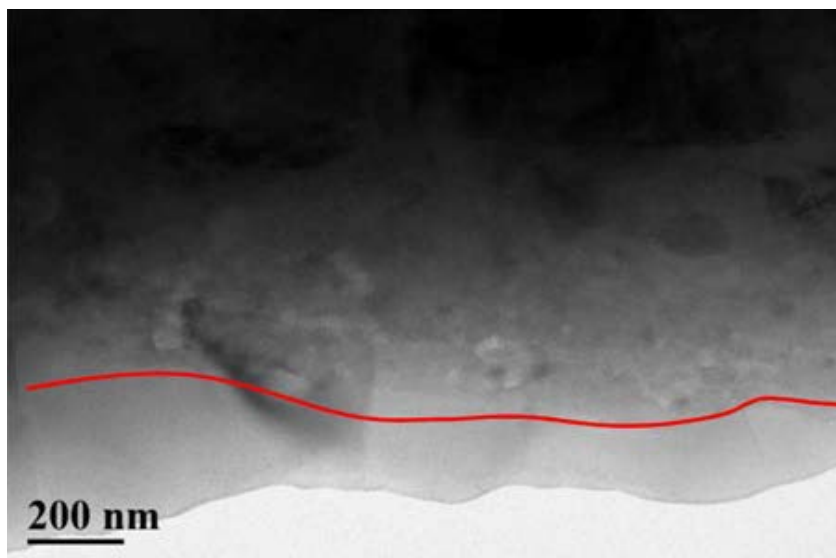


Figure 14. UFG structures at interface due to high strain rate deformation [108].

The bonding mechanism of the cold spray process is analogous to that of explosive welding, which is another type of solid phase welding process where bonding is also the result of plastic deformation of the metals to be bonded. Bonding occurs when two surfaces under extreme pressure are forced together such that the surface oxide layers are disrupted and bonding takes place between the opposing clean metal surfaces [112]. Grujicic et al., describe the sequence of events associated with a typical time evolution of the particle and substrate interaction during impact, as predicted by the finite element analysis, which is similar to the stages of the explosive welding process shown in Table 4. Stages of the Explosive Welding Process [113] The two processes have been described by researchers as being similar in nature and it is important to note that the shock wave plays a pivotal role in bonding during the explosive welding process. It strips away oxides and forms a ‘jet’ (Figure 15).

Table 4. Stages of the Explosive Welding Process [113]

1. Shockwave is transmitted through the two metal layers in a fashion similar to ripples in water.
2. The shockwave is able to produce a slight wave effect in the material due to super plasticity.
3. The high velocity of this shock wave effect strips away oxides on both surfaces.
4. The detached oxides are expelled as a flow of matter just ahead of the detonation front. This flow of matter is also known as a 'jet'.
5. This action leaves behind clean metal surfaces allowing a metallic bond to be formed.
6. The bond is produced as a result of high pressure which causes the valence electrons to cross into each other's sphere of influence.
7. Process is carried out at ambient temperature.

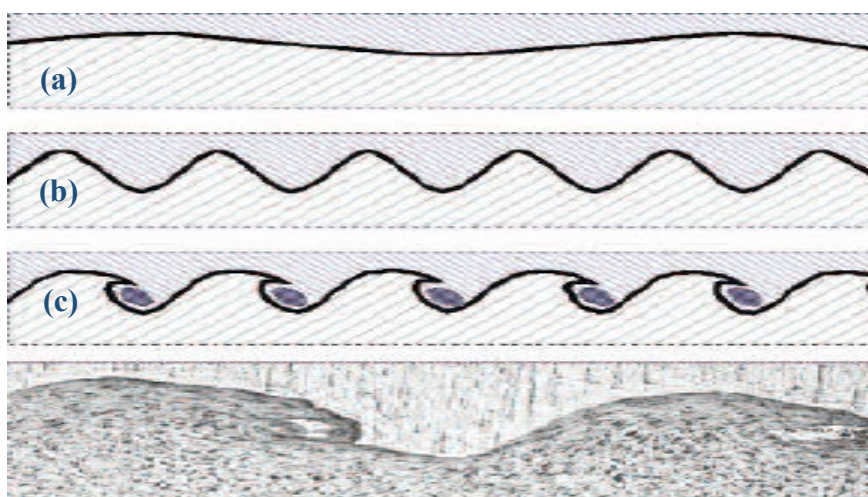


Figure 15. Types and transitions resulting from explosion welding: (a) laminar, (b) wavy, (c) turbulent.

Researchers, including Dykhuizen et al. have investigated the effect of particle diameter on the flattening ratio and crater depth numerically to develop an understanding of the bonding mechanism. A comparison was drawn between the cold spray process and explosive cladding whereas the formation of a solid-state jet of metal at the impact point of two metal plates promotes bonding [30]

Assadi et al provides a hypothesis for the bonding observed in the cold spray process, by numerical modeling of the deformation during particle impact demonstrating that bonding can be attributed to adiabatic shear instabilities which occur at the particle surface at or beyond the critical velocity [54]. Li et al revealed that most metallic spray materials experience some level of localized melting at the contact interfaces between the particles of materials consolidated by the cold spray process [114]. Bae et al. studied the adiabatic shear instability based bonding mechanism numerically by impacting many particles onto a substrate and subsequently comparing the results to experimental data [115]. Champagne et al. [116] studied material mixing between copper particle and aluminum substrates as a result of mechanical interlocking Figure 16. Mechanical interlocking of a Cu coating applied by cold spray onto 6061 AL-T6..

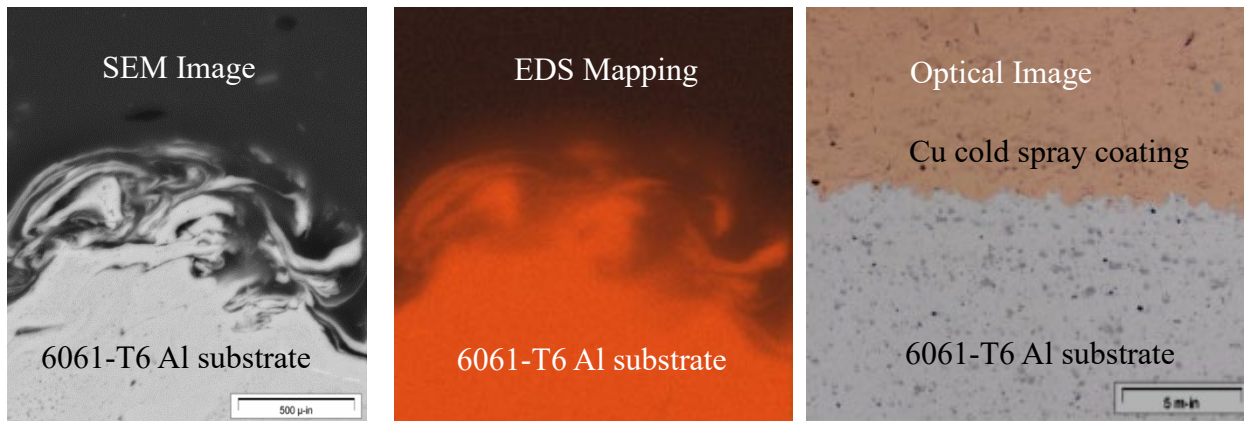


Figure 16. Mechanical interlocking of a Cu coating applied by cold spray onto 6061 AL-T6.

Hussain et al. suggests that the bonding is largely due to mechanical interlocking, where the substrate physically entraps the particles but that claim doesn't adequately take into account the effects of adiabatic shear instability [117]. The outer region of the particle that impacts the substrate experiences severe plastic deformation at high impact velocities and a corresponding temperature increase, which can result in local melting and subsequently a strong bond with the substrate [118].

Benefits of the type of bonding associated with the cold spray process include the retention of the original microstructure of the feedstock powders, since consolidation of the particles takes place in the solid state. Additionally, the high impact velocities of the solid particulatespeen the underlying material and form a state of compressive stress [35]. Impact between the particles and the substrate result in interfacial instability due to differing viscosities, along with the resulting interfacial roll-ups and vortices, promote interfacial bonding by increasing the interfacial area, giving rise to material mixing at the interface and providing mechanical interlocking between the two materials [119].

Therefore it has been deduced based upon empirical evidence that both metallurgical bonding, in combination with mechanical interlocking, are the predominate bonding mechanisms in cold spray, and under certain high process parameter settings for main gas temperature and pressure, melting can be observed.

2.6 Critical Impact Velocity Literature Review

Grujicic et al., claim that their simple one-dimensional model for the onset of adiabatic shear localization can be used to assess the critical impact particle velocity (CIV) required for successful cold-spray deposition [29]. Therefore, an explanation of the CIV and its significance is warranted. It has been reported that during cold spray the kinetic energy of impacting particles must be sufficient to allow plastic deformation of the substrate and/or disrupt the surface oxide film [56,35]. Researchers throughout the years, have defined a critical value of particle velocity, as being that which is necessary for the impacting particles to bond with the substrate during the cold spray process [6,30,54,56,57,60,72,78,118,120-129]. This critical velocity is dependent on a variety of factors including the substrate material and is also a function of the physical and mechanical

properties of the powder material [6,30,54,56,57,60,72,78,118,120-131]. Numerous researcher studies have determined that feedstock materials with higher moduli are more difficult to deposit, [6,30,54,56,57,60,72,78,118,120-131] requiring higher main gas temperatures (i.e. increased particle velocity), or by being encapsulated, mechanically alloyed or blended with a ductile material (i.e. ceramic– metal composites) [132]. The softer and more ductile feed stock powder allows the harder powder particles to be co-deposited. Theoretical approaches for determining the CIV have been proposed and reported by Grujicic et al., [78] Assadi et al., [54] and Moridi et al., [133]. Numerous studies suggest that particle deposition is dependent on the impact velocity. These studies concluded that only the particles that attain a sufficiently higher velocity than the CIV can be successfully deposited (Figure 17a. Particle impact and bonding.

Figure 17b. Particle impact and rebound., while those which fall below the CIV would only cause erosion of the substrate [134,135] and/or rebound off of it (Figure 17a. Particle impact and bonding.

Figure 17b. Particle impact and rebound.). When the particles impinge at extremely high velocities, much greater than the CIV, solid particle erosion of the substrate surface is once again observed, and deposition discontinues [136]. The technical challenge in defining the CIV has been determining the criteria that governs particle/substrate and particle/particle bonding, then quantifying the bond strength and finally, correlating the values to the CIV.

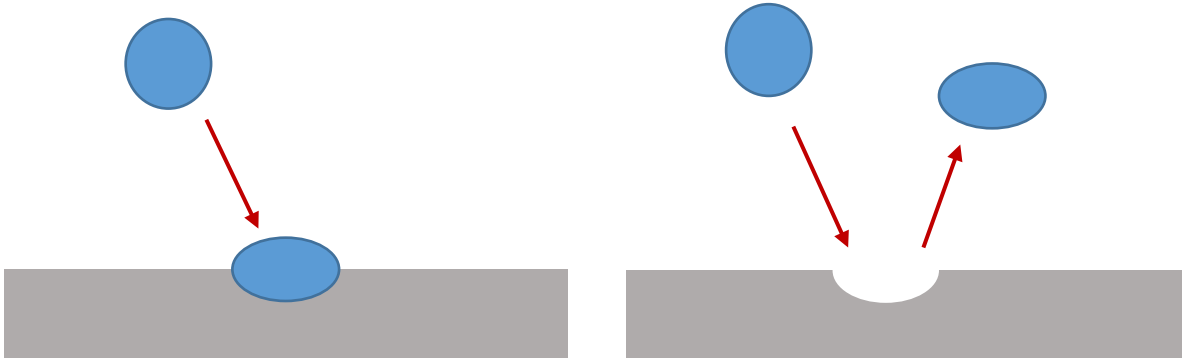


Figure 17a. Particle impact and bonding.

Figure 17b. Particle impact and rebound.

Grujicic et al., study the particle/substrate interaction bonding mechanism using a one-dimensional thermo-mechanical model for adiabatic strain softening and the accompanying adiabatic shear localization [29]. The authors conclude that the onset of adiabatic shear instability in the particles/substrate interfacial region plays an important role in promoting particle/substrate bonding during the cold spray process and their work leads to a theoretical prediction of CIV [29]. Since CIV is defined by the bonding of particles to the substrate and particles to particles, a deeper understanding of the criteria used by researchers to explain this phenomenon is important to a discussion of the results and the conclusions reached by the authors.

Since the material properties of a cold spray deposit determine the application where it can be put into practical use, the quantification of those desirable material characteristics is essential. If the deposit is to be used to form a coating, then properties as corrosion and/or wear resistance could be important, while other applications may demand high strength/ductility and fatigue resistance. In all of these examples, adhesive and cohesive strength is necessary. Adhesive strength is a

measure of the bond at the particle/substrate interface, while cohesive strength constitutes the bond between individual particles. Researchers have employed various methods to measure the adhesive and cohesive strength of cold spray deposits and have used these values to substantiate theoretical derivations of the CIV. Maäkinen et al. presented the influences of powder, substrate and heat treatment on the adhesive strength [137] and used European Standard EN 582 “Thermal Spray Determination of Tensile Adhesive Strength as did many other researchers, including Assadi et al., [54]. This method is similar to ASTM C633, “Standard Test Method for Adhesion or Cohesion Strength of Thermal Spray Coatings”, which is utilized extensively throughout the thermal spray industry to measure the bond strength of thermal spray coatings. This particular method incorporates the use of 25mm (1 inch) bar stock representing the substrate material, which is subsequently prepared on one cylindrical face to accept a cold spray coating that is applied to a sufficient thickness where it can then be glued to a respective counter-body of the same size. The ends of the cylindrical bar stock are threaded and inserted into a tensile test machine and subjected to tensile forces along their axes until failure and a value of bond strength is recorded. The ruptured specimens are subsequently examined to determine the origin of failure, which could be at the interfaces between the coating/substrate (adhesive failure) or within the cold spray deposit (cohesive failure) [54, 137]. A flaw in this type of test is the limitation of the strength of the epoxy/glue that is used, which has a tensile strength of only 69-83 MPa (10,000 – 12,000psi). Adhesive and cohesive strengths of cold spray deposits have been reported by Champagne, III et al., to be much greater and in the range of 186-214 MPa (27,00-31,000psi) [111]. Therefore, many instances of bond strength of cold spray deposits have not been reflective of actual values. Such values have been reported throughout the years by researchers. This raises the question of their use for determining CIV and to validate theoretical models, including those of Grujicic et al.

Assadi et al., has reported that a rough theoretical estimation reveals that for impact velocities of 580 m/s, only about 15–25% of the entire interface is subject to shear instability and states, “*So far, the modeling has not been able to explain if this amount of surface area would be sufficient for a successful bonding*” and additionally further explains, “*this could explain the relatively low bond strength of cold gas sprayed coatings as compared to bulk material or thermally sprayed coatings*, and recommends the use of tensile tests to provide additional information for assessing extent of critical conditions at the interface,” [54]. His statements summarize an obvious concern and reveal a significant flaw in the approach that researchers have relied on to report the bond strength of cold spray coatings and the use of these values to substantiate theoretical models for predicting the CIV. In addition, his general statement concerning the inferior bond strength of cold spray deposits have been proven inaccurate, by recent published research [81,108,111].

In summary, the current accepted definition of the CIV is the ability of impacting particles to bond with the substrate, during the cold spray process. The practical use of the CIV in establishing adequate cold spray process parameters or as a determination of the structural integrity of the cold spray deposit is limited, since it is not currently a measure of bond strength and cannot be correlated to material properties.

2.7 Single Particle Impact Literature Review

Jae-Hwang Lee et al. while at MIT, revolutionized the study of particle impact with the design of an apparatus, dubbed the laser-induced projectile impact test (LIPIT), which was initially used in 2010, to investigate the mechanical behavior of nanomaterials under extremely high deformation rates [138]. The system enables real-time observations of single particle impacts with micron-scale and nanosecond-level resolution at velocities equal to those attained during the cold spray process. Gangaraj et al., [139,53] also from MIT, later carried on this work in 2015, utilizing the apparatus designed by Jae-Hwang Lee et al., but with some improvements regarding the ability to take multiple images. Jae-Hwang Lee has since left MIT but is still carrying out single particle impact experiments, specific to the cold spray process, at the University of Massachusetts, Amherst utilizing another system that he built at the Mechanical Engineering Department.

Figure 18 shows a schematic of the apparatus [138,1] used by Jae-Hwang Lee et al., and Gangaraj et al., to observe the flight characteristics and subsequent impact of a single micron-sized particle in real time [140,141].

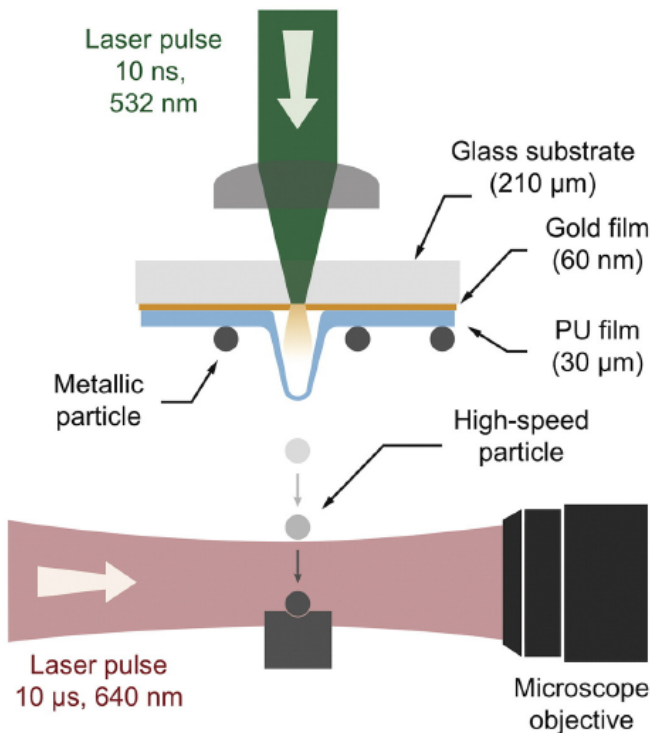


Figure 18. Single particle impact apparatus with micron-scale and nanosecond-level resolution [53].

The single particle impact experiment warrants a detailed description because the level of precision associated with isolating, manipulating and ultimately accelerating and tracking the trajectory of a micron-sized particle using an ultra-high speed camera is so revolutionary, from a scientific perspective to accurately measure the CIV.

The following step by step description of the experiment is taken directly from Gangaraj et al., [53] whereas “a laser excitation pulse is focused onto a launching pad assembly from which single metallic particles are launched toward a target sample by ablation of a gold layer and rapid expansion of an elastomeric polyurea film. The particle approach and impact on the target are observed in real time using a high-frame-rate camera and a synchronized quasi-cw laser imaging pulse for illumination. The launching pad assembly follows the design described by Lee et al. and Veysset et al. [1,140]. 210- μm -thick glass substrates (Corning No. 2 microscope cover slip) were sputter-coated with a 60-nm thick gold film. A mixture of polycarbodiimide-modified diphenylmethane diisocyanate (Isonate 143 L MDI, Dow Chemicals) and oligomeric diamine (Versalink® P-650, Air Products) with a weight ratio of 1:3 was spin-coated on the gold-coated substrates at 750 RPM for 5 min to yield a film thickness of 30 μm after 24-hour curing at room temperature. Film thicknesses were measured using a 3D laser scanning confocal microscope (VK-X200 series, Keyence). Metallic particles were deposited on the substrates using lens cleaning papers to spread drops from a suspension of particles in ethanol. For each experiment, a laser excitation pulse (pulsed Nd:YAG, 10-ns duration, 532-nm wavelength) was focused onto the launching pad assembly from where the metallic particles were ejected. Upon laser ablation of the gold film, particles were accelerated to speeds ranging from approximately 100 to 1200 m/s, controllable by adjusting the laser excitation pulse energy (from 2 up to 60 mJ). 16-image sequences showing impact were recorded with a high-frame-rate camera (SIMX16, Specialized Imaging) using a laser pulse (30- μs duration, 640-nm wavelength SI-LUX640, Specialized Imaging) for illumination. The high-speed camera comprises 16 CCDs that can be triggered independently to record up to 16 images with exposure times as short as 3 ns”.

Figure 19 is a montage of ultra-high speed photographs showing a time evolution of a 45 μm aluminum particle impacting an aluminum substrate, whereas the velocity is 605m/sec for (a) the top multi-frame sequences and 805m/sec for (b) the bottom multi-frame sequences.

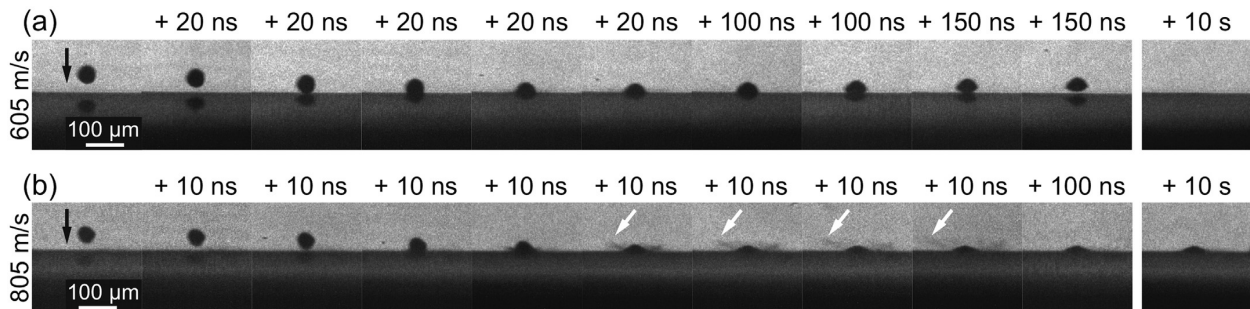


Figure 19. Multi-frame sequences with 5 ns exposure times showing 45- μm Al particle impacts on Al substrate at 605 m/s (a) and 805 m/s (b), respectively below and above critical velocity. Material jetting is indicated with white arrows [53].

Below the critical impact velocity, (Figure 19a) the spherical particle undergoes significant plastic deformation upon impact in the lower half, distorts into a hemispherical shape but does not have the ability to adhere and eventually rebounds off of the substrate. The top half of the particle shows only slight evidence of distortion. In contrast, (Figure 19b) shows significantly more pronounced plastic deformation of the entire particle, at or above the critical impact velocity, such that the

entire particle has deformed into a ‘pancake’ shape, forming a splat. The white arrows indicate material ejection and fragmentation at the periphery of the splat and in this case, the particle adheres to the substrate and does not rebound.

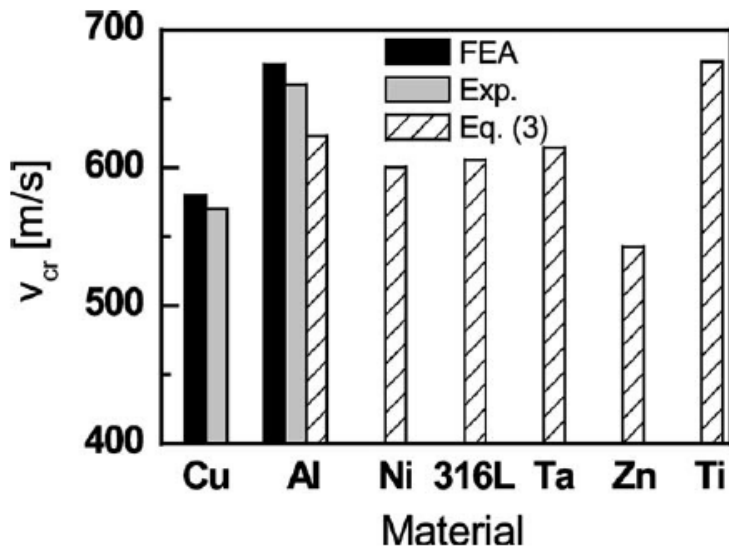
Table 5 lists values of CIV, obtained by Jae-Hwang Lee et al., and Gangaraj et al., through the single particle impact experiments in comparison to the work by Asaadi et al., using FEA and Grujicic et al., also using FEA, as well as the 1D model. The initial starting temperature of both the substrate and the particles was 295K (room temperature) for all values listed in Table 5. It is important to note that in order to make a direct comparison of all the values of CIV, other important features of the particle (i.e. oxide layer and microstructure) should be taken into account, as well as particle size. Not all of this data was included in these studies. The measurements of Gangaraj et al., confirm a shift in CIV, from 810 m/s for 14- μm particles to 770 m/s for 30- μm Al particles.

Table 5. Critical Impact Velocity for Three Pure Metals (Empirical vs. Theoretical)

Particle/ Substrate Material	Threshold particle velocity (m/s) Particle Size (μm) as denoted				
	Jae-Hwang Lee et al [142] Particle Size (μm) as denoted	Gangaraj et al., [139,53] Empirical/Actual Particle Size (μm) as denoted	Assadi et al. [54] Theoretical Particle Size <45- μm	Grujicic et al FEA [29] Theoretical Particle Size 5- μm and 25- μm	Grujicic et al. 1D [29] Theoretical Particle Size 5- μm and 25- μm
Cu/Cu	-	568 (10- μm)	570-580	575-585	571
Al/Al	830 (20- μm)	810 (14- μm) 770 (30- μm)	660-670	760-770	766
Ni/Ni	-	660 (14- μm)	600-610	620-630	634

This is consistent with the accepted notion that larger particles should have lower critical velocities due to the deformation characteristics resulting from higher momentum. However, Asaadi et al., conclude that their experimental method could not give an unambiguous correlation between particle sizes and velocities and tested particle sizes in the range of 5 to 100 μm . [54]. Grujicic et al., varied the particle size between 5- μm and 25- μm but did not report any significant differences from the results obtained using theoretical models, which is in contrast to actual results measured by the single particle impact experiments. Asaadi et al., reports that the critical velocity was determined to be 660 m/s for inert-gas-atomized 99.93% aluminum powder with a particle size below 45 μm , (see Table 6 and on pages 4383 and 4391 of ref 1.) however the values listed in the Grujicic paper (2004) incorrectly list those values as 760-770m/s. The difference between the results obtained by Asaadi (2003) as compared to those of Grujicic (2004) are approximately 100m/s and the disparity is significantly greater when compared to the values generated from the single particle experiments of Jae-Hwang (2017) and Gangaraj (2016). The empirical results clearly show a difference in CIV depending upon particle size, which raises question regarding the validity of those values of CIV generated by theoretical models, since the results are given for a particle range of particle diameters. Grujicic et al., report values for a particle range (5- μm and 25- μm) while Asaadi et al., (<45- μm).

Table 6. Critical Impact Velocity for Various Metals (Empirical vs. Theoretical) [54]



A comparison of the CIV for two aluminum particles with different diameters as reported by Gangaraj et al., is used to illustrate the importance of the particle size. Table 6 lists the CIV of an aluminum particle with a diameter of 14- μm as 810m/s, which can be compared to that of an aluminum particle with a diameter 30- μm in which the CIV is 770m/s (a difference of 35 m/s). Some of the theoretical values of CIV could compare more favorably, such as those for copper and larger particle sizes of aluminum but since the theoretical models do not delineate differences in particle size then it is not clear how such values can be of practical use.

The CIV is used to optimize cold spray process parameters and should be a useful tool to mitigate trial and error. To further accentuate the importance of particle size and the relationship to cold spray process parameters, the velocity of particles with three different diameters (15 μm , 20 μm and 30 μm) was calculated under a constant set of cold spray process parameters. The cold spray process parameters used are listed in Table 7. A graph of the corresponding exit velocities is shown in Figure 20 and was derived according to the study published by Helfritsch and Champagne [82] in which they examine the effect of particle size on velocity and deposition efficiency in the cold spray process by means of flow modeling and gas-particle dynamics.

Table 7. Cold spray process parameters used to generate Figure 20.

SPRAY MACHINE Gen III Max	
P=550 psi	T=447 C
SPRAY ANGLE 90 degrees	2 by 6.3 nozzle
VELOCITY 200 mm/sec	STANDOFF 15/25 mm
SPRAY GAS Helium	NOZZLE 2-6.3x170mm TYPE PBI-VRC
ACTUAL GUN TEMP 446.5C	PRESSURE SET POINT 550 psi
PF GAS FLOW SETTING 100 slm	MAIN GAS FLOW 1595 slm
POWDER FEEDER RATE 2-2.5 rpm	PF ACTUAL FLOW 157 slm

Particle trajectories were modeled from the nozzle chamber to the impact with the substrate. Optimum particle size was identified for various particle characteristics and spray configurations. The x-axis defines the distance away from the exit of the nozzle. The values show a large difference of approximately 200m/s when comparing the impact velocity of an aluminum particle with a diameter of 15 μ m, to an aluminum particle having a 30 μ m diameter at an exit distance of one inch, which is a typical stand-off distance between the nozzle exit and the substrate. This further substantiates the importance of considering particle size. Gangaraj et al., report these series of images as the first direct observations of the rebound-adhesion transition and of material ejection and fragmentation associated with a particle that has adhered upon impact. This study has served to provide invaluable information enabling a much more thorough fundamental understanding of the sequence of events leading to bonding during cold spray, substantiating earlier predictions and raising questions about the origin of jetting.

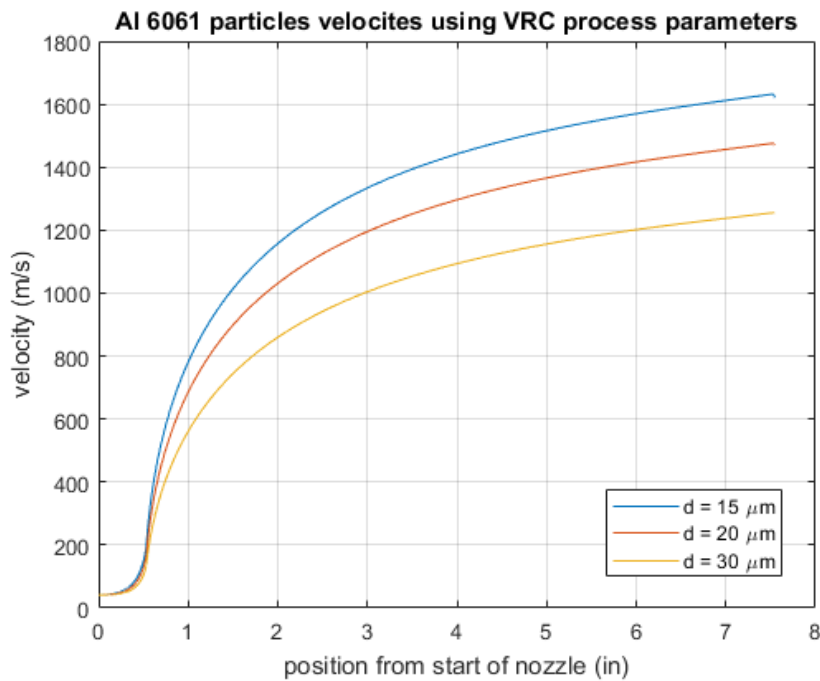


Figure 20. Graphical representation of velocity of particles with varying diameters keeping the cold spray parameters constant [144, 82].

The microstructural analysis conducted of the impact region between the particle and substrate by Gangaraj et al., has confirmed earlier observations [143,145] of the formation of material jets and have concluded that this condition is necessary to promote bonding during cold spray because the contact surfaces between particles and/or the substrate are cleaned by the action of severe plastic deformation and the accompanying ejection of oxidized surface layers, analogous to explosive welding [30,46,152,146]. The surfaces are activated by the removal of surface oxides [5,6,147,148] and atomic contact between particles and/or the substrate becomes possible, as the oxide shells are broken and the two surfaces are pressed together under tremendous pressure. Papyrin et al. reported that the dislocation density is increased by the initial impinging particles enhancing the chemical activity of the surface on the very top layer [148,149].

Previous to the work conducted by Gangaraj et al., jetting and subsequent material fragmentation were not observed in real time with micron-scale and nanosecond-level resolution, at velocities equal to those attained during the cold spray process. Gangaraj et al., argue that this observation substantiates the fact that jet formation and subsequent material fragmentation is triggered at the critical impact velocity, and that this is directly associated with adhesion [53]. The authors also make a comparison to the phenomenon of jetting that takes place in liquid drops [150,151], whereas conservation of volume requires that the contact area of the periphery of the particle laterally accelerates upon impact [53]. This principal is true for either a fluid or a solid and the resultant lateral velocity along the contact edge approaches infinity during the initial contact and is higher than the shock wave that is generated upon impact [53]. Subsequent to particle impact, the shock wave is attached to the leading edge but as the lateral velocity at this region falls below that of the shock wave, a reflective wave or as Gangaraj et al., refer to it, a ‘release’ wave is reflected back into the particle. This causes a localized area to be subjected to extremely high tensile forces, which in turn forms a jet and leads to material fragmentation. Gangaraj et al., argue that adiabatic localization is not the cause of material jet formation, although it may be a consequence and occurs as the jet expands further [53] which contradicts Grujicic et al., as well as many other subsequent researchers. Instead, Gangaraj et al., propose that the primary cause of jetting and material fragmentation and ejection is the result of a high intensity pressure wave that interacts with the leading edge of an impacting particle just a few nanoseconds after the initial contact [53]. These authors further explain that subsequent to the action of the high intensity pressure wave, the increase in temperature between contact areas resulting in shear localization, melting, and/or viscous flow are most likely, trailing consequences of extensive jetting.

3.0 Experimental Approach

This thesis was comprised of five major stages (Figure 21) consisting of (1) Characterization of as-received gas atomized powder, (2) Performing controlled exposure tests to form a prescribed oxide and/or hydroxide using dry air at elevated temperatures for four powder groups and humidity at room temperature for three powder groups, (3) Conducting single particle impact experiments of all seven powder groups, as well as the as-received powder, (4) Cold spraying to produce bulk samples for testing and (5) Materials characterization of all powders subsequent to and after (a) the temperature and humidity exposure tests, (b) the single particle impact tests and (c) of the cold spray bulk samples.

3.1 Design of Experiment

Published literature regarding the oxidation kinetics of aluminum powder discussed the complexity and variation associated with the growth and change in oxide/hydroxide over time, temperature and exposure to oxygen and/or water vapor. The initial oxide layer is amorphous, which transforms into γ -Al₂O₃ at elevated temperatures and increased oxide thicknesses [153]. Research has shown the formation of hydroxides of Al powders at room temperature, in the presence of water vapor. The oxidation reaction products are aluminum oxide and varying concentrations of hydrated Al oxide incorporated into an amorphous oxide surface film.

There are fundamental differences in the oxide/hydroxide on the powder formed at various temperatures and the progression in the nature of the surface film as the temperature increases. For instance, the oxide is amorphous at low temperature up to about 300°C. Above 300°C it starts to turn to gamma alumina and crack, which increases the oxidation rate slightly. There are various other changes at higher temperatures, such as cracking of the alumina due to thermal expansion close to the melting point, causing more rapid oxidation. Hongqi Nie et al., [153] measured net mass gain of pure Al powder using Thermo-gravimetric techniques which compared favorably to calculations using oxidation kinetics (Figure 22 and Figure 23). These results assisted in the determination of appropriate time and temperature exposure tests which are commensurate with the range of the cold spray operating parameters. The work of Flumerfelt, [21] formed the basis of the humidity exposure tests for the HP aluminum powder.

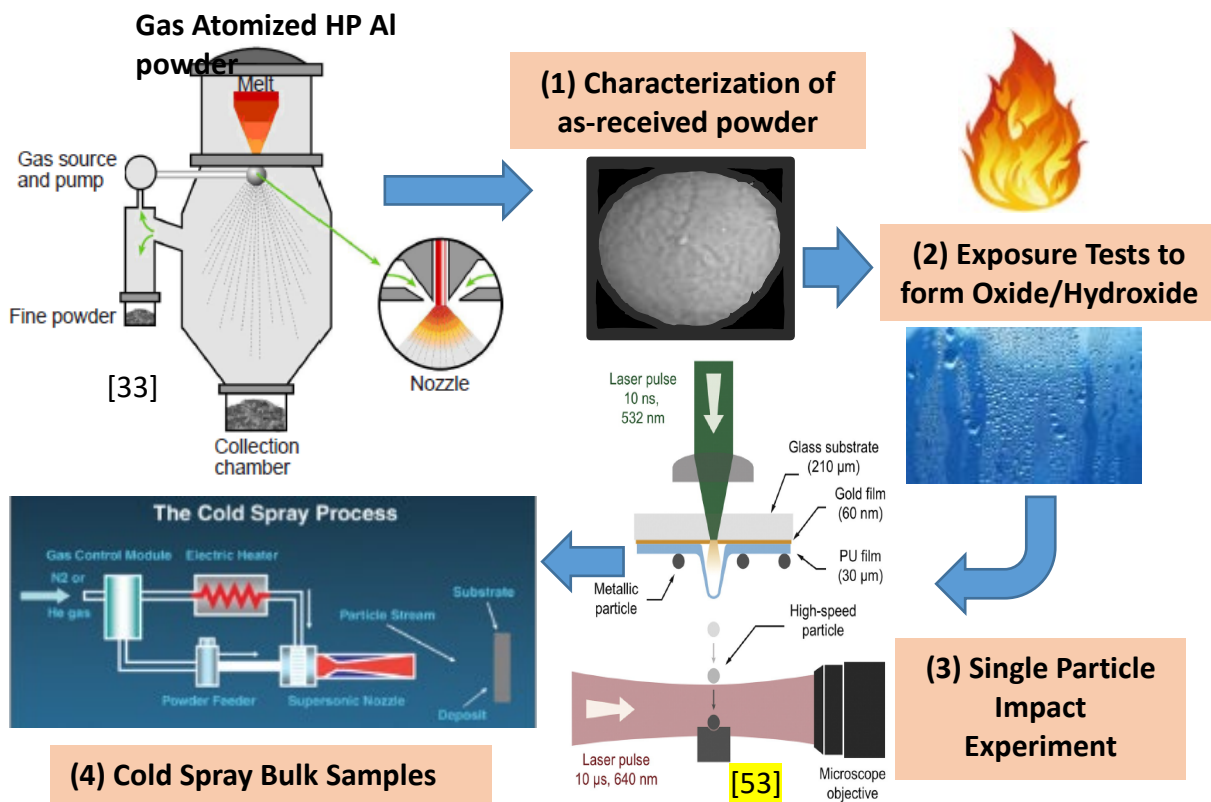


Figure 21. Schematic showing the major stages of the proposed research.

Hongqi Nie et al., studied the reaction kinetics for pure aluminum powders and compared predicted results from an oxidation model to measured oxidation rates from literature, using thermo-gravimetric methods for micron and nanosized and aluminum powders. Exposure tests were performed on aluminum powder heated at 20 K min⁻¹ to different temperatures. The powders were initially heated in an argon environment until the target temperature was reached and afterwards oxygen was introduced for a prescribed time period. Precise time at temperature exposures were accomplished in this manner. Figure 22 and Figure 23 show the results.

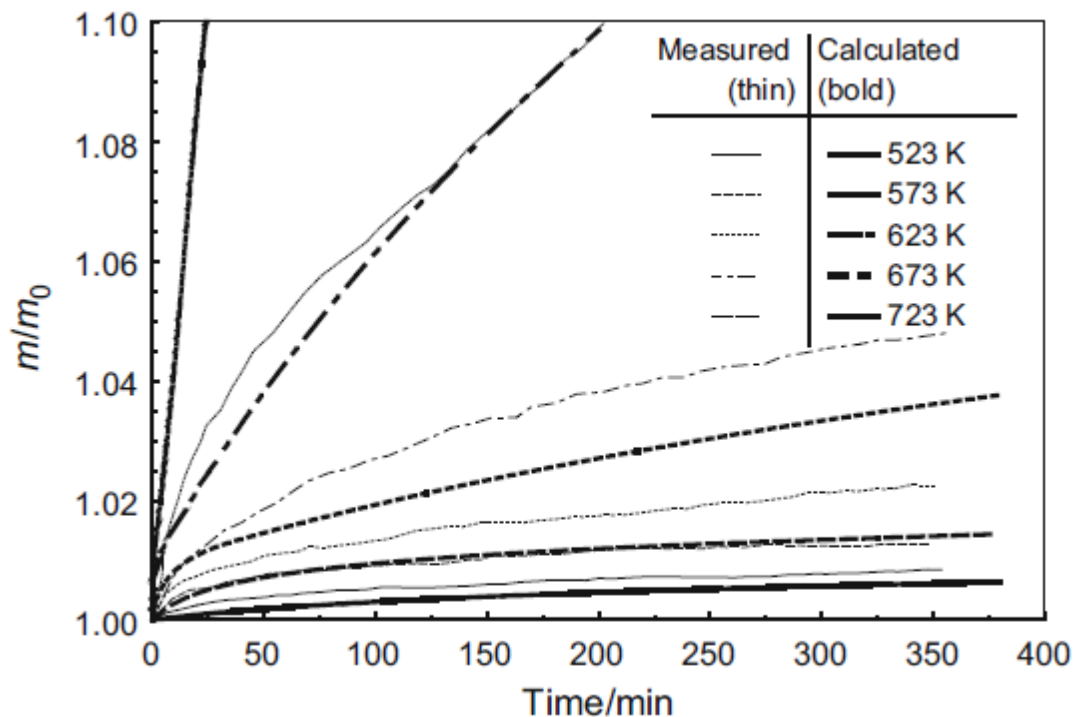


Figure 22. Measured isothermal TG traces of pure aluminum and theoretical calculations using kinetics by Hongqi Nie et al., for respective temperatures [153].

3.2 Test Procedure

Place High Purity (HP) gas atomized, aluminum powder (as received from the powder supplier and stored with desiccant packs), in the apparatus as shown in Figure 24. This apparatus was designed and fabricated specifically for this thesis research and incorporated a fluidized bed for the heat treatment of powder. The operation of this device included the supply of a fluidizing gas to the base of the device constantly maintaining motion of the powder. The gas used was either argon, air or humidified air, as specified in the DOE.

Two methods for developing oxides on the surface of powders were evaluated as part of this study. The first used dry air at temperature, while the second used humidified air. In the dry air case, the experiments ran as follows. Dry argon was fed into the fluidized bed reactor fluidizing the powder while the temperature of the reactor and the fluidizing gas was increased at a rate of approximately 10°C/minute to 300°C. Once at temperature, the argon flow was maintained for 30 minutes to ensure that the entire reactor and all of the powder reached a stable 300°C. The argon was then shut off and replaced with a flow of dry air for the prescribed period of exposure, as shown in Table 8. At the completion of this time, the flow was switched back to argon and maintained until the reactor was at temperature for a total of 4.5 hours, including the 30 minute soak then an additional 4 hours at temperature. The argon flow was continued during the cool down at approximately 10°C/minute. Once cool, a valve was closed on the vessel trapping argon inside. The entire apparatus was transferred into a dry nitrogen or dry nitrogen glovebox and the powder

inside was placed into bottles, which were distributed to the participants of the research team to perform tests and characterization of the powder.

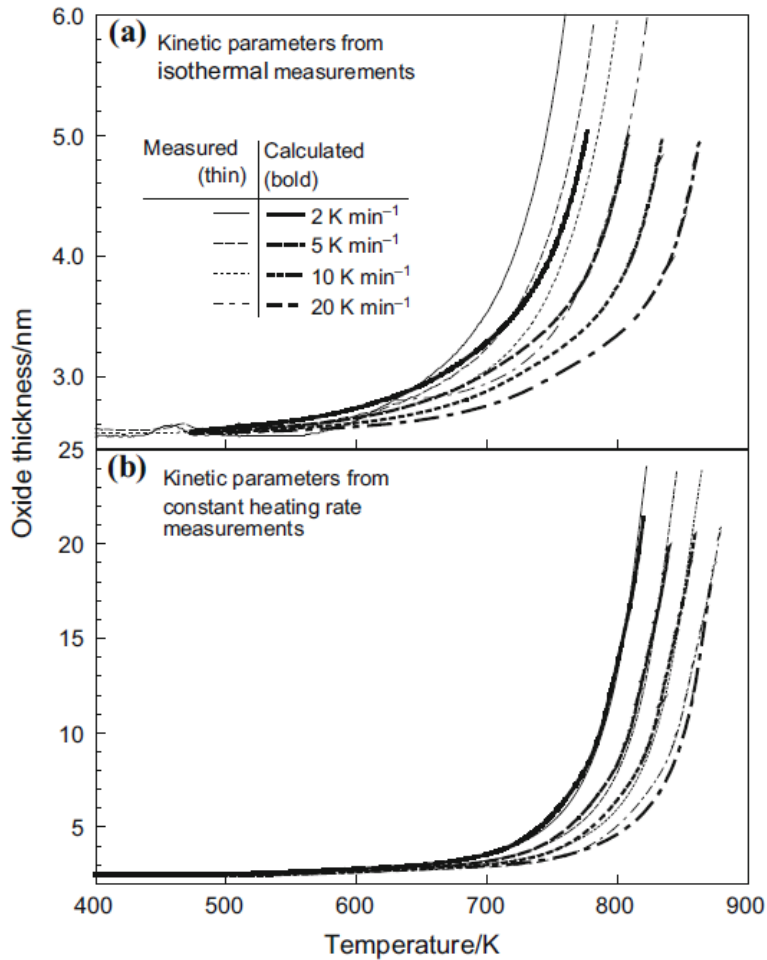


Figure 23. Aluminum oxide thickness as a function of temperature for constant heating rates. Thin lines represent measurements; bold lines show calculations. Calculations are based on kinetics derived from isothermal measurements and b constant heating rate measurements [153].

The humidity exposure tests utilized a similar setup and the same fluidized bed, but incorporated two air flow valves, as shown in Figure 25. One of these valves ran through a humidifying water bubbler and both ran into a mixing chamber with a humidity and temperature sensor. From this mixing chamber the mixed air at the correct temperature and humidity level flowed into the bottom of the fluidized bed. The mixing chamber as well as the fluidized bed, were all contained inside an insulated box with a low temperature heating element. Exposure conditions were either 50% or 95% relative humidity and 29°C as shown in Table 9. These humidity levels represent laboratory conditions (50%) and those that are typical (95%) at Corpus Christi Army Depot or Pearl Harbor Naval Shipyard, where cold spray facilities are located.

Table 8. Heat Treatment of Aluminum HP Powder under dry conditions

Powder Group Identification	Exposure Times to Dry Argon at 300°C	Exposure Times to Dry Air at 300°C
HT-Baseline	270 minutes	0 minutes
HT-30	240 minutes	30 minutes
HT-60	210 minutes	60 minutes
HT-240	30 minutes	240 minutes

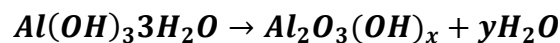
Table 9. Exposure of Aluminum HP Powder under humid conditions

Powder Group Identification	Humidity / Temperature	Exposure Times to Air at 29°C	Exposure Times to Helium at 450°C	Powder Condition
As-received	No Exposure	No Exposure	No Exposure	As Received
RH-50%	50% RH / 29°C	4 days	No Exposure	As Received
RH-95%	95% RH / 29°C	4 days	No Exposure	As Received
RH-95%-450	95% RH / 29°C	4 days	2 seconds	As Received

Table 9 lists exposure times of the HP-Al powder to air at two humidity levels (50% RH and 95% RH) at a temperature of 29°C, in order to investigate the growth of hydroxides to powder that has been opened in a hot, humid environment. The time durations were selected based upon previous research [21] and were also meant to simulate the conditions that might occur at actual cold spray facilities. Powders are contained in plastic bottles, bags and buckets of various sizes and are typically not used up in a single spray operation. In fact, most metal cold spray powders do not have a specified shelf life and as such, are sometimes kept for many months or even years before being totally consumed or discarded due to poor flowability or performance. Therefore, the powder will be repeatedly exposed to hot, humid conditions and adsorb water vapor in the process of being opened and reopened.

Table 9 also contains a special group (RH-95%-450) which represents HP-Al powder that has been exposed to hot, humid conditions and subsequently used in the cold spray process. The short exposure to elevated temperature (2 seconds) of this powder simulates the time that it would remain in a heated helium gas stream during the cold spray operation and Figure 26 depicts the apparatus that was used to accomplish this. The 2 second time duration is ample time to allow partial dehydration, based upon the dehydration kinetics reported by L. Rozic et al., who investigated the dehydration kinetics of gibbsite to activated alumina at four different temperatures, as summarized in Table 10 [154].

These researchers concluded that thermal treatment of gibbsite results in its partial dehydration which can occur within seconds of exposure, as listed in Table 10. The extent of gibbsite amorphization is affected by its physico-chemical properties and the exposure conditions (temperature, atmosphere, and exposure time) [155,156].



[154,155,156]

Table 10. Dehydration of Gibbsite $\text{Al}(\text{OH})_3$ to alumina [154]

Converted (%)	Temperature (°C)	Residence Time (seconds)
90	450	17
	500	8
	600	2.5
	650	1.5
25	450	2

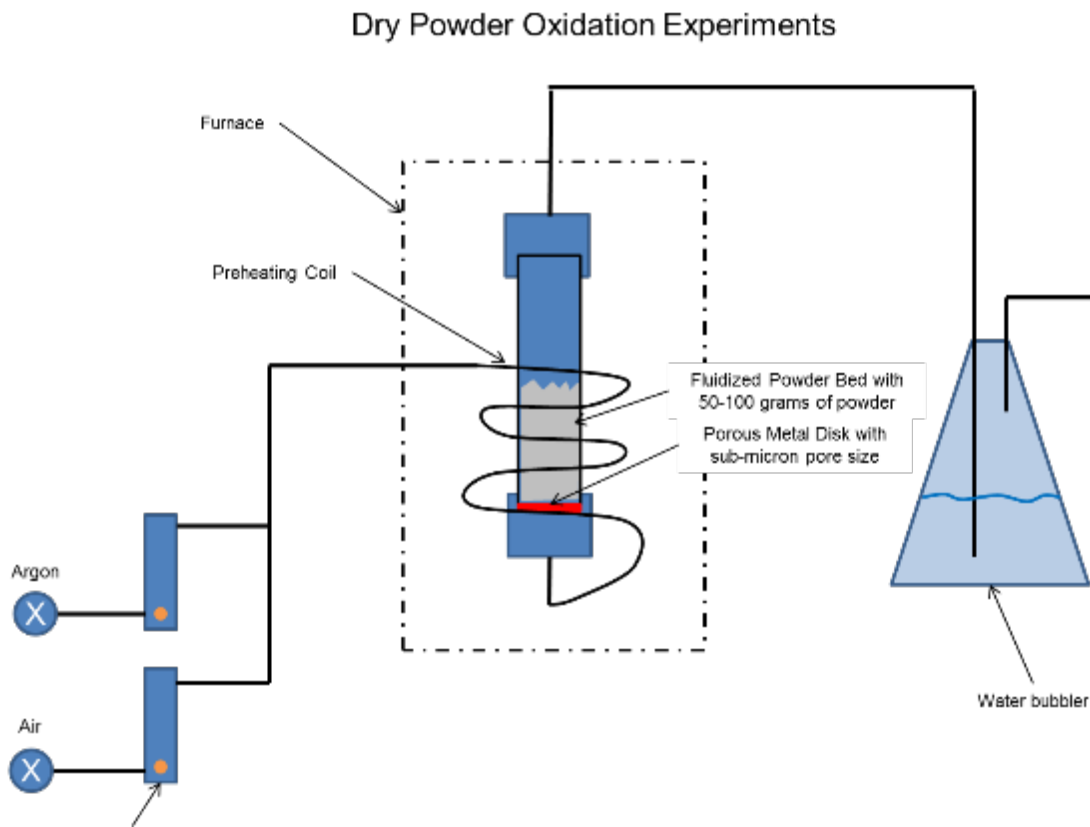


Figure 24. Apparatus to perform elevated temperature exposure tests on powder.

Humid Powder Oxidation Experiments

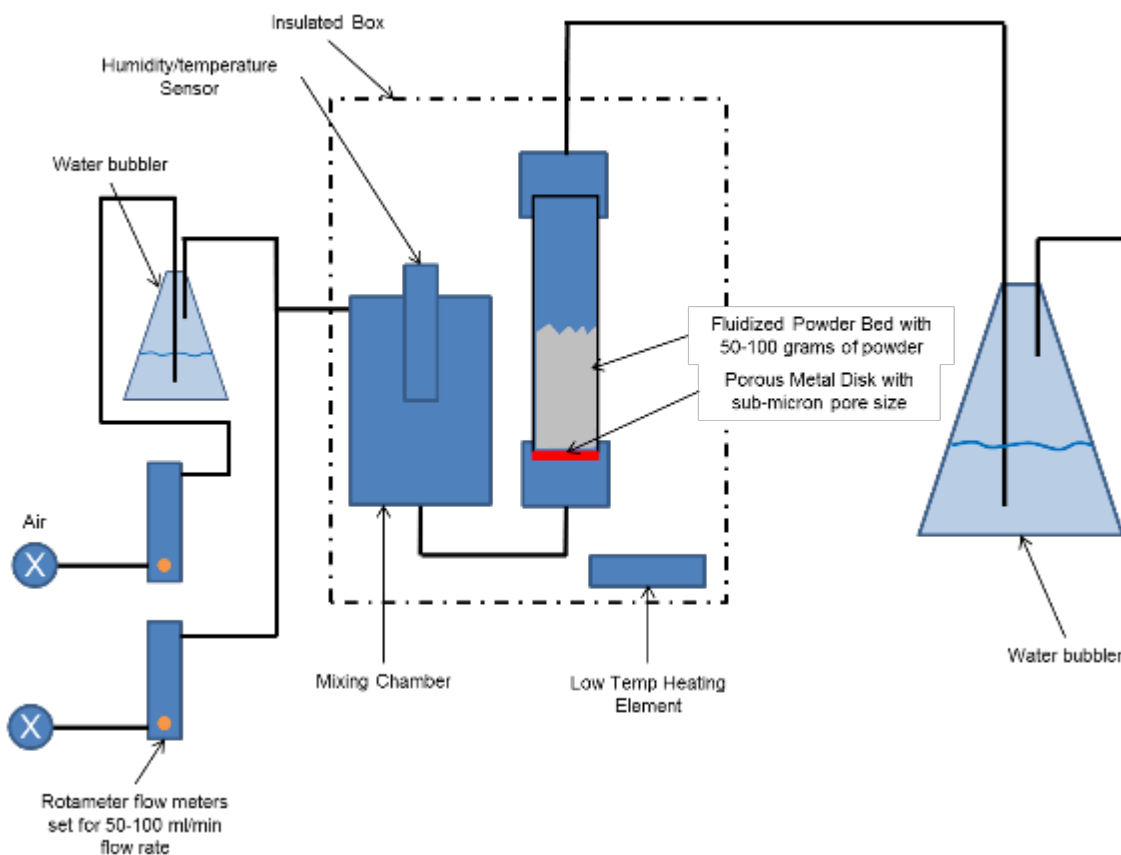


Figure 25. Apparatus to perform humidity exposure tests on powder.

Extensive characterization was performed prior and subsequent to single particle impact experimentation through a collaborative effort from a variety of academic and industry research facilities. Specifically, the US Army research Laboratory (ARL), United Technologies Research Center (UTRC), Worcester Polytechnic Institute (WPI), University of Massachusetts, (UMass), Bucknell University, University of Connecticut (UConn), University of California, Irvine (UCI) and Massachusetts Institute of Technology (MIT). Analytical techniques including X-ray photoelectron spectroscopy (XPS), inductively coupled plasma mass spectrometry (ICP-MS), direct current plasma emission spectroscopy, inert gas fusion (IGF), differential scanning calorimetry (DSC), thermogravimetric analysis (TGA), electron energy loss spectroscopy (EELS), transmission electron microscopy (TEM, high angle annular dark field scanning transmission electron microscopy (HAADF-STEM), auger analysis, focused ion beam (FIB) scanning electron microscopy (SEM) and Fourier Transform Infrared Spectroscopy (FTIR Analysis) were performed to determine the species of oxide and/or hydroxide, bulk chemical composition, oxygen content and thickness of the surface oxide/hydroxide layer. Samples of impacted particles bonded to a commercially pure (CP) Al substrate were also studied and the deformation characteristics recorded. Microprobe analysis was conducted at areas of interest along the particle/substrate bond line to determine the chemical composition and contrasted against that of the substrate and HP Al

particle. Microstructural features influencing bonding were subsequently identified and characterized.

Bulk samples of material were produced from each powder group by the cold spray process. The main gas temperature used to cold spray Al, under standard industrial operating conditions, was in the range of 300°C-450°C, and its influence on oxide formation was incorporated into the design of experiment (DOE). The tensile properties from the bulk material were measured and used as an indicator of the influence of the surface film on the mechanical properties, especially the ductility. The bulk samples were produced from powder representing select test groups and also characterized to determine hardness, chemistry, microstructure and conductivity.

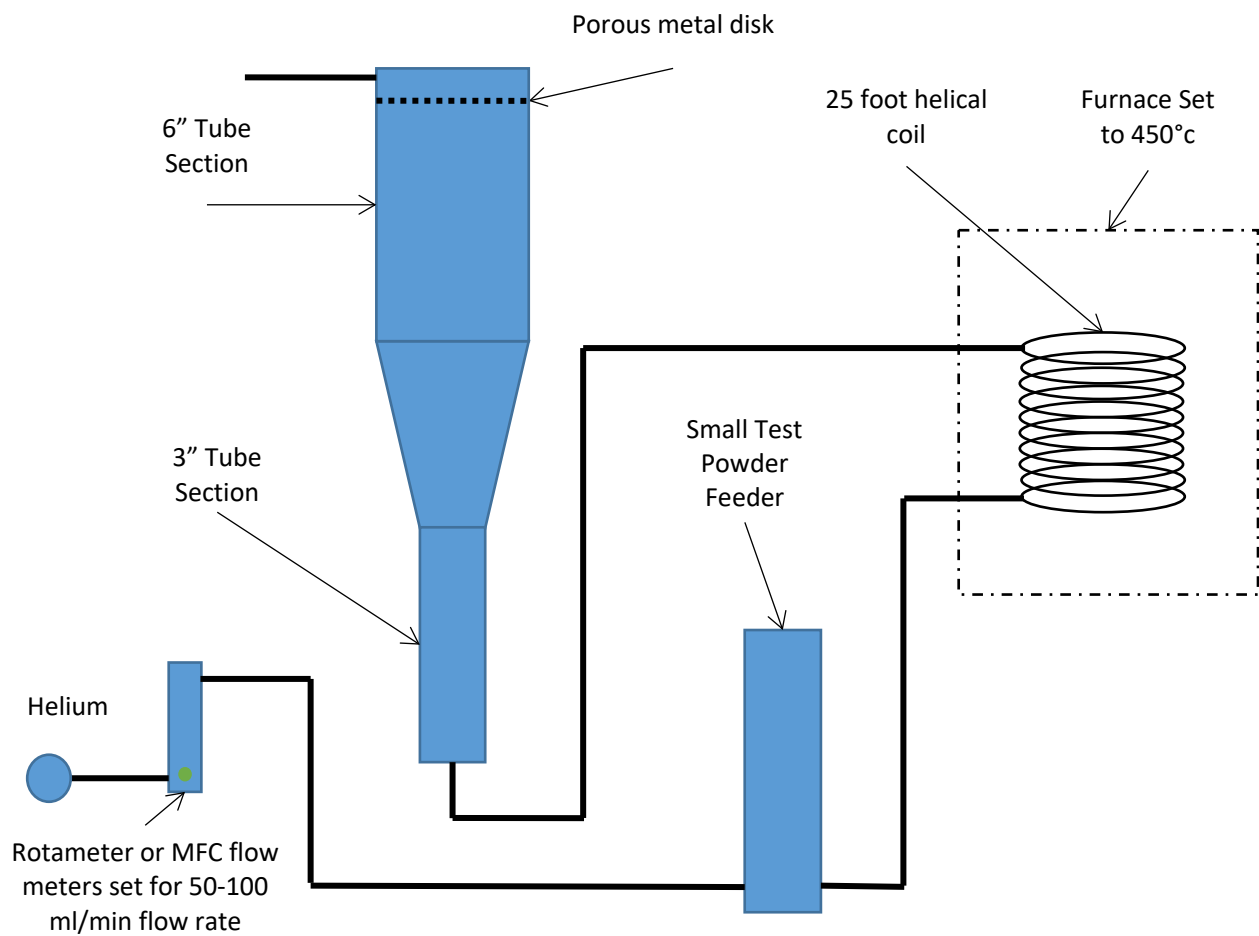


Figure 26. Apparatus to perform short duration temperature exposure test on powder.

The heat treated HP aluminum powders under dry and humid conditions were performed as described and the powders were kept in a glove box under nitrogen flow to keep them dry and protect them from the environment.

The flow of the dry and wet stream were 1000 mL/min and 60 mL/min, respectively, for the powders treated under humid conditions. The humidity levels ranged from 14% to 75% at 80°F for the RH-50% sample. After 4 days of exposure to humidity, the wet stream was closed and the humidity chamber temperature was raised to 100°F for 2 hours to remove any excess of water. The removal of the powder from reactor was easy, the powder was still loose (see Figure 27a). The powder was placed in a mortar and pestle and passed through a -270 mesh sieve.

The flow of the dry and wet stream were 300 mL/min and 750 mL/min, respectively, for the RH-95% samples. Humidity ranged between 87-93% at 89°F. After 4 days of exposure to humidity, the wet stream was closed and the humidity chamber temperature was raised to 100°F for 2 hours to remove any excess of water. However, the removal of the powder was difficult due to solidification of the powder inside the reactor. The powder was broken up and put in a mortar & pestle and passed through a -270 mesh sieve (see Figure 27b and Figure 27c).

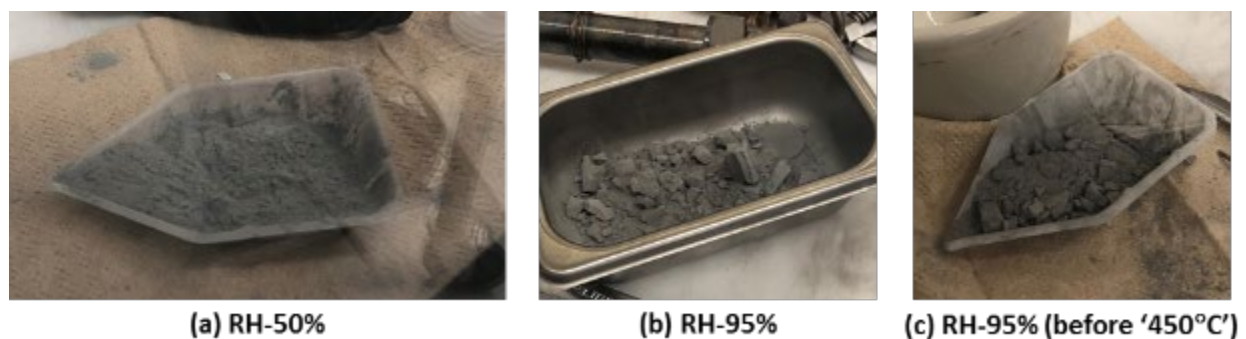


Figure 27. Appearance of powder after exposure to humid conditions.

3.2.1 Sequence of Tests Performed

UTRC completed the powder exposure tests and the powder was placed in small glass vials that were purged with inert gas (nitrogen) to keep them preserved prior to testing. Immediately thereafter approximately 10 grams of each powder were sent to each test facility. WPI, UCI and Bucknell analyzed the powder for chemical composition, species of surface film and nanohardness. Single particle experiments were performed at MIT and UMass. Splat samples representing single particle impacts on HP Al substrates were sent to UConn for examination. UTRC produced cold spray bulk samples and measured conductivity and bulk cold spray samples were sent to UConn for micro-tensile testing.

3.2.2 Analytical Testing Roles and Facilities

UTRC and ARL: The role of UTRC was to perform all exposure testing and then characterize the powders through XPS and Auger analysis. Additionally, metallographic examination was performed on each powder group and the hardness was measured. Small bulk samples of material representing each powder group were consolidated by the cold spray process for micro-tensile testing at UConn. UTRC also measured the electrical conductivity using eddy current. In addition, UTRC bottled and shipped samples of each powder to each of the universities involved in glass vials purged with nitrogen to prevent any further oxidation. *The instructions to each test facility was to consume the powder samples immediately upon opening.*

The X-ray Photoelectron Spectroscopy (XPS) characterization was used to understand the near surface composition and thickness of oxygen containing species associated with the dry HP aluminum powders. A small sample of each batch was transferred from the glovebox, where they were stored in dry nitrogen following processing, to the XPS vacuum chamber in a sealed sample transfer vessel that was specially designed to keep the samples from atmospheric exposure. With each sample, a suitably large powder particle was selected for analysis under a 20 micron monochromated aluminum X-ray beam and a larger area analysis of 300x300 microns around this particle was concurrently performed. Specific analysis included surface elemental analysis, surface high resolution (binding energy) analysis and depth profile through any oxygen containing layer. The data from this effort provided elemental atomic ratio of elements, relative binding energy differences, a connection between binding energy and bonding states based off of literature references and an understanding of the thickness of any oxygen modified surface.

WPI: WPI performed bulk powder characterization through DSC and TGA analysis. Additional powder samples were sent to Luvak for IGF to quantify both the chemical composition and the oxygen gas content of the powder and cold spray bulk samples.

Bucknell: The Role of Bucknell University was to perform FIB/SEM and TEM examinations of the powders produced looking primarily for oxide/hydroxide thickness and identification of phases. The analysis described below is for a single location on a single particle of each powder condition provided. Additional analysis was conducted on more sites from down-selected samples after initial results were obtained to obtain a better representation of the species and thickness of the surface film.

Task 1: Specimen preparation- *Cryogenic FIB was used to avoid heat generation during sample preparation which may affect oxide layer.*

Task 2: Cryo TEM analysis- A Talos TEM at 200kV was used. TEM high resolution (HRTEM) was used to locate lattice fringes and measure the size of oxide layer on a single particle. The oxide layer was also identified as crystalline or amorphous.

Task 3: Identification of and quantification of species (oxide and hydroxide analysis)- STEM-EDS and STEM HAADF was utilized with rastering across a 5 um x 100nm thick area getting a map of the species over a wide area. An attempt was made to analyze for differences on the surface of the powders, particularly regarding oxides and hydroxides such as Gibbsite, $\text{Al}(\text{OH})_3$ (one of the mineral forms of aluminum hydroxide) and Diaspore (aluminum oxide hydroxide mineral). Any differences in the interiors of the particle which correlate with the secondary phases were noted and quantified. It was anticipated that there would be an observable larger secondary phase on the powder surface as a function of exposure time. The surface was also evaluated in regards to roughness and uniformity. A STEM image was acquired by displaying the integrated intensities of the electrons in synchronism with the incident probe position. EDS mapping was performed at the edge of particles in an attempt to detect surface oxide and mapping of various elements. A line scan was generated across the surface of the oxide layer to quantify elemental amounts.

Task 4: FTIR Analysis (Fourier Transform Infrared Spectroscopy) – was utilized to complement the TEM analysis; infrared spectrometry is ideal for the identification of functional groups present within a sample. This analysis technique assisted with determining and quantifying the species of oxide and/or hydroxide in the surface layers of particles by identifying differences in acquired mid-IR and near-IR spectra. The microscope was equipped with brightfield, darkfield, and fluorescence illumination as well as polarization capabilities to enhance contrast and facilitate sample visualization. In addition to single point measurements, more extensive imaging was also used to map species across the particles with a positioning accuracy of $\pm 3 \mu\text{m}$. Diffraction limited mid-IR imaging was executed in areas as large as $340 \times 340 \mu\text{m}$ to obtain an accurate representation of the species which comprised most of the surface area of particles in each condition.

UConn: UConn performed characterization experiments on the HP Al powders supplied by UTRC and perform micro-tensile tests on bulk cold spray samples representing each powder group.

Task 1: Powder Characterization. As-atomized and exposed powders produced at UTRC was provided to UConn. Examples of each powder were cross-sectioned by FIB and examined in SEM and STEM. The aim was to measure the thickness of the oxide/hydroxide layer; to reveal the crystallinity (if any) of the layer; and to map the chemical species present in the layer using EDXS and EELS. These data was then compared with the XPS data from UTRC and UCI, as well as the TEM data from Bucknell to determine the initial state of the powder surface layers prior to cold spraying.

Task 2: Characterization of Single Particle Impacts. Examples of single-particle impacts on CP-Al substrate representing conditions above the critical velocity as determined by UMass/MIT, were provided for analysis. The splats were sectioned by FIB and examined in SEM and STEM. The emphasis in these studies was to determine the character of the oxide/hydroxide layer at the particle/substrate interface. The thickness, crystallinity and chemical species of the layer at this interface were compared with the data from the corresponding feedstock powder in Task 1.

Task 3: Mini-Tensile Testing. Bulk cold spray samples produced by UTRC were machined to a scaled-down version of the ASTM standard E8 geometry (Figure 27). A total of 3-5 samples were produced from each powder. These samples were provided to UConn for testing. The tensile specimens were tested to failure using digital image correlation to monitor strain (since the gage length was too short to allow for the use of an extensometer). The fracture surfaces of failed samples were examined to determine the origin of the fracture. Where fracture initiates within the sample, the origin site will be sectioned by FIB and examined in SEM and STEM. The objective will be to compare the character of these sites with the oxide/hydroxide layer characteristics determined in Task 1.

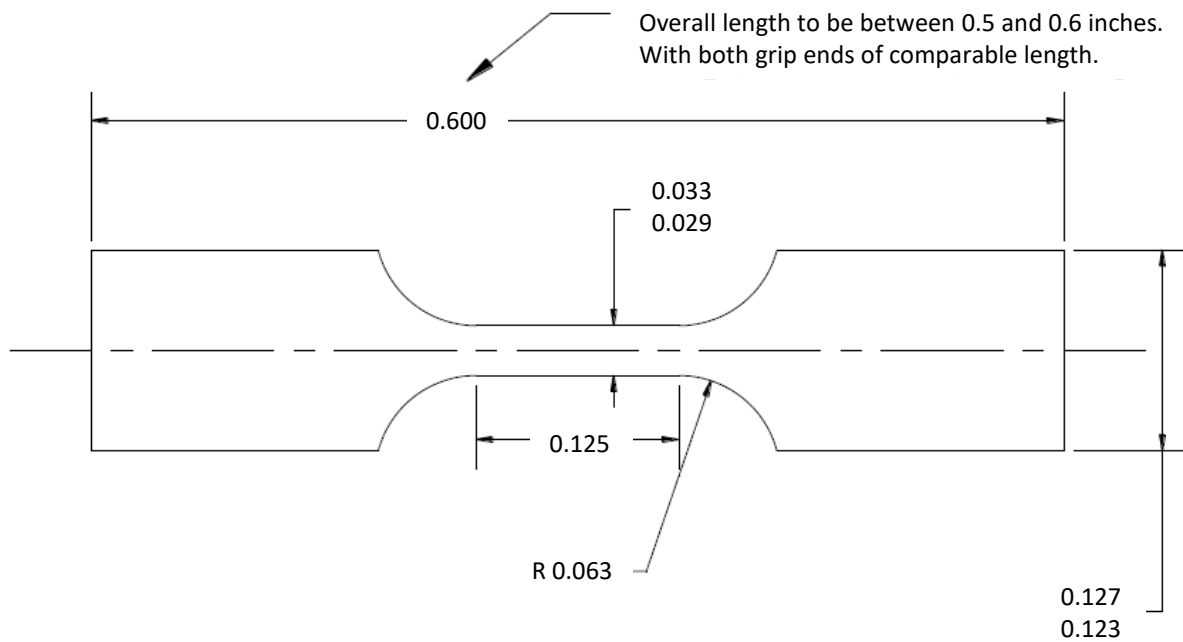


Figure 28. Mini-tensile specimen for characterization of bulk cold spray material.

UCI: UCI performed characterization experiments on the HP Al powders supplied by UTRC.

Task 1: XPS. To determine oxide chemistry and microstructure as a function of oxide depth, allowing distinction of oxides from hydroxides.

Task 2: TEM. To analyze the oxide scales and obtain accurate thickness and assess whether these layers are amorphous or crystalline. In addition, analysis of the EELS data will provide information about the nature of these layers through analysis of oxidation states.

MIT and UMass: The roles of both MIT and UMass were to conduct the single particle impact experiments to determine the critical impact velocity for each powder. These experiments commenced using the powder in the as gas-atomized condition, from the powder supplier (Valimet Corporation, CA) to determine a baseline critical impact velocity. Then the CIV was determined of powders representing the exposure test groups.

4.0 Experimental Results

4.1 Characterization of HP Aluminum Powder Groups

4.1.1 Particle Size Distribution

The as-received (AR) -270 mesh, high purity (HP) aluminum powder was obtained from Valimet Inc., Stockton, CA and the actual inspection certification is shown in Figure 29. The certification shows the chemical composition at 99.98 wt. % pure aluminum with trace amounts of Fe (73ppm), Cu (14ppm), Mg (5ppm), Si (82ppm), Ti (2ppm), V (7ppm) and Zn (3ppm).

The aluminum powder chosen was produced according to the MIL-DTL-32495A titled, “Powders for Cold Spray Deposition”, written and maintained by the US Army Research Laboratory and is used across the globe. This specification covers all cold spray powders used by industry, Government research laboratories, depots, shipyards, air bases and academia. Therefore, it is representative of the user community.

Table 11 shows a particle size distribution (PSD) of the AR powder, as determined by a Microtrac analyzer, which uses three precisely placed red laser diodes to measure particle diameters in the range of .02 -2,800 microns in diameter. Powder that conforms to a 270 mesh size equates to a particle diameter of 53 μm or 0.0021 inches. The PSD indicates that ~97% of the particles are below 50 μm , which was anticipated from a -270 mesh size.

Table 11. Particle Size Distribution

Size(μm)	%Tilt
1.000	0.00
2.000	0.00
5.00	4.39
10.00	20.17
15.00	37.76
20.00	56.19
25.00	72.16
30.00	82.98
50.00	96.78
100.0	100.00

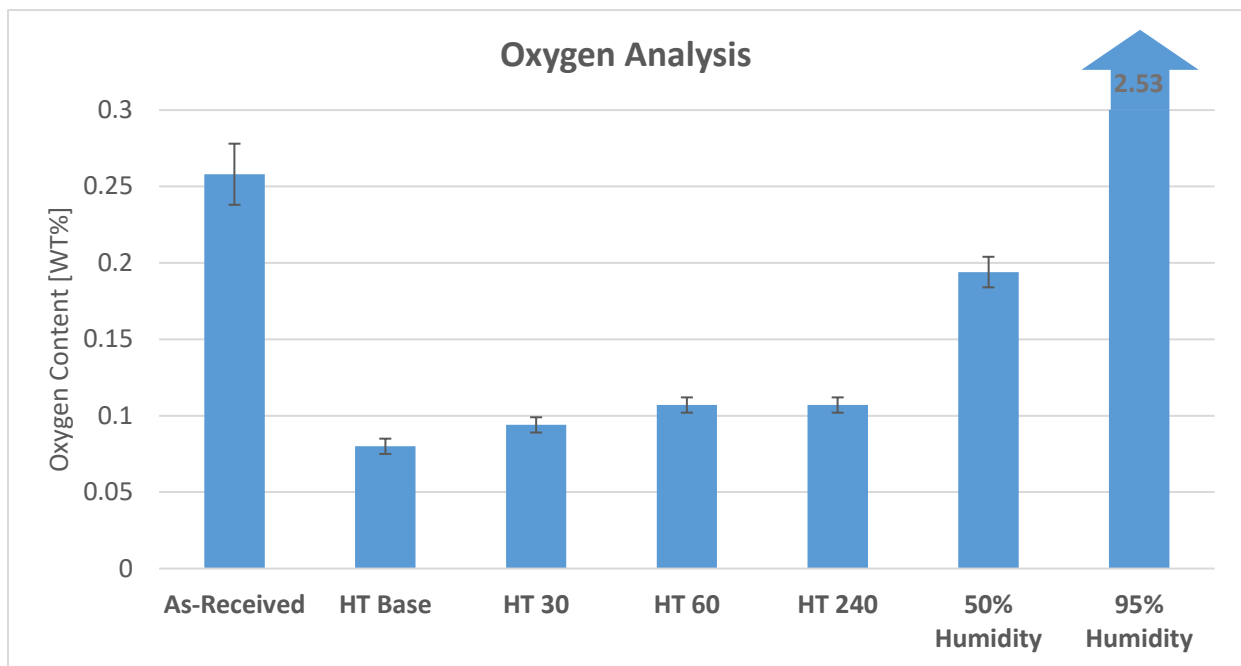
4.1.2 Inert Gas Fusion (LECO Elementrac ONH-p)

The oxygen and nitrogen content of all powders was measured by LUVAK, MA using the requirements outlined in ASTM E 1019-11, “*Standard Test Methods for Determination of Carbon, Sulfur, Nitrogen, and Oxygen in Steel, Iron, Nickel, and Cobalt Alloys by Various Combustion and Fusion Techniques*”. The LECO Elementrac ONH-p instrument was used and determines oxygen and nitrogen in inorganic samples by inert gas fusion using an impulse furnace with temperatures in excess of 3,000 °C. Table 12 lists these results.

Table 12. Inert Gas Fusion Measurements of Oxygen of All Seven Groups of Powders

Sample	Oxygen Composition WT%	Tolerance WT%
As-Received	0.258	0.02
HT Base	0.08	0.005
HT 30	0.094	0.005
HT 60	0.107	0.005
HT 240	0.107	0.005
RT 50	0.194	0.01
RT 95	2.53	0.05

Table 13. Graphical representation of the measurements from Table 12 for ease in comparison. Bar representing sample RH95% has been truncated to allow the remaining groups to be plotted.



4.1.3 Inert Gas Fusion (LECO ONH836)

The LECO ONH836 was used by ARL to measure the hydrogen content of the powder samples (only .1 g of powder required). It is an analytical combustion method that utilizes an electrode furnace, inert carrier gas, and both infrared and thermal conductivity detection to simultaneously detect oxygen, nitrogen, and hydrogen. A high-power electrode furnace quickly releases the target gases from within the powder sample and the measurement is taken very efficiently in about 3.5 minutes [157]. Table 13 lists the instrument used and the test method and standards required, based on recommendations from LECO, the manufacturer.

Table 14. Summary of Inert Gas Fusion (IGF) Test Apparatus, Methods and Standards

Instrument:	LECO 836: Oxygen/Nitrogen/Hydrogen by Inert Gas Fusion Infrared and Thermal Conductivity Detection
Method:	Based on application note 203-821-427: Oxygen, Nitrogen, and Hydrogen in Refractory Metals
Standards Used:	Titanium 502-891; Titanium 502-888

Table 14 shows the concentrations of oxygen, nitrogen and hydrogen obtained from IGF measurements of the titanium samples (502-891) and (502-888). The titanium standards used were most appropriate for the as-received (AR) powder sample but less so for the sample exposed to high humidity (RH95). To improve this data, standards with higher hydrogen and oxygen concentrations are required but the results can be used for good comparisons between groups.

Table 15. Inert Gas Fusion (IGF) of Calibration Standards

Std. 502-891

Element	Composition	Unit	Used for Calibration? (Y/N)
O	0.117 ± 0.009	wt.%	Y
N	0.010 ± 0.001	wt.%	N
H	101 ± 8	ppm	Y

Std. 502-888

Element	Composition	Unit	Used for Calibration? (Y/N)
O	0.353 ± 0.009	wt.%	Y
N	0.006 ± 0.001	wt.%	Y
H	24 ± 4	ppm	N

Table 15 and Table 16 list the results of the as-received AR powder and RH95, which was exposed to 95% relative humidity for 4 hours. Table 17 is a summary of the average content of oxygen, nitrogen and hydrogen from both sets of samples. AR powder represents HP-Al powder obtained directly from Valimet, the supplier without any type of exposure to temperature or humidity (besides that associated with the gas atomization process, as well as shipping, storage and handling).

Table 16. LECO ONH836 Inert Gas Fusion Measurements of Powder AR

Sample Number	Weight (g)	Oxygen (wt.%)	Nitrogen (wt.%)	Hydrogen (ppm)
1	0.1064	0.422	0.00557	152
2	0.1219	0.417	0.00727	151
3	0.1025	0.405	0.00946	150

Table 17. LECO ONH836 Inert Gas Fusion Measurements of Powder RH95

Sample Number	Weight (g)	Oxygen (wt.%)	Nitrogen (wt.%)	Hydrogen (ppm)
1	0.1231	2.54*	0.0431*	2410*
2	0.1213	2.83*	0.0467*	2450*
3	0.1221	2.26*	0.0351*	2400*

Table 18. Comparison of Inert Gas Fusion Measurements of Powder AR and RH95

Sample	Oxygen (wt.%)	Nitrogen (wt.%)	Hydrogen (ppm)
(AR) As-Received	0.415 ± 0.009	0.00743 ± 0.00195	151 ± 0.707
(RH-95%) Relative Humidity 95%	2.54 ± 0.285*	0.0416 ± 0.00594*	2420 ± 26.5*

Note the great disparity in hydrogen content, as well as in oxygen content between powder samples AR and RH95. The hydrogen measurements were extremely important in delineating the difference between oxygen representative of an oxide species and that indicative of a hydroxide.

4.1.4 Differential Scanning Calorimetry

DSC was performed using a TA Instruments Discovery DSC with LN2P cooler. DSC was used to measure the difference in heat flow rate between the powder sample and the reference, as a function of time and temperature. The heat flow is dictated by whether the samples undergoes an exothermic or endothermic reaction, (i.e. as a result of melting or a crystallographic phase change) [158,159]. Samples were placed in alumina crucibles and sealed with hermetic lids. Scans were

run with a nitrogen purge gas at 50mL/min at a scanning rate of 10°C/min. Laboratory test conditions for temperature and humidity were 73°F and 58% respectively.

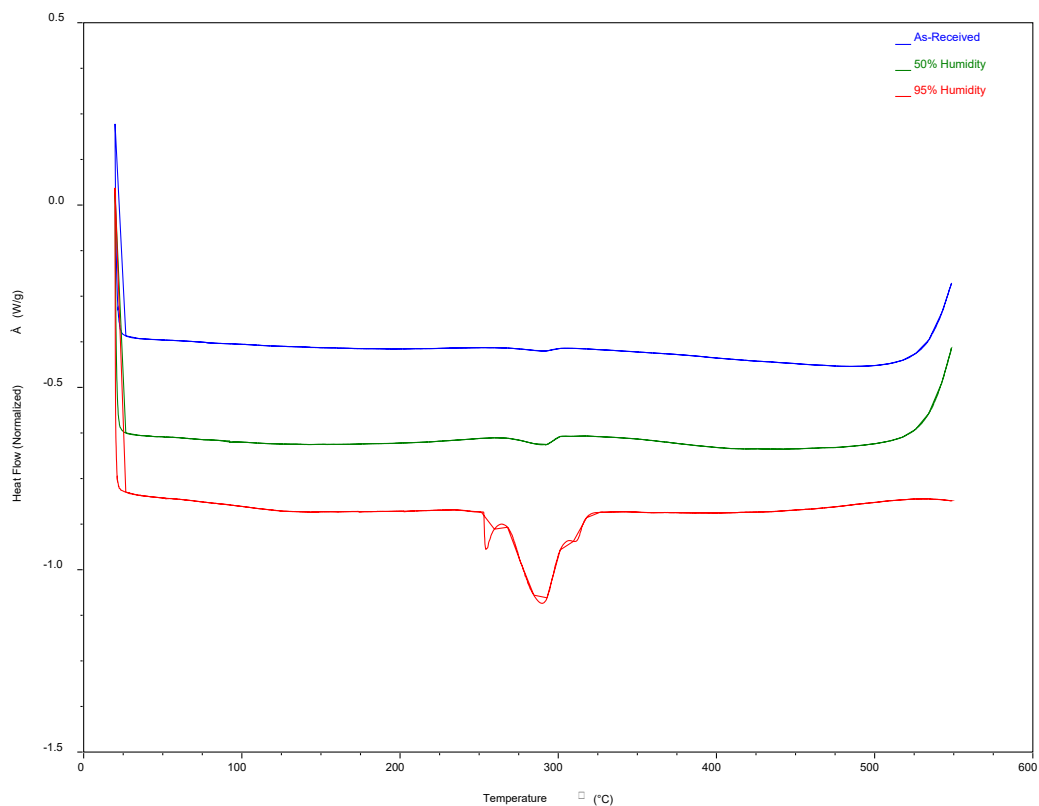


Figure 30. DSC scans of As-received, 50% humidity, and 95% humidity samples. 20°C to 550°C with 10°C/min ramp

In Figure 30 the graphs were shifted vertically for easier viewing and comparison. The enthalpies of the reaction occur near 290°C (see major endothermic peak) and resulted in an average enthalpy for AR, 50%, and 95% of 0.903 J/g, 2.612 J/g, and 41.823 J/g respectively.

This data indicated that between 250 °C and 290 °C a phase transformation was occurring. This phase change was most pronounced in sample RH95% but the same phase change can be observed in the AR and RH50% samples as well, but to a much lesser degree. Figure 31 represents a graphical presentation of the oxygen content determined by Inert Gas Fusion, shown previously in Table 12, compared to the associated enthalpies of reaction of the main endothermic peak near 290°C, from the DSC scan shown in Figure 30. This side by side comparison indicates that the phase transformation may be rich in oxygen and combined with the data from Table 18 may also contain a high concentration of hydrogen as determined by IGF. Considering the IGF and DSC data in its entirety, there is a strong argument that the transformation is consistent with an aluminum hydroxide. The, endothermic peak at 283°C, may have been due to decomposition of aluminum hydroxide to γ (gamma)-Al₂O₃ [160].

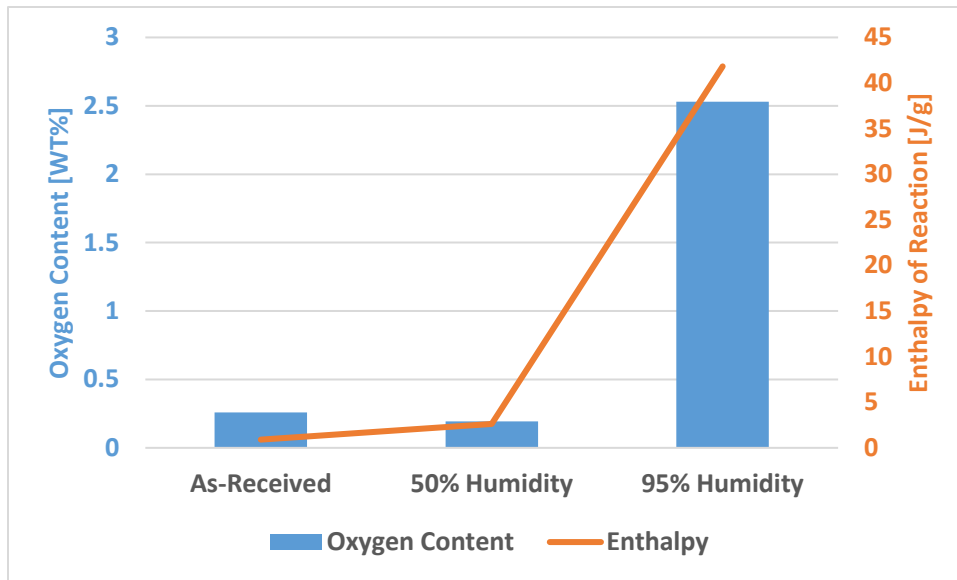


Figure 31. Comparison between oxygen content and associated enthalpies of reaction of the main endothermic peak near 290°C.

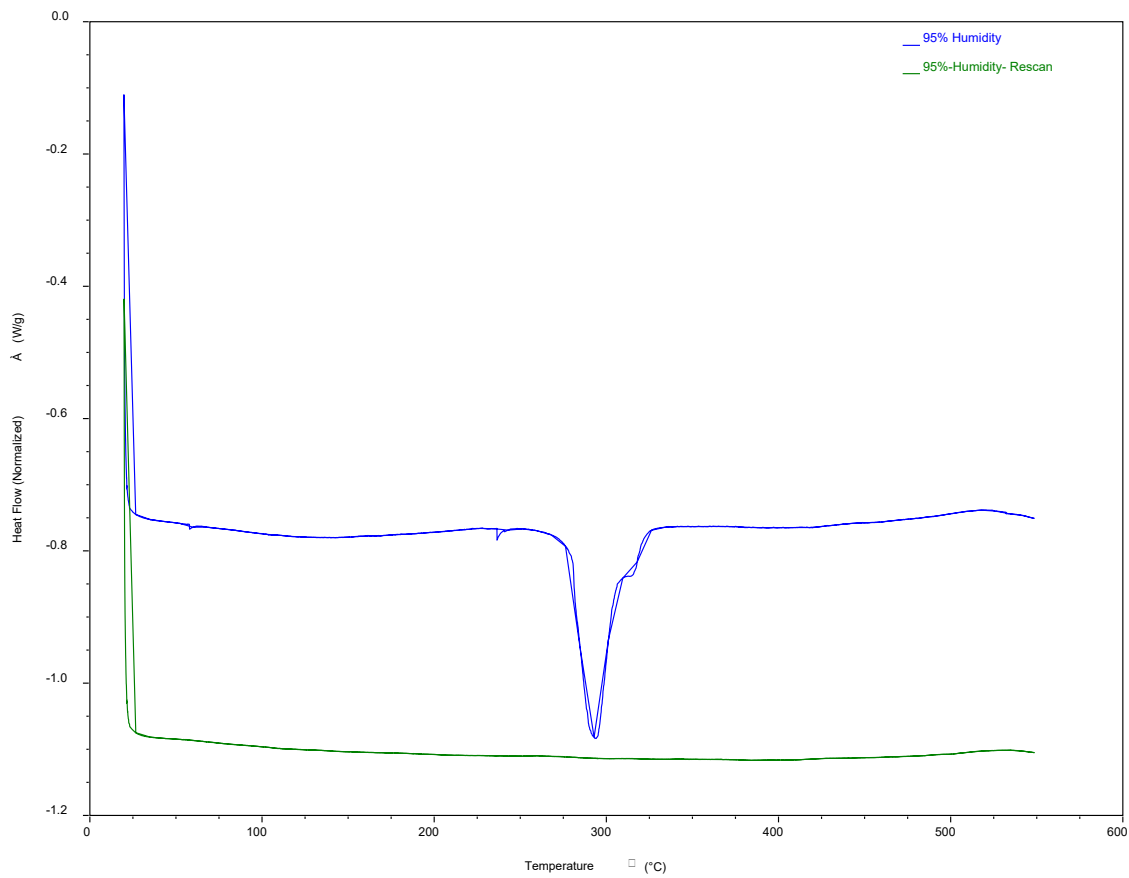


Figure 32. DSC scans of RH 95% sample. 20°C to 550°C with 10°C/min ramp.

In Figure 32, the bottom green line represents the data obtained from a rescans of the RH95% sample that was previously shown in Figure 30 and is superimposed on the figure for comparative purposes, as the blue plot. The RH95% sample was retested under the identical conditions, and the data represents the complete removal of the phase reacting at a temperature of about 290°C. The practice of reheating the same sample can be very informative and in this instance the data shows that this phase, which occurs at approximately 290°C, does not reform again.

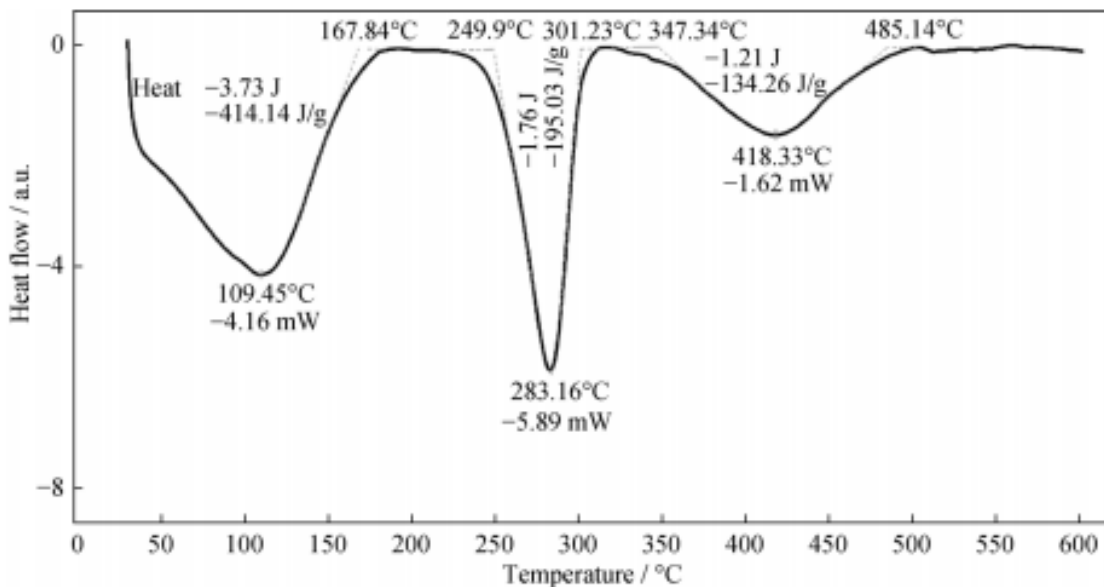


Figure 33. DSC thermogram of aluminum hydroxide taken from published literature [160].

Sarker, Md Saifur Rahman, et al, performed a DSC of aluminum hydroxide, as shown in Figure 33. The endothermic peak observed at 283.16°C corresponds well to that shown in Figure 30 and in Figure 32 and serves to substantiate the presence of an aluminum hydroxide in sample RH95%.

Figure 34 represents DCS scans of the heat treated HP-Al powder samples and the results indicate the absence of any major phase change. No discernable $\text{Al}(\text{OH})_3$ peaks can be observed in any of the DSC scans of the heat-treated samples This was anticipated since the exposure temperature during the heat treat was 300°C which is at the onset of the transformation temperature of aluminum hydroxide. Sarker, Md Saifur Rahman, et al, show the decomposition of aluminum hydroxide to γ (gamma)- Al_2O_3 at this temperature [160,161, 162].

Figure 35 contains the DSC scans for all of the powder groups and the graphs were intentionally shifted vertically for ease in viewing and comparison. There is no evidence of adsorbed water observed (no reactions around 100°C). The notable peaks are those at approximately 290 °C on samples AR, RH50% and especially RH95% and indicate the decomposition of aluminum hydroxide.

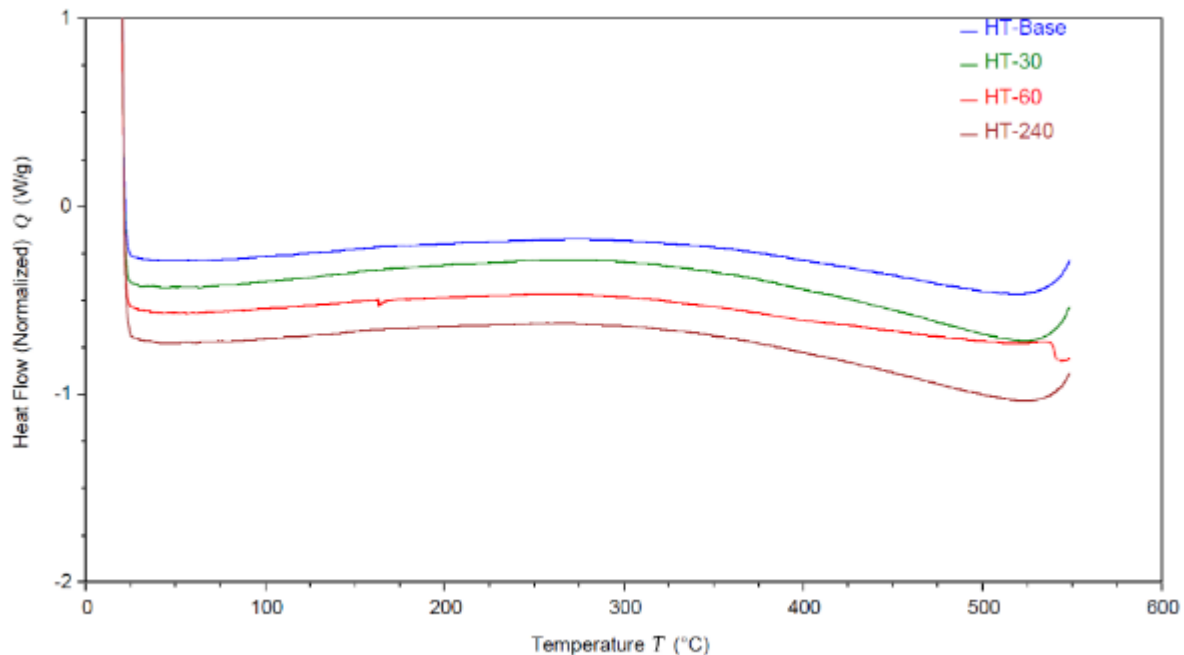
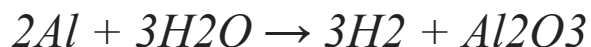


Figure 34. DSC scans of the heat-treated samples (HT). 20°C to 550°C with 10°C/min ramp. Graphs were shifted vertically for easier viewing and comparison.

4.1.5 Thermogravimetric Analysis

TGA analysis measures the mass of a sample over time as the temperature changes and was performed to compliment the DSC results. Figure 36 shows the loss of a volatile component at approximately 220°C, which may be related to the removal of water from the sample as denoted by the reaction equation. This temperature correlates well with the DSC results.

Reaction of water with aluminum:



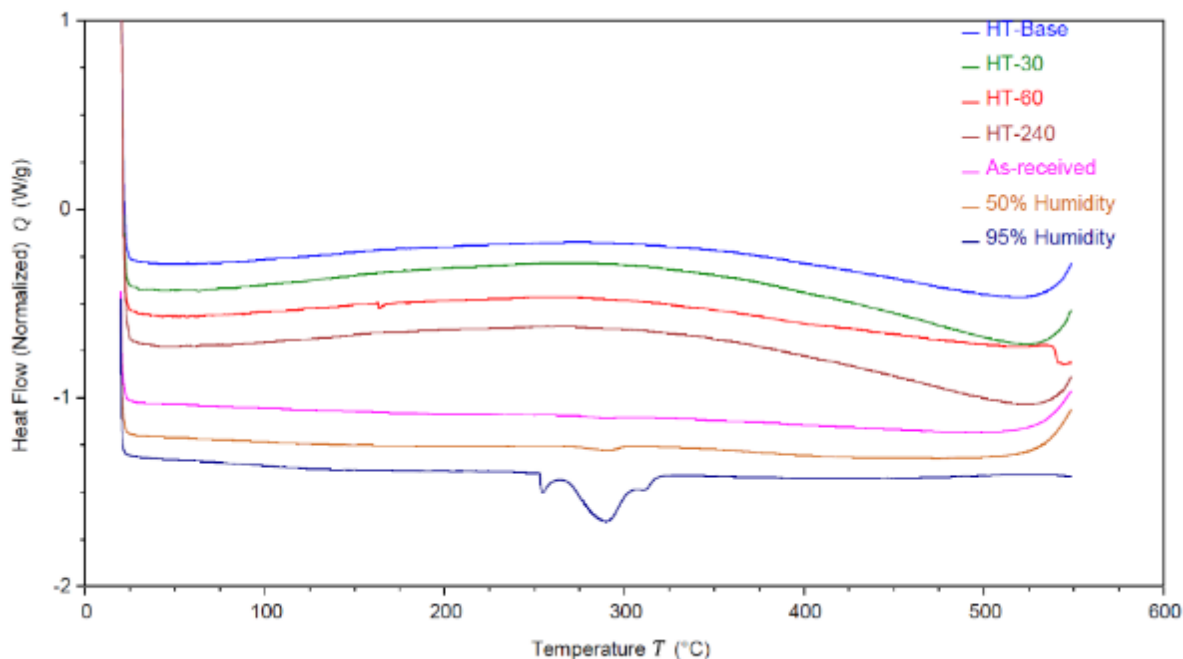


Figure 35. DSC scans of all runs for comparison purposes. 20°C to 550°C with 10°C/min ramp. Graphs were shifted vertically for easier viewing and comparison.

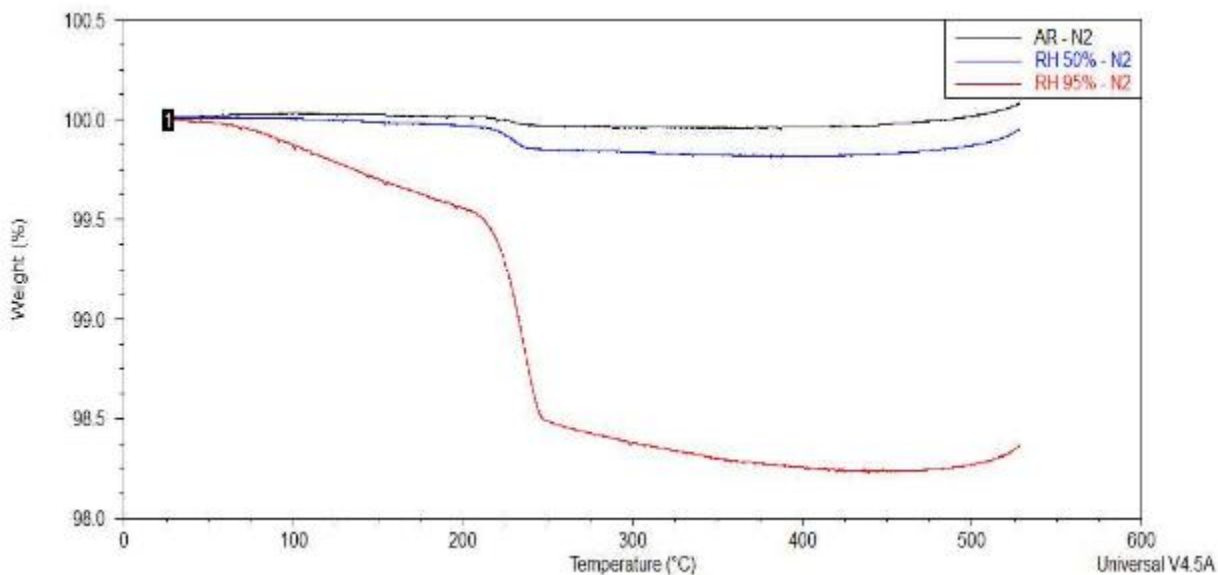


Figure 36. TGA curves of As-received, 50% humidity, and 95% humidity samples run in nitrogen.

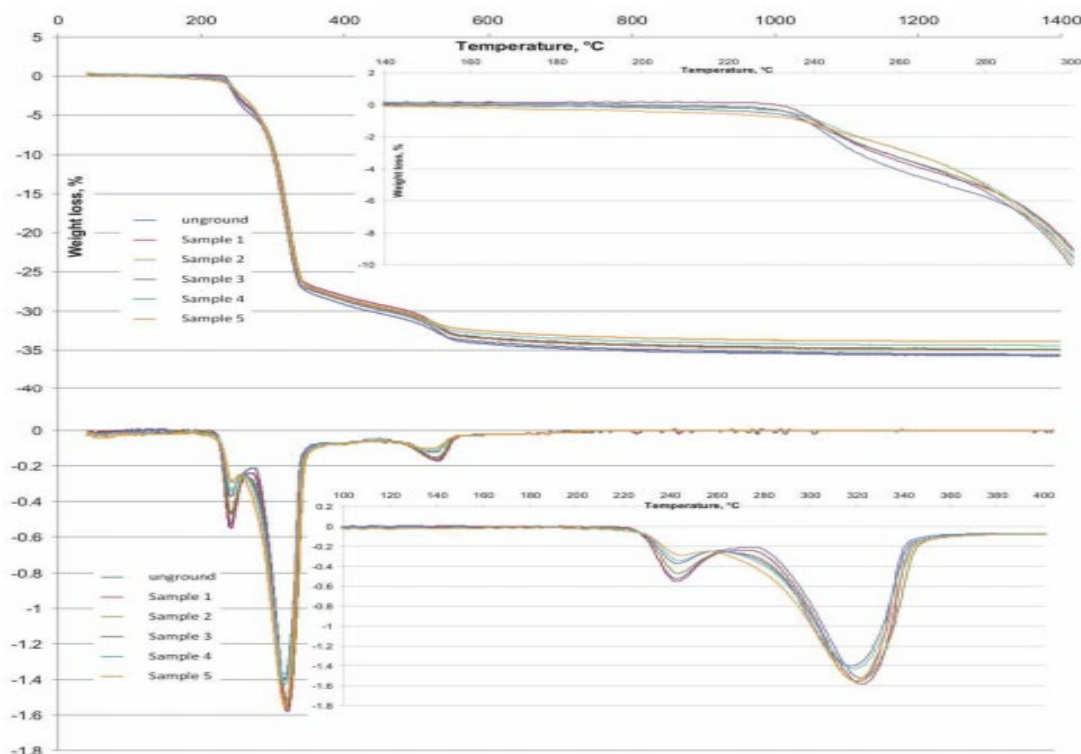


Figure 37. “TG and DTG curves of unground or ground and previously not heat treated aluminum hydroxide samples, in the function of temperature. Above: TG, %; below: DTG, mg/min” [161].

Figure 37 shows reference TG and DTG curves produced by Baranyai et al., who argued that the dominant thermal decomposition of aluminum hydroxide is directly to oxides, which is consistent with the results observed from the DSC scans shown Figure 34 and Figure 35, as well as the TGA results shown in [161].

4.1.6 Fourier Transform Infrared Spectroscopy

The FTIR analysis technique was used to determine the chemical properties of the powders incorporating infrared radiation to scan the test samples. The method employs absorbed radiation which is converted into rotational and/or vibrational energy by the sample molecules and a detector displays the results in the form of a spectrum, that serves as a unique ‘fingerprint’ of the molecule [163].

FTIR-DRIFTS spectra were collected using a controlled atmosphere (argon gas) / variable temperature cell. Spectra were collected at room temperature (~ 30C). Using this cell allowed for the acquisition of much cleaner spectra in the OH region (2800-4000 cm⁻¹) because the effects of adsorbed water in the KBr spectra (the spectrum used to reference all sample spectra) can be mitigated.

All seven powder samples were analyzed by FTIR.

Powder Samples

- 1) AR-As received (Exposure Time to Air at Room Temperature - No Exposure)
- 2) HT-Baseline (Exposure Times to Dry Air at 300°C 0 minutes)
- 3) HT-30 Air (Exposure Times to Dry Air at 300°C 30 minutes)
- 4) HT-60 Air (Exposure Times to Dry Air at 300°C 60 minutes)
- 5) HT-240 Air (Exposure Times to Dry Air at 300°C 240 minutes)
- 6) RH-50% (50% RH / 29°C for 4 days)
- 7) RH-95% (95% RH / 29°C for 4 days)

The as received AR, RH 50%, and RH 95% spectra indicated the presence of an Al-OH species, appearing to consist primarily of bayerite (Figure 38). However, gibbsite and bayerite are both alumina trihydrate ($\text{Al}(\text{OH})_3$) [164]. The HT-Base, HT-30, HT-60, and HT-240 spectra did not show any indication of aluminum hydroxides. Gibbsite decomposes to oxide above the temperature of 300 °C [161]. For HT-Base, HT-30, HT-60, and HT-240 a preliminary semi-quantitative analysis (peak area integration) of the Al-O peak at 935 cm^{-1} indicated the oxide layers on these four samples were of a similar thickness and structure. These analyses were performed on triplicate measurements collected for each sample using a standard DRIFTS accessory (not controlled atmosphere/temp).

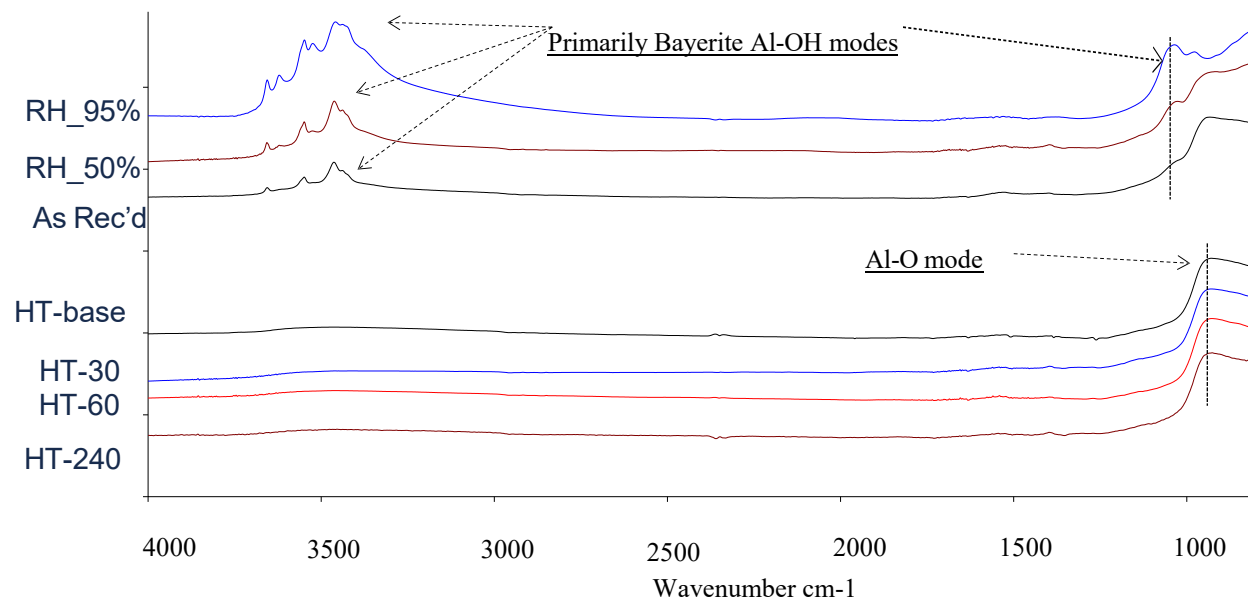


Figure 38. FTIR-DRIFTS: Spectra collected under Argon purge at ~30C.

4.1.7 X-ray Photoelectron Spectroscopy

XPS is a surface analysis technique that can be used for a wide range of materials providing quantitative and chemical state information. XPS was used to measure the elemental composition on the surface of powders and measure oxide thickness. The kinetic energy spectrum of photoelectrons ejected from the surface of a specimen is determined through XPS analysis by the irradiating X-ray having a constant energy, $h\nu$, in vacuum (normally better than 10^{-7} Pa) [165]. XPS experiments were performed using a Physical Electronics VersaProbe II instrument equipped with a monochromatic Al $K\alpha$ x-ray source ($h\nu = 1,486.7$ eV) and a concentric hemispherical analyzer. Charge neutralization was performed using both low energy electrons (<5 eV) and argon ions. The binding energy axis was calibrated using sputter cleaned Cu (Cu $2p_{3/2} = 932.62$ eV, Cu $3p_{3/2} = 75.1$ eV) and Au foils (Au $4f_{7/2} = 83.96$ eV) [166]. Peaks were charge referenced to CH_x band in the carbon 1s spectra at 284.8 eV. Measurements were made at a takeoff angle of 45° with respect to the sample surface plane. This resulted in a typical sampling depth of 3-6 nm (95% of the signal originated from this depth or shallower). Quantification was done using instrumental relative sensitivity factors (RSFs) that account for the x-ray cross section and inelastic mean free path of the electrons.

Species detected on the surfaces included: Al^0 , Al^{3+} and organics including CH_x , C-O, O-C=O and carbonates. The carbonate concentration seemed to systematically decrease with increasing heat treat time for the HT powder samples. The oxide thickness was calculated using a uniform overlayer model. No correction for the curvature of the sample was included. The thickness varied from 4 nm (as received) to 6 nm (RH 95%). Most of the samples were clustered around 4 nm. Table 19 lists the O/Al ratio and Figure 39 the binding energy associated with representative powder samples (AR, HT240 and RH95%). The values were highest on the as received, 50% RH and RH 95% samples. The position of the O 1s positions on these same samples (531.6 ± 0.1 eV) suggested a higher fraction of OH compared with the HT air samples (530.8 ± 0.3 eV).

Table 19. Concentration of Elements Detected (in atom%).

Sample	Al ³⁺	Al ⁰	O	Ctotal	Carbon species (in atom% C)				tox (Å)	O/Al ³⁺
					CH _x	C-O	O-C=O	CO ₃		
As rec'd	27.7	5.7	61.4	5.2	3.0	0.4	1.1	0.7	41.8	2.1
HT Baseline	30.3	6.1	58.4	5.2	3.3	0.5	0.4	1.0	42.4	1.8
HT-30 min Air	30.7	6.0	58.4	4.9	3.0	0.6	0.5	0.8	42.7	1.8
HT-60 min Air	30.8	5.7	58.1	5.4	3.6	0.5	0.7	0.6	43.8	1.8
HT-240 air	31.0	5.9	58.6	4.6	3.1	0.4	1.0	0.1	43.4	1.8
RH-50%	27.9	6.0	60.7	5.4	3.3	0.5	0.5	1.1	41.2	2.0
RH 95%	27.0	2.0	66.0	5.0	2.8	0.6	0.7	0.9	60.7	2.3

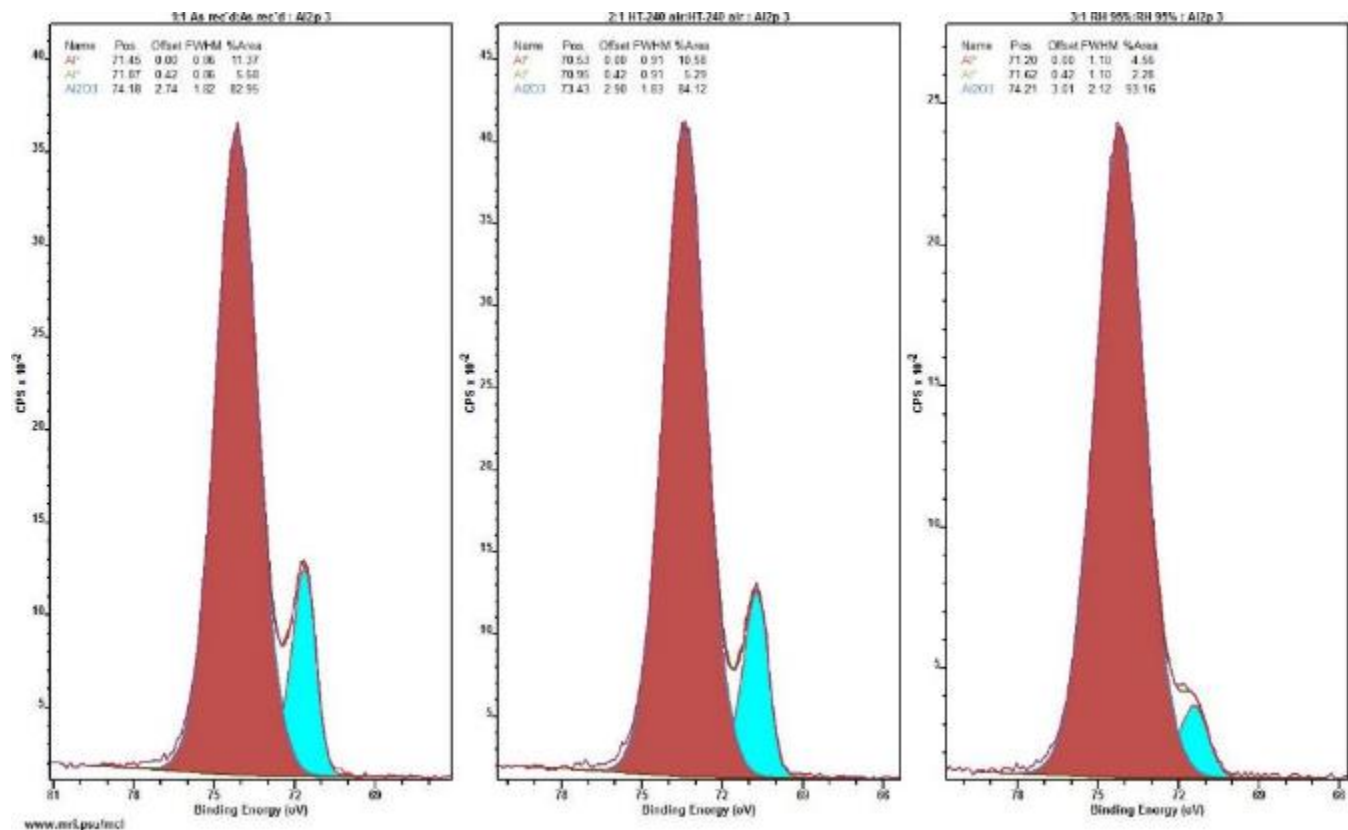


Figure 39. High resolution Al 2p spectra curve fit into Al⁰ and Al³⁺.

4.1.8 Transmission and Scanning Transmission Electron Microscopy

Powder samples were prepared for TEM and STEM using focused ion beam (FIB) milling with cryo-compatible accessories to help prevent excess thermal input and avoid phase transformation. A protective carbon coating was first deposited on the surface in FIB. Both TEM and STEM was accomplished using a Talos TEM at 200kV and Energy Dispersive X-Ray Spectroscopy (EDS) mapping was performed at the edge of particles to try to detect surface oxide. High Angle Annular Dark Field (HAADF) STEM allows for better mass contrast than TEM. The contrast is approximately proportional to Z^2 and is reversed, as compared to TEM.

The oxide layer looked similar for most of the powder samples from all seven groups, having a thickness of approximately ~ 4 nm, except for the RH95% sample that had a surface layer that was approximately 6 nm in thickness. The ratio of aluminum to oxygen was the same at 40:60 at%. The surface film appeared relatively uniform and smooth for the AR and HT samples with the exception of HT240 which had some 'rough' areas. The RH 50% sample had some spikey surface features that could be indicative of hydroxide formation and the RH95% had some rough areas as well.

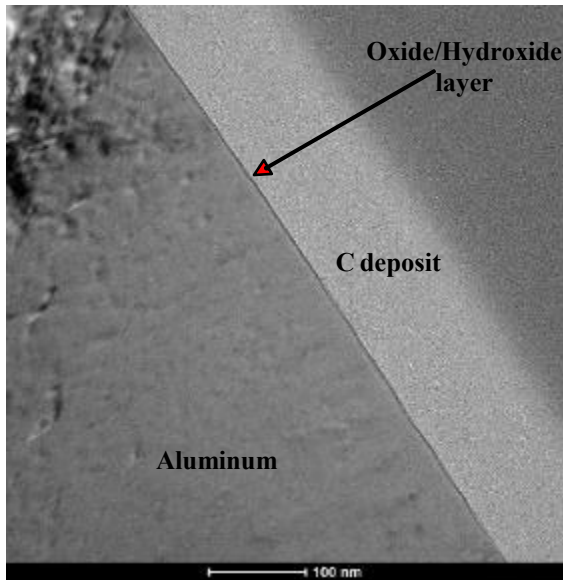
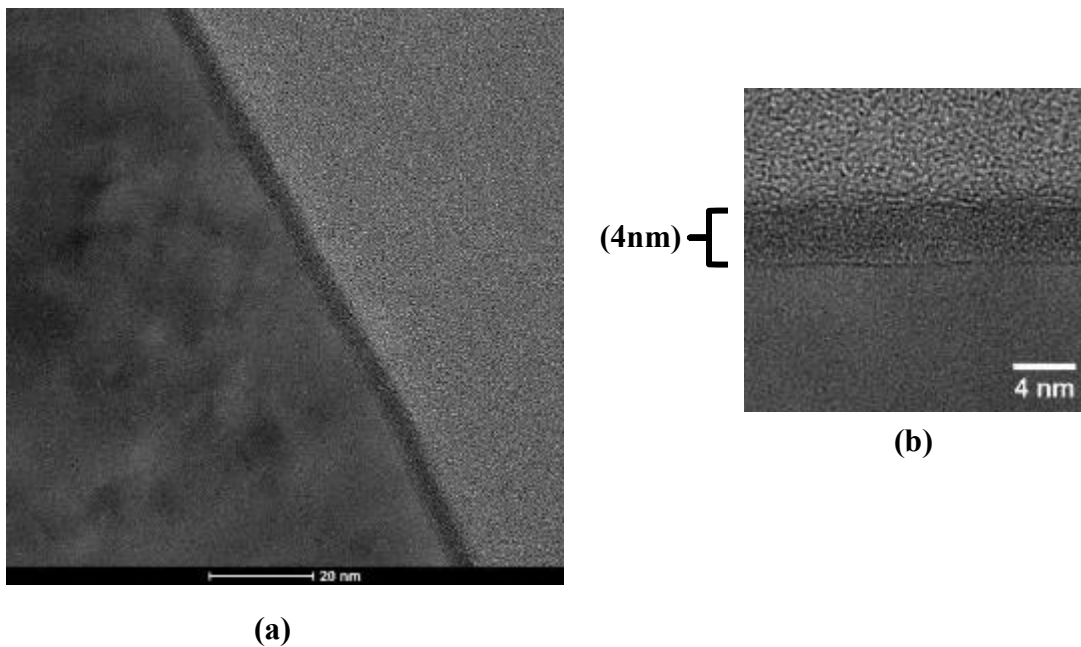


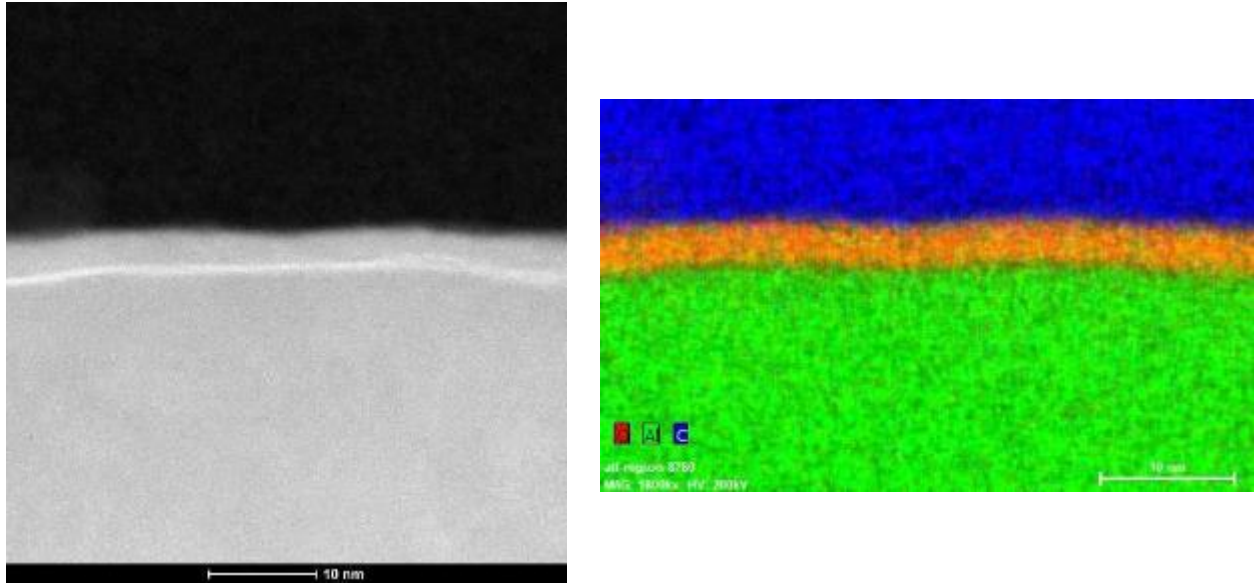
Figure 40. TEM of as-received (AR) powder showing surface layer.

Figure 40 is a TEM image representing powder from the as-received (AR) group. The surface film is clearly denoted and is quite uniform and smooth in appearance. Electron beam carbon deposition was used to coat the sample, as identified in the figure.

Figures 41a and b shows the same surface layer as depicted in Figure 39 at higher magnification. The surface layer is approximately 4 nm thick and appeared amorphous. Figures 42a and b are a high contrast STEM and corresponding EDS mapping of the AR powder, clearly delineating the surface film shown in Figure 39 and Figure 40.



Figures 41a and b. Higher magnification TEM of as-received powder showing surface film.



Figures 42a and b. STEM and EDS mapping of the as-received (AR) powder.

Figures 42a and b shows STEM and EDS mapping respectively, of the as-received AR powder to show the sharp contrast of the surface layer. The layer is about 4 nm in thickness and is uniform and relatively smooth in appearance.

Figure 43 is representative of the HT samples with the exception of HT-240. The surface layer is approximately 4 nm thick (Figures 44a and b) and is relatively uniform, whereas sample HT-240 displayed evidence of a courser layer with areas that were protruding from the surface.

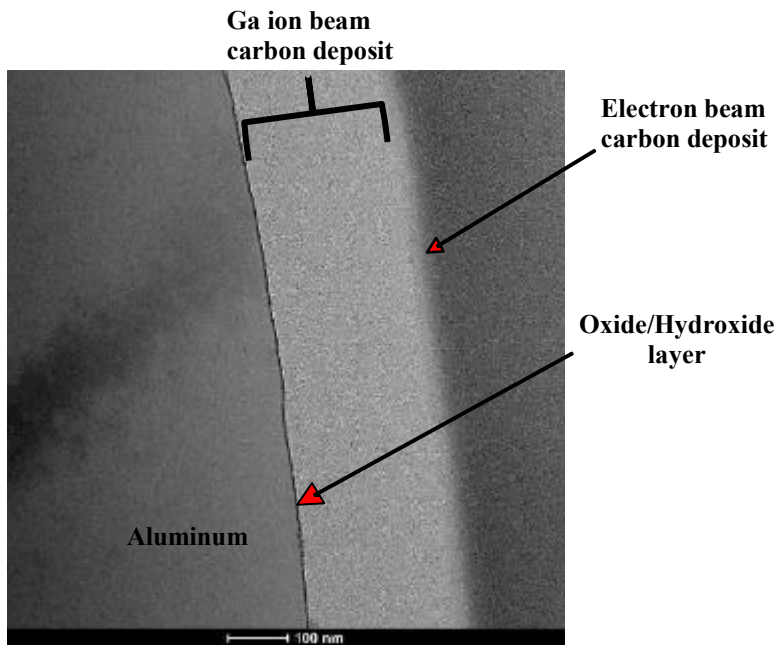
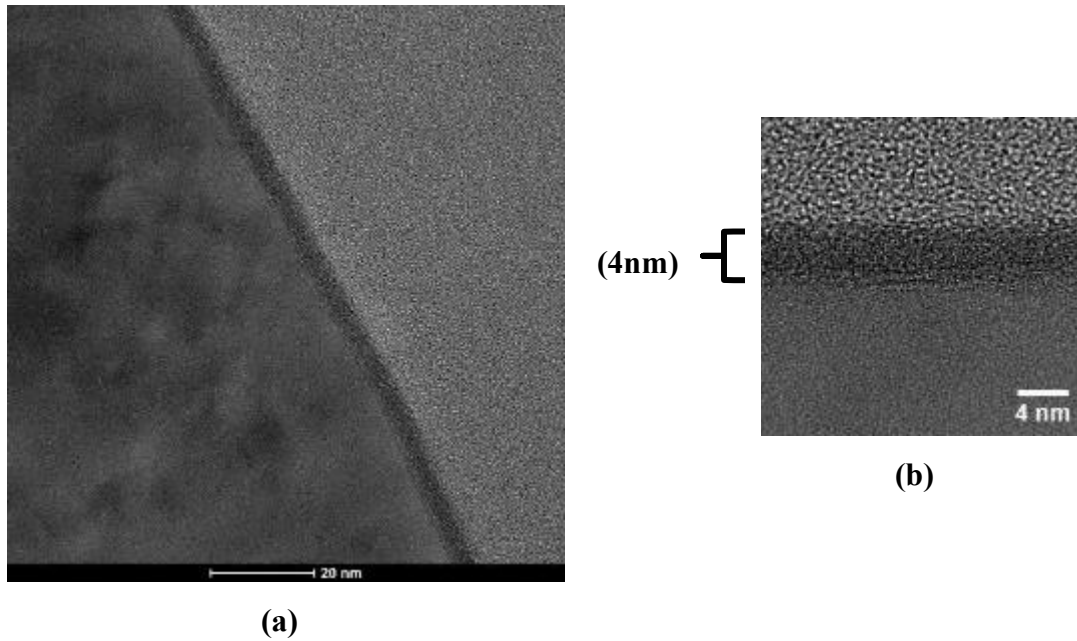
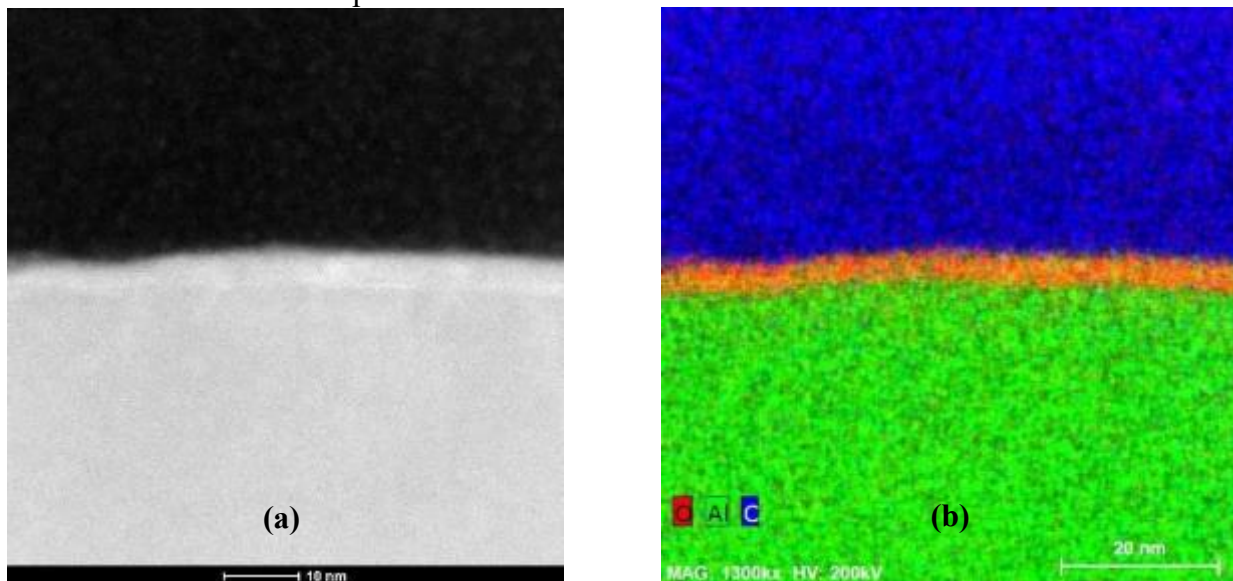


Figure 43. TEM of powder sample HT-Baseline showing surface layer.

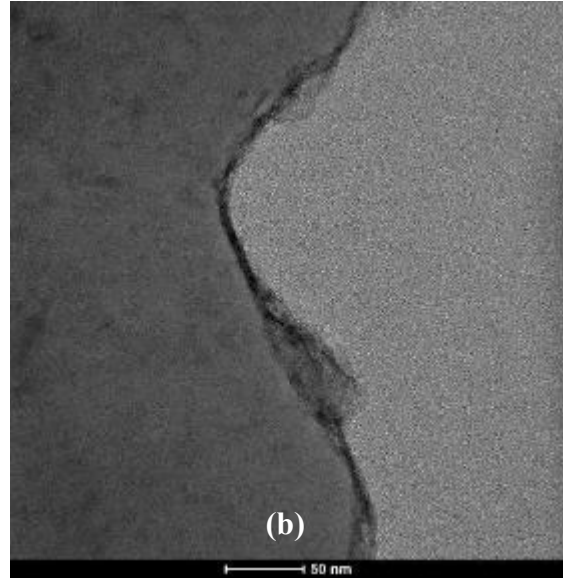
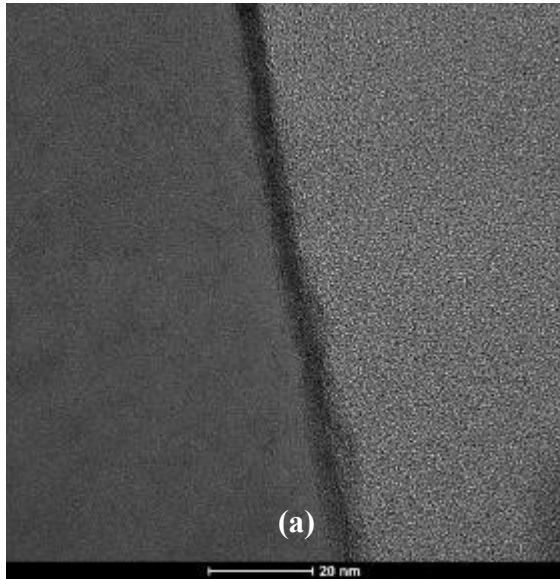


Figures 44a and b. Higher magnification TEM of HT-Baseline powder showing surface film.

Figures 44a and b shows STEM and EDS mapping respectively, of the HT-Baseline powder to show the sharp contrast of the surface layer. The layer is about 4 nm in thickness and is uniform and relatively smooth in appearance. Figures 45a and b show STEM and EDS mapping of the relatively uniform and smooth surface layer on HT-Baseline. Figures 46a and b show high resolution TEM of sample HT-240 where the surface layer is thicker ~5nm and much less uniform than AR and other HT samples.

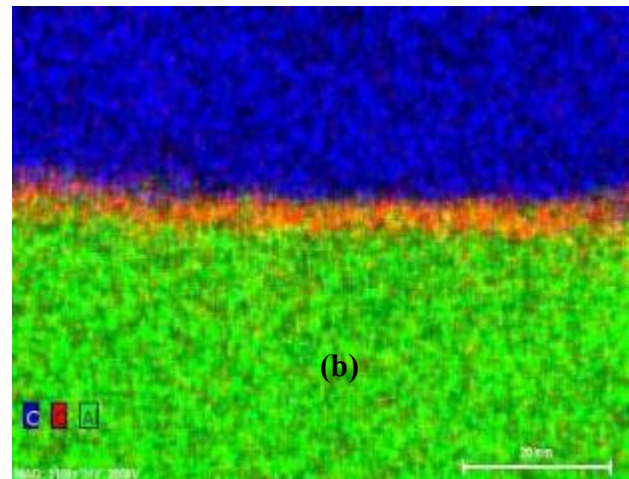
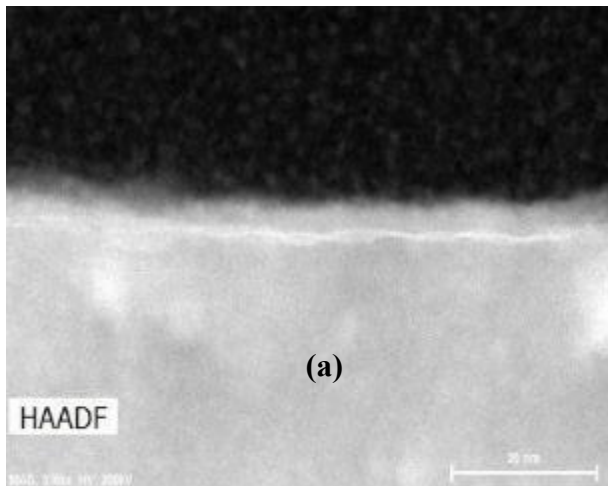


Figures 45a and b. STEM and EDS mapping of the HT-Baseline powder.



Figures 46a and b. TEM high resolution (HRTEM) of HT-240 layer approximately 5 nm although much less uniform as compared to AR and remaining HT samples.

Figures 47a and b show a high angle annular dark field STEM image and corresponding EDS mapping of an RH50% powder sample. The Al:O present in the surface oxide/hydroxide is approximately 40:60 at%. The RH50% sample also displayed ‘spiky’ features protruding from the surface layer as shown in shows sample RH95% where the surface roughness and ‘spiky’ features protruding from the surface layer were most pronounced. Figures 50a and b show STEM and EDS mapping of the RH95% powder sample supporting the physical features of the surface layer found by HRTEM, including roughness and the protruding spikes.



Figures 47a and b. HAADF-STEM and EDS mapping of RH50% powder sample.



Figure 48. TEM of RH50% showing spikes protruding from the surface layer.

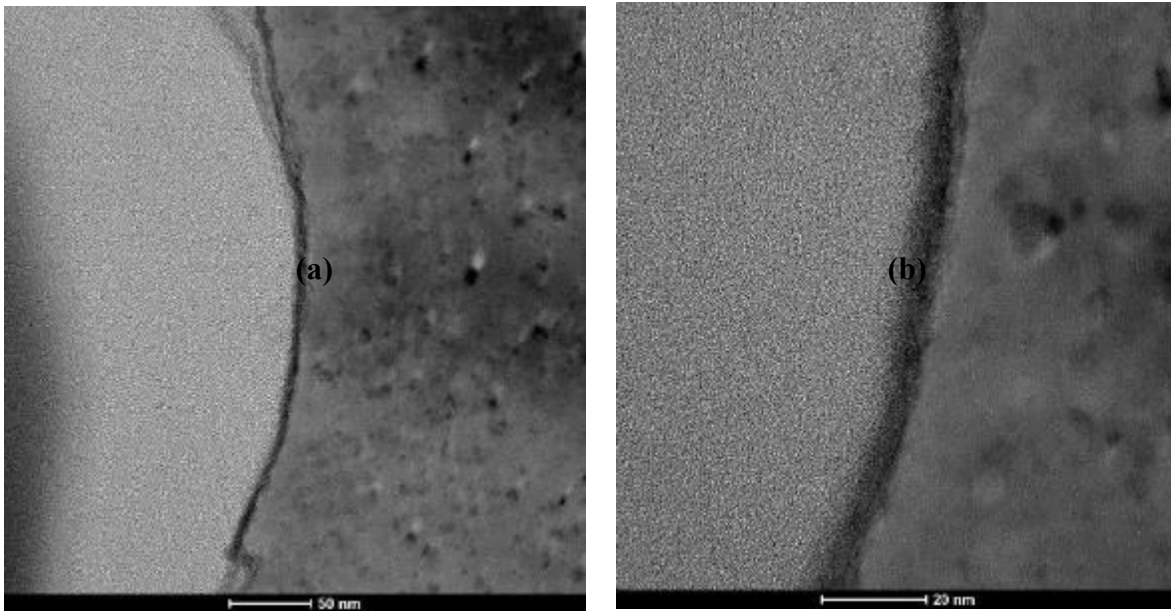
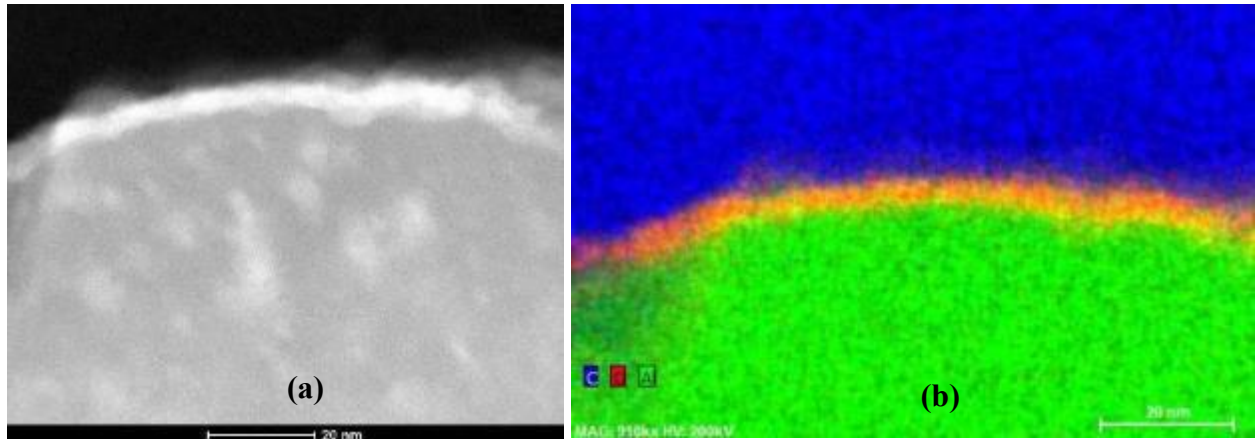


Figure 49. TEM high resolution (HRTEM) of RH95% showing the surface layer to be approximately 6 nm although much less uniform as compared to RH50% and HT-240.



Figures 50a and b. STEM and EDS mapping of the RH95% powder sample.

4.1.9 Scanning Electron Microscopy

All seven groups of powders were mounted on a pin mount SEM stub using double-sided carbon tape. The excess was blown off with canned air. Samples were imaged in a Nano SEM Nova 630. (ThermoScientific, Hillsboro, OR) at 500, 1000, 5000, 10,000, 50,000, 100,000 and 200,000x.

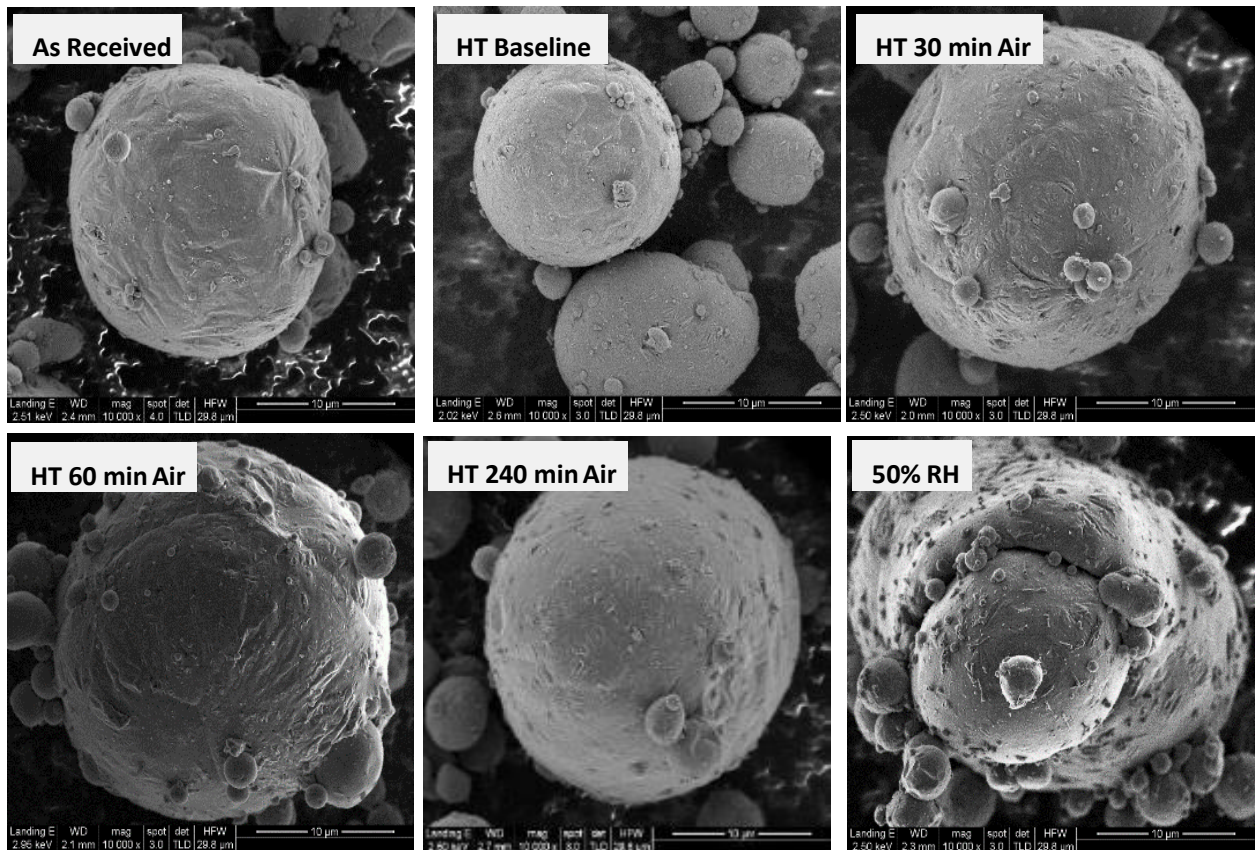


Figure 51. Representative SEM images of all the powder groups except for RH95%.

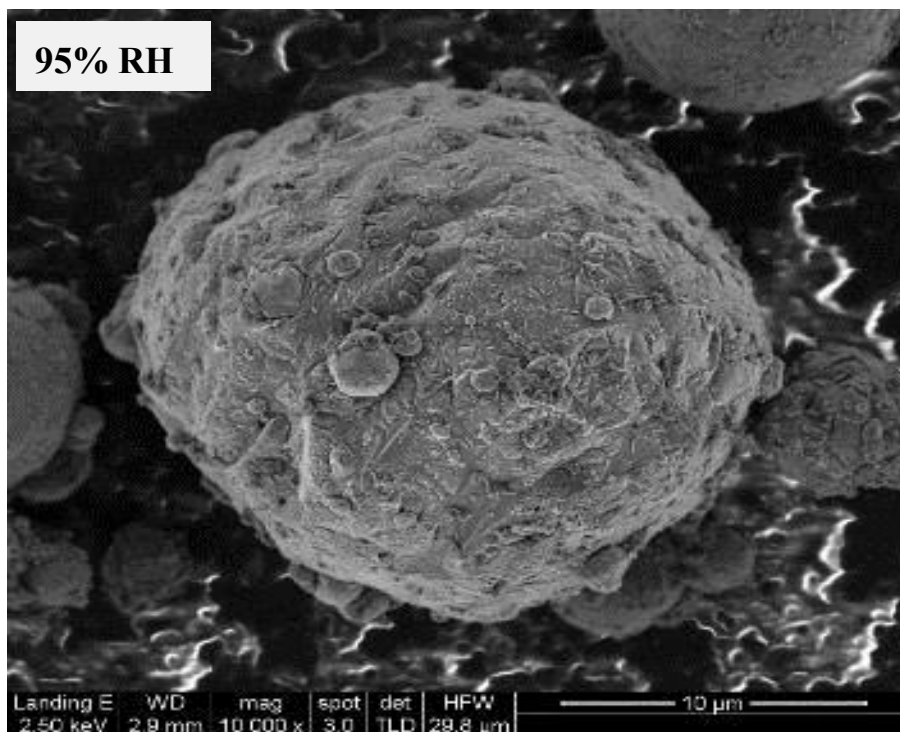


Figure 52. SEM image of a powder particle from RH95%.

Figure 51 shows representative images of six of the powder groups, while Figure 52 shows a representative SEM image of the final powder group, RH95%. The images were taken to obtain a comparison of the surface powder morphology. All the powder groups were spherical to irregular in shape, containing small satellites, in varying degrees. There are some coarse surface features associated with the as-received powder, which become more pronounced on the RH samples. The texture of the AR and HT samples is mixed (smooth and coarse) but there are significant smooth areas that are not found on RH95%, which was primarily very coarse in appearance. ‘Spikey’ features and ‘patches’ are predominate on the RH samples.

4.1.10 Raman Spectroscopy

Raman spectroscopy (RS), a vibrational spectroscopic technique, was used to provide information on molecular vibrations and crystal structures, making it possible to identify substances including polymorphs. The vibrational spectra of organic materials are determined by the interatomic bonds. Raman spectroscopy maps obtained from powder samples were taken to assess the spatial distribution of surface oxide/hydroxides and to identify the nature of the surface films.

Laser threshold tests were performed on the baseline powder to ensure that 2 mW @ 488 nm incident laser power with the 100x/0.9 NA objective did not induce any irradiation damage/phase shift in the material. Isolated particles were identified and then mapped with a 2 micron step size to determine any variation in the composition.

Figure 53 shows the Raman spectrum obtained from powder sample RH-95%, whereas the x-axis frequencies were plotted relative to that of the laser. A linear regression was used to identify the

best fit of the function to the spectrum and the program is a Classical Least Squares (CLS) linear regression. Raman spectroscopy provides both spectral and spatial resolution, where images are shown of the sample when plotting the peak frequency as a function of the spatial location (Figure 54 and Figure 55).

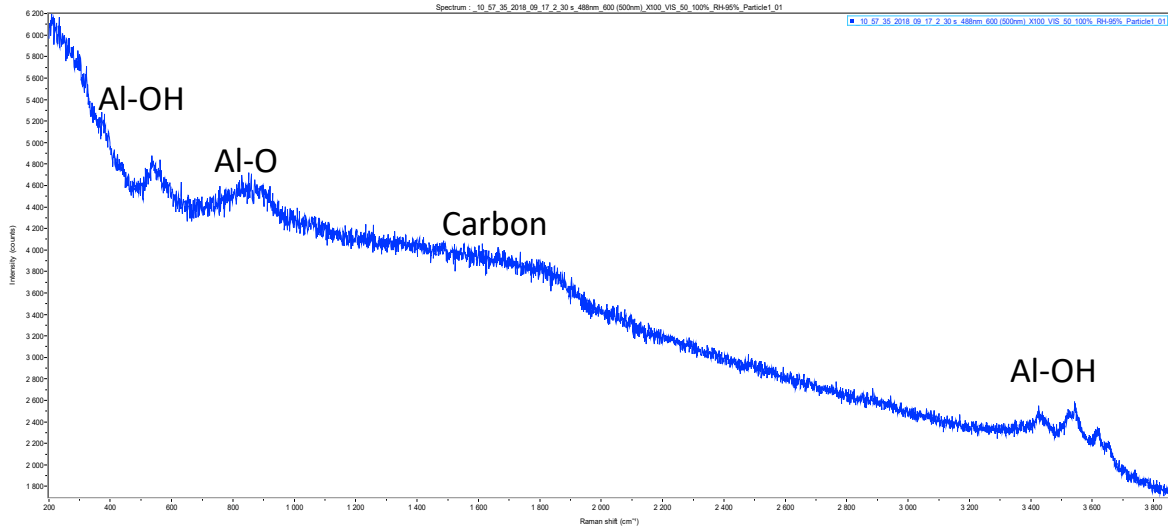


Figure 53. Raman spectrum obtained from powder sample RH-95%.

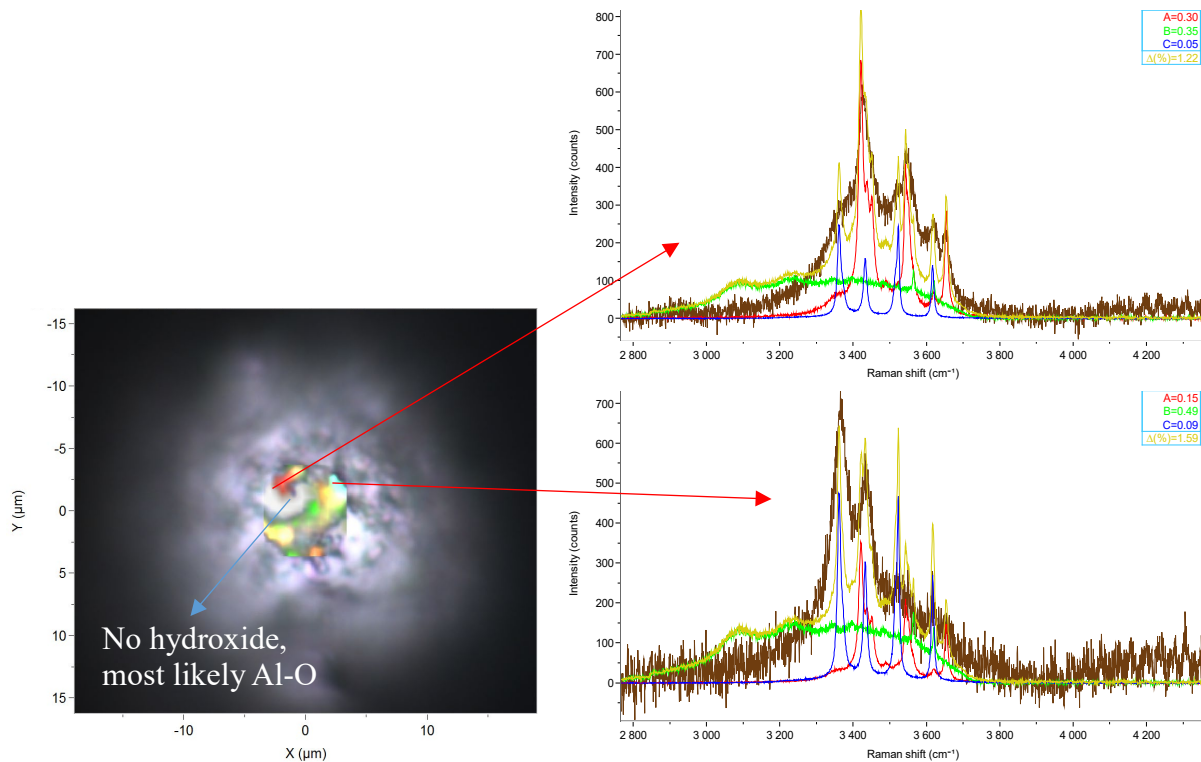


Figure 54. Raman spectroscopy micron map (CLS fit) of RH-95%.

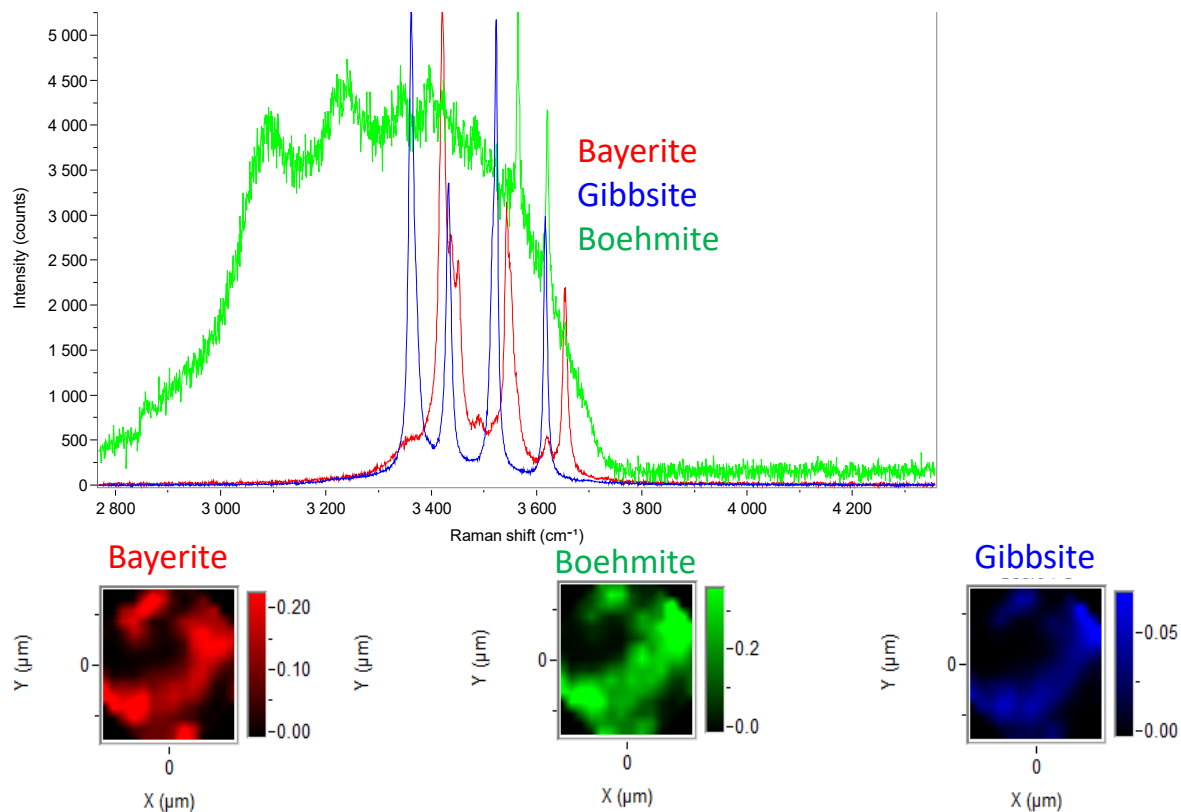


Figure 55. Al hydroxide polymorphs from sample RH-95% identified by Raman spectroscopy.

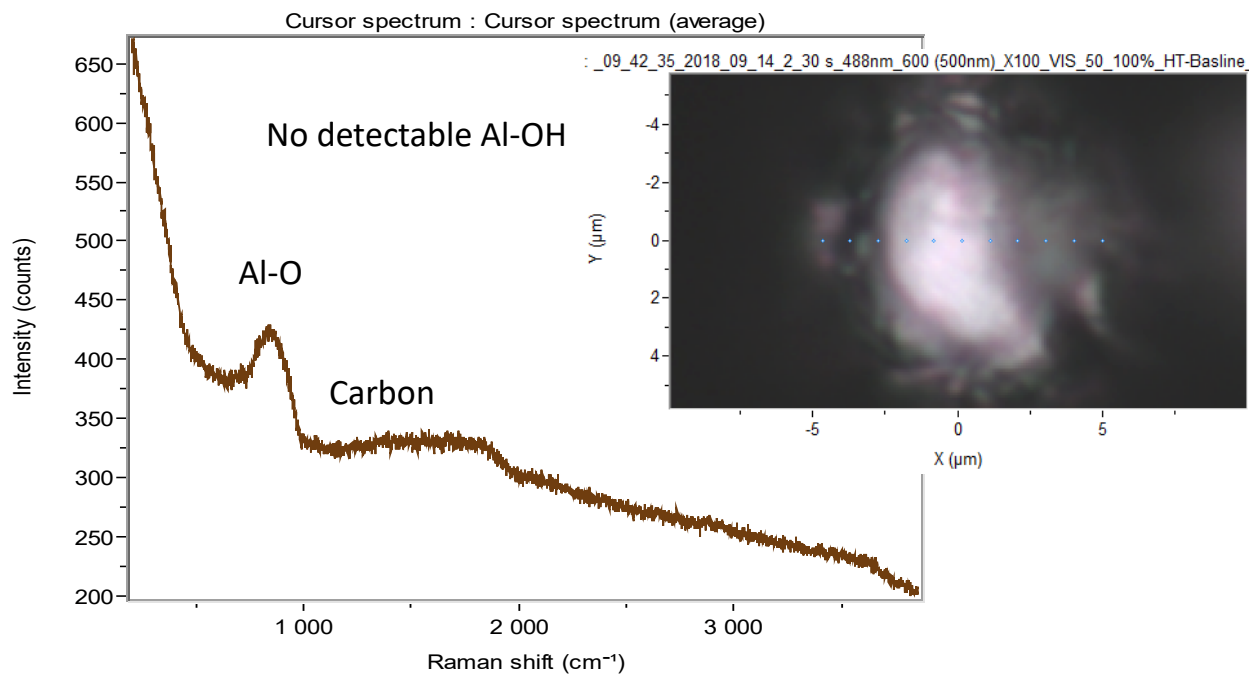


Figure 56. Raman spectrum obtained from powder sample HT-Baseline.

The Raman images of the corresponding spectra of RH-95% are shown and characterized in Figures 53-55. Aluminum hydroxide polymorphs Bayerite, Boehmite and Gibbsite were identified and areas of aluminum oxide were present. It is interesting to note that the formation of oxide or hydroxide surface films occurred in a random fashion and as ‘patches’ across the particle surface.

In contrast to Figures 53-55, the analysis of sample HT-Baseline revealed no evidence of aluminum hydroxides, as shown in Figure 56. However, the presence of aluminum oxide was observed. This was anticipated as the heat treat exposure temperature would have converted any surface hydroxides to an oxide.

4.1.11 Dynamic Nanoindentation

A series of nanoindentations were produced on separate powder particles from three of the powder groups (As-received, RH-50% and RH-95%). From these measurements an attempt to find a correlation between the mechanical behavior of the oxide film under load and its hardness and thickness were pursued. Bahr et al. [167] as well as Weppelmann and Swain [168], have reported a technique that incorporates nanoindentation as a tool to cause through thickness fracture events for thin oxide films on metals and from these results it was deduced that estimations of oxide film thicknesses could be determined for gas atomized HP-Al powders. Figure 57 illustrates the manner by which hard brittle oxide layers are thought to fail as thin surface films on ductile and soft substrate metals.

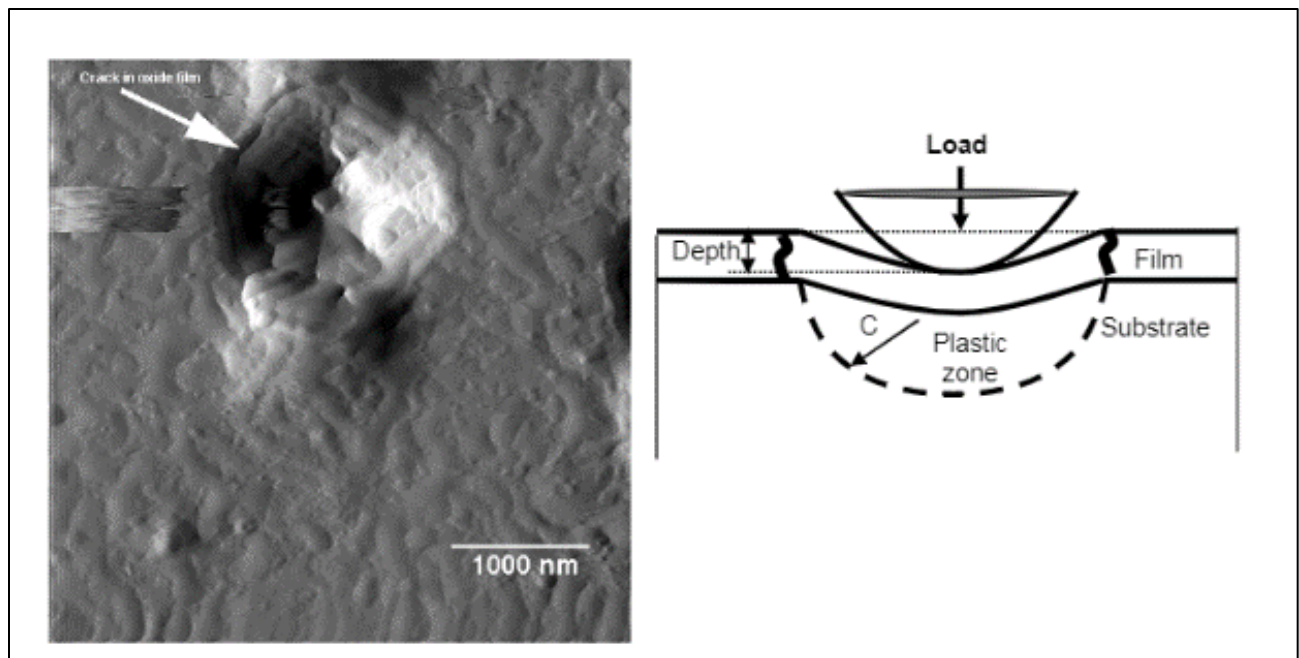


Figure 57. Taken from [167]. On the left, “Surface (through thickness) cracks surrounding the residual impression from a nanoindentation into an anodically grown oxide film on Ti.” On the right, “Schematic of cracking development during nanoindentation of a hard film on soft substrate.”

Minor et al. [169] and Venkataraman, Kohlstedt, and Gerberich [170], have shown that “negative force swings” in the load vs. depth curves and “displacement excursions” can be examined in the pursuit of understanding the mechanical behavior of oxide surfaces as well as polycrystalline aluminum systems. In accordance with the degree of compliance associated with the soft pure Al substrate, the film thicknesses are calculated by dividing the depth immediately before a load-decreasing excursion event by a value of 2.0.

To illustrate the concept of dynamic nanoindentation, consider the RH-95% powder group. The load-displacement curve for one of the particles indented is depicted in Figure 58, with emphasis upon the first sudden decrease in load that is accompanied by a depth increase. The depth value immediately prior to the change in the load-displacement curves slope, to a negative value, is the depth value that is then divided by 2.0 in determining an approximate film thickness.

Alternatively, Figure 59 represents one of the hardness vs. load trajectories. The superimposed arrows within the figure highlight the sudden drop-off in load as well.

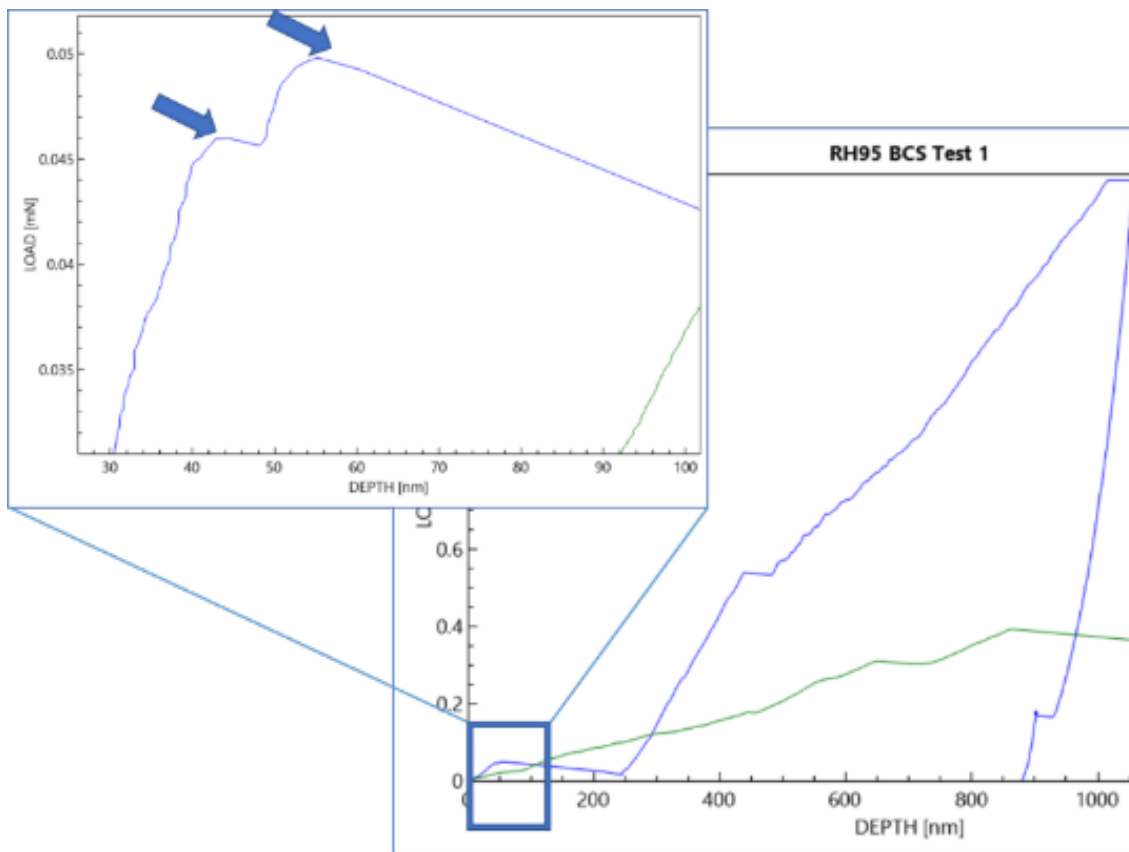


Figure 58. A load-displacement curve for an RH 95% HP Al powder particle. Note the initial excursion in the load via the enlarged area of the graph as indicated by the left most arrow.

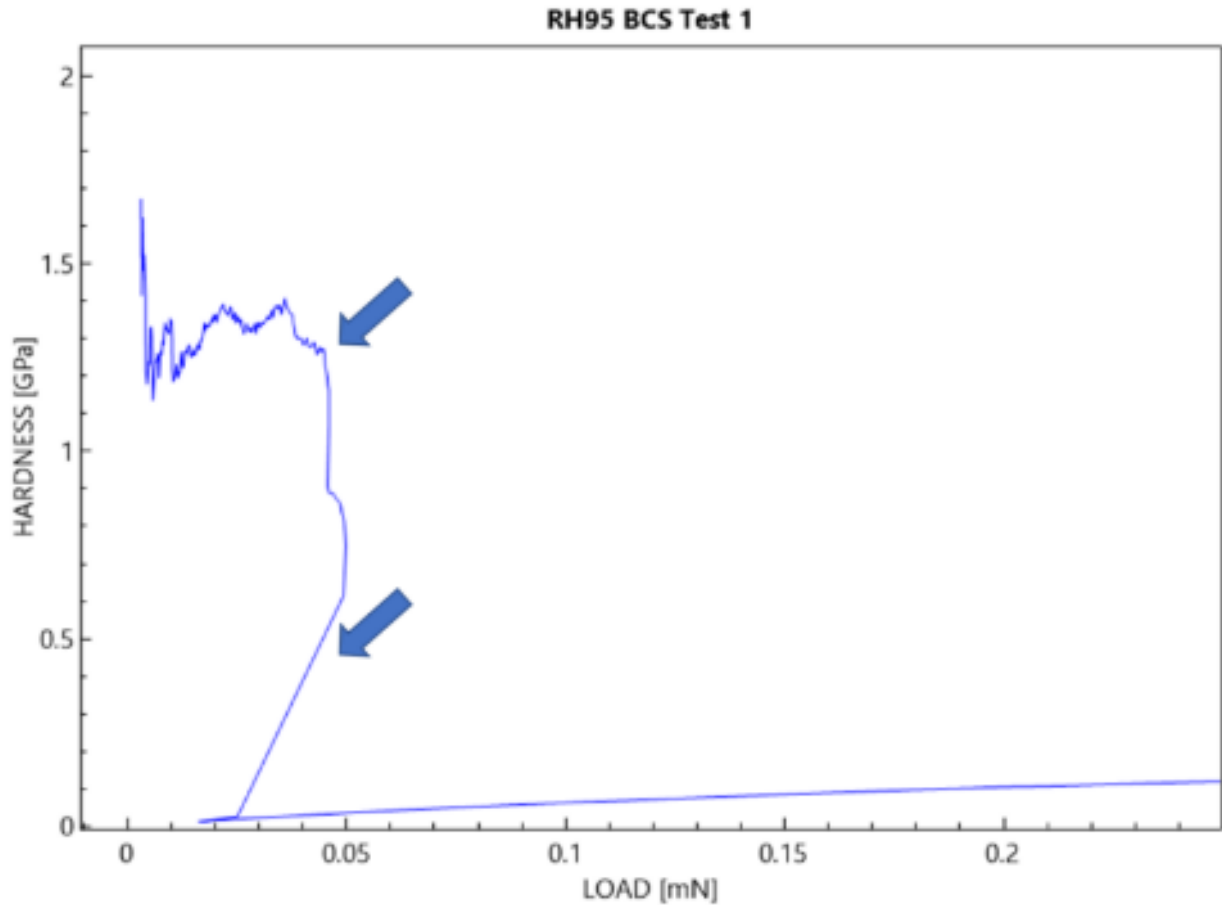


Figure 59. A hardness vs. load curve in direct relation to the sample defined in Figure 58.

The nano indents were produced using an iMicro Pro was equipped with a diamond Berkovich tip with a blunted end that was rounded to a spherical apex radius of 87.06 nm. The Advanced Dynamic E and H method produced by Nanomechanics, Inc., was utilized. The powder was loosely sprinkled onto carbon paste and painted onto a stiff metal puck. Figure 60 shows the aluminum powder within the carbon paste and an actual indent subsequent to testing.

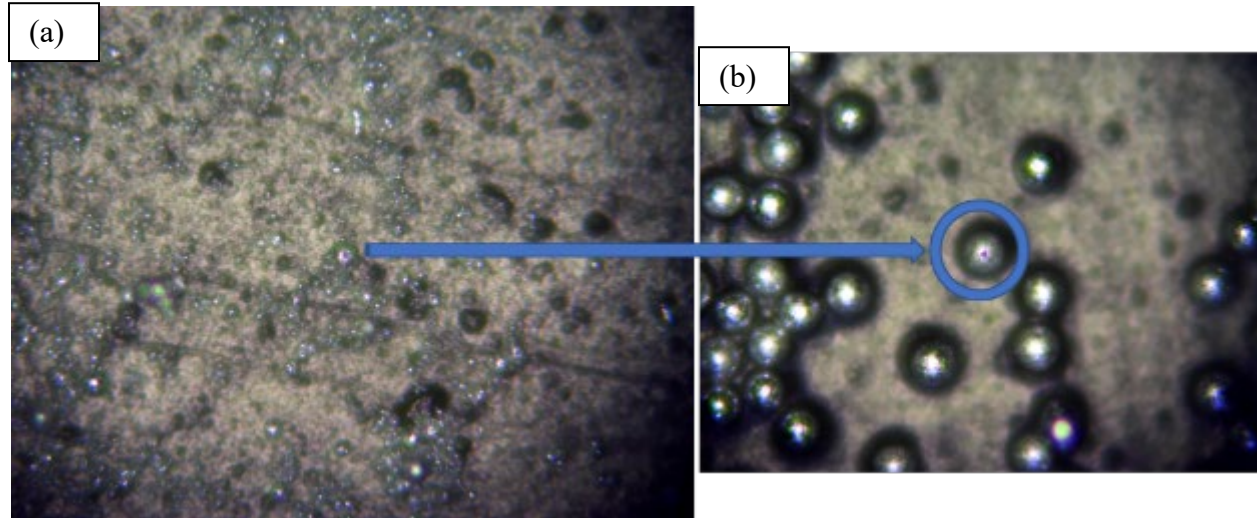


Figure 60. (a) Enlargement of area identified by arrow and blue circle of Al powder was placed onto carbon paste. (b) Shows the residual imprint left on the powder particle after testing.

To confirm the state of the nanoindenter tip, the respective area function and frame stiffness calibrations, a reference sample made of fused Si was tested using the iMicro Pro nanoindentation system with a low-force InForce 50 actuator installed. The data acquired from the Si calibration sample is presented in Figure 61. Table 20 contains the individual measurements and test data substantiating the calibration. The data presented in Figure 61 confirmed that the system was well calibrated [171].

Figure 62 depicts the hardness vs. depth curves for three particles from the as-received (AR) HP-Al powder group. The arrows point to each of the reporting depths for determining the oxide layer thicknesses. The average depth before load-displacement excursion was determined to be 7.88 nm, which corresponds to an estimated oxide/hydroxide thin film thickness of approximately 3.9 nm. The average peak hardness recorded while indenting the surface layer was 1.50 GPa. Figure 63 presents the load-depth curve for the high purity Al powder exposed to 50% humidity (RH-50%). The resultant excursion in the curve is enlarged and accompanies the full load vs. depth graph. The average oxide/hydroxide layer thickness of this sample was estimated to be 4.0 nm. Furthermore, the average peak hardness, i.e., the hardness of the oxide layer, was estimated to be 1.73 GPa. Figure 64 and Figure 65 report data related to the 95% humidity exposed powders. In this case, the thickness evaluated was determined to be significantly higher at about 9.2 nm, while the average peak hardness approached 2.28 GPa. Figure 66 summarizes the findings.

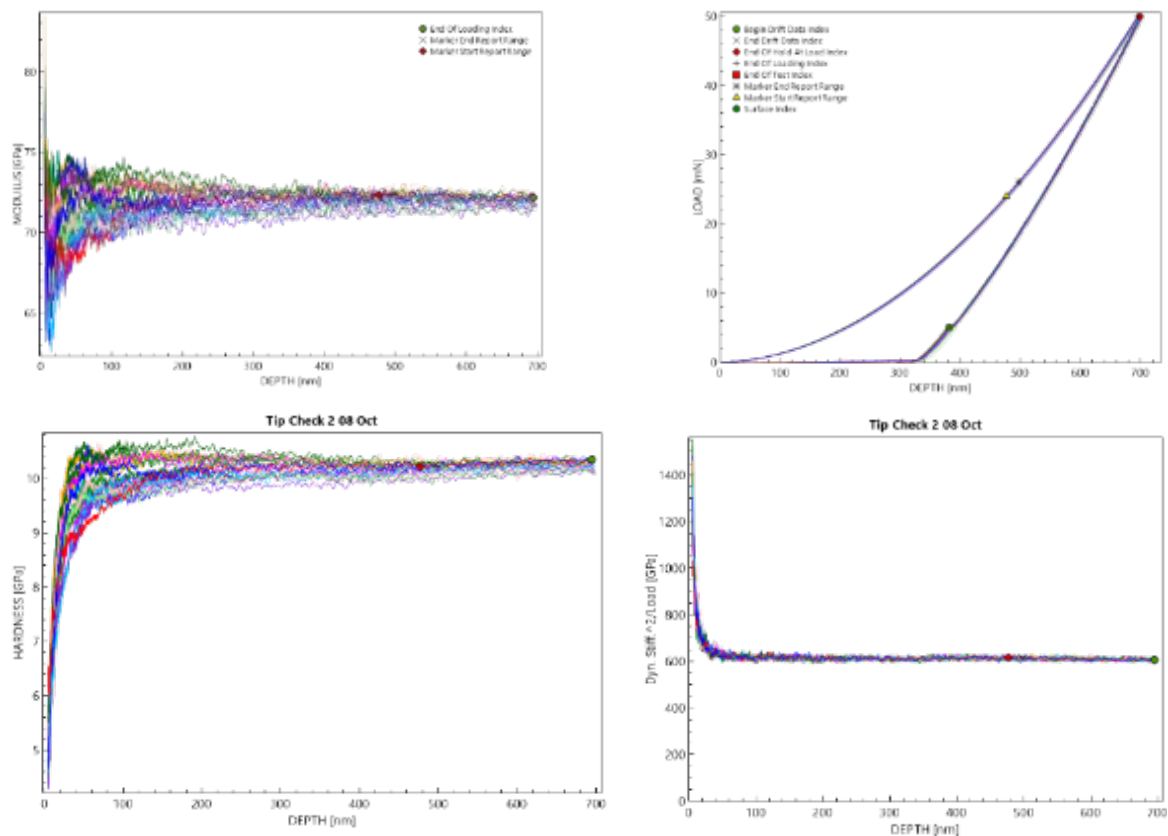


Figure 61. Fused Si data that demonstrated that the system was well calibrated and consistent with the known Elastic modulus and hardness values of reference materials.

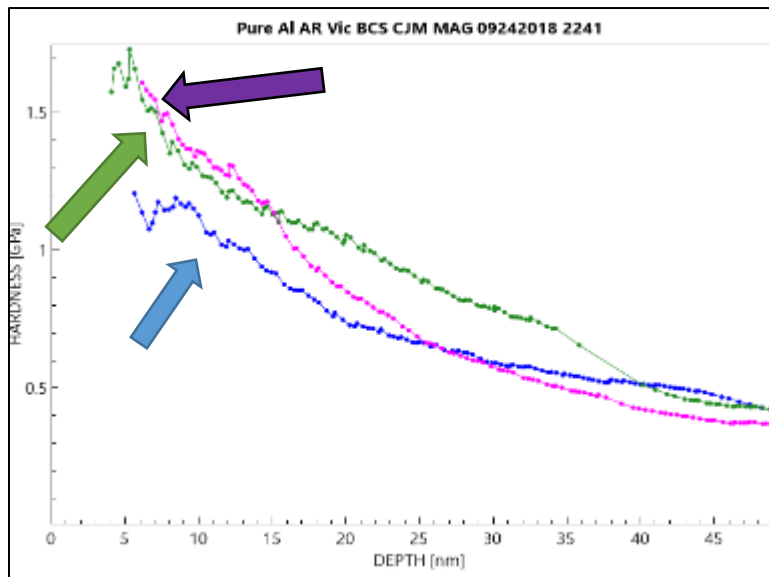


Figure 62. Comparison of indentation hardness vs. depth curves for three particles of AR HP Al powder. Arrows indicate the depth used in calculating the native oxide film thickness.

Table 20. Nanohardness Measurements of Single Powder Particles Representing all Groups

Test	Pmax	hmax	Reporting Depth	HV	Hardness	Modulus
	mN	nm	nm	None	GPa	GPa
1	49.931	701	488.7	964	10.19	71.6
2	49.983	700	486.2	973	10.30	72.3
3	NaN	NaN	NaN	NaN	NaN	NaN
4	49.958	700	485.9	974	10.30	72.4
5	49.928	700	487.3	966	10.22	72.2
6	49.939	702	488.1	965	10.21	71.8
7	49.901	703	489.9	954	10.10	71.5
8	NaN	NaN	NaN	NaN	NaN	NaN
9	49.964	699	485.3	977	10.34	72.5
10	49.962	703	488.9	958	10.14	71.8
11	49.925	699	486.6	971	10.27	72.3
12	NaN	NaN	NaN	NaN	NaN	NaN
13	49.938	700	487.4	965	10.21	72.2
14	49.924	705	490.7	944	9.99	71.5
15	49.970	704	488.5	957	10.12	72.1
16	49.908	700	486.9	967	10.23	72.4
17	49.911	700	487.2	970	10.26	72.0
18	49.913	700	486.8	969	10.25	72.4
19	49.941	704	491.6	945	9.99	71.1
20	49.908	704	490.1	952	10.07	71.6
21	49.938	704	490.5	948	10.03	71.6
22	49.947	702	487.7	964	10.20	72.1
23	49.967	700	486.3	970	10.26	72.6
24	49.993	700	486.9	968	10.24	72.3
25	49.951	699	486.8	967	10.23	72.4
Average	49.941	701	487.9	963	10.19	72.0
Standard Deviation	0.025	1.8	1.7	9.2	0.097	0.39
Coefficient of Variation	0.05%	0.30%	0.35%	1.00%	0.95%	0.54%

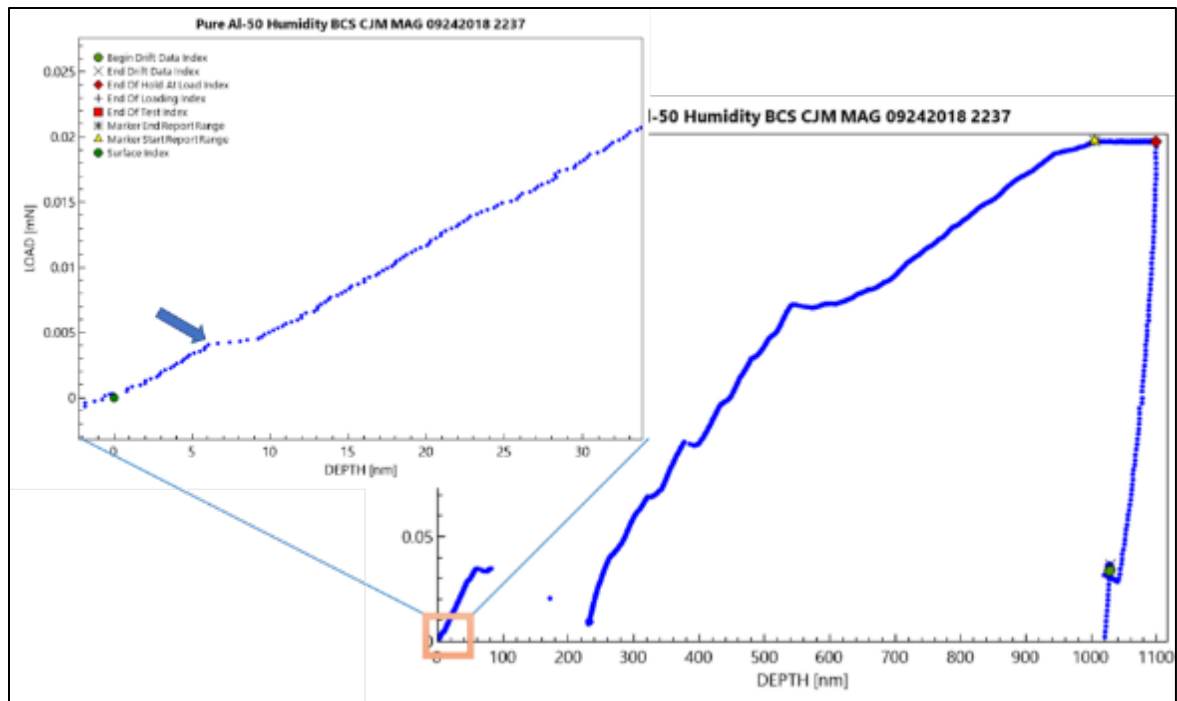


Figure 63. A load-displacement curve for an RH 50% HP Al powder particle.

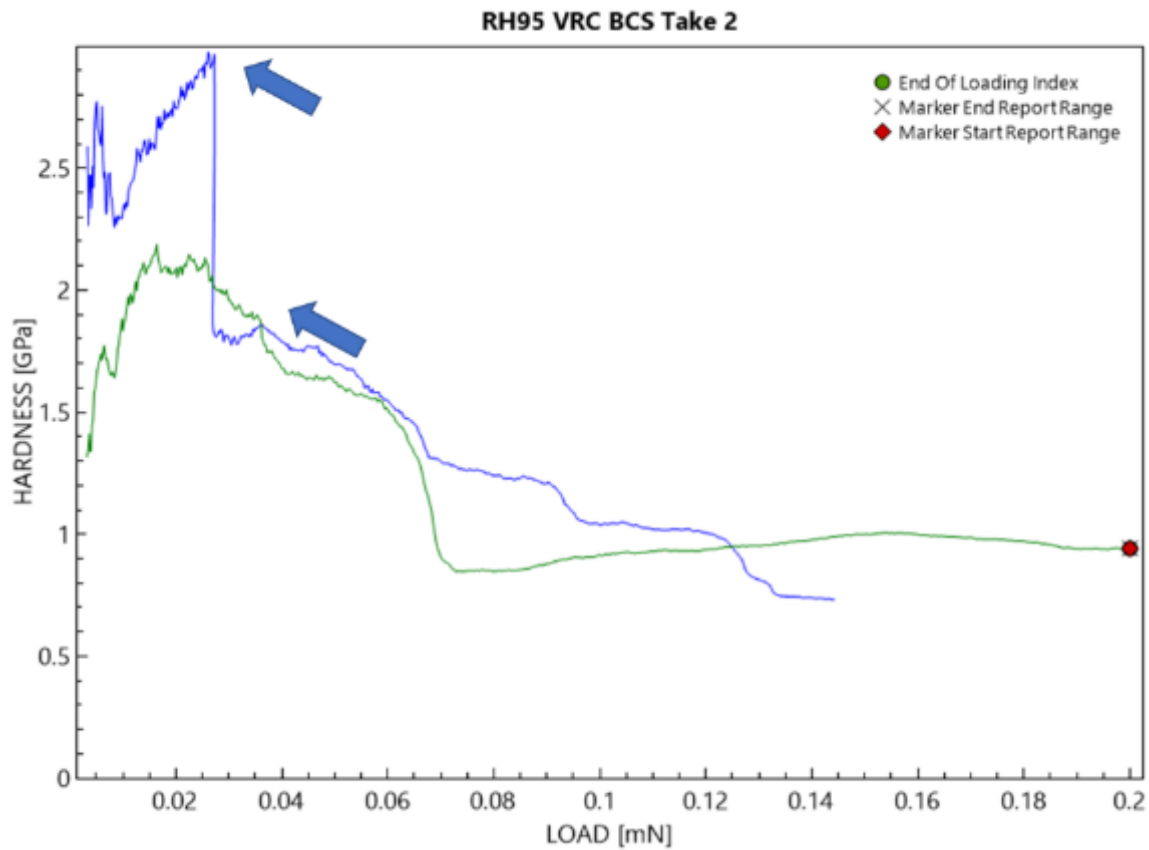


Figure 64. Plot of two hardness-load curves for two RH 95% HP Al powder particles.

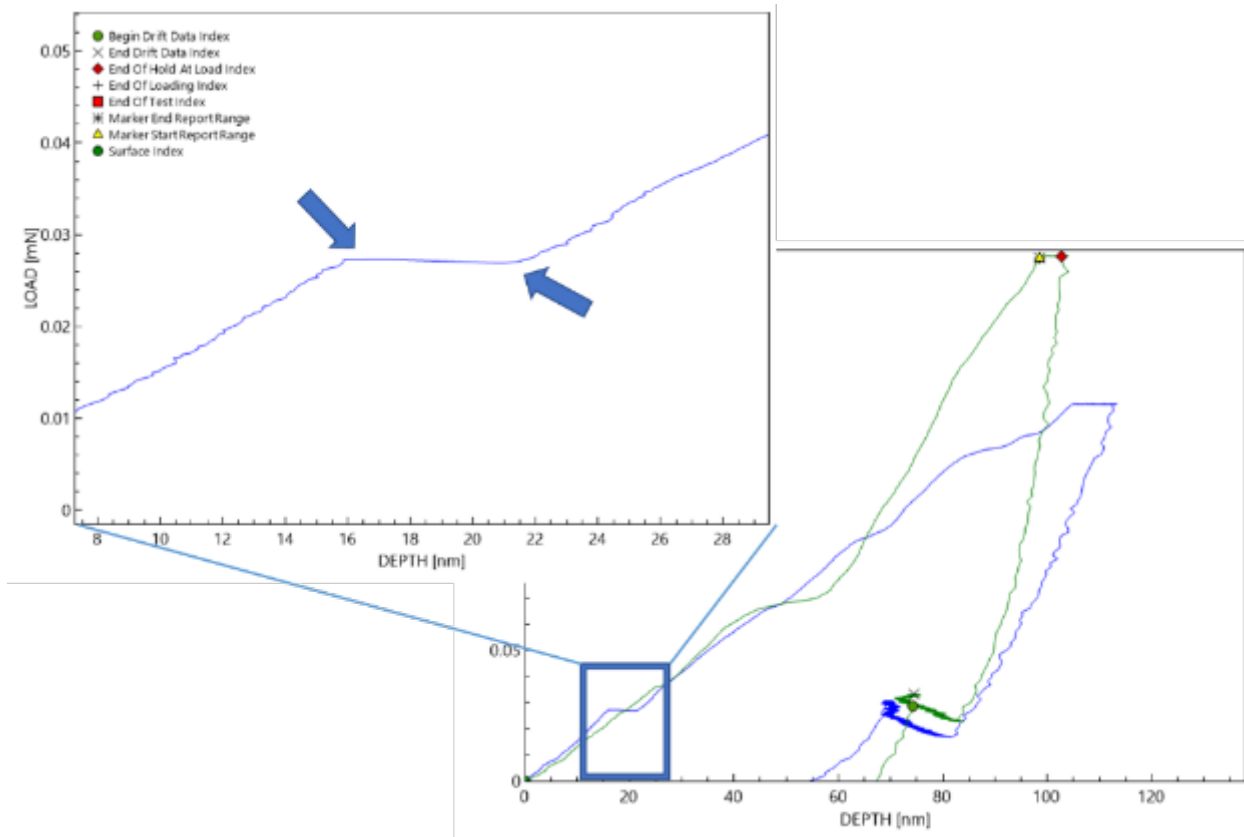


Figure 65. Plots of two load-displacement curves for two RH 95% HP Al powder particles.

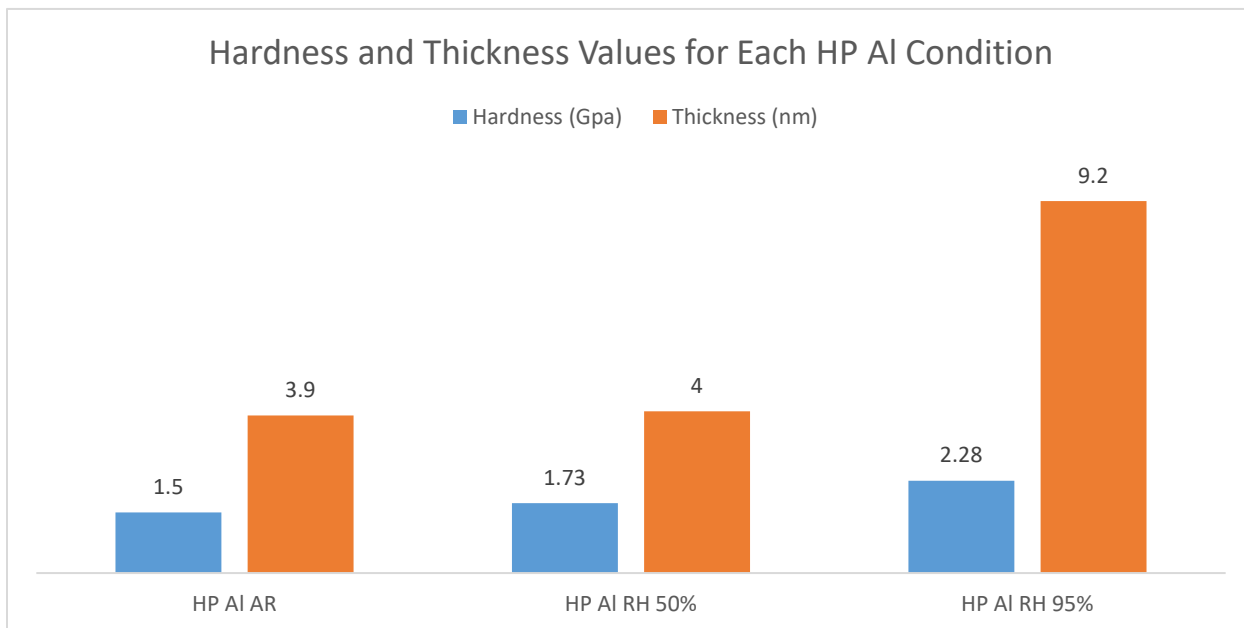


Figure 66. Categorical comparison of each of the three samples studied herein in terms of indentation hardness and average thickness for each.

4.2 Single Particle Impact and Critical Impact Velocity

In-situ single particle impact experiments were conducted on two different sets of aluminum powders at UMASS and MIT. One set of powder was exposed to high temperature dry air for three different lengths of time. A second set of powders was exposed to different levels of relative humidity for a fixed amount of time and fixed temperature. For both sets of experiments, the same electro-polished 99.999% purity research grade aluminum was used as the impact substrate.

4.2.1 Substrate Preparation

Initially, commercial grade high-purity (99.9%, McMaster-Carr) and research-grade high-purity (99.999%, Sigma-Aldrich) were purchased and polished to determine which substrate would be suitable for the SPI. Due to the softness of the pure aluminum substrates, mechanical polishing methods often left traces of sub-micrometer-scale abrasive particles embedded in the polished surface. To achieve smooth and clean surfaces, all substrates were prepared by electro-chemical polishing using a perchloric acid bath (Figure 67).

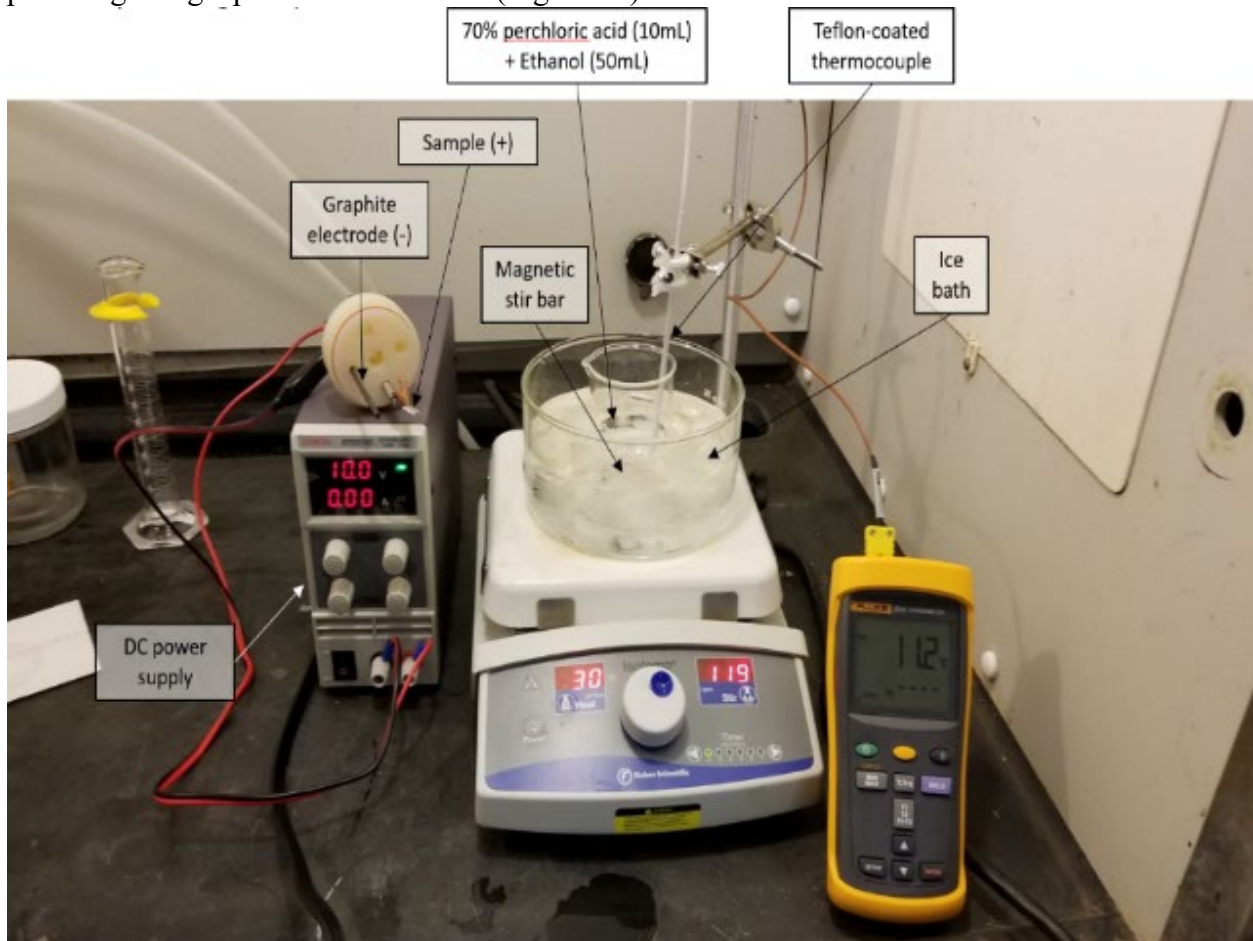


Figure 67. Apparatus used by UMASS to electro-polish the substrates prior to SPI testing.

The top part of the electro-polishing assembly is made of Teflon and the cathode is a high purity graphite rod. A piece of high-purity aluminum foil was immersed into the electro-polishing solution (70% perchloric acid + 99% ethanol) and an ice bath lowered the temperature of the solution below 10°C during the electro-polishing. Due to the initial roughness of the foil, electro-polishing was performed for 5 min with a voltage of 10 V. The electro-polished substrate was rinsed with running distilled water, and dried by blowing air.

Even the slightest amount of surface contamination could result in erroneous SPI test results because embedded inclusions would interfere with particle bonding and as the figures indicate these inclusions can be in the order of a few microns in size. Since the commercial-grade aluminum contained more inclusions at the surface than the research-grade aluminum, all the SPI experiments were performed with the electro-polished research-grade pure aluminum substrates (Figure 68). Electro-polished substrates were used within 24 hours. UMASS also provided these polished substrates to MIT for its SPI experiments to maintain consistency.

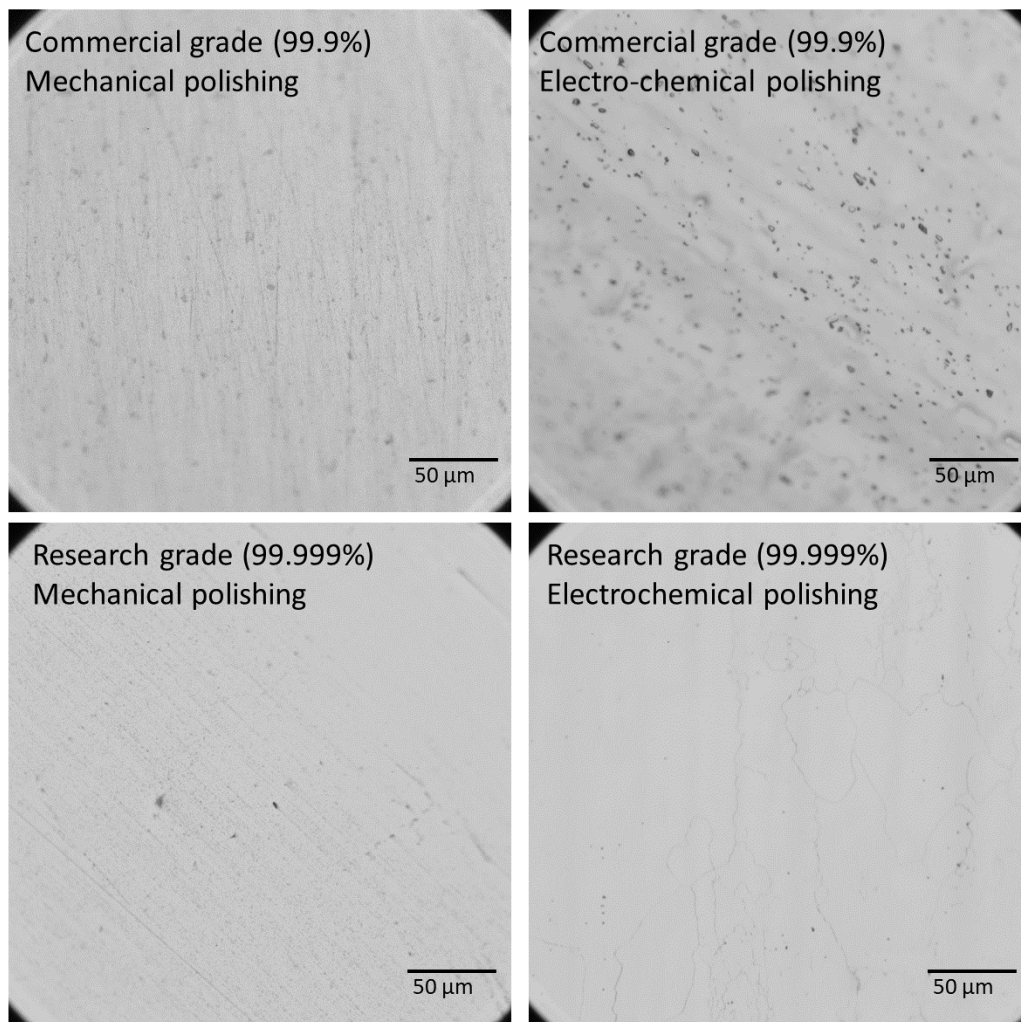
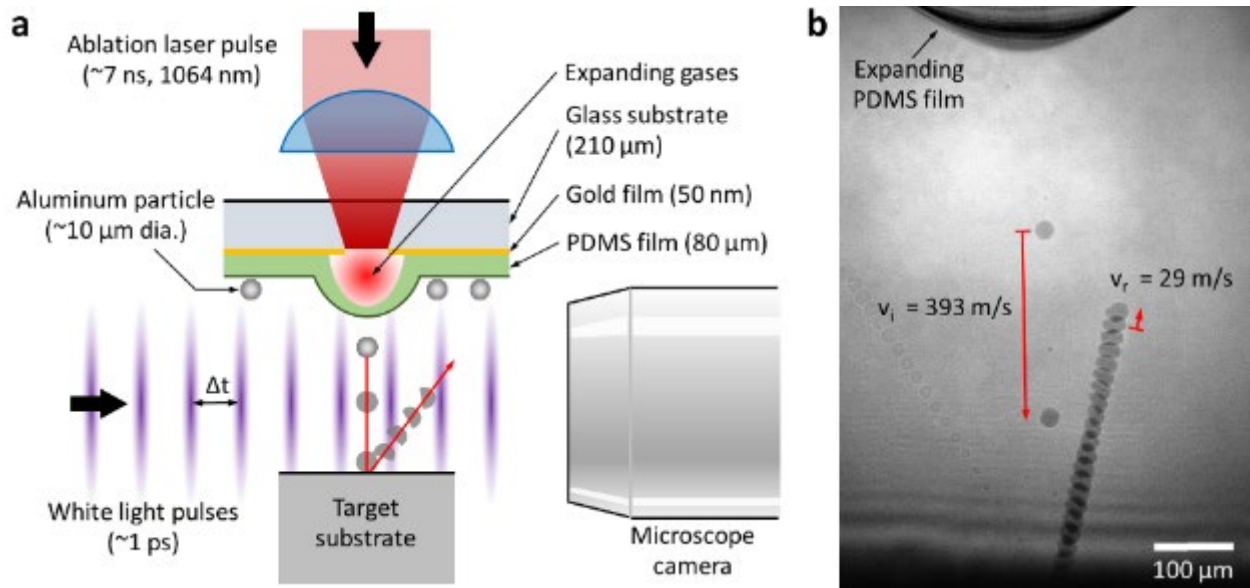


Figure 68. Comparison of polishing results of the two grades of pure aluminum.

4.2.2 Single Particle Impact Test-UMass

Aluminum particles from each powder group were dispersed on a launch pad with a brush. A single individual particle having a diameter near $10\ \mu\text{m}$ was selectively accelerated by localized laser ablation of the gold layer behind the particle (Figures 69a). During the flight of the particle, ultrafast ($<10^{-12}\ \text{s}$) white light pulses illuminated the moving particle and a microscope camera recorded all the projected images of the particle in a single frame (Figures 69b). Impact and rebound speed of the particle were calculated using this multi-exposure image and the time difference between adjacent illumination pulses (or an interframe time).



Figures 69a and b. Single particle experiment using the UMass LIPIT system. (a) Schematic illustration of SPI. (b) An ultrafast photograph shows a collision/rebound motion of an aluminum particle with an interframe time of 603 ns.

Rebound speeds (v_r) of particles near $10\ \mu\text{m}$ diameters were measured as a function of impact speeds (v_i) using the UMass LIPIT system. Because the rebound motion of some particles cannot be recorded when their rebound speed is very slow and they are moving in an out-of-focus direction, every impact area was inspected by an optical microscope to confirm the bonded particle. The individual particle impact can be varied by a small variation of the particle's conditions such as shape, surface roughness, rotational motion, and the thickness of hydroxide/oxide. Thus, CIV is understood by two characteristic speeds, a highest impact speed of rebounding particles (HSRP) and a lowest impact speed of bonding particles (LSBP). HSRP indicates existence of some unfavorable factors including the hydroxide/oxide layer while LSBP shows a bonding event under the most favorable conditions.

Figure 70 shows a negligible difference between “As-received” and “RH-50” powders. This is also shown in HSRP and LSBP in Figure 71. However, a trend of “RH-95” particles was largely deviated from that of “As-received”. Both LSBP and HSRP were substantially increased due to

the 4-day exposure to high humidity. Moreover, the widened difference between LSBP and HSRP indicates that particle bonding became more unstable.

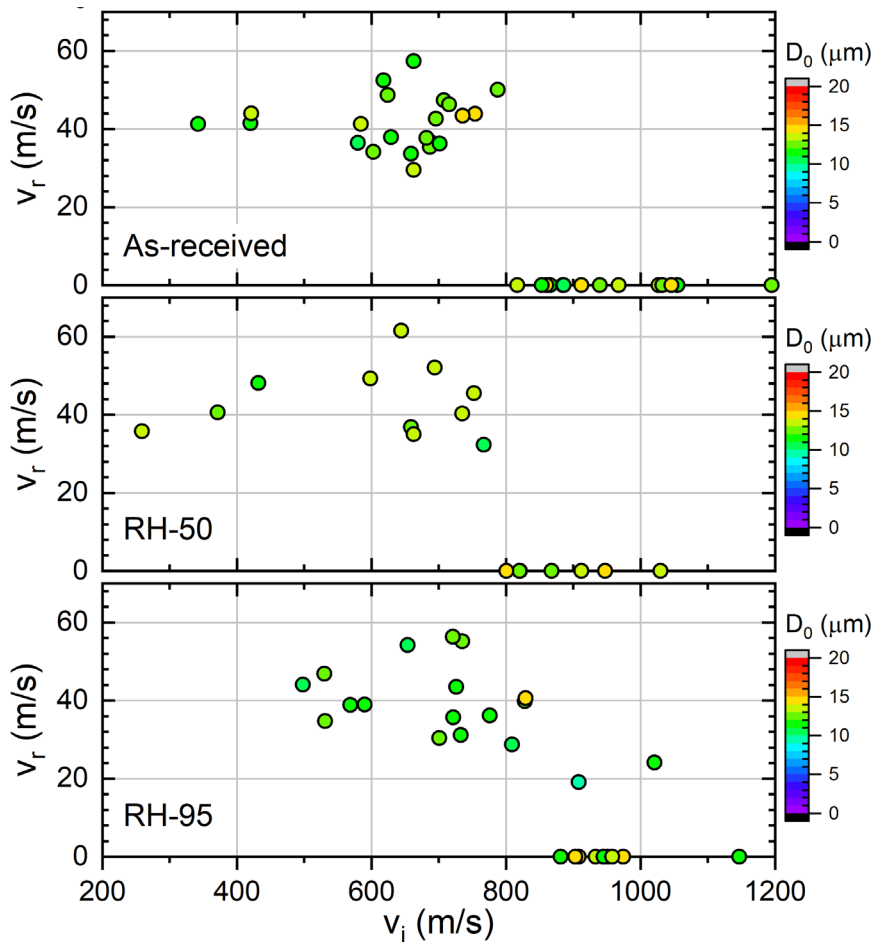


Figure 70. Rebound speeds of “As-received”, “RH-50”, and “RH-95” powders. The symbol color represents the impacting particle’s diameter.

Table 21. Lowest Speed Bonded Particle vs Highest Speed Rebounding Particle.

Group Identification	LSBP (m/s)	HSRP (m/s)
As-received	817	788
RH-50%	801	767
RH-95%	881	1021

Table 21 compares the highest impact speed of rebounding particles (HSRP) to the lowest impact speed of particles to bond (LSBP). Comparing to HSRP and LSBP, the mean values of rebound speeds show a less distinctive trend regarding the humidity effect. However, widening of the distribution of rebound speeds may reflect unstable bonding strengths of particles in the elastic relaxation stage.

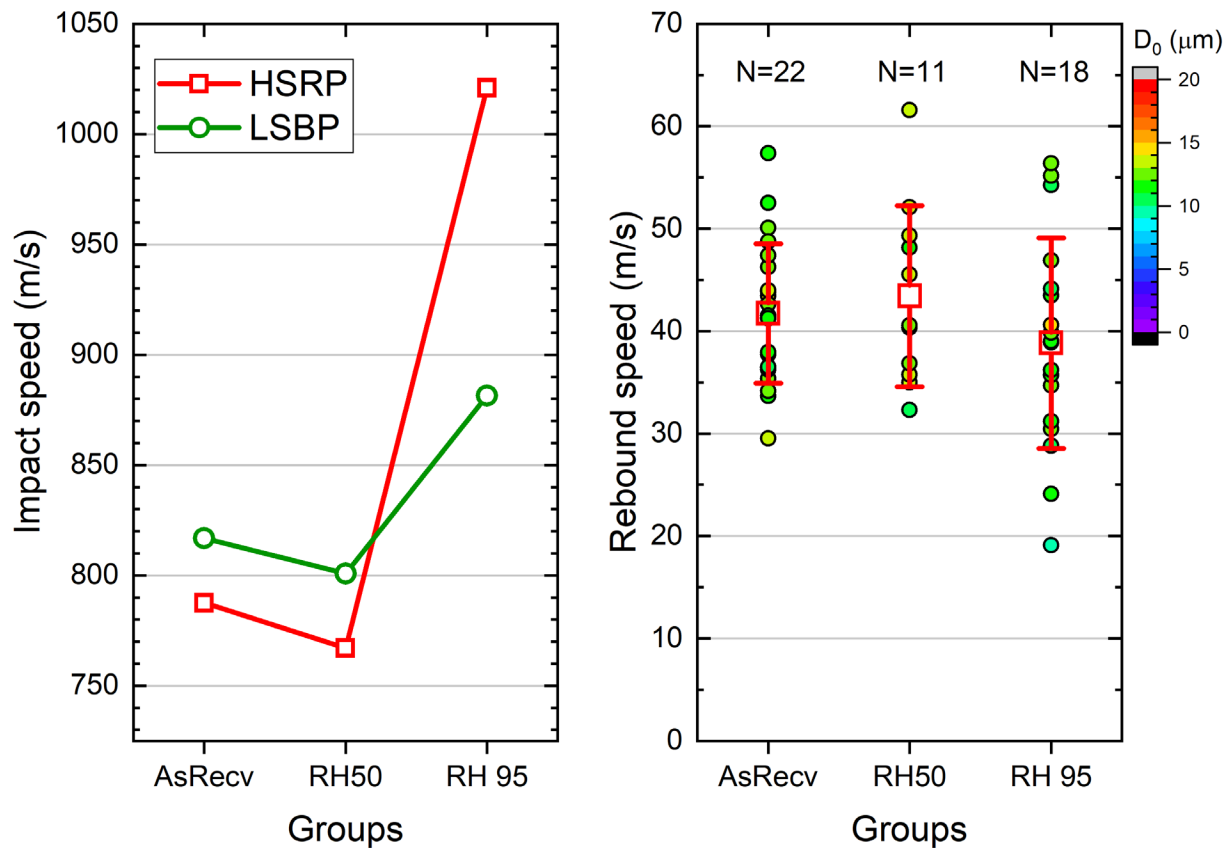


Figure 71. Trend of rebound speeds of “As-received”, “RH-50”, and “RH-95” powders. The symbol color represents impacting particle’s diameters.

Figure 72 shows trends of rebound speeds of the four HT powders, “HT-baseline”, “HT-30”, “HT-60”, and “HT-240”. The exposure of these powders in air at 300°C for up to 240 minutes did not appear to have an effect on bonding and the LSBPs were almost identical. Furthermore, the HSRP values did reveal any discernable trend. Table 22 compares the highest impact speed of rebounding particles (HSRP) to the lowest impact speed of particles to bond (LSBP).

Table 22. Lowest Speed Bonded Particle vs Highest Speed Rebounding Particle.

Group Identification	LSBP (m/s)	HSRP (m/s)
HT-baseline	817	843
HT-30	820	832
HT-60	817	812
HT-240	819	856

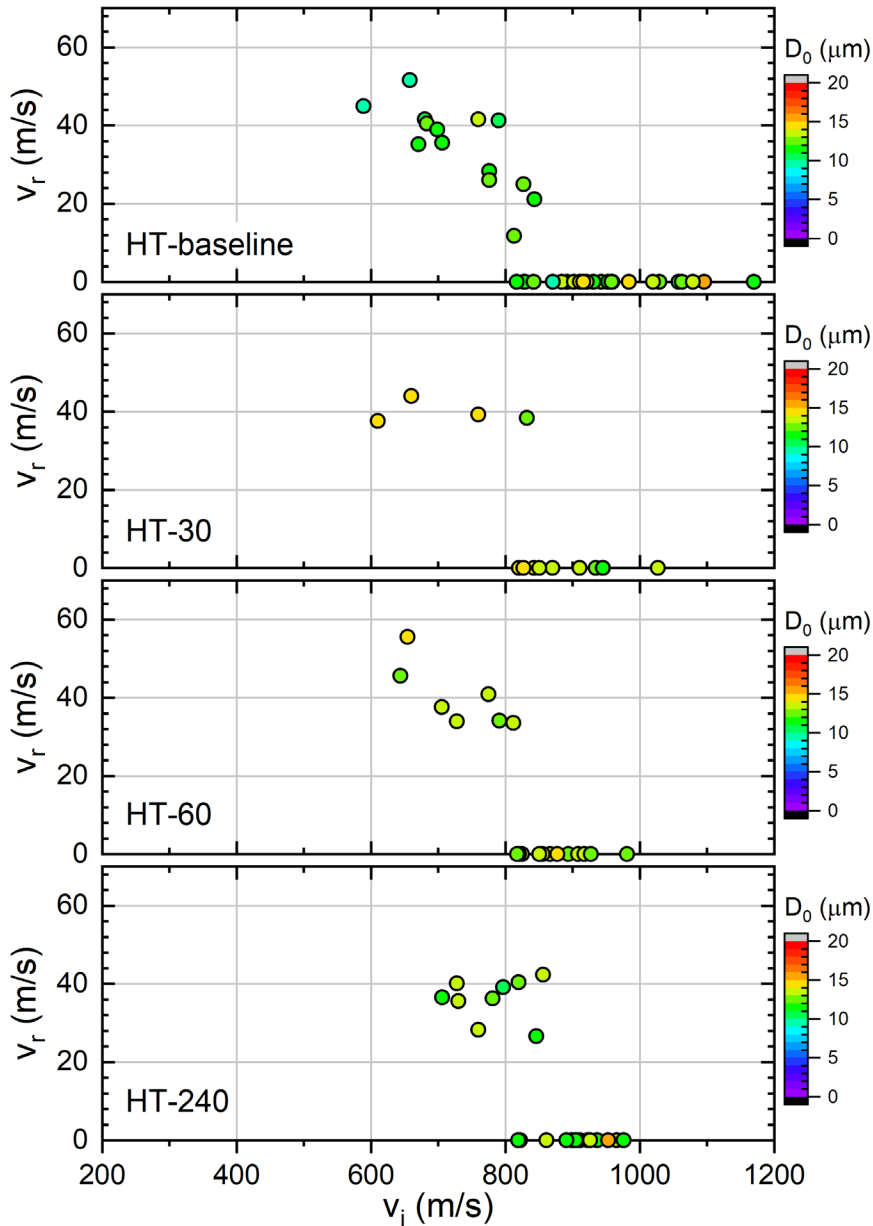


Figure 72. Rebound speeds of “HT-baseline”, “HT-30”, “HT-60”, and “HT-240” powders. The symbol color represents the diameter of the impacting particle.

The mean values of rebound speeds between the HT powder groups contained in Figure 73 showed a minor change without a consistent trend.

Through the UMASS SPI experiments, it was revealed that long-term exposure of feedstock powders to humid air (simulating a storage environment) can alter the characteristics of cold spray and can potentially deteriorate the quality of the cold spray deposit by adversely affecting the bonding. However, a few hours of exposure to high-temperature dry air, which occurs during the cold spray process, may not cause any significant effect on bonding.

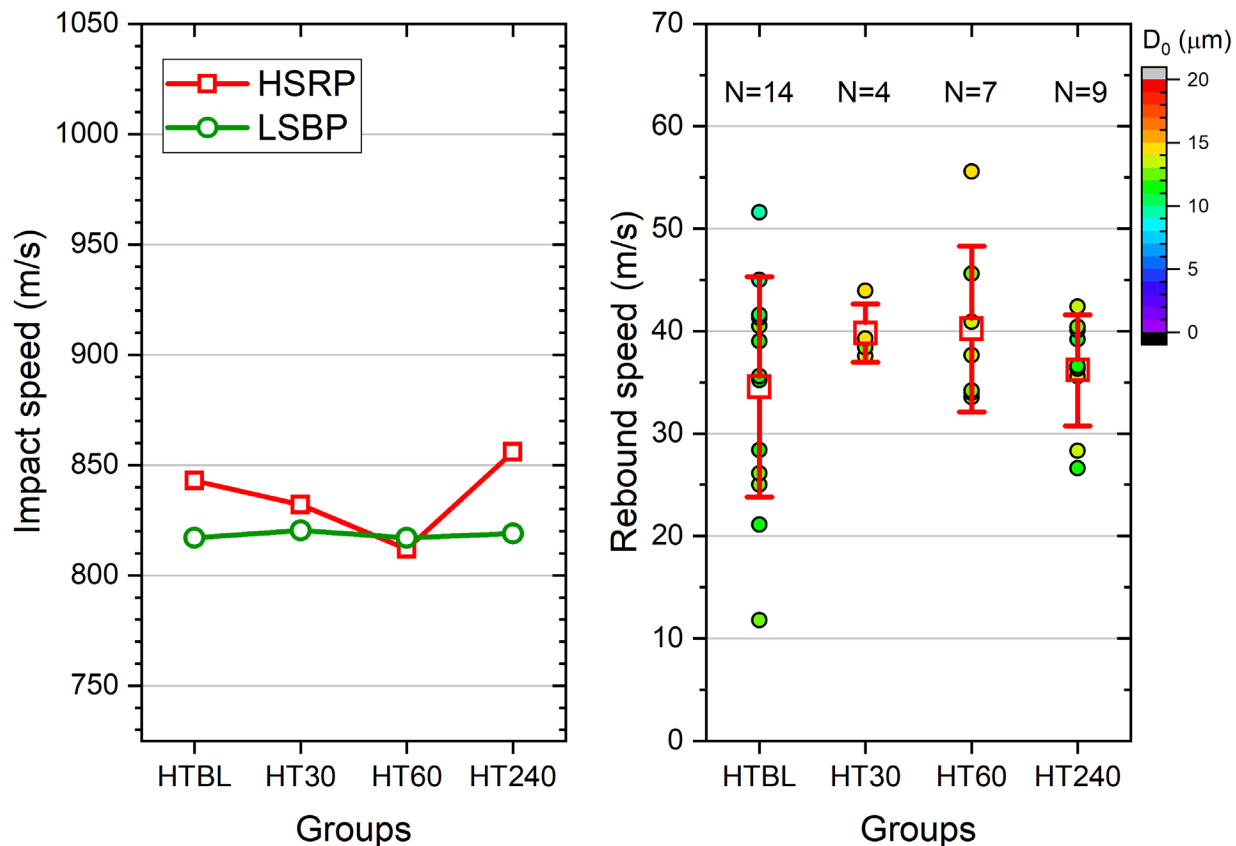


Figure 73. Trend of rebound speeds of “HT-baseline”, “HT-30”, “HT-60”, and “HT-240” powders. The symbol color represents the diameters of the impacting particles.

4.2.3 Single Particle Impact Test-MIT

HP-Al powder particles were taken from each vial prepared at UTRC and spread onto a launch pad made of a glass substrate, a gold layer and a polyurea film. A laser excitation pulse (pulsed Nd:YAG 10-ns duration, 532-nm wavelength) was then targeted at the launch pad, causing ablation of the gold layer, expansion of the elastomeric film, and as a result acceleration of an individual aluminum particle. The in-flight velocity of the individual aluminum particle was recorded using a high-frame-rate camera (SIMX 16, Specialized Imaging), and the moment of impact onto the substrate was observed. Multiple particles were accelerated at a range of velocities, by varying the laser pulse energies and the impact velocities of particles that were found to adhere to the substrate were recorded. Particles accelerated at a velocity below the critical velocity threshold were observed to rebound off the substrate, and the post-impact rebound velocity was recorded, in addition to the initial impact velocity.

To avoid any further environmental effects on the oxide/hydroxide surface layers, each set of powders was stored in a glove box prior to conducting impact experiments. Testing was performed

on the same day as the initial opening of the powder vial to avoid any further oxidation or hydrolysis of the powder. All tests were carried out at room temperature. All tests were conducted using particles of approximately 10 microns in diameter, as particle size is known to affect the impact behavior and the critical velocity required for adhesion. Individual particles were selected prior to launch using a CCD camera.

Initially, the impact behavior of the HP-Al powder exposed to humidity were tested (RH groups), to measure the effect of any surface layers on the CIV. The “As-Received” (AR) batch of powders that had no prior exposure to humidity and temperature (other than that associated with gas atomization and subsequent shipping and handling) was tested as a control group, along with a batch of powders exposed to 50% relative humidity (RH-50) for four days and another batch exposed to 95% relative humidity (RH-95) for four days.

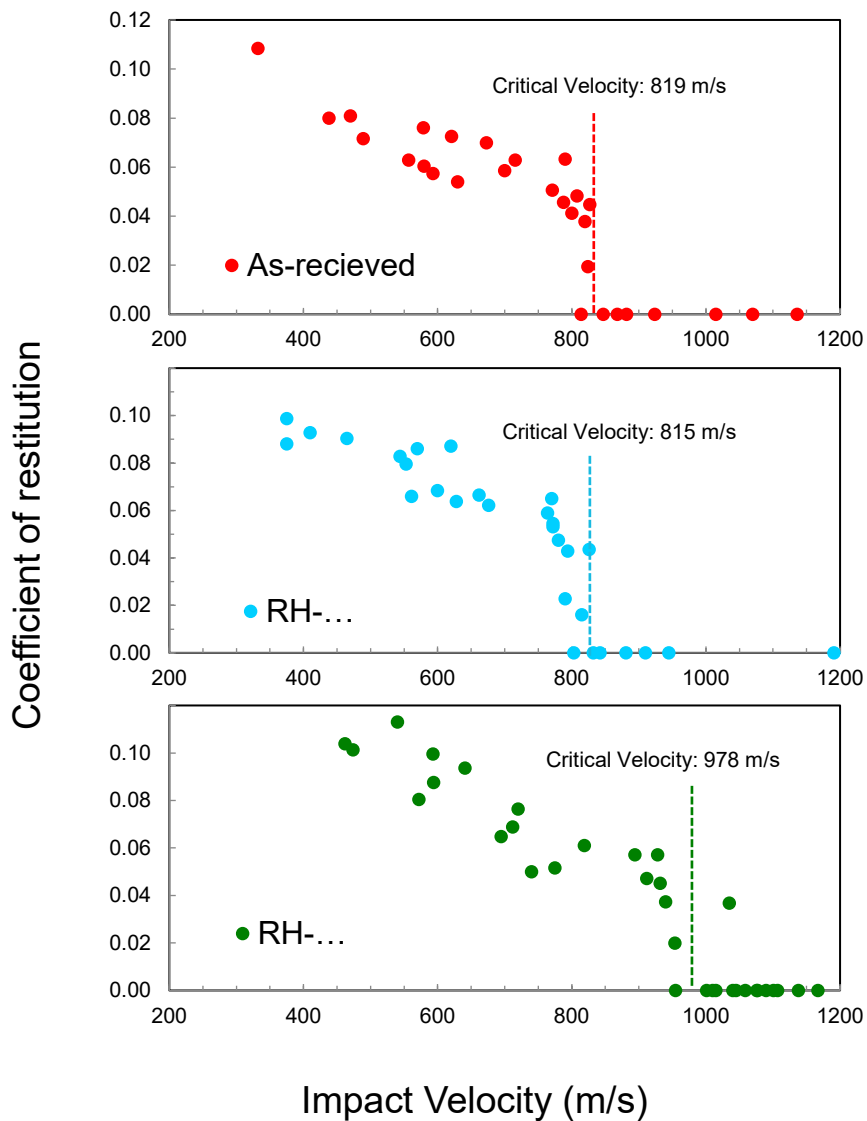


Figure 74. Coefficient of restitution as a function of CIV for AR, RH-50% and RH-95%.

Figure 74 shows the impact testing results for each of the three different batches of powder. The coefficient of restitution, which is the ratio between the rebound velocity and the impact velocity, is shown as a function of impact velocity. The coefficient of restitution decreases with increasing impact velocity until it reaches zero, indicating that bonding has occurred.

The critical impact velocity (CIV) is defined as the velocity at which the coefficient of restitution reaches zero, and can be extracted from these plots by averaging the highest velocity at which rebounding occurs and the lowest velocity at which adhesion occurs. Table 23 reports the measured critical velocities for the as-received and the powder samples exposed to humidity.

Table 23. Critical velocity ranges for the As-received powder, RH-50% and RH-95%

Name	Description	Critical Velocity (m/s)
No exposure	As-received powders	[814 - 824]
RH-50%	50% relative humidity, 4 day exposure at 29°C	[803 - 826]
RH-95%	95% relative humidity, 4 day exposure at 29°C	[954 - 1001]

The lower bound of the range indicates the highest velocity at which rebound behavior was observed and the upper bound indicates the lowest velocity at which adhesion was observed.

There was not a significant difference in critical impact velocity between the as-received particles and the 50% relative humidity particles. Both had a critical velocity transition in the range of approximately 800 to 830 m/s. However, there was a significant increase in the critical velocity observed for the 95% relative humidity powders. The 95% relative humidity powders displayed a critical velocity between 950 and 1000 m/s. The dramatic increase in critical velocity associated with the 95% relative humidity exposure suggests that the surface chemistry of these powders, which likely incorporates more water in the form of a hydroxide, significantly inhibits bonding.

To further examine the results obtained with the 95% relative humidity powders, a second test was conducted using the same powder after being stored in a desiccator. A small amount of the 95% relative humidity powders was placed in a vacuum desiccator for three days with the goal of removing as much water from the surface of the particles as possible. The impact behavior was tested after drying. The results from this additional test are shown in Figure 75. The result revealed a decrease in velocity required for adhesion to the substrate with the desiccated 95% relative humidity powders. This served as further evidence that moisture, specifically hydroxide surface chemistry, played a significant role in critical velocity.

The data obtained for the 95% relative humidity powder that was desiccated and dried displayed a critical velocity that was less well defined than the other batches of powders. There was a range of velocities, roughly between 870 and 1000 meters per second, in which a mixture of both adhesion and rebound behavior was observed. This may have been the result of non-uniform drying in the desiccator, as particles at the bottom of the powder vial were less likely to have undergone a change in surface chemistry than particles directly exposed to the desiccator vacuum environment.

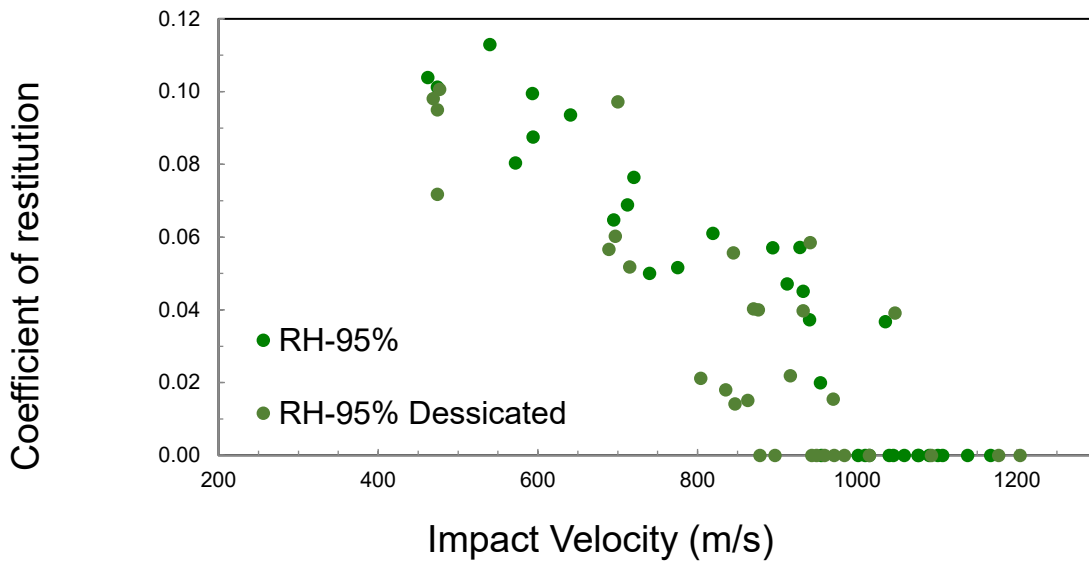


Figure 75. Coefficient of restitution as a function of impact velocity for the 95% relative humidity particles and desiccated 95% relative humidity particles.

In addition to the powders exposed to varying levels of humidity, impact experiments were also conducted on powders with different lengths of exposure to 300° C dry air (HT samples). A control sample, along with a thirty-minute, one-hour, and four-hour exposure were tested. Results from these tests are shown in Figure 76. Table 24 contains the measured critical velocities for the HT-baseline, HT-30, HT-60 and HT-240. Variations in the impact behavior and critical velocity of these four groups of powders were minimal. The thirty-minute exposure, one-hour exposure, and four-hour exposure powders all displayed a critical velocity between 820 to 850 m/s. The critical velocity range of the baseline powder was slightly lower, falling between 800 and 830 m/s. However, a statistically meaningful conclusion can be drawn from this data about an increase in critical velocity with increased high temperature exposure.

Table 24. Critical velocity ranges for the HT-baseline, HT-30, HT-60 and HT-240

Name	Description	Critical Velocity (m/s)
HT-Baseline	High temperature baseline	[801 - 827]
HT-30 min	Dry air exposure at 300° C for 30 minutes	[839 - 848]
HT-60 min	Dry air exposure at 300° C for 60 minutes	[819 - 840]
HT-240 min	Dry air exposure at 300° C for 240 minutes	[846 - 848]

The lower bound of the range indicates the highest velocity at which rebound behavior was observed and the upper bound indicates the lowest velocity at which adhesion was observed.

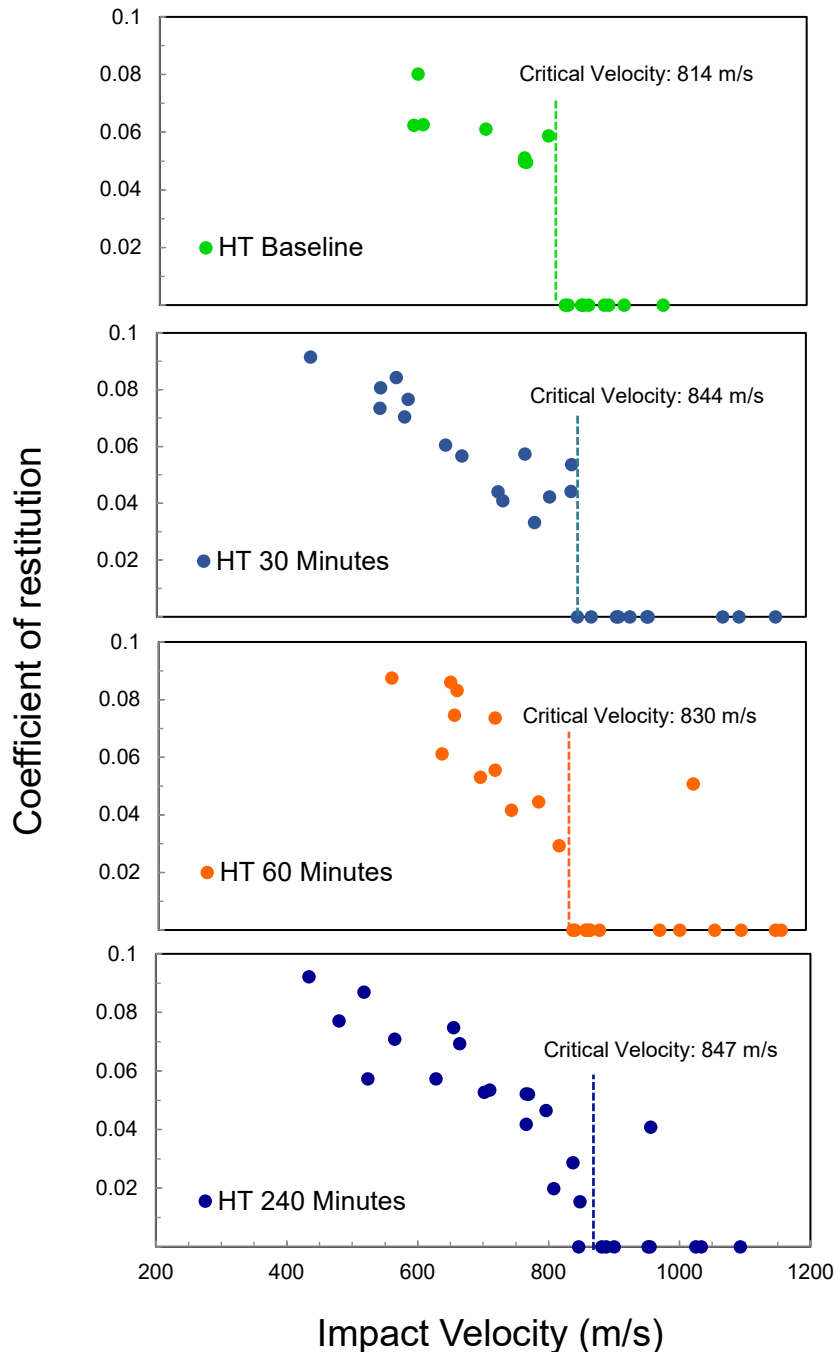


Figure 76. Coefficient of restitution as a function of CIV for HT-baseline, HT-30, and HT-240

4.3 Characterization of Bulk Cold Spray Samples

Bulk samples of material were produced from each of the six powder groups to determine the effects of the surface films produced on the feedstock HP-Al powder on the material properties; including tensile, hardness, and conductivity. The cold spray process parameters used to produce each sample of bulk material remained constant, as shown in Table 25. The fracture surfaces of the broken tensile specimens were also examined to determine the crack origin, fracture morphology and to discern any important features that may relate to the prior powder treatments.

Table 25. Cold Spray Parameters for Producing Bulk Samples from HP-Al Powder

Cold Spray Process Parameters	
SPRAY MACHINE VRC Gen III Max	ROBOT VELOCITY 200 mm/sec
T=300 C	SPRAY ANGLE 90 degrees
P=290 psi (20 bar)	STANDOFF 28.575 mm
SPRAY GAS Helium	STEP SIZE 1mm
PF GAS FLOW SETTING 100 slm	POWDER FEEDER RATE 4 rpm
NOZZLE 2-6.3x170mm TYPE PBI-VRC	GUN SPEED 200mm/sec

All the powders were cold sprayed with the VRC cold spray using helium with a gas pressure of 20 bar and a gas temperature of 300°C, (measured at the nozzle). A solid block of material was produced from 35 g of powder from each group and the cold spray process parameters remained constant for spraying the blocks of all of the powder groups, regardless of prior powder processing conditions. The spray pattern used was 25 mm by 33 mm incorporating the Robot Studio program.

The relative geometry of the cold sprayed blocks were evaluated by taking side and top view pictures of the samples. Figure 77 shows the resulting blocks of the heat treated powders under dry conditions. The side-view images reveal a decrease in the ‘ski-jump slope’ proportional with exposure to dry air. These results were consistent with the understanding that oxide layers of aluminum weaken the bond between particles during cold spray hence less deposition occurs. Less surface film build-up was anticipated with the heat treated samples as opposed to those associated with exposure to humidity. Similar results were observed for the powders treated under humid conditions (see Figure 78).

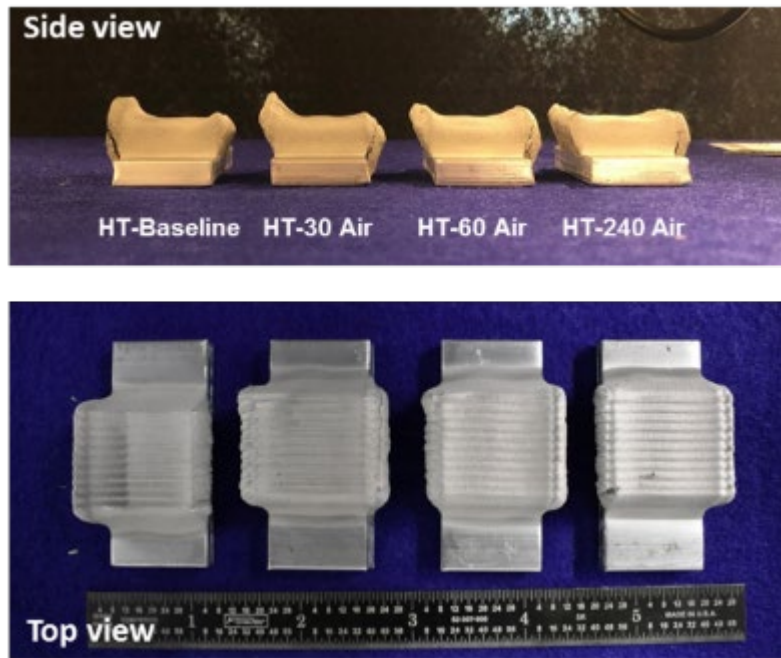


Figure 77. Images of Cold Sprayed deposits of heat treated powders under dry conditions.

Figure 78 showed no build-up on the sides of the RH-95% block, probably due to the formation of a thick layer of hydroxide on the powder, during high humidity exposure conditions. The side view images of the As-received and RH-50% showed no particular trend and this may have been due to the wide range of humidity that RH-50% samples was exposed to (RH=17-75%).

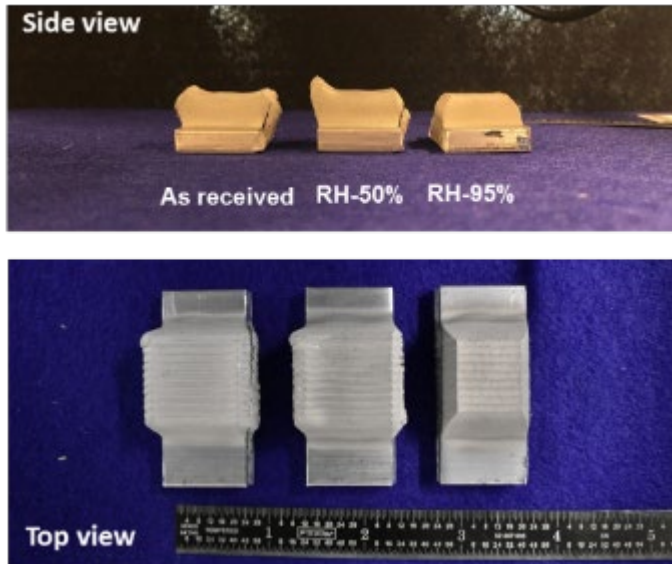


Figure 78. Images of Cold Sprayed deposits of heat treated powders under humid conditions.

The characterization of the cold sprayed blocks is summarized in Table 26, where thickness, conductivity and hardness was recorded, prior to tensile testing. To measure conductivity, the cold sprayed blocks were machined to a rough surface. An Eddy current probe of $\frac{1}{4}$ " diameter was used and the average of five measurements was reported along with its standard deviation. The micro-hardness was measured using a 200g diamond indenter. The average of five measurements was reported along with its standard deviation.

The conductivity of the block with powder treated under dry conditions showed the highest conductivity levels, about 59%. This result was not surprising as the aluminum particles were partially annealed during this treatment, which was performed at 300°C while the typical annealing temperature for pure aluminum is 343°C . Annealing would increase the ductility of the powder making it more amenable to the cold spray process and increase its deposit efficiency. In contrast, the samples exposed to humid conditions showed the lower conductivity measurements with RH-95% showing the lowest level at 44% which is most likely the direct effect of the amount of oxide/hydroxides in the cold spray bulk material. The similar value of conductivity for As-received and RH-50% samples could be due to the wide range of humidity that the RH-50% samples was exposed to (RH=17-75%).

The micro-hardness measurements have a similar trend to that of conductivity. The set of samples heat treated under dry conditions show the lowest micro-hardness (47 HV) while those exposed to humid conditions showed the higher values, with the highest value for RH-95% (55.6 HV). Annealed material would exhibit lower hardness and material that contained a higher level of oxides/hydroxides would have higher hardness. Again, the similar value of micro-hardness

between As-received and RH-50% samples could may be due to the wide range of humidity that RH-50% samples was exposed to (RH=17-75%).

Table 26. Summary of Conductivity and Hardness of the Cold Spray Bulk Samples

Powder Group Identification	Conductivity (%)	Micro-hardness 200g (HV)	Thickness as sprayed (in)	Deposition time (min)
HT-Baseline	59.5 ± 0.7	47.4 ± 0.6	0.335	10.0
HT-30Air	59.1 ± 0.7	47.3 ± 0.9	0.347	10.0
HT-60Air	59.12 ± 0.3	47 ± 2.1	0.343	11.0
HT-240Air	59.0 ± 0.7	47.14 ± 0.7	0.345	10.0
As- received	57.5 ± 0.7	49.74 ± 1.6	0.350	10.0
RH-50%	56.2 ± 1.5	49.5 ± 1.0	0.350	12.5
RH-95%	44.4 ± 2.1	55.6 ± 2.4	0.310	13.0

Mini-tensile specimens were machined from the cold-spray blocks produced from powder representing the seven powder conditions.

1. As-received: AR1, AR2 and AR3
2. 95% relative humidity: RH-95%
3. 50% relative humidity: RH-50%
4. Heat treated baseline: HT-Baseline
5. Heat treated at 30 min: HT-30
6. Heat treated at 60 min: HT-60
7. Heat treated at 240 min: HT-240

4.3.1. Mechanical tests

There were three groups of as-received specimens, in addition to the other 6 groups of specimens. All samples were tested using an Instron 5500r universal testing machine utilizing a strain rate corresponding to $3 \times 10^{-4} \text{ s}^{-1}$. Yield strength was measured using 0.2% offset of nominal strain, which is (displacement)/(gauge length). Ultimate tensile strength and fracture strength were obtained directly from engineering stress-strain curve. Ductility was measured separately by using video-recording the motion of two marks in the gauge section (Figure 79). The marks were made by black permanent ink, and the motion of the most outer region of the two marks was monitored with the single pixel resolution (Figure 79). Ductility was measured by tracking the motion of two most outer region of black dots in the gauge section with a single pixel resolution. We measured the distance at the beginning of the test (L_o) and that at the moment of fracture (L_f), and ductility (% elongation) was calculated by $(L_f - L_o)/L_o \times 100$ (%).

The brief summary of mechanical data is available in Table 27. RH-95% specimens exhibited higher strength but significantly lower ductility than the as-received powder and the heat treated powders. Heat treated baseline specimens exhibited the highest ductility. AR1 and AR2 samples showed similar mechanical behavior, but AR3 had a higher yield and ultimate tensile strength with slightly lower ductility.

All measured data are listed in Table 28. Stress-strain data are also contained in Figure 80. Stress-strain Curves of Cold Spray Bulk Samples of HP-Al. Note that the strain value in the stress-strain curves was calculated simply by (displacement)/(gauge length). This calculation does not provide the accurate strain value, and this method was used for plotting purposes. The precise measurement of ductility was determined separately with video measurement.

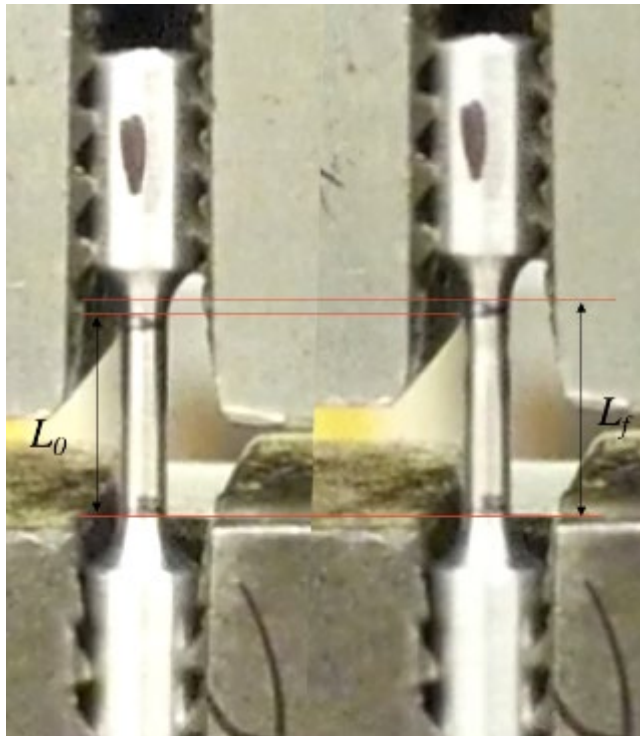


Figure 79. Video measurement of ductility.

Table 27. Summary of Mechanical Properties of Bulk Cold Spray HP-Al

Sample ID	Yield Strength MPa	Ultimate Tensile Strength MPa	Fracture Strength MPa	Ductility
AR1	101.08 ± 4.47	145.12 ± 3.57	119.74 ± 3.43	7.14 ± 0.57
AR2	105.73 ± 13.60	147.52 ± 4.19	122.86 ± 2.02	6.14 ± 0.26
AR3	124.34 ± 3.34	150.74 ± 2.05	129.22 ± 3.26	5.94 ± 0.88
AVERAGE AR1-AR3	110.38	147.79	123.95	6.41
RH-95%	124.64 ± 5.01	151.30 ± 14.80	150.73 ± 14.34	1.83 ± 0.12
RH-50%	125.31 ± 5.21	151.05 ± 2.03	129.22 ± 4.13	6.65 ± 0.51
HT-Baseline	109.60 ± 2.41	140.18 ± 1.77	106.20 ± 1.88	10.48 ± 0.59
HT-30Air	105.78 ± 4.98	145.32 ± 1.99	111.82 ± 4.07	9.00 ± 1.21

HT-60Air	103.02 ± 4.16	143.44 ± 3.78	108.30 ± 1.11	9.39 ± 0.96
HT-240Air	110.08 ± 5.93	143.02 ± 2.61	115.48 ± 4.73	8.20 ± 0.81

Table 28. Mechanical Test Data of all HP-Al Powder Groups

	YS	UTS	FS	Ductility		YS	UTS	FS	Ductility
AR1	101.40	145.12	119.74	0.0714	HT-Baseline	109.00	140.18	106.20	0.0968
STD DEV	4.39	3.57	3.43	0.0057	STD DEV	2.24	1.77	1.88	0.0059
1	100.00	148.40	122.90	0.0790	1	110.00	141.50	109.00	0.0930
2	105.00	142.20	115.00	0.0750	2	108.00	137.30	104.90	0.1070
3	107.00	142.60	118.90	0.0710	3	112.00	141.60	104.70	0.0930
4	97.00	149.60	123.30	0.0650	4	106.00	140.70	105.10	0.0940
5	98.00	142.80	118.60	0.0670	5	109.00	139.80	107.30	0.0970
AR2	103.40	147.52	122.86	0.0614	HT-30	105.40	145.32	111.82	0.0900
STD DEV	9.99	4.19	2.02	0.0026	STD DEV	3.58	1.99	4.07	0.0121
1	112.00	153.30	122.60	0.0590	1	110.00	147.10	116.70	0.0696
2	110.00	149.40	120.50	0.0630	2	106.00	146.50	112.80	0.0897
3	110.00	145.60	123.90	0.0650	3	106.00	146.40	114.00	0.1000
4	93.00	147.20	125.70	0.0610	4	105.00	144.30	109.30	0.0982
5	92.00	142.10	121.60	0.0590	5	100.00	142.30	106.30	0.0926
AR3	124.00	150.74	129.22	0.0594	HT-60	103.20	143.44	108.30	0.1039
STD DEV	2.00	2.05	3.29	0.0088	STD DEV	2.77	3.78	1.11	0.0096
1	125.00	151.10	125.60	0.0570	1	102.00	141.20	107.50	0.0990
2	126.00	150.90	133.20	0.0530	2	105.00	139.50	109.70	0.1138
3	123.00	151.00	129.40	0.0660	3	102.00	145.80	108.00	0.1000
4	121.00	153.20	131.60	0.0500	4	100.00	148.80	109.20	0.1142
5	125.00	147.50	126.30	0.0710	5	107.00	141.90	107.10	0.0927
RH-95	123.50	151.30	150.73	0.0183	HT-240	109.80	143.02	115.48	0.0820
STD DEV	5.07	14.81	14.34	0.0012	STD DEV	5.81	2.61	4.73	0.0081
1	116.00	129.30	129.30	0.0190	1	115.00	147.40	121.60	0.0840
2	126.00	156.00	156.00	0.0190	2	116.00	143.30	119.30	*
3	125.00	158.90	158.90	0.0170	3	103.00	142.10	111.30	0.0714
4	*	*	*	*	4	105.00	140.80	113.90	0.0814
5	127.00	161.00	158.70		5	110.00	141.50	111.30	0.0910
RH-50	123.25	151.05	129.23	0.0565					
STD DEV	5.50	2.03	4.13	0.0051					
1	126.00	149.90	125.20	0.0530					
2	126.00	153.80	134.00	0.0520					
3	126.00	149.20	126.40	0.0630					
4	115.00	151.30	131.30	0.0580					

* Denotes missing data resulted from either video recording malfunction or grip failure.

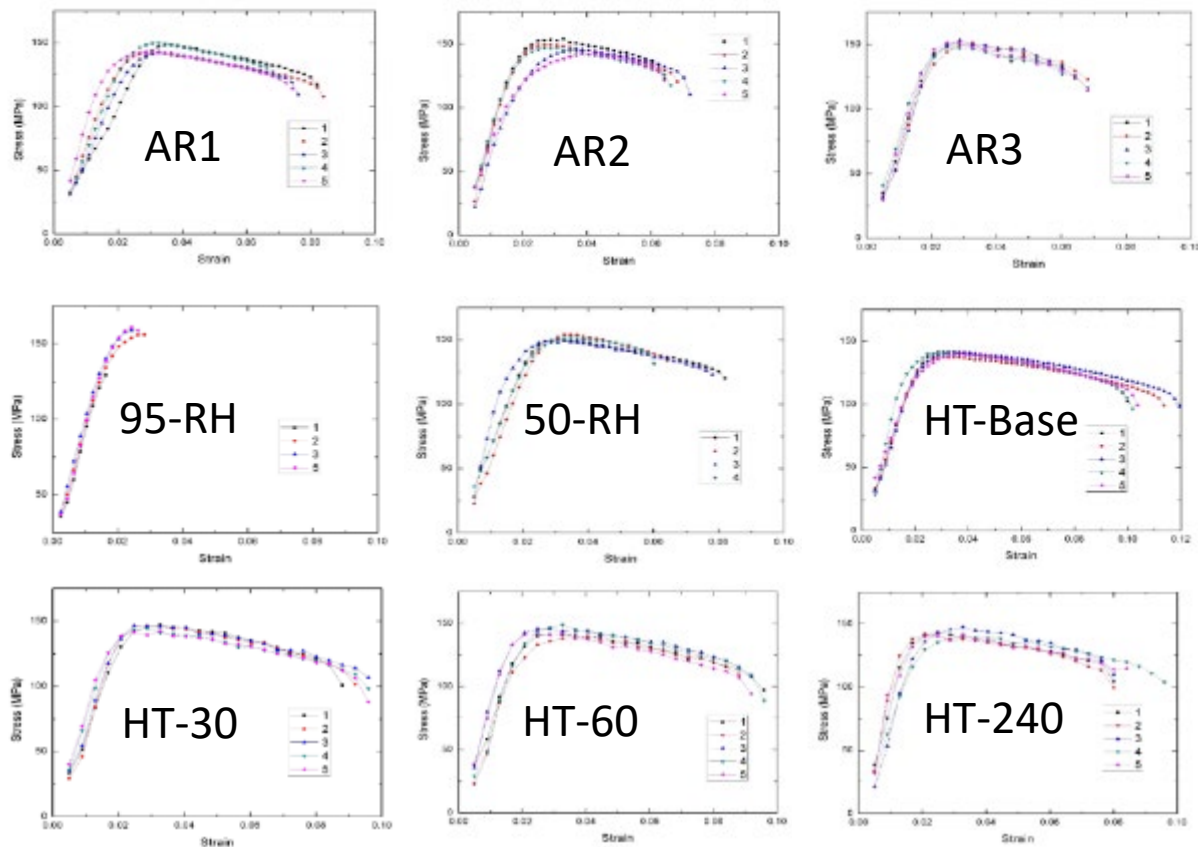


Figure 80. Stress-strain Curves of Cold Spray Bulk Samples of HP-Al.

4.3.2. Fractography

Fractography was conducted on two sets of tensile samples representing the greatest disparity in ductility; “95% relative humidity (most brittle)” and “Heat treated baseline (most ductile)”. The fracture surface of other remaining samples were similar with that of the heat treated baseline and as-received, due to their similar mechanical properties.

The fractured tensile samples were attached onto aluminum scanning electron microscope (SEM) stubs using carbon tape and imaged using an FEI Teneo. The instrument was set to a 10 kV accelerating voltage, 0.40 nA current, and a working distance of ~10 mm for all samples. The images were collected using the “Standard” lens configuration and an Everheart-Thornley detector. Images were taken of the fracture surface in low and high magnification in order to determine the failure initiation point and to study the fracture morphology. Energy Dispersive X-ray Spectroscopy (EDS) point analyses were performed on the initiation site, as well as in other locations throughout the same sample in order to determine if there was a noticeably different chemical nature to the site.

The heat treated samples experienced fracture in a ductile manner, as substantiated by the dimpled morphology. A typical cup-cone fracture pattern was observed. Significant necking was captured

in the SEM images, resulting in a smaller overall diameter. Dimpled patterns of ductile fracture were present everywhere (Figure 81). Micro-pores and greatly variable height on the fracture surface were observed, which is all indicative of significant plastic deformation and stable crack growth, during the applied stress. Other observations include large internal pores and multiple initiation sites. The pores may be the result of void coalescence or opening of the pre-existing pores. This ductile behavior was seen in all the HT “mini” tensile samples tested. The as-received powder samples also exhibited a certain degree of ductility but less than the HT samples.

The 95-RH samples, however, exhibited brittle fracture. The samples showed very little evidence of necking. The fracture surface appears flat relative to the other mini-tensile specimens, which serves as evidence of low plastic deformation and unstable crack growth (Figure 82). The fracture surface can be characterized as wavy, almost as if the fracture occurred along bond-lines of successive cold-spray splats. The intact surface of powder particles were also observed. These results point towards incomplete bonding in the cold-spray deposit.

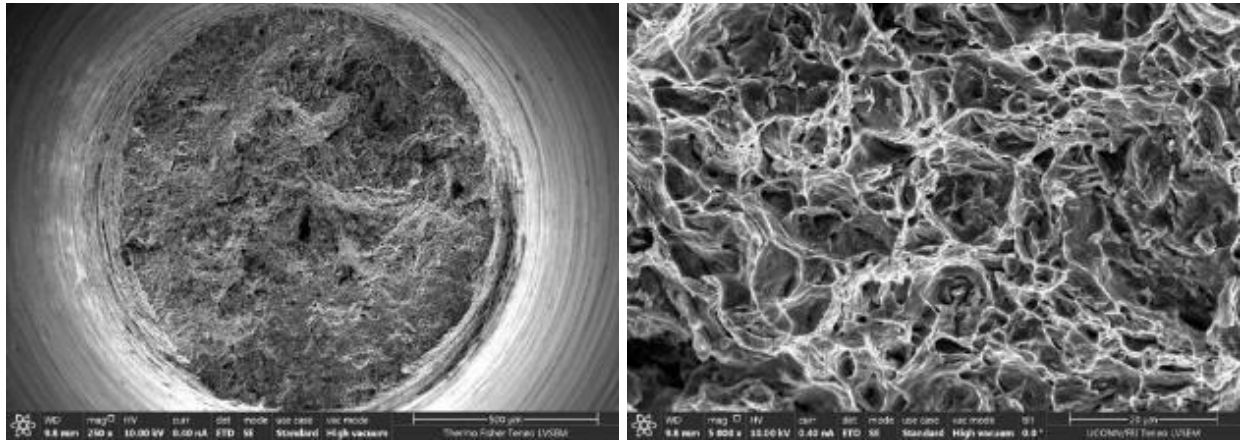


Figure 81. (a) Fracture surface of HT-Baseline specimen; (b) The magnified view of fracture surface. Dimpled morphology support the ductile fracture of HT-Baseline specimen.

Figure 83a (low magnification) and Figure 83b (high magnification) show examples of the type of brittle fracture observed in cold spray bulk material produced from the powder exposed to 95% humidity at room temperature (RH-95%). Note the disparity from the HT-Baseline bulk material where a ductile dimpled morphology dominated the fracture. In Figure 83a and Figure 83b the featureless morphology that is predominately characterized by cleavage and remains of splat boundaries is clearly visible. There are some small areas of ductile dimples but there are dispersed sparingly throughout. Figure 84 (low magnification) and Figure 85 (high magnification) illustrate further evidence of the brittle nature of the RH-95% sample and highlight numerous ‘half- moon’ features, which are the remnants of prior particle impact sites. Another important observation is the evidence of charging in the SEM which is caused by an insulating material, such as an oxide/hydroxide. Charging creates an imaging artifact, which is characterized by a significant increase in brightness of the insulating material, which was later confirmed to be rich in oxygen by analysis in a Super-X SDD EDXS system. These areas served as the primary crack paths.

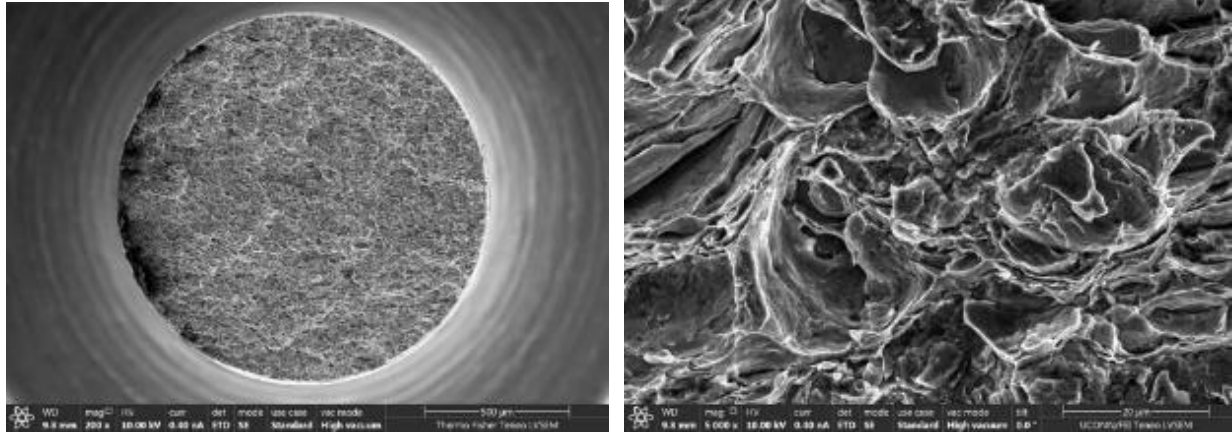


Figure 82. (a) Fracture surface of RH-95% specimen. The fracture surface is much flatter than other groups; (b) Magnified view of fracture surface.

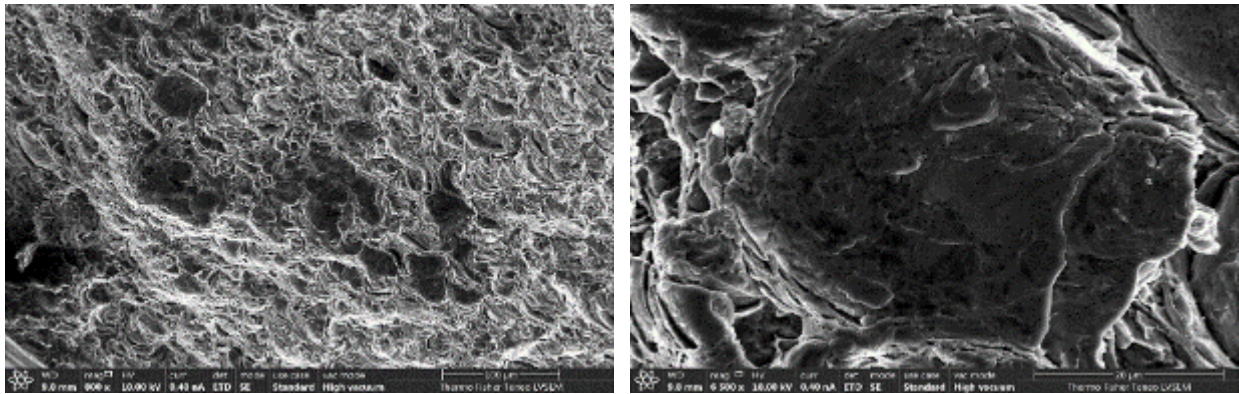


Figure 83. (a) Fracture surface of RH-95% specimen; (b) Magnified view of fracture surface.

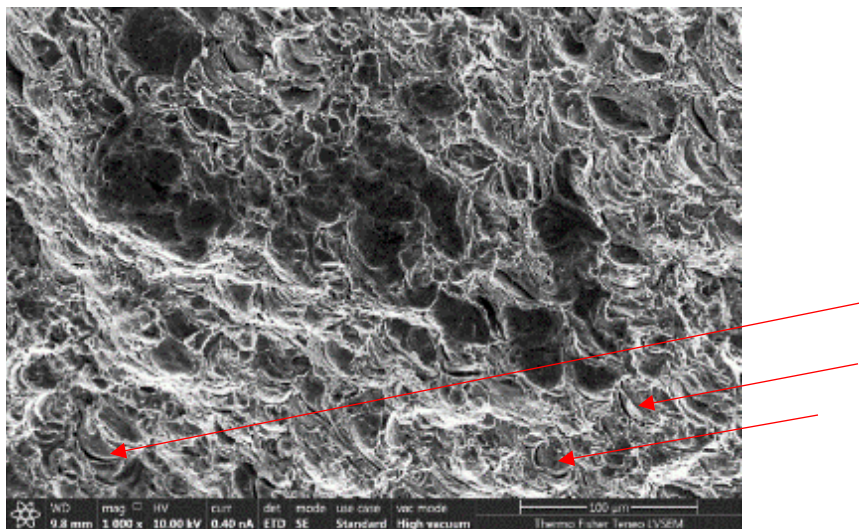


Figure 84. Fracture surface of RH-95% specimen. The fracture surface contains evidence of particle impact sites not completely bonded and ‘half-moon’ features denoted by the red arrows.

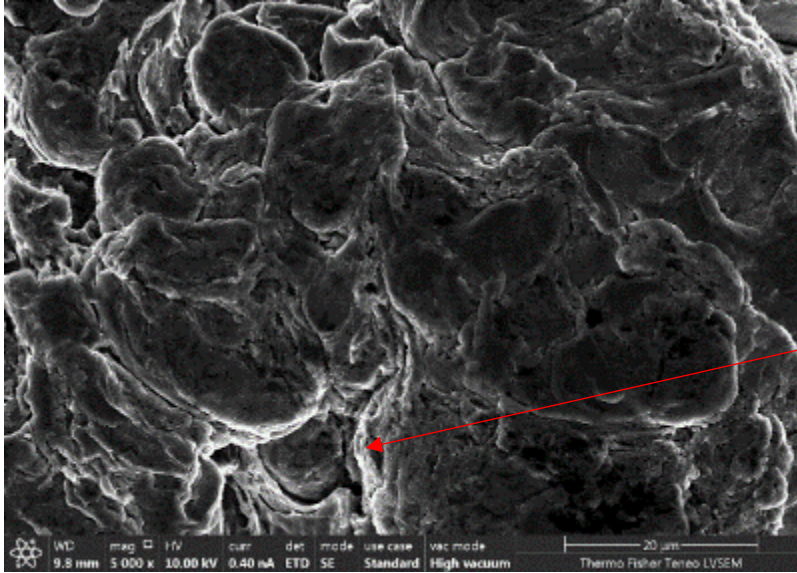


Figure 85. Magnified view of fracture surface of Figure 84, showing a featureless fracture morphology associated with decohesion of splats. Note some SEM charging indicative of oxides.

Figure 86a and Figure 86b show examples of individual decohesion sites of splats covering the fracture surfaces of the broken tensile specimens representing RH-95%. Note the

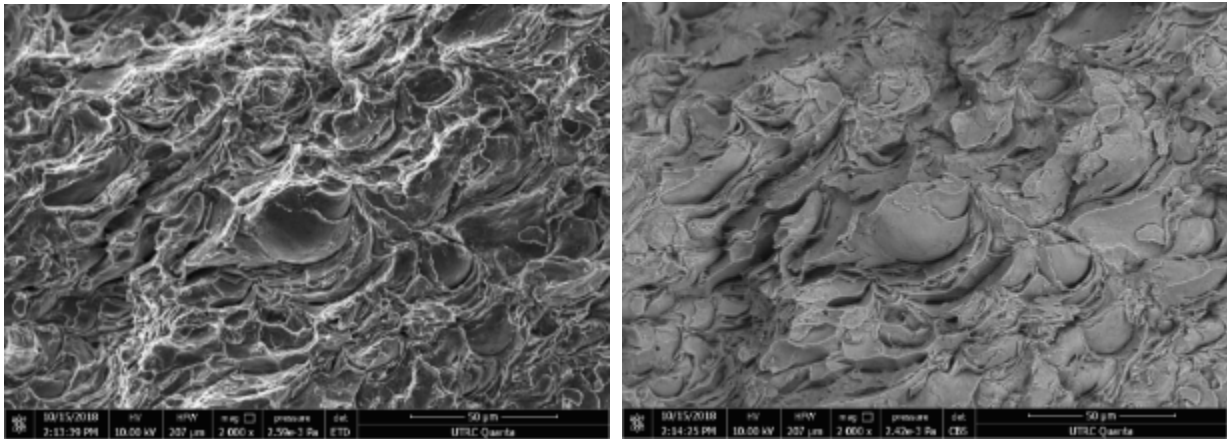


Figure 86. (a) SEM and BSE (b) of RH-95% tensile fracture showing decohesion of splats.

Finally, to illustrate the contrast in fracture behavior between a material that exhibited high ductility to that which failed in a brittle fashion, groups HT-Baseline and RH-95% were chosen for comparison. Figure 87a and Figure 87b show a side by side comparison of a representative fractured tensile specimen from HT-Baseline and RH-95%. The distinction between these two groups was very pronounced, even at the macro-scale. The first feature that revealed the overall condition of the material was the amount of necking observed at the fracture site. The HT-Baseline specimen exhibited a classic ‘cup-cone’ fracture and the cup half of the fracture is shown in Figure 87a. This type of fracture is associated with ductile materials whereas a large amount of plastic deformation occurs before final rupture as substantiated by the decrease in cross-sectional area adjacent to the final fracture area. The distinctive cup and cone shape was observed and the ends of the fracture.

In contrast, Figure 87b, which is a fracture half from a tensile specimen representing RH-95%, displayed a brittle fracture, as evidenced by the lack of plastic deformation and absence of necking adjacent to the final fracture site. The RH-95% was characterized by an abrupt rupture at the end of the fracture and almost no change in cross-sectional area. Another important note are the cracks that formed at the grip ends of the tensile specimen, which also serve as evidence of the brittle nature of the material produced from HP-Al powder exposed to high humid conditions prior to cold spray. Figure 88a and Figure 88b are the final fracture areas of HT-Baseline and RH-95% shown respectively at high magnification to further illustrate the contrast in ductility. Elongated grains characterize the regions at adjacent to the final fracture zone of HT-Baseline while there is no evidence of plastic deformation of the grains along the final fracture zone of RH-95%.

4.3.3 X-ray Mapping of Fracture Surfaces

Energy Dispersive Spectroscopy (EDS) was used to determine the atomic composition of oxygen to aluminum metal and provide a basis of comparison between the HT-Baseline and RH-95% powder samples. EDS was not used to provide the nature of the oxidation state or chemical bonds. It was understood that EDS is not really suitable for light elements (like O) for quantitative analysis. However, EDS can detect the presence of oxygen and a metal, and the proportion between them and the comparison of these data between the HT-Baseline and RH-95% powder samples proved invaluable.

Figure 89a shows a representative fracture area, on one half of a broken tensile specimen, from HT-Baseline while, Figure 89b is the resultant EDS, X-ray map taken in an attempt to determine the relative oxygen content across a large surface area of the fracture. Figure 90 contains the spectrum obtained from the X-ray mapping from Figure 89. Note that the levels of oxygen are relatively small. Figure 91a shows a representative fracture area, on one half of a broken tensile specimen, from RH-95% while, Figure 91b is the resultant EDS, X-ray map. Figure 92 contains the spectrum obtained from the X-ray mapping from Figure 91. Note the significant increase in the oxygen content on the fracture surface of specimen RH-95%. The areas highlighted in blue on Figure 91b show the areas high in oxygen concentration, which were associated with splat boundaries. The presence of Si could be due to segregation of Si impurities to the particle surfaces as a result of solidification during the primary gas atomization process.

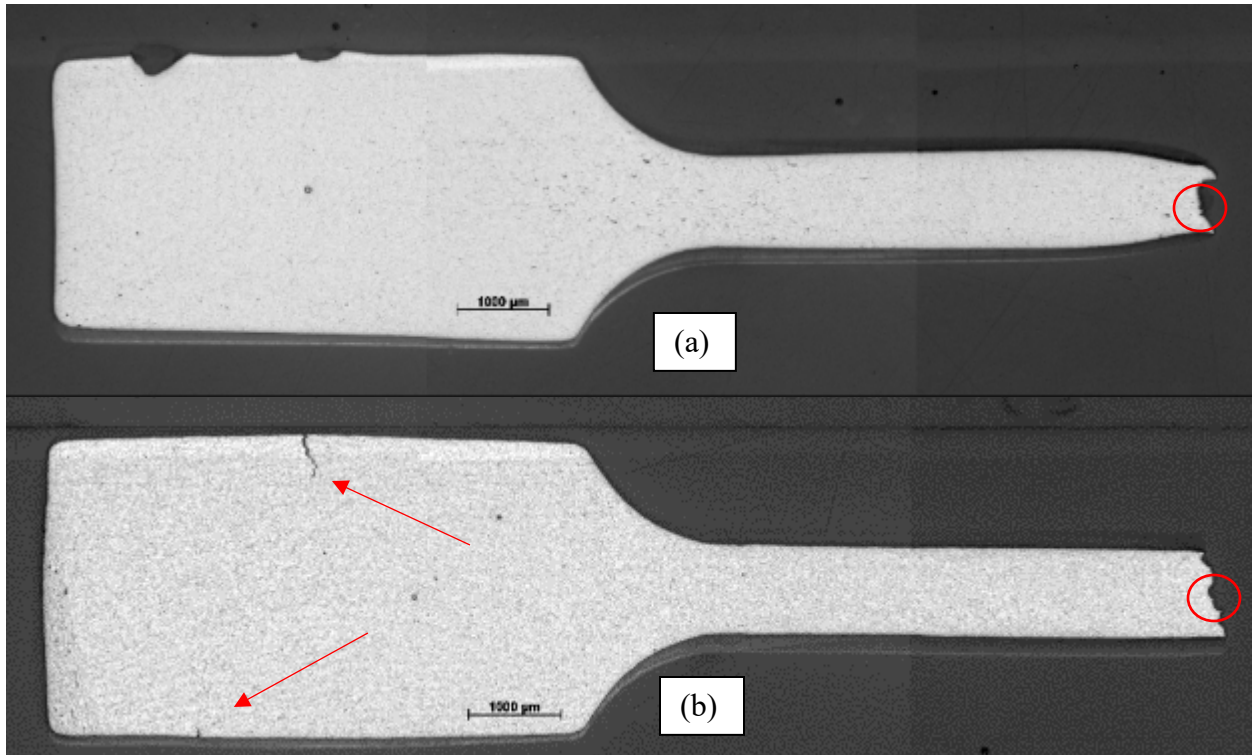


Figure 87. (a) Fractured tensile bar representing HT-Baseline and (b) fractured tensile bar representing RH-95%. Note the differences in necking and the brittle nature of RH-95%. Arrows denotes cracks in grip section. Red circled regions are enlarged in Figure 83.

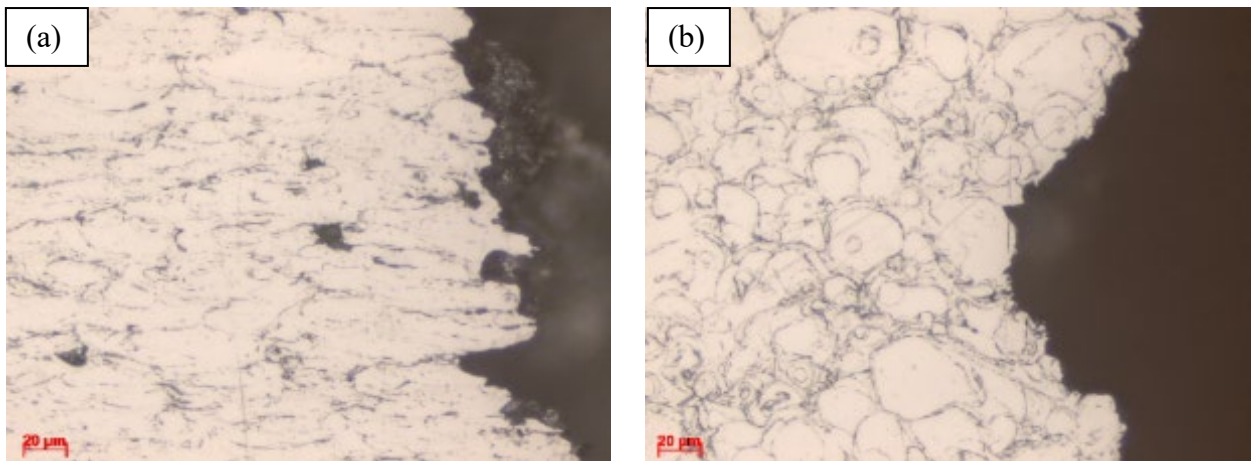


Figure 88. (a) Circled area on Figure 83a enlarged showing elongated grains and (b) Circled area on Figure 83b showing abrupt fracture with little evidence of ductility before final fracture.

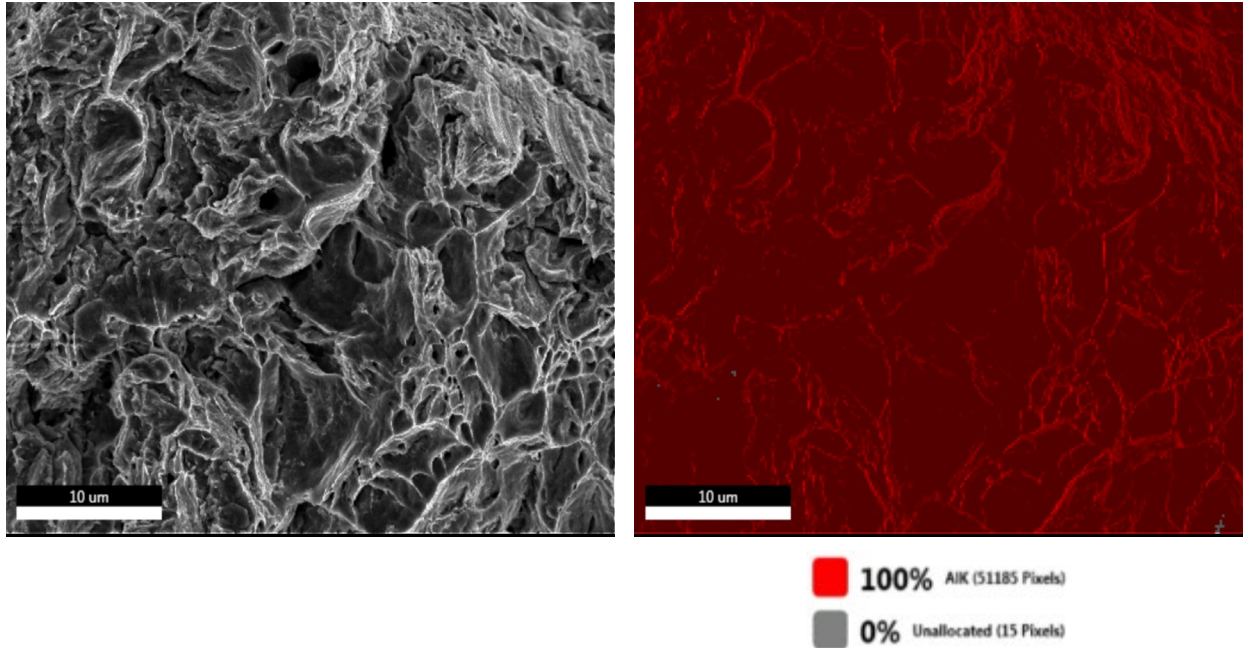


Figure 89. (a) SEM of tensile fracture surface from HT-Baseline and (b) corresponding X-ray map.

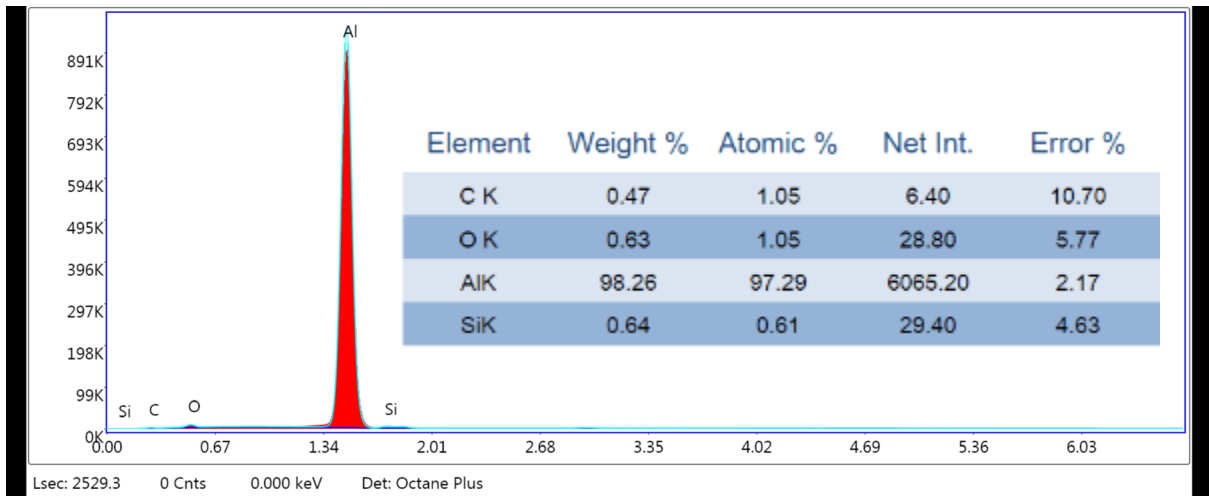


Figure 90. Spectrum obtained from X-ray mapping obtained from Figure 85.

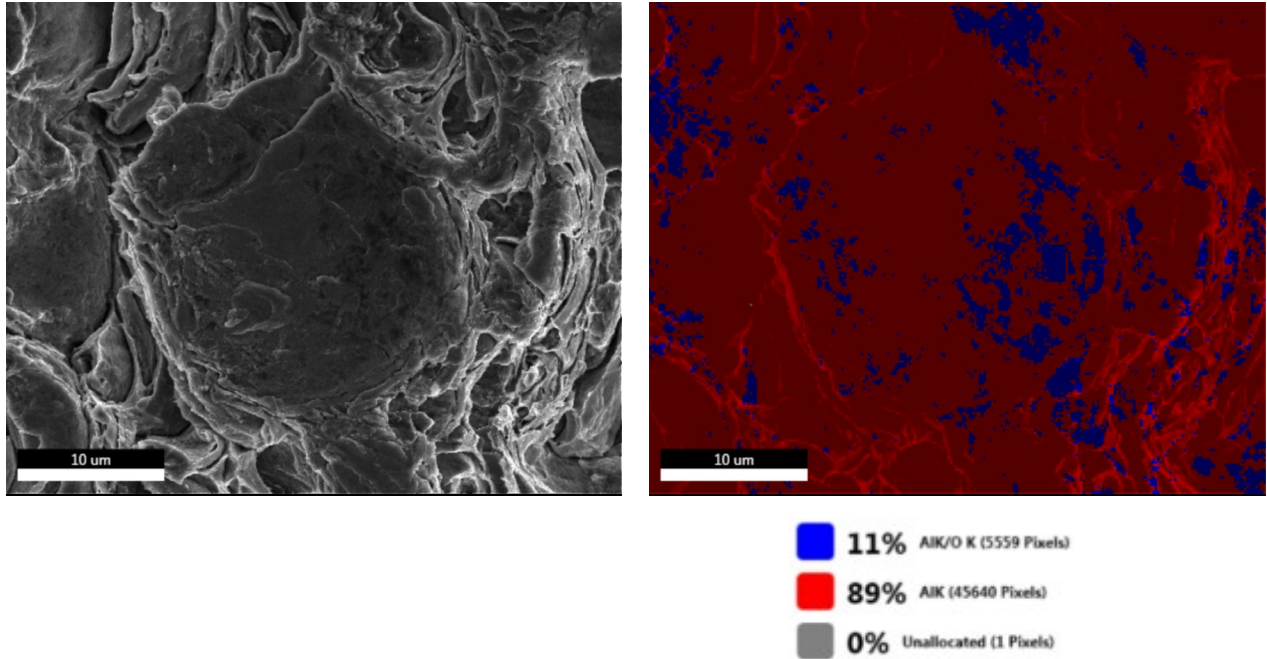


Figure 91. (a) SEM of tensile fracture surface from RH-95% and (b) corresponding X-ray map.

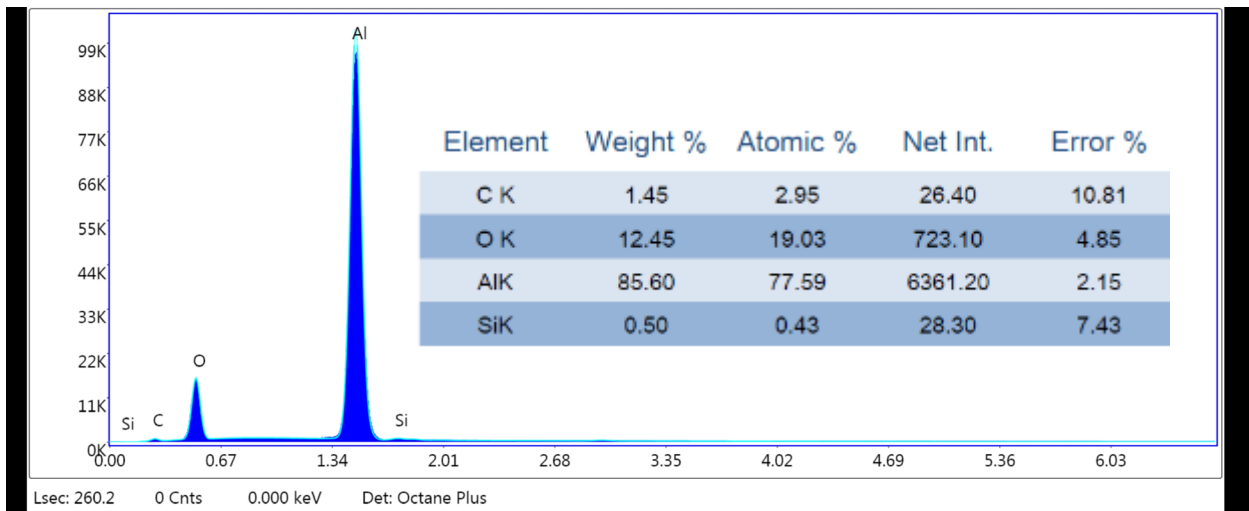


Figure 92. Spectrum obtained from X-ray mapping obtained from Figure 86. Note the high oxygen concentration of RH-95% as compared to that of HT-Baseline.

4.4 TEM and EDS Analysis of Single Particle Impact “Splats”

UMass, Amherst produced four samples containing a series of single particle impacts onto high purity aluminum substrates which were sent to UConn for analysis. The exposure conditions of these powders were: as-received (AR), heat treated baseline (HT-B), heat treated 240 (HT-240), and 95% relative humidity (RH-95%). Visible light images are shown in Figure 93 which indicate the precise areas where each splat was located on the respective substrates. Table 29. Particle Diameter and Impact Velocity of bonded HP-Al Powder Particles contains the particle diameter and impact velocity recorded for each impact site or ‘splat’. The nomenclature V_i refers to the impact velocity at which the particle bonded to the substrate and formed a splat while V_r is the velocity at which rebound of the particle occurred. Since each particle bonded and formed a splat, the rebound velocity is 0 or not applicable.

Secondary electron (SE) micrographs of each splat were collected using a scanning electron microscope (SEM). A Thermo Fisher Helios 460S dual-beam Ga^+ FIB was used to prepare cross-sectional lamellas from the individual splats for TEM analysis. The conditions chosen for analysis were the splats with the highest and lowest velocities, along with two splats with intermediate velocities. A total of four splats were prepared (Figure 94) from the as-atomized, heat treated baseline, and 95% relative humidity samples. To protect the surface of the splats, platinum was deposited in two steps. The first layer was deposited using a 10kV electron beam at 6.4nA and a second thicker layer was deposited using a 30kV gallium ion beam at 0.43nA, to crack the organic-metallic precursor. Samples were thinned to electron transparency at 30kV by reducing the current iteratively to minimize Ga^+ implantation, and by tilting $\pm 2^\circ$ to obtain a parallel sided lamella. Figure 9390 shows an example of the FIB lift-out procedure to extract a cross-section of a splat for analysis. Table 30 lists the samples that were completed for this study.

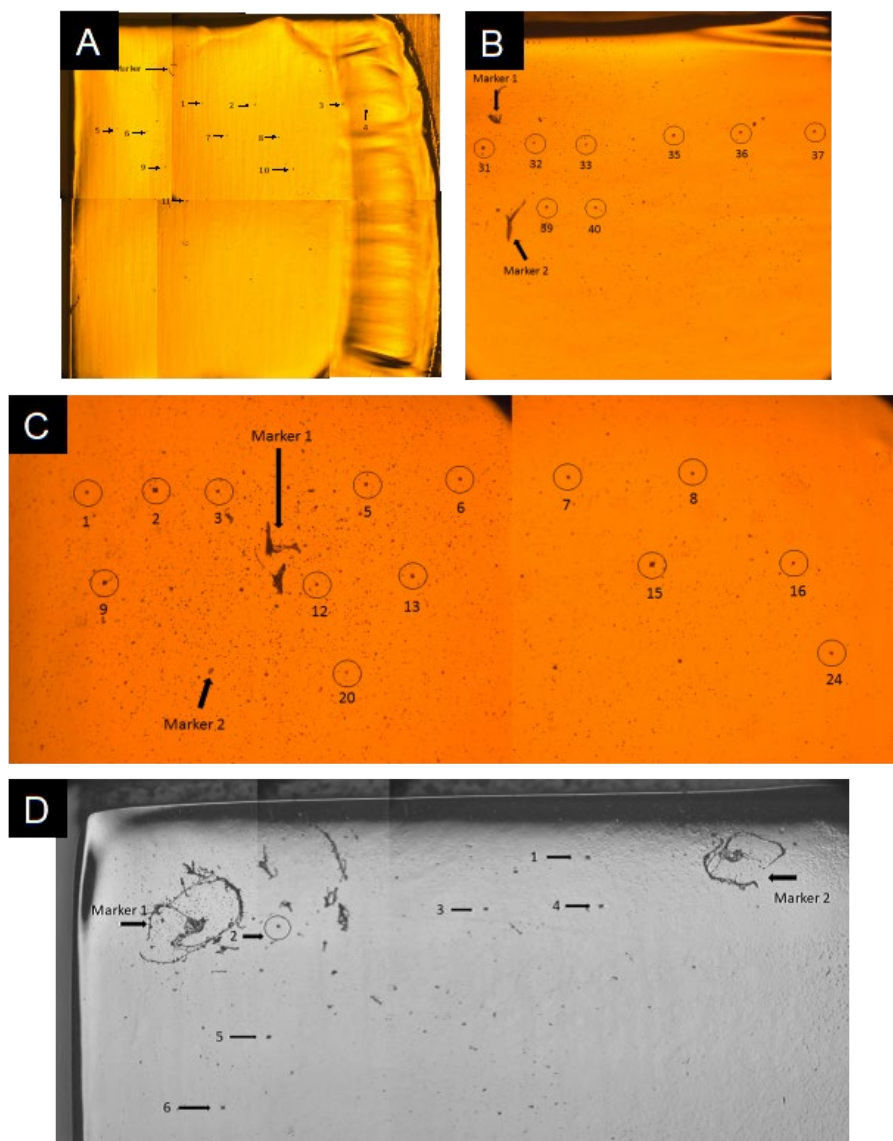


Figure 93. Visible light microscopy images indicating where each of the different powder splats are located on each substrate. A) As-received powders. B) Heat treated baseline powders. C) HT-240 powders. D) RH-95% relative humidity powders.

Table 29. Particle Diameter and Impact Velocity of bonded HP-Al Powder Particles

Powder Type	Impact #	V_i (m/s)	V_r (m/s)	Diameter (μm)
As Received (AR)	1	816.8706	0	14
	2	1194.885	0	12
	3	912.3281	0	15
	4	939.6211	0	13
	5	967.9068	0	13
	6	1055.181	0	11
	7	865.645	0	11
	8	1027.009	0	14
	9	1032.881	0	12
	10	1045.933	0	14
	11	884.6448	0	14
Heat Treated Baseline (HT-B)	31	1020	0	13
	32	953	0	11
	33	817	0	11
	35	911	0	14
	36	921	0	14
	37	916	0	14
	39	958	0	12
	40	842	0	12
Heat Treated 240 (HT-240)	1	899	0	11
	2	926	0	14
	3	911	0	11
	5	966	0	13
	6	923	0	12
	7	976	0	11
	8	905	0	11
	9	822	0	15
	12	937	0	11
	13	926	0	13
	15	953	0	15
	16	891	0	11
	20	819	0	11
	24	861	0	13
95% Relative Humidity (RH-95%)	1	951.15	0	14
	2	908.34	0	14
	3	933.74	0	13
	4	903.32	0	14
	5	881.41	0	11
	6	974.56	0	14

Table 30. Description of the 12 TEM Lift Out Samples Made from Bulk Material.

Powder Type	Impact #	V_i (m/s)	V_r (m/s)	Diameter (μm)
As Received (AR)	2	1194.885	0	12
	7	865.645	0	11
	8	1027.009	0	14
	10	1045.933	0	14
Heat Treated Baseline (HT-B)	31	1020	0	13
	32	953	0	11
	33	817	0	11
	39	958	0	12
95% Relative Humidity (RH-95%)	2	908.34	0	14
	3	933.74	0	13
	5	881.41	0	11
	6	974.56	0	14

The twelve lamellas were analyzed in a FEI Talos F200X at an operating voltage of 200kV with a Super-X SDD EDXS system. EDXS was used to analyze the elemental composition of the oxide layer at the interface of the splat and substrate by EDXS mapping and the use of probe line scans. FWHM was used to analyze oxide thickness from obtained line scans. If the intensity value of oxygen line scan was under 3, the data was considered noise and was not included in data set. Data was separated based on location of impact and the number of peaks for a given line scan.

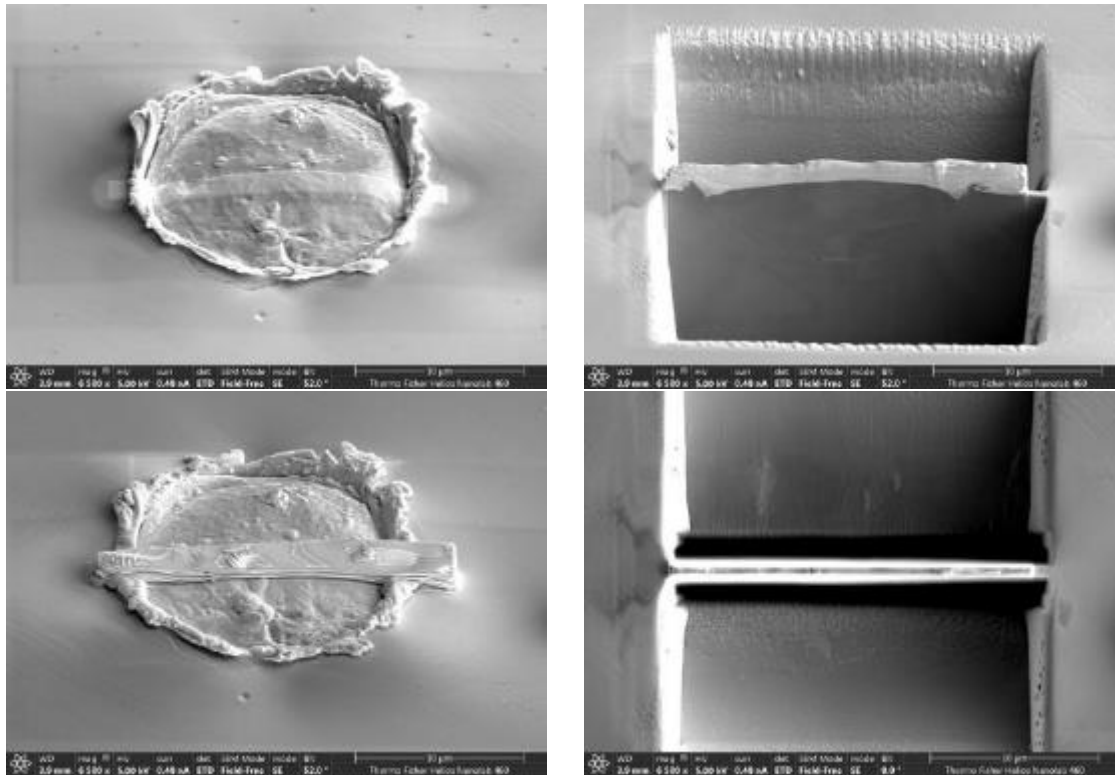


Figure 94. Example of FIB lift-out procedure to extract a cross-section of a splat for analysis.

4.4.1 Analysis of RH-95% Splats

Figure 94 shows the general overview of the FIB sectioning procedure used for every splat sample. All cross-sectional specimens were prepared in a similar manner. Figure 95 contains an SE SEM image from each of the RH-95% splats that were sectioned in this manner. It is clear from these images that there was significant particle-to particle variation in the morphology of the splats. Additionally, the surface morphology associated with the oxide/hydroxide film was very inconsistent and ‘patches’ were observed on the exterior of these powder particles.

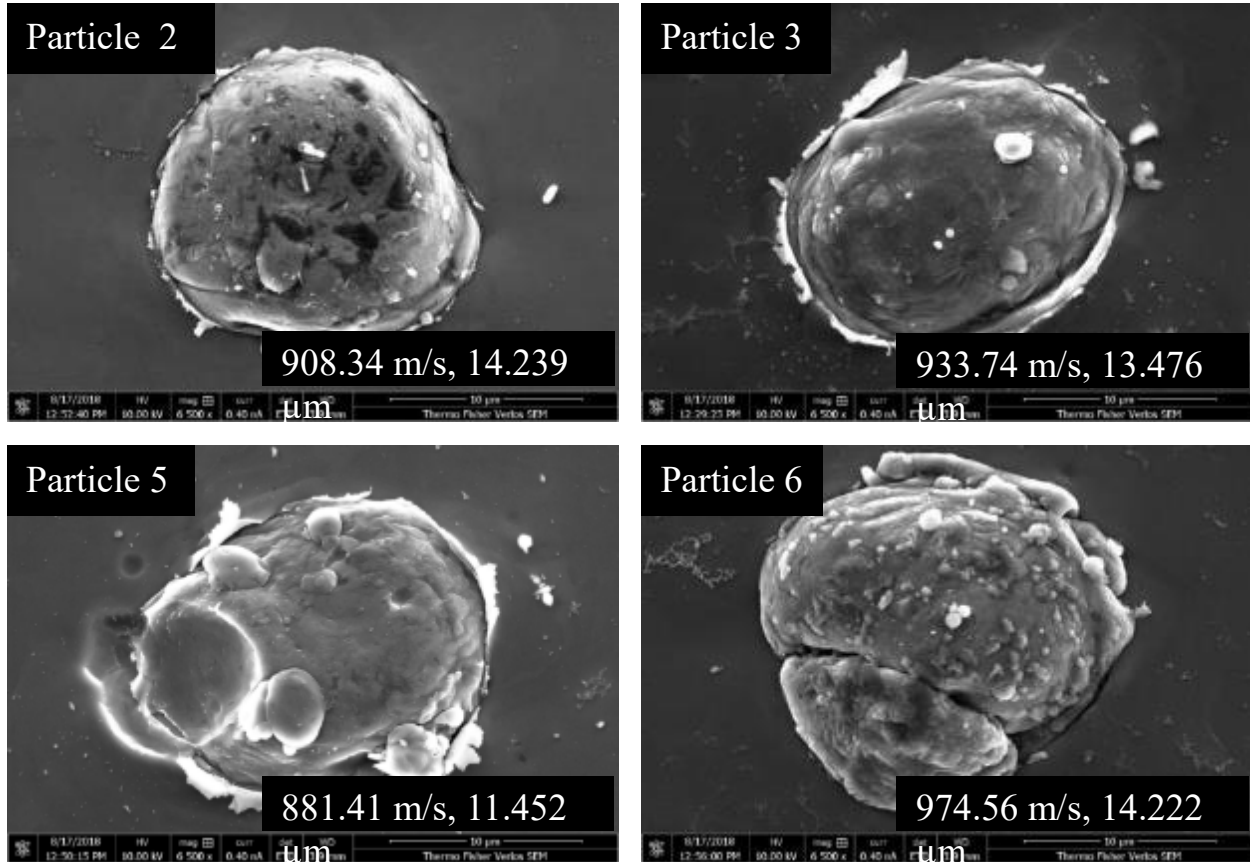


Figure 95. SE SEM image from each of the RH-95% splats that were sectioned for analysis.

Figure 96 shows a low-magnification bright field (BF) image, a high-angle annular dark field image (HAADF), and EDXS maps for O, Al, Si, Pt and Ga.

It was clear that in this region there were localized areas with oxide/hydroxides at the splat/substrate interface, but there were other areas along the bond line where no oxide/hydroxide was present. This was confirmed by obtaining data at yet higher magnifications and then by taking multiple line scans perpendicular to the interface (Figure 97).

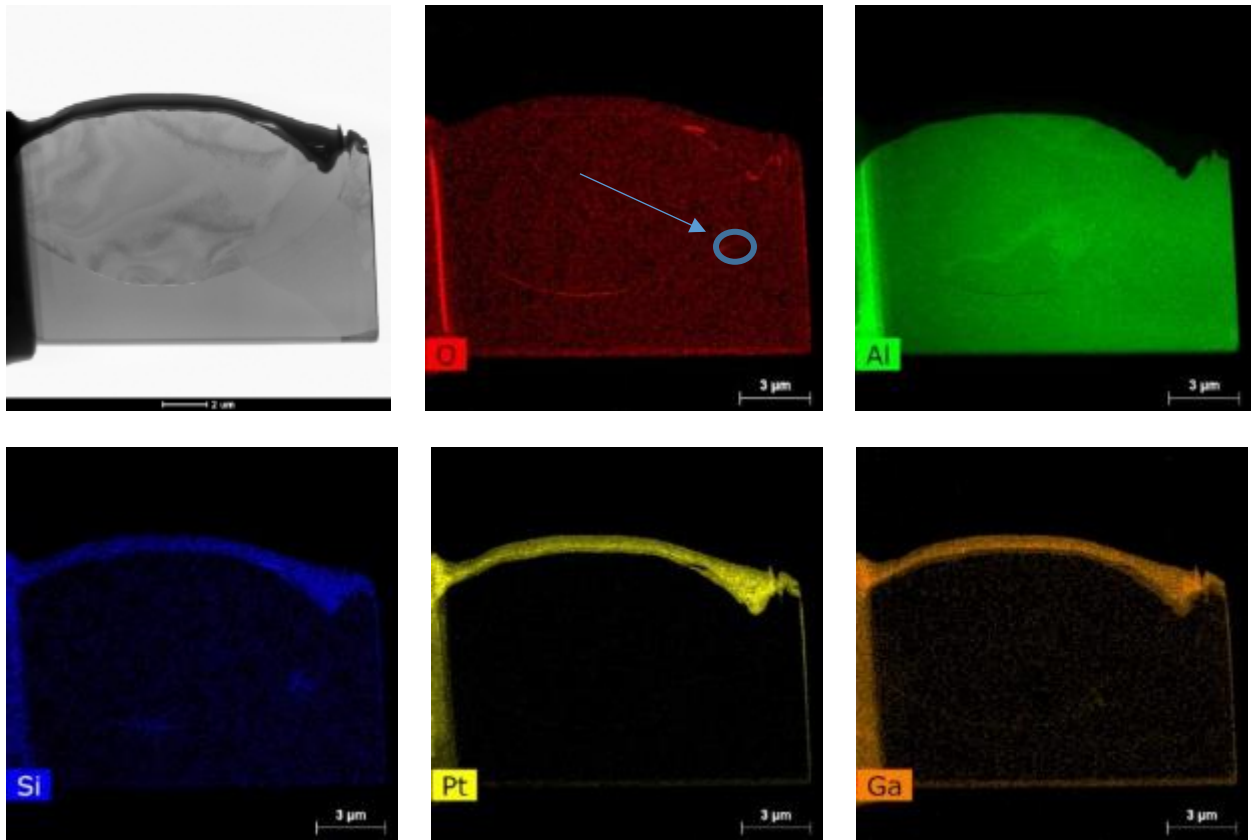


Figure 96. STEM and EDX analysis of Particle 3 from splat sample RH-95%.

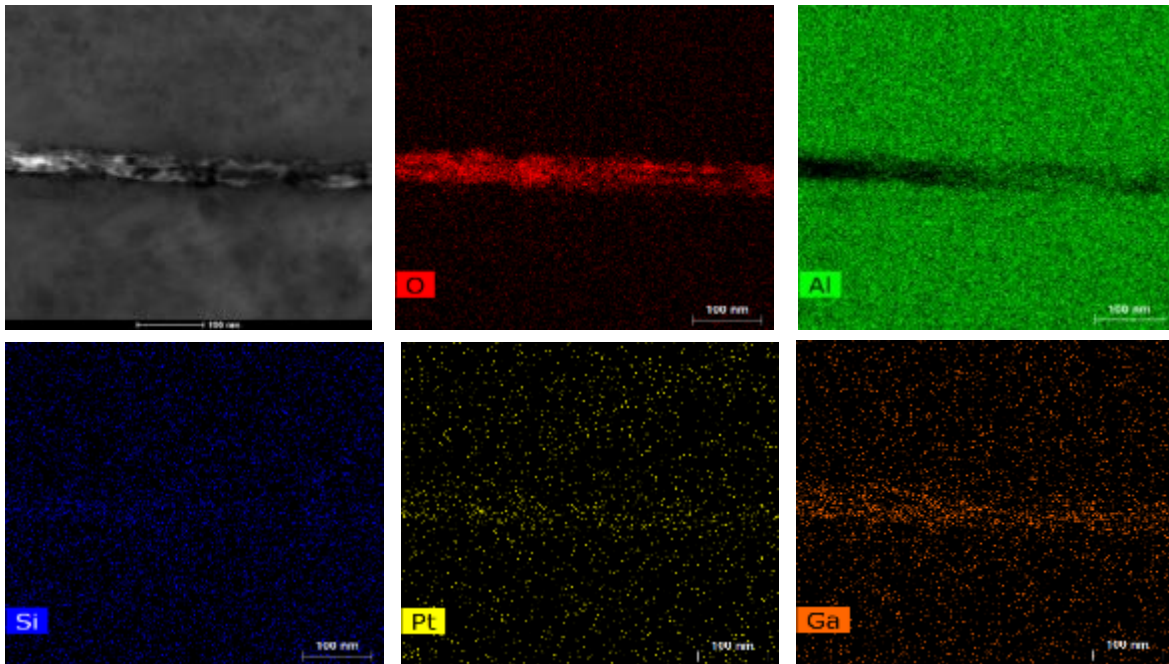


Figure 97. Enlargement of high oxide area from Figure 96 denoted by blue circle and arrow.

Data obtained from the oxide patch at the splat/substrate interface identified by the arrow and within the blue circled region on Figure 96 are shown in Figures 98-105. The Al maps on Figures 98-105 show distinct dips in the Al content at the interface where O is present, suggestive of an oxide “double layer” on the O map. This was consistent with the presence of an interfacial crack which was actually a delaminated area along the splat/substrate interface. Most of the line scans shown in Figures 98-105 contain corresponding dips in the Al signal and a double peak in the O signal. The asymmetry of the Al trough and the merging of the O peaks into one broad peak was likely due to the delamination not being exactly edge-on in this area.

Such effects were seen more clearly from the bottom splat/substrate interface, as shown in Figure 106, which reveals a crack-like feature which is an area that is not bonded, across the field of view, with a very distinct oxide double-layer (one on each side of the crack). Higher magnification data obtained from this area (Figure 107) show a clear uniform oxide double-layer, with some Pt and Ga accumulation from the preparation procedure. Each of the (10) line scans show sharp Al troughs corresponding to the crack-like feature, with well-defined O peaks. It was interesting to note that several of these scans also show enhancements in Si, which could be due to segregation of Si impurities to the particle surfaces during solidification. A representative scan is shown in Figure 108.

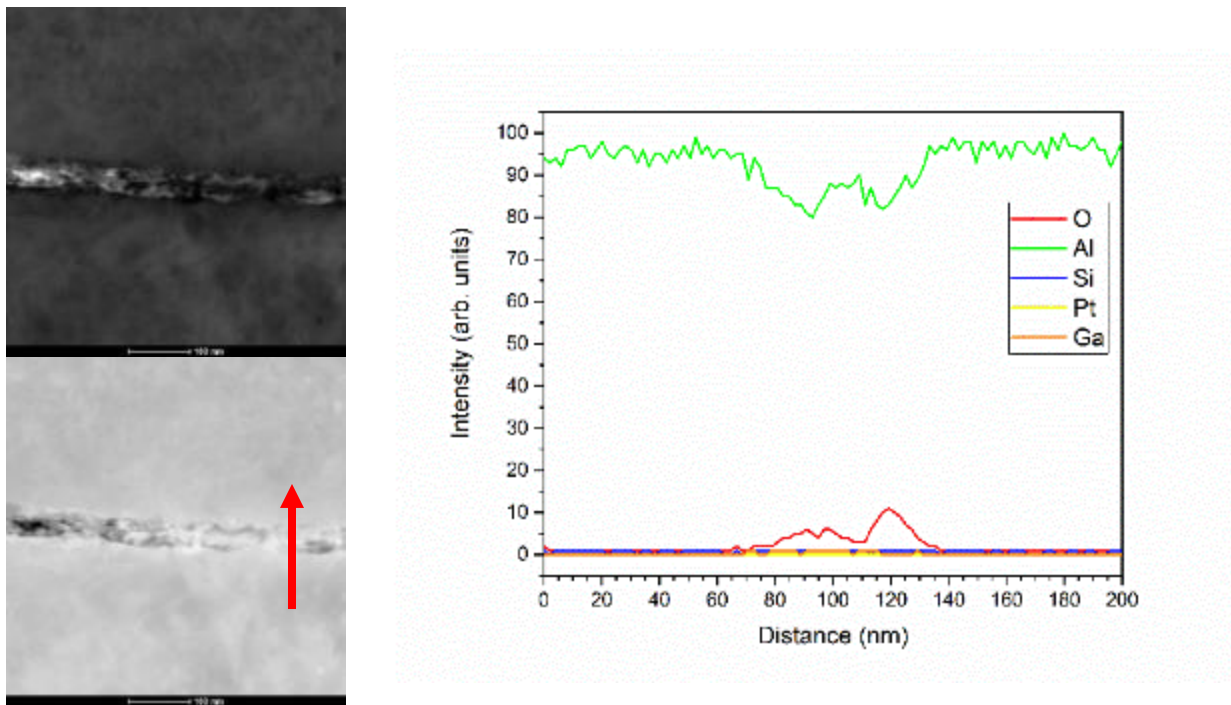


Figure 98. Line scan (1) of interface between substrate and splat of Particle 3 from splat RH-95%.

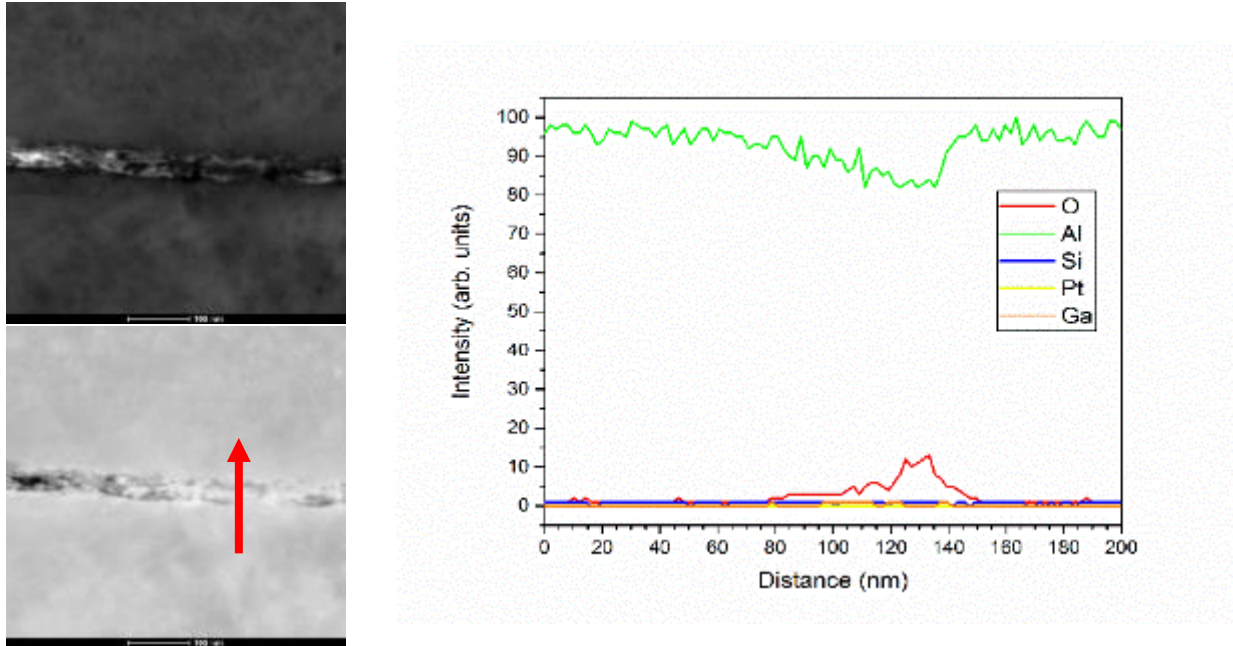


Figure 99. Line scan (2) of interface between substrate and splat of Particle 3 from splat RH-95%.

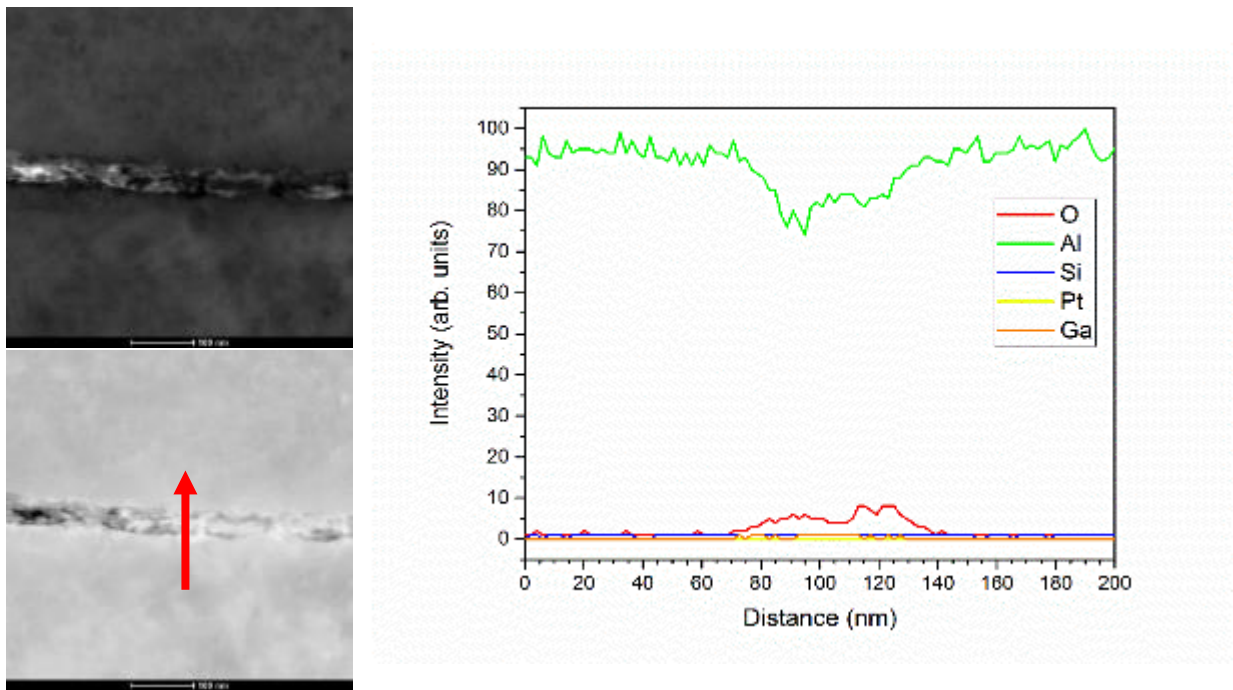


Figure 100. Line scan (3) of interface between substrate and splat of Particle 3 from splat RH-95%.

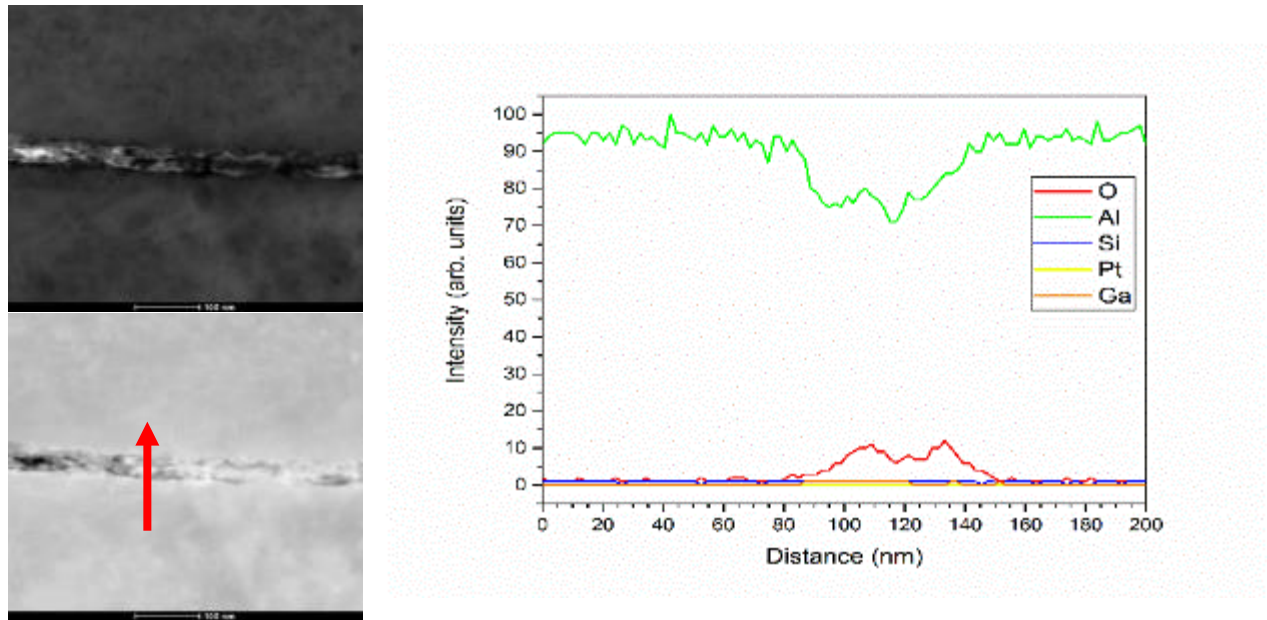


Figure 101. Line scan (4) of interface between substrate and splat of Particle 3 from splat RH-95%.

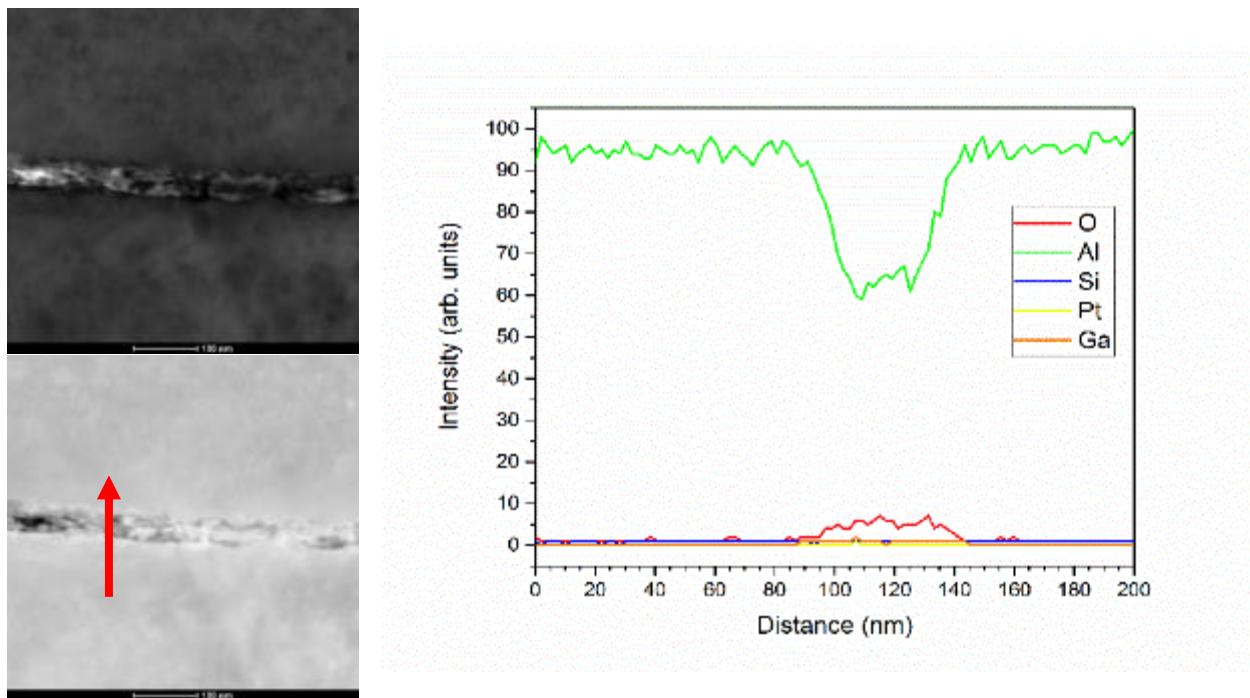


Figure 102. Line scan (5) of interface between substrate and splat of Particle 3 from splat RH-95%.

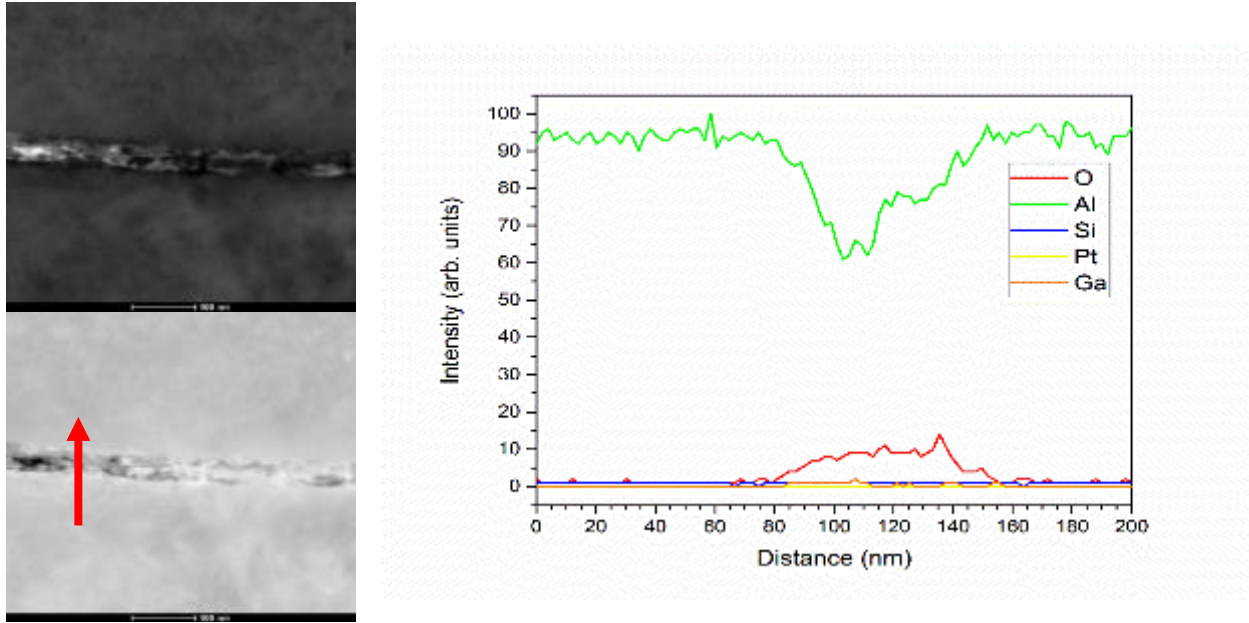


Figure 103. Line scan (6) of interface between substrate and splat of Particle 3 from splat RH-95%.

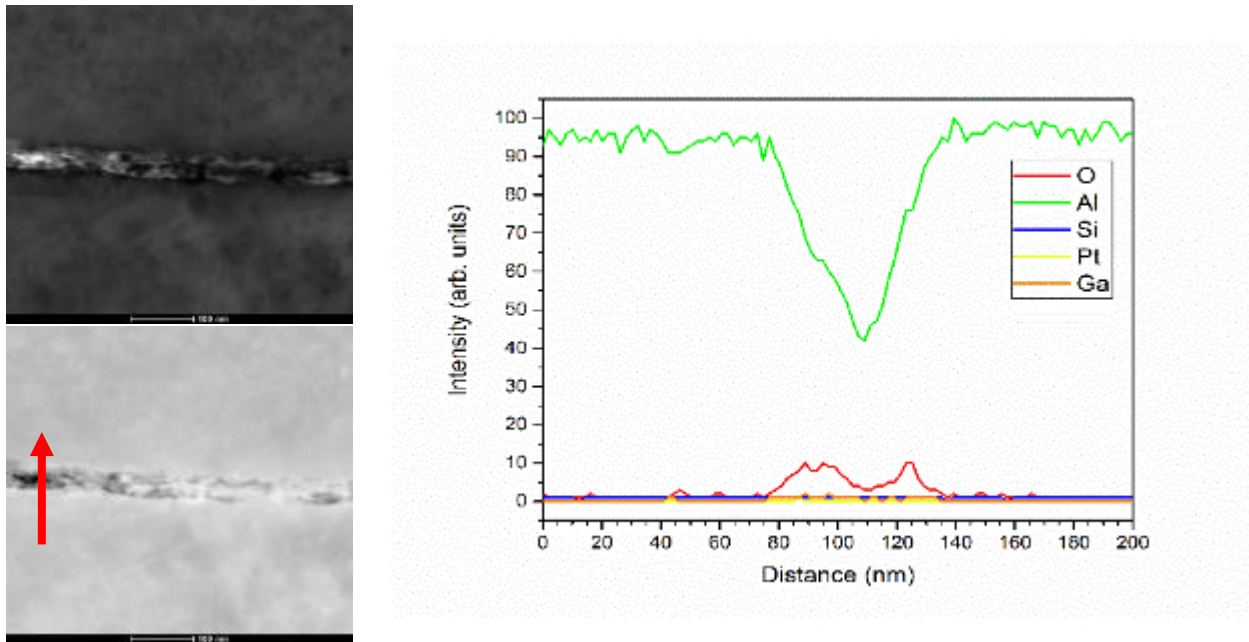


Figure 104. Line scan (7) of interface between substrate and splat of Particle 3 from splat RH-95%.

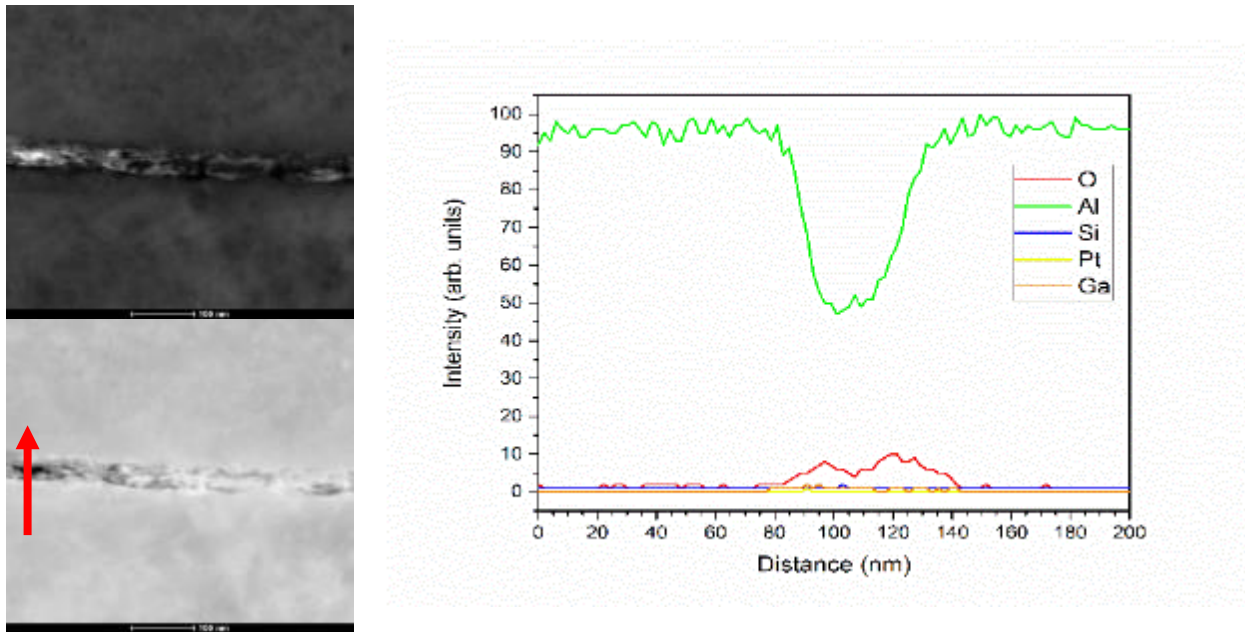


Figure 105. Line scan (8) of interface between substrate and splat of Particle 3 from splat RH-95%.

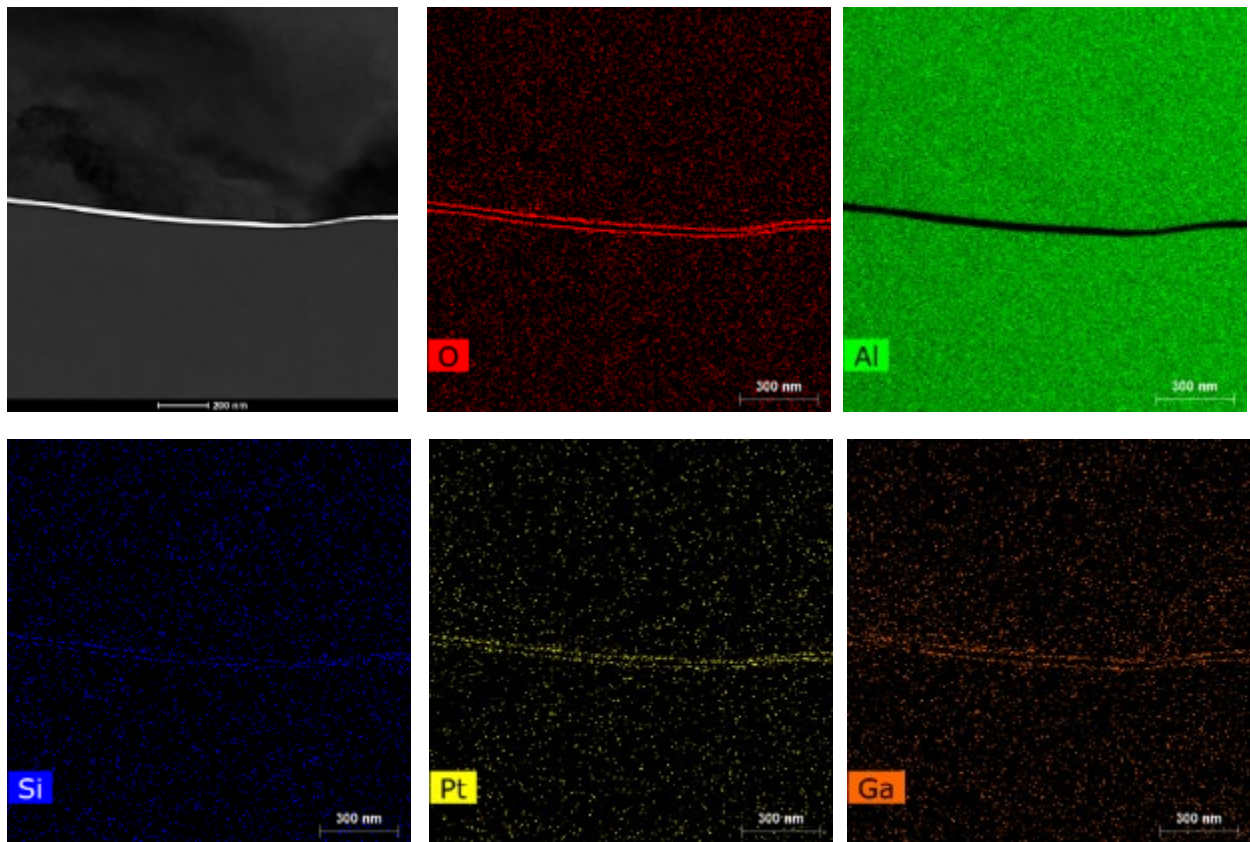


Figure 106. STEM and EDXS of the bottom splat/substrate interface from RH-95% Particle 3.

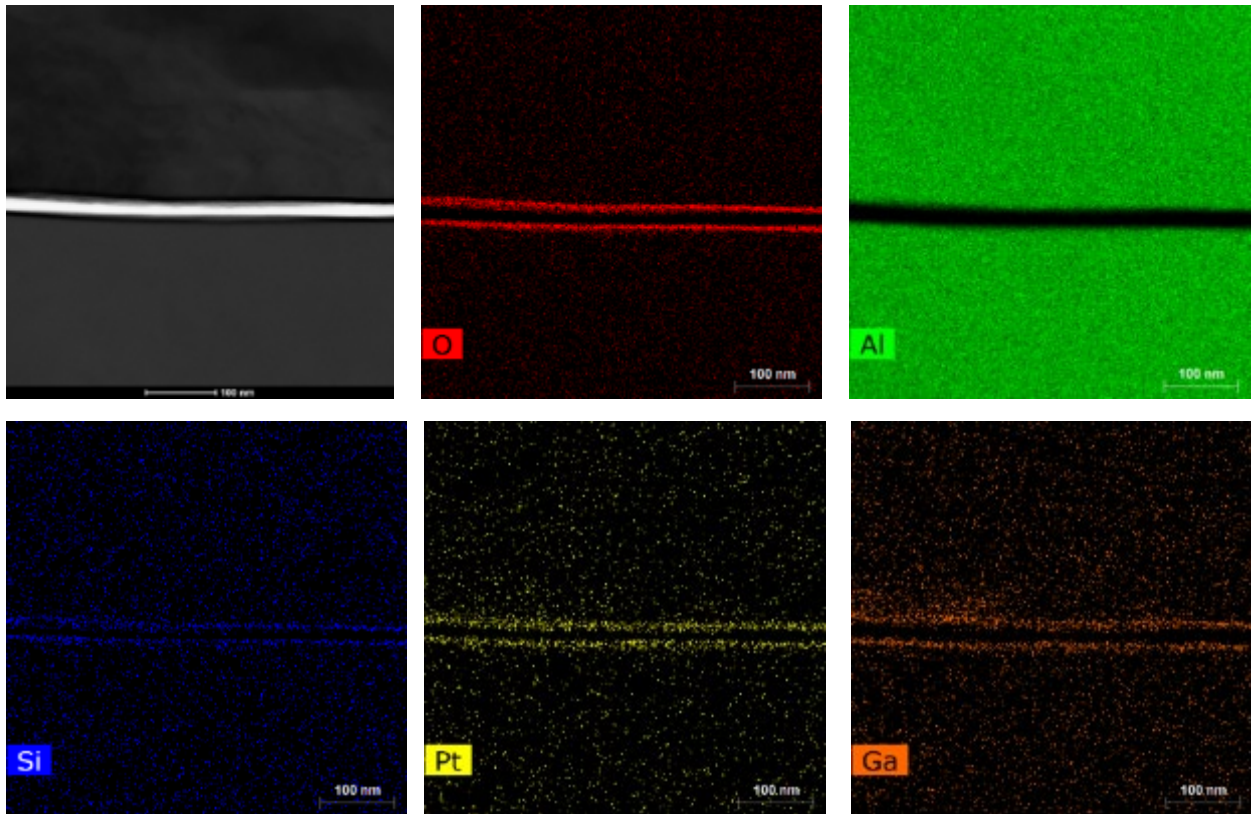


Figure 107. Enlargement of STEM and EDXS image shown in Figure 98 of the bottom splat/substrate interface from RH-95% Particle 3.

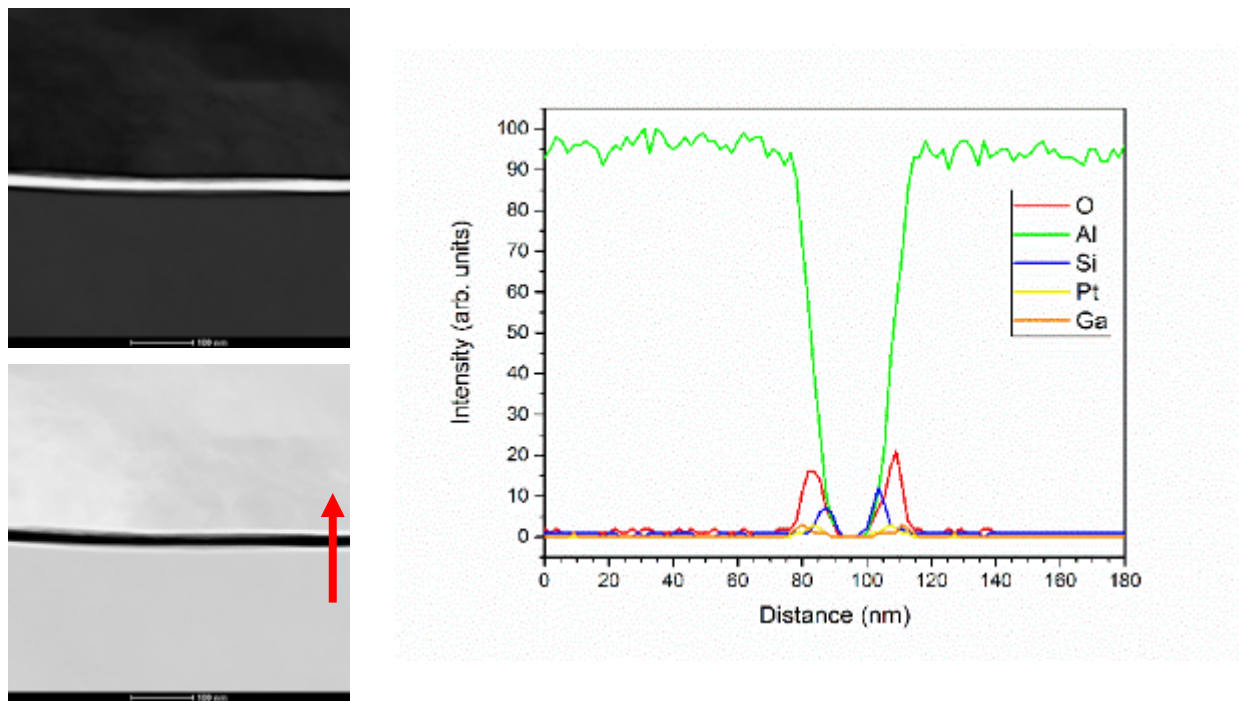


Figure 108. Line scan (10) of the bottom splat/substrate interface of RH-95% Particle 3.

For comparison, data from particle 2 is presented in Figure 109. In this case, there appears to be oxide across the entire splat/substrate interface and there is no clear evidence of interfacial cracking/debonding. The high magnification data from the bottom interface do show a distinct dip in the Al signal at the interface, but there is no clear O double-peak in the line scans. Similar effects were observed on the side interfaces. The enhancement in the Si signal at the interface was much more pronounced for particle 2 than it was for particle 3.

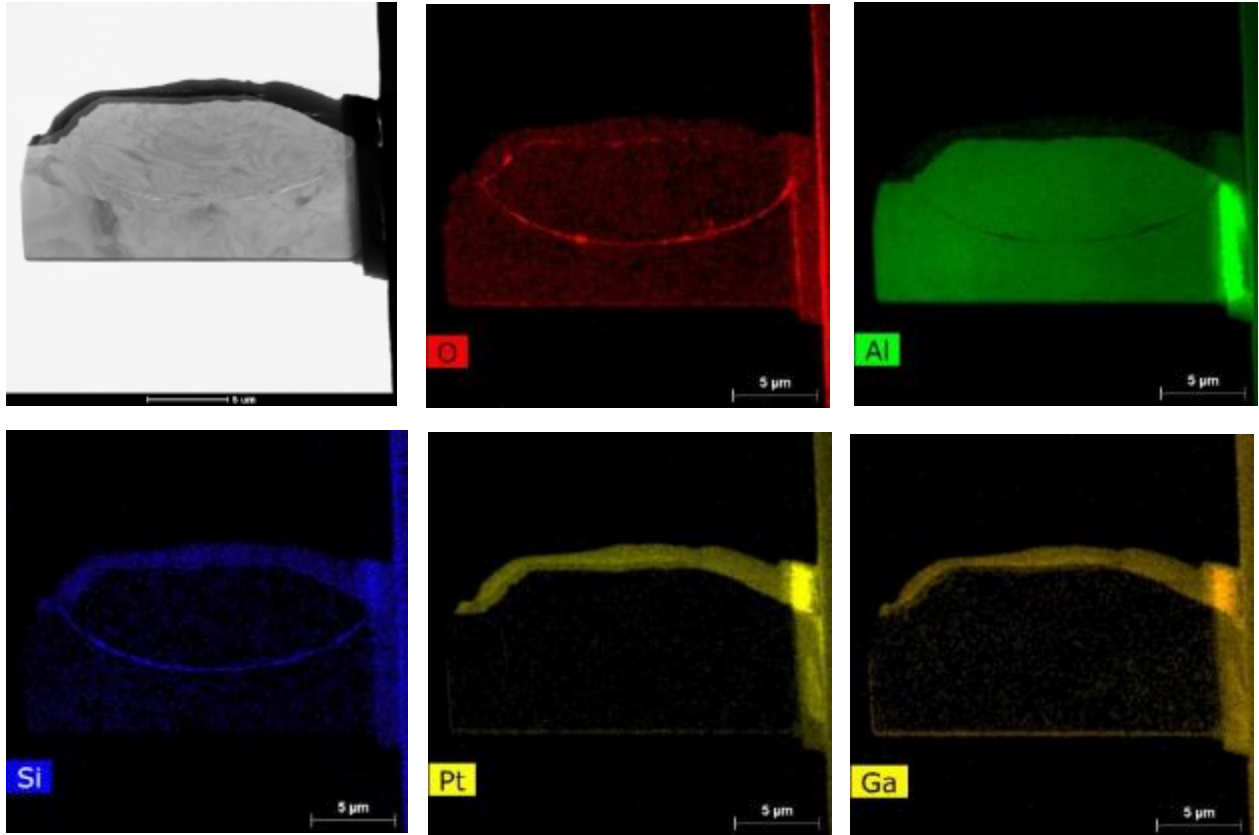


Figure 109. STEM and EDX analysis of Particle 2 from splat sample RH-95%.

The analysis of additional particle splats revealed similar trends to those observed from particles 2 and 3. There are patches of interfacial oxide separated by apparently oxide-free regions. There were instances where the bottom interface appeared to be delaminated from the substrate but exhibited a complex oxide morphology suggesting non-planar interfacial cracking. This was consistent with the asymmetric Al and O profiles recorded and the line scans representative of these areas. The sides of the particle/substrate interface exhibited good metallurgical bonding substantiated by weak enhancements of the O signal with no clear evidence of an oxide layer.

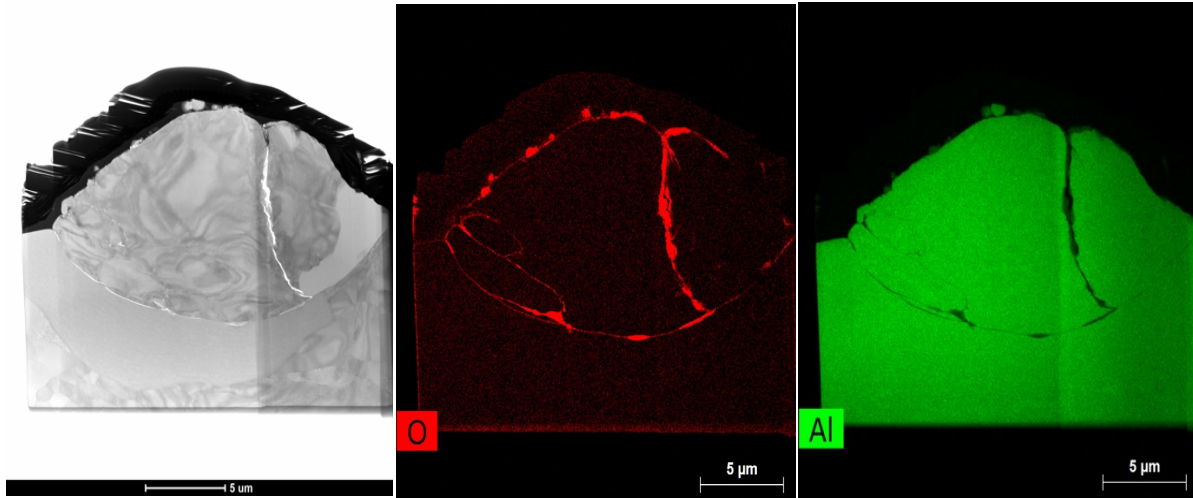


Figure 110. STEM and EDX analysis of Particle 6 from splat sample RH-95%.

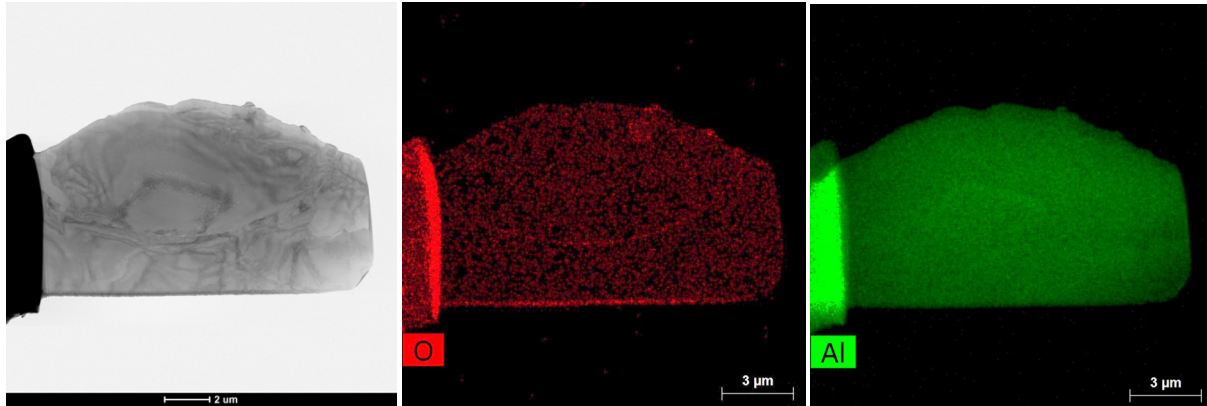


Figure 111. STEM and EDX analysis of Particle 2 from splat sample As-Received.

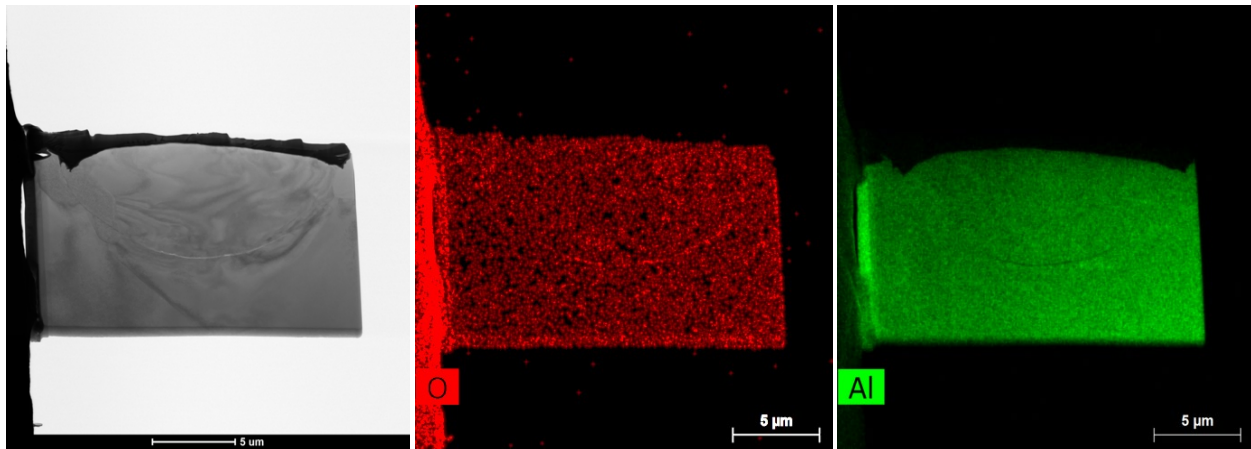


Figure 112. STEM and EDX analysis of Particle 32 from splat sample HT-Baseline.

In other particles analyzed, there was a greater variety of features. For instance, there were cracks observed through the splat from particle 6 (Figure 110), suggesting that this discontinuity may have been the result of two particles impacting and forming an aggregate. On the side interface there was significant variation in oxide thickness, but line scans showed that there was a single well-defined oxide peak. This suggested that there was bonding of the particle in this region despite the oxide. In other areas on the side of the particle/substrate interface there was a clear oxide double-layer indicating that there was interfacial delamination.

Figure 111 and Figure 112 represent particles from powder samples As-Received and HT-Baseline respectively. The first image in each figure shows an SEM of the splat followed by an X-ray map of oxygen and then an X-ray map of aluminum. Note the difference in oxygen detection at the splat/substrate interfaces all along the entire bond line. There are only faint traces of oxygen indicative of a thin oxide/hydroxide surface film. Such a thin film would have less adverse effect on particle to particle and particle to substrate bond strength.

5.0 Analysis

The use of active alumina as a desiccant, is widely known [172]. The premise of this research study relied on the fact that aluminum powders can continue to oxidize/hydrolyze during and subsequent to gas atomization. This premise is substantiated by the fact that during gas atomization, aluminum powders are passivated by the formation of thin protective surface films of oxides and hydroxides, which is sometimes accomplished by exposure of the liquid atomized droplets of aluminum to oxygen at lowered partial pressure and water vapors [165 to 173]. Additionally, subsequent to gas atomization, exposure to high temperature during the cold spray process and/or to humidity (50% RH or higher) at room temperature, during powder packaging, handling and storage, can contribute to further growth of the surface films [21].

According to Dr. George Campbell, President and Chief Operating Officer of Valimet, Inc., (the producer of all the HP-Al powders used in this study) during gas atomization, the molten droplets were passivated in an inert chamber consisting of dry nitrogen and 1-2% dry oxygen. This results in a more spherical shaped powder particle and prevents the formation of hydroxides. Care is taken to stay below the dew point to prevent hydration of the oxide film. The recommended dew point is less than -40°C , which corresponds to a maximum moisture content of 120 parts per million by atomic percent [21,174]. The final product is packed in containers with a desiccant, but the powder is not packaged in an inert environment and can adsorb moisture.

5.1 Previous Research

Figure 113 shows the stages of oxidation of aluminum metal at various temperatures [175,176]. It was difficult to predict the actual species of oxides of powder particles because of the influence of particle size and distribution, water entrapment during atomization and the formation of hydroxides, which affect the core and shell structure [177-179].

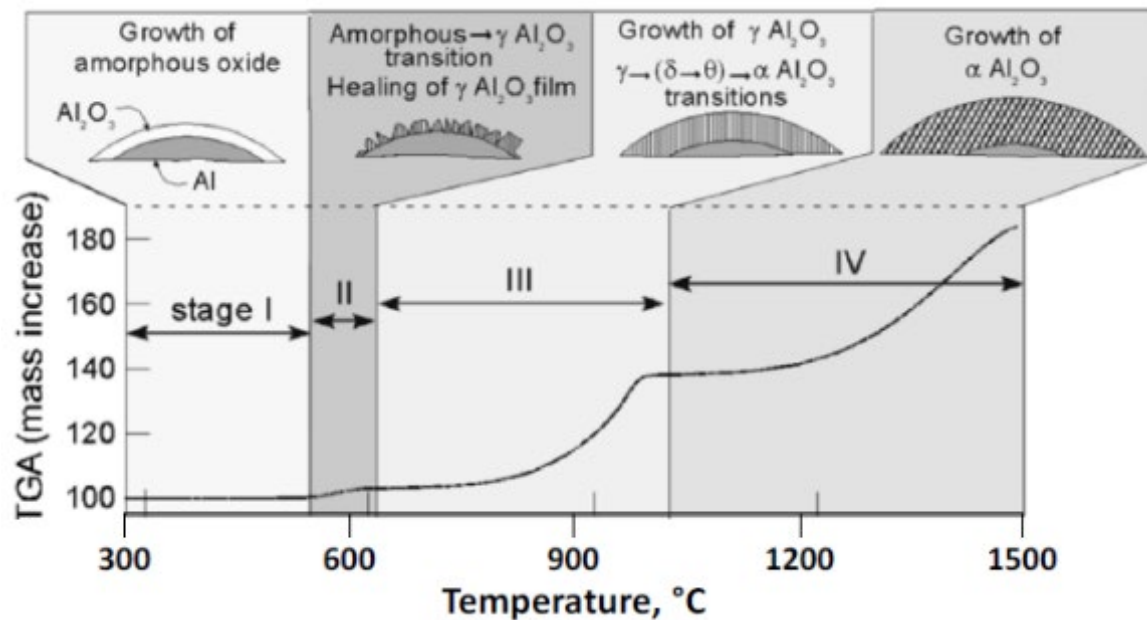


Figure 113. Stages of oxidation occurring on aluminum metal in relation to temperature, superimposed on a typical TGA plot [157,158].

The effect of humidity of aluminum powders, on the oxidation rate and the nature of the aluminum oxide scale has been explored [21,97,98,100,102,107,177-179,180,181]. It can be surmised from the results of various exposure tests, as the relative humidity increases the initial oxidation rate increases and results in a hydrated amorphous oxide scale and upon continued exposure, a layer of hydrated oxide grows and can have several different crystalline phases depending on the temperature and humidity level [181]. H.B. Peacock et al., has shown that bayerite ($\text{Al}_2\text{O}_3 \cdot 3\text{H}_2\text{O}$) forms at temperatures less than about 80°C while boehmite ($\text{Al}_2\text{O}_3 \cdot \text{H}_2\text{O}$) forms above 80°C [163]. These hydrated oxides have a structure that is reported to be more porous compared to the layer of dry amorphous alumina and therefore would be more prone to further oxidation [173]. The differences in the coefficient of thermal expansion between the oxide and the hydroxide which may be adjacent to each other on the surface of an aluminum powder particle can also lead to cracking and further oxidation of the base metal.

The metallic aluminum beneath these layers can further oxidize through the ability of protons to diffuse through the oxide-hydroxide shell [183]. Cook has reported that the oxidation of aluminum in water can release “2.5 times as much heat as is generated from pure nitroglycerin” [184] plus the reaction forms fine hydrogen bubbles that can further sensitize the mixture. Figure 114 shows the results of hydrogen blistering that produced cracks on bulk cold spray material produced by ARL from 6061 aluminum powder. The hydrogen gas formed during solution heat treating at 530°C and caused the cracking shown.

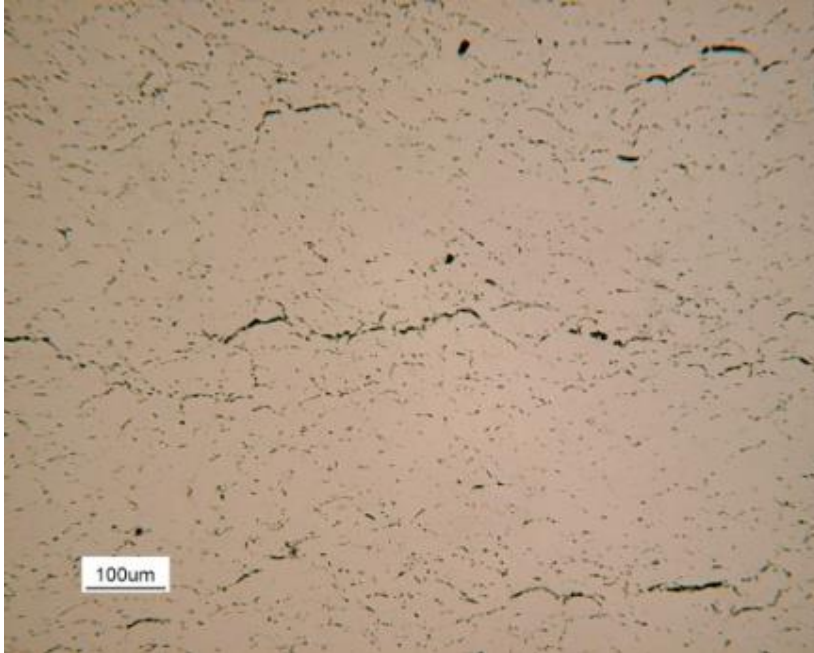


Figure 114. Hydrogen blisters in 6061 Al cold spray bulk material after solution heat treat.

Nascent hydrogen evolution is the result of the breakdown of water and hydroxides that comprise the surface film on gas atomized aluminum powders. The atomic hydrogen diffuses to hydrogen traps which are grain boundaries, pores and other defects within the material and combines to form hydrogen gas. Hydrogen can even facilitate the detachment of the protective oxide layer from aluminum [185-188].

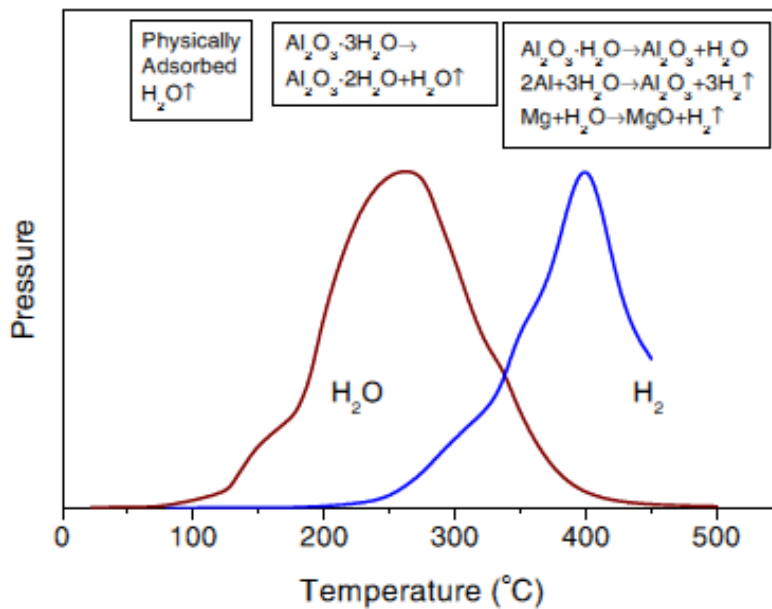


Figure 115. Degassing behavior of aluminum and its composites [189].

This phenomena can also occur during degassing of aluminum powder, which is performed at temperatures conducive to hydrogen blistering as illustrated in Figure 115 [189]. The steps are simplified below:

- Free water evolves at 200-300°C
- Hydroxides break down between 375 and 450°C
- When hydroxides break down atomic hydrogen evolves
- Atomic hydrogen migrates to areas of lowest free energy (GB, defects)
- Atomic hydrogen combines with itself to form molecular or hydrogen gas
- Blisters form which can lead to cracks

In 2014, Busca conducted a critical review of the data reported in the literature concerning the transformation, morphology, physico-chemical properties and the surface properties of transitional aluminas [190] and concluded that there is still much controversy and that much more extensive research is still required to develop a complete understanding of this topic. A summary of the most relevant paths in alumina poly-morphic transformations can be shown schematically in Figure 116 [190-192]. Busca reports that Al_2O_3 (corundum, S.G.R 3c, $Z = 6$) is formed at the end of the thermal transformation of aluminas. Much of the analysis of aluminum oxidation in published literature has been carried out using sheet metal aluminum. Although this is convenient in that it simplifies surface area calculations, the powder morphology and size distribution complicate interpretation of the oxidation kinetic calculations, when micron-sized powders are utilized. In addition, the surface oxide/hydroxides remnant from gas atomization, packaging, storage and handling can vary significantly between batches of powder.

Busca concluded in his extensive review that, “*In spite of the new experimental and theoretical techniques developed today, still a comprehensive picture of this subject is far from obtained.*”

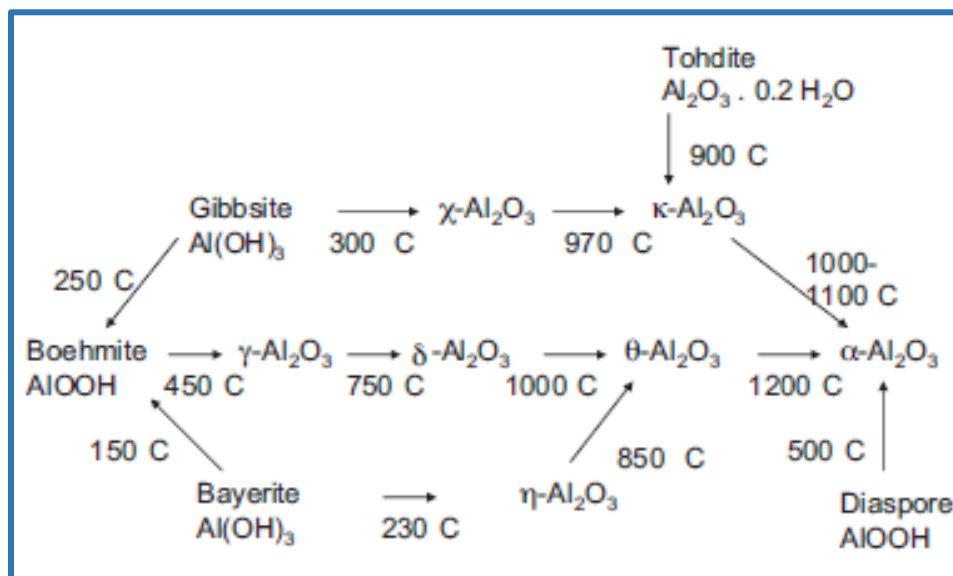


Figure 116. Schematic of the primary solid state transformations of alumina [190-192].

Figure 117 shows a schematic of the thermal dehydration sequence of aluminum hydroxide, as reported by Wefers and Bell from Alcoa and VAN DIJK [193,194]. The decomposition of aluminum hydroxides is complex and there are numerous metastable oxides formed. Some of these reactions occur at relatively low temperatures (room temperature) and the thermal decomposition of the aluminum trihydroxides could proceed via the aluminum oxide/hydroxide (path a) or without intermediate hydroxide phase in a direct conversion to aluminum oxide (path b) as listed in Table 31 taken directly from the work of VAN DIJK [193].

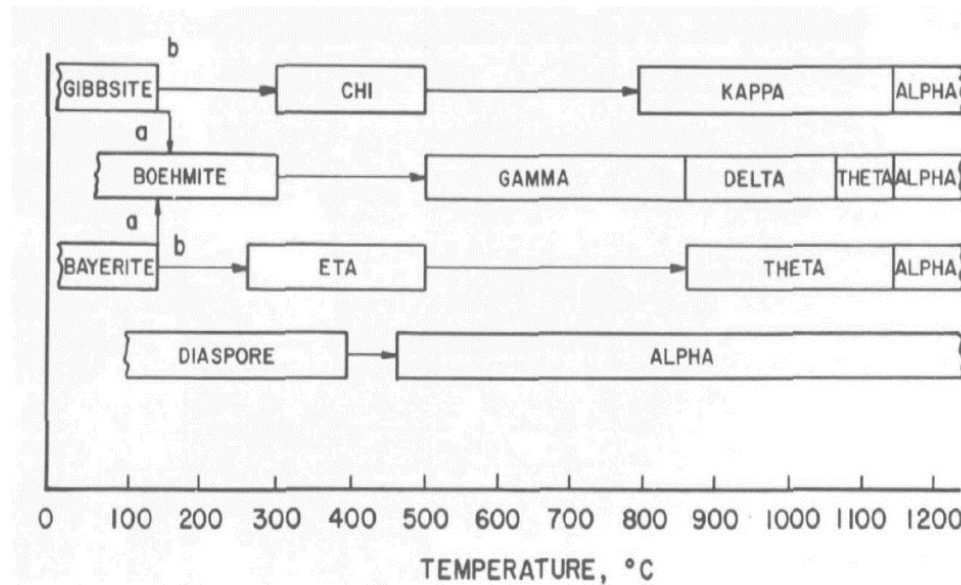


Figure 117. Thermal dehydration sequence of aluminum hydroxide [193,194].

Table 31. Decomposition of Aluminum Hydroxides [193].

Conditions	Path a	Path b
Pressure	> 1 atm	1 atm
Atmosphere	Moist air	Dry air
Particle size	>100um	< 10 um
Heating rate	< 1 C/min	> 1 C/min

The thickness of the surface layer is dictated by oxidation kinetics and the conditions in each stage of the GA process, such as the available water vapor and oxygen, solidification rate and time of flight during atomization [98]. The rate of oxidation is directly proportional to the relative humidity and oxygen concentration in the air of the GA, the collection chamber and the handling

and storage atmospheres [21, 97]. The powder exposed to the various conditions of elevated temperature and humidity resulted in variations of oxides and hydroxides.

Based upon prior research, it is clear that the exposure of the gas-atomized, HP-Al powder to either air at elevated temperature and/or humidity at room temperature will result in the growth of surface films.

5.2 Results of Characterization of the HP-Al Powder Groups

The objective of this thesis was to understand the particle/substrate interaction of hydrolyzed micron-sized High Purity (HP) aluminum (Al) powder particles with varying surface oxide/hydroxide layers, during single particle impact and determine the critical impact velocity (CIV). Therefore, identification of the exact polymorph of aluminum oxide/hydroxide was not essential nor the goal of this thesis. However, the in-depth analytical techniques employed and the data generated provided an insight as to the nature of the polymorphs of aluminum hydroxide.

The results obtained from some of the various analytical tests relied heavily on proper specimen preparation and interpretation of the data, while others were quantifiable and less subjective. Previous experience and available reference standards along with reputable, published literature were essential for proper identification and characterization of the surface films. Some of the data generated to determine elemental composition of the powders was relatively straightforward, such as the results from Inert Gas Fusion and ICP, because available standards were used and the detection of the elements could easily be obtained and quantified by these techniques. However, it was understood beforehand, that other methods could alter the surface chemistry and/or induce phase transformation and were pursued with caution. Additionally, micro elemental techniques using X-rays vary considerably in the depth of penetration into the material and this was also taken into consideration to assure proper interpretation of results. It is well known that X-Rays will penetrate a few micrometers and as much as several millimeters down into a material, depending on its composition and matrix. X-Rays are detectable from a few millimeters within the sample, but in many situations this could be reduced to a few micrometers or less depending on certain factors.

There were two important variables that were taken into account when analyzing the data obtained from the X-ray analysis techniques employed during this study; (a) the depth of penetration of the primary X-Ray beam into the sample, and (b) the escape depth from which fluorescent X-Rays could be detected [195]. Both are directly dependent upon the energy of the X-Rays, whereas the higher the X-Ray energy the deeper the X-Ray penetration. Detection was also an issue, especially during EDS-X-ray mapping of the fracture surfaces of the tensile specimens. The surface topography caused problems with X-ray emission and detection but experience from analyzing fracture surfaces during failure analysis investigations dictated that longer detection times resulted in obtaining data that was not detectable under shorter dwell times and smaller spot sizes.

Focused Ion Beam (FIB) micromachining was used to extract samples for high level electron microscopy and could easily induce enough heat into a sample to cause a phase change. The FIB micromachining process can induce damages due to the displacement of atoms and heating in the

substrate [196]. This occurred on several occasions when preparing samples for STEM/TEM and Auger analysis and resulted in erroneous data. However, the possibility of overheating was anticipated and cryogenic means of specimen extraction were employed, where available, such as for the TEM, Raman Spectroscopy and the Fourier Transform Infrared Spectroscopy performed at Bucknell University.

5.2.1 IGF, DSC and TGA

It could be deduced from the Inert Gas Fusion results obtained when using the LECO ONH836 instrument, that the RH-95% powder group contained water and hydroxides, as evidenced by the extremely high increase in hydrogen content as compared to the remaining groups. Adsorbed water and hydroxides were present on As-Received, RH-50%, and RH-95% powders, but levels were significantly higher for the RH-95% samples, lower on RH- 50%, and the lowest were the AR powder. No water or hydroxides were present on any HT samples analyzed. This was also supported by both DSC and TGA.

The results from the IGF tests conducted using the LECO Elementrac ONH-p instrument were interesting and revealed a few important points regarding gas atomization and the fluidized bed apparatus used to process all of the powder groups, with the exception of the AR group. The AR powders that were analyzed in the as-received condition, contained an unusually high concentration of oxygen. This may have been the result of two primary factors; (1) the fluidized bed removed the fine powder particles from the remaining powder, prior to bulk analysis and (2) the powder producer (Valimet) processes large quantities of powder in a single batch which can remain in storage for long periods of time before being purchased.

(1) The fine powder particles have a high percentage of surface area and would increase the overall relative amount of oxygen present in the analysis of a bulk sample. The fluidized bed was designed with a disengaging zone to allow the particles to remain in the bed even if they floated up, but this may not have been sufficient to stop the finest powder. When the powder was process over several runs grey material was observed in the collecting section, which confirmed this deduction.

(2) Aluminum powder produced by Valimet, can remain in inventory for months and even years before being purchased and consumed. Although some precautions are normally taken to avoid water absorption and adsorption, these methods do not completely insulate the powder from exposure to moisture. The as-atomized powder is classified by Valimet in air and then packaged in black polymer bags that are zip tied and then subsequently placed into metal containers that have desiccant in them. The polymer used for the bags are carbon filled for anti-static purposes, to prevent spontaneous combustion. The metal container has an elastomeric seal that is clamped shut but it is not completely air tight.

The DSC results showed (Figure 30 and Figure 35) the enthalpies of the reaction occur near 290°C (see major endothermic peak) and resulted in an average enthalpy for AR, 50%, and 95% of 0.903 J/g, 2.612 J/g, and 41.823 J/g respectively. This data indicated that between 250 °C and 290 °C a phase transformation was occurring. Since melting of a material involves absorption of energy, it

is an endothermic process and appears on the DSC curve as a large, temporary decrease in heat flow and a negative peak. [197,198].

This phase change was most pronounced in sample RH95% but the same phase change can be observed in the AR and RH50% samples as well, but to a much lesser degree. Figure 31 represents a graphical presentation of the oxygen content determined by Inert Gas Fusion, shown previously in Table 12, compared to the associated enthalpies of reaction of the main endothermic peak near 290°C, from the DSC scan shown in Figure 30. This side by side comparison indicates that the phase transformation may be rich in oxygen and combined with the data from Table 18 may also contain a high concentration of hydrogen as determined by IGF. Considering the IGF and DSC data in its entirety, there is a strong argument that the transformation is consistent with an aluminum hydroxide. The, endothermic peak at 283°C, may have been due to decomposition of aluminum hydroxide to γ (gamma)-Al₂O₃ [160]. Takashi et al. has shown that water can be incorporated in the α -Al₂O₃ crystal structure resulting in the formation of aluminum hydroxides such as gibbsite. [199]

Sarker, Md Saifur Rahman, et al, performed a DSC of aluminum hydroxide, as shown in Figure 33. The endothermic peak observed at 283.16°C corresponds well to that shown in Figure 30 and in Figure 32 and serves to substantiate the presence of an aluminum hydroxide in sample RH95%.

Figure 34 represents DCS scans of the heat treated HP-Al powder samples and the results indicate the absence of any major phase change. No discernable Al(OH)₃ peaks can be observed in any of the DSC scans of the heat-treated samples This was anticipated since the exposure temperature during the heat treat was 300°C which is at the onset of the transformation temperature of aluminum hydroxide. Sarker, Md Saifur Rahman, et al, show the decomposition of aluminum hydroxide to γ (gamma)-Al₂O₃ at this temperature [160,161, 162].

Figure 35 contains the DSC scans for all of the powder groups and the graphs were intentionally shifted vertically for ease in viewing and comparison. There is no evidence of adsorbed water observed (no reactions around 100°C). The notable peaks are those at approximately 290 °C on samples AR, RH50% and especially RH95% and indicate the decomposition of aluminum hydroxide.

Baranyai et al., have reported that the conversion of aluminum hydroxides to aluminum oxides can occur via monohydroxide boehmite [γ - AlO(OH)], but the dominant decomposition is directly to oxides [161].

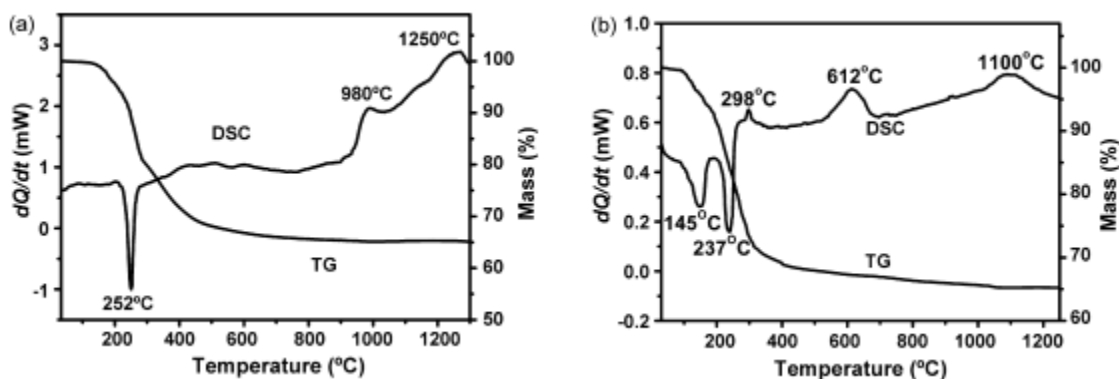


Figure 118. (a) TG and DSC curves of unground bayerite and (b) bayerite ground for 2h. [200]

Jinwang Li et al., studied the mechanism and kinetics of aluminum nitride powders exposed to moist air at room temperature and determined that the powders were initially hydrolyzed to amorphous aluminum oxyhydroxide, which subsequently transformed into mixtures of crystallized aluminum trihydroxide ($\text{Al}(\text{OH})_3$) polymorphs, i.e., bayerite, nordstrandite, and gibbsite, forming agglomerates around the unreacted AlN . [201]. Although these authors investigated AlN powders, the mechanism of hydrolysis of aluminum powders can be used as a basis of comparison, in regards to the formation of certain polymorphs of aluminum hydroxide and the analytical methodology employed. Specifically, the proper analytical techniques used to identify the pedigree of the surface films.

These types of studies are found less frequently in open literature and those that are available can often times be controversial. Abid et al. [202] reported that AlN did not readily react with atmospheric moisture at room temperature [201], however, the results of Kameshima et al. [203] in their analysis of surface state and stability during storage of AlN powders discovered that the surface of the powders reacted slowly with atmospheric moisture during several years of storage in a capped container. The contradiction in conclusions between Abid et al., and Kameshima et al., may be attributed to the techniques used to analyze the surface films. Kameshima et al., incorporated X-ray photoelectron spectrometry (XPS) which revealed evidence of hydrolysis.

Digne et al., [204] predicted limiting temperatures of stability of the various polymorphs through calculations which compared favorably with experimental data available on the transition temperatures of aluminum hydroxides. This research team provided a short commentary on the use of X-ray diffraction (XRD) for the determination of the cell shape and of the locations of aluminum and oxygen atoms and explained the limitations with associated references, of XRD and neutron diffraction, [205-210] as well as Raman and IR spectroscopies [211,212,213] or NMR spectroscopy [214] in determining the positions of the hydrogen atoms.

L.H.Ni. et al., and Yong Liu et al., have showed the use of Raman spectra in studies of polymorphs of aluminum oxide and hydroxides [213, 215].

5.2.2 FTIR, XPS, SEM, TEM and Raman Spectroscopy

The as received AR, RH 50%, and RH 95% FTIR spectra indicated the presence of an Al-OH species, appearing to consist primarily of bayerite (Figure 38). However, gibbsite and bayerite are both alumina trihydrate ($\text{Al}(\text{OH})_3$) [164]. The HT-Base, HT-30, HT-60, and HT-240 spectra did not show any indication of aluminum hydroxides. This was anticipated since the HT powders were heat treated at 300°C and Gibbsite decomposes to oxide above the temperature of 300°C [161]. For HT-Base, HT-30, HT-60, and HT-240 a preliminary semi-quantitative analysis (peak area integration) of the Al-O peak at 935 cm^{-1} indicated the oxide layers on these four samples were of a similar thickness and structure. Therefore, at a temperature of 300°C although the decomposition of the hydroxide polymorphs occurred there was no detectable growth of the surface film.

Species detected on the surfaces by XPS included: Al^0 , Al^{3+} and organics including CH_x , C-O, O-C=O and carbonates. The carbonate concentration seemed to systematically decrease with increasing heat treat time for the HT powder samples. The thickness varied from 4 nm (as received) to 6 nm (RH 95%). Most of the samples were clustered around 4 nm. Table 19 lists the O/Al ratio and Figure 39 the binding energy associated with representative powder samples (AR, HT240 and RH95%). The values were highest on the as received, 50% RH and RH 95% samples. This result was the hydrolysis of the aluminum powders exposed to moisture with the growth of a hydroxide layer. The position of the O 1s positions on these same samples (531.6 ± 0.1 eV) suggested a higher fraction of OH compared with the HT air samples (530.8 ± 0.3 eV).

SEM and TEM analysis showed the oxide layer looked similar for most of the powder samples from all seven groups, having a thickness of approximately ~ 4 nm, except for the RH95% sample that had a surface layer that was approximately 6 nm in thickness. The ratio of aluminum to oxygen was the same at 40:60 at%. The surface film appeared relatively uniform and smooth for the AR and HT samples with the exception of HT240 which had some 'rough' areas. The RH 50% sample had some spikey surface features that could be indicative of hydroxide formation and the RH95% had some rough areas as well. STEM and EDS mapping of the RH95% powder sample supporting the physical features of the surface layer found by HRTEM, including roughness and the protruding spikes. TEM found the thickness of the surface film on the as- received powder and the "HT" powders were all ~ 4 nm. The RH 95% powder sample had a thickness of 6 nm.

The Raman spectrum collected of RH-95% revealed aluminum hydroxide polymorphs Bayerite, Boehmite and Gibbsite and areas of aluminum oxide were present. It was interesting to note that the formation of oxide or hydroxide surface films occurred in a random fashion and as 'patches' across the particle surface. In contrast, the Raman analysis of sample HT-Baseline revealed no evidence of aluminum hydroxides. However, the presence of aluminum oxide was observed. This was anticipated as the heat treat exposure temperature would have converted any surface hydroxides to an oxide.

In summary, the FTIR, XPS, SEM, TEM and Raman spectroscopy results were in agreement with each other and provided insight as to the nature of the surface films and also their morphology.

Figure 119 is a schematic illustrating the morphology of the resultant hydroxides that formed on the powder samples exposed to moisture at room temperature. Note that the hydroxide polymorphs can actually form in patches as opposed to a continuous layer. This is very important to note from a characterization perspective because if FIB samples are taken from areas outside of the patches of hydroxide, then the results could be misleading and evidence of misinterpretation occurred as data was being generated until this discovery was made.

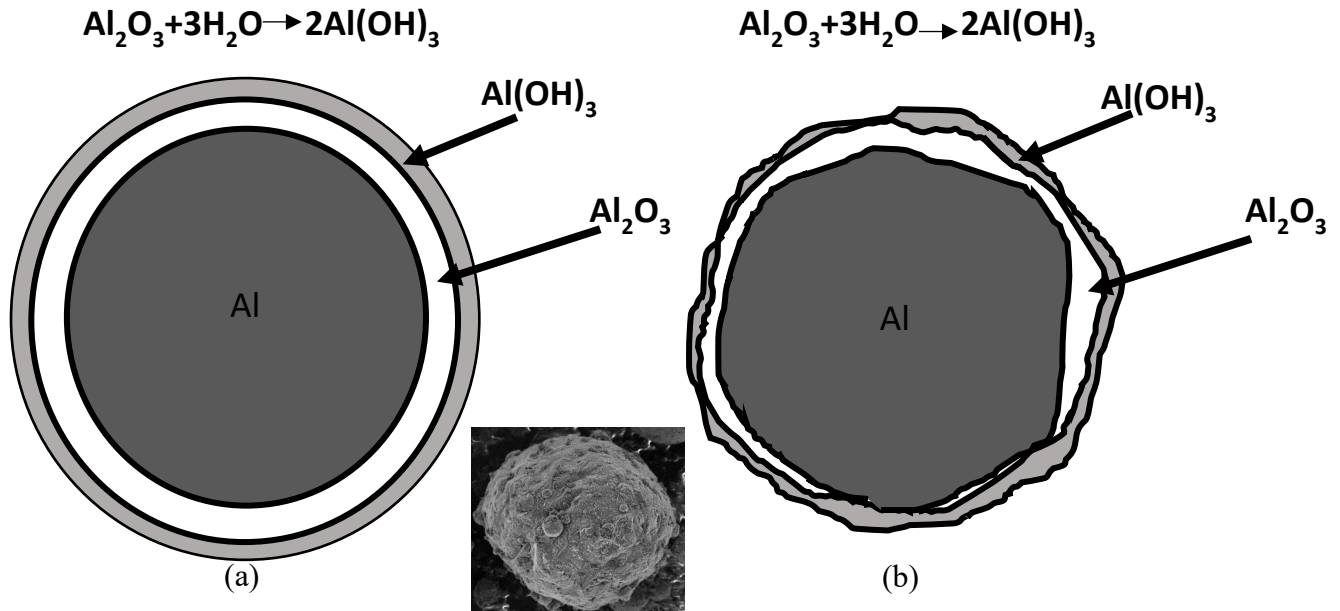
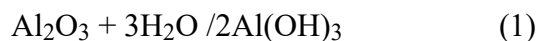


Figure 119. (a) Schematic illustrating the hydrolysis of an Al particle [216] and (b) real-life. SEM image in the center is of the morphology of a powder particle from group RH-95% for comparison.

Previous studies have determined the reaction between aluminum particles and water and the chemical reaction equations are list below [216-220]:



The HP-Al gas atomized powder had a passive oxide layer that may have already contained hydroxide polymorphs depending on the exposure to humidity prior to testing. The oxide layer could inhibit the reaction between aluminum and water but did not prevent hydrolysis when exposed to high humidity. The hydration reaction occurred on the alumina protective layer, as shown in eqn (1). The hydration reaction produced hydroxide phases such as $\text{Al}(\text{OH})_3$ and polymorphs such as Gibbsite, Boehmite and Bayerite. Subsequent to the hydration reaction, the hydroxide phases could react with the aluminum core and generate hydrogen, as described previously and shown in eqn (2) [37,185-189,216,218]. Water molecules can also be transported through the aluminum hydroxide layer and react with the aluminum core directly, as shown in eqn (3)[216,217].

5.2.3 Dynamic Nanoindentation

A series of nanoindentations were produced on separate powder particles from powder groups (As-received, RH-50% and RH-95%). From these measurements an attempt to find a correlation between the mechanical behavior of the oxide film under load and its hardness and thickness were pursued. Bahr et al. [167] as well as Weppelmann and Swain [168], have reported a technique that incorporates nanoindentation as a tool to cause through thickness fracture events for thin oxide films on metals and from these results it was deduced that estimations of oxide film thicknesses could be determined for gas atomized HP-Al powders. The data obtained for the AR, RH-50% and RH-95% powder groups showed that the corresponding hardness and surface film thickness were consistent with the trend determined by the electron microscopy and X-ray analysis techniques, although the thickness reported for the RH-95% was a bit higher but this could be attributed to the characteristics of a hydroxide patch, where the surface film thickness varies considerably.

Table 32. Results of Hardness and Surface Film Thickness by Dynamic Nanoindentation

Powder Group	Hardness (Gpa)	Thickness (nm)	TEM, XPS and Raman
As-received	1.50	3.9	4
RH-50%	1.73	4.0	4
RH-95%	2.28	9.2	6

5.2.4 Single Particle Impact and Critical Impact Velocity

The CIV is used by experimentalists and users to optimize cold spray process parameters and should be a useful tool to mitigate trial and error. Researchers throughout the years, have defined a critical value of particle velocity, as being that which is necessary for the impacting particles to bond with the substrate during the cold spray process [6,30,54,56,57,60,72,78,118,120-129]. This critical velocity is dependent on a variety of factors including the substrate material and is also a function of the physical and mechanical properties of the powder material [6,30,54,56,57,60,72,78,118,120-131].

Grujicic et al., [29] rely on the assumptions and work of Asaadi et al., [28] to conclude that the onset of adiabatic shear instability in the particles/substrate interfacial region plays an important role in promoting particle/substrate bonding during the cold spray process, which in turn led to a theoretical prediction of CIV. Asaadi et al., determine through their modeling efforts a very non-uniform development of strain and temperature at the interface, suggesting that bonding is confined to a fraction of the interacting surfaces and substantiate their claim by reporting the relatively low bond strength of the copper coatings [28]. Since CIV is defined by the bonding of particles to the substrate and particles to particles, the quantification of the cold spray bond is essential for an accurate prediction but as previously discussed the means of testing the cold spray bond strength has not been satisfactory to be incorporated into theoretical models. The measurement of particle bond strength must be determined at the micron scale to be confirmed as valid data to substantiate theoretical models. Dykhuizen [30], Asaadi [28], Grujicic [29], Bae et al., [115] and most other researchers all relied on the inferior method of bond strength testing, incorporating either the European Standard EN 582 “Thermal Spray Determination of Tensile Adhesive Strength or ASTM C633, “Standard Test Method for Adhesion or Cohesion Strength of

Thermal Spray Coatings, which relies on the strength of an adhesive, thus limiting values to 85MPa (~12,000psi).

Gangaraj et al., and Jae-Hwang Lee et al. both employ the single particle impact (SPI) experiment and are able to actually measure the CIV and generate visual evidence of particle bonding. It was determined that the actual measured values of CIV differed from the theoretical calculations because of the discussion points argued in previous sections. Additionally, the surface film(s) (hydroxides and/oxides) inhibited bonding and therefore higher values of CIV were measured for the RH95% powder group and the data obtained by UMass can be summarized as follows:

- *The exposure to ordinary air (29°C, RH 50%) for 4 days did not make a meaningful change in the CIV and single particle dynamics.*
- *The exposure to high-humidity air (29°C, RH 95%) for 4 days caused substantially deteriorated bonding characteristics.*
- *The exposure to high-temperature air (300°C) for 4 hours does not produce meaningful change in the bonding characteristics.*

A standard method is needed to determine a meaningful value of critical velocity. Ideally this method would weigh the particles with velocity closest to the resulting critical velocity highest on both the bonded and unbonded side of the graph with those furthest from the critical velocity being weighted lowest. In addition, a means to quantify the bond must dictate what the actual value of the CIV should be. In other words, the fact that a particle ‘sticks’ to the substrate does not indicate the strength of that bond and if that bond is weak what practical use is that value of the CIV?

The CIV must be correlated to the bond strength and/or ultimate tensile strength to be of practical use.

In lieu of this correlation, the HSUP and LSBP data points can be used to determine the average, and the difference between the HSUP and LSBP can be used to determine the error on the average. A correlation to strength would be optimal as well as a more rigorous statistical method but if this approach is taken the results yield the following:

AR = 802 ± 14.5 m/s

50% = 784 ± 17 m/s

95% = 951 ± 70 m/s

HTB = 828 ± 1 m/s

The conclusion would be that AR and 50% RH are effectively the same, while the HT-Baseline is a bit higher, and the 95% is the highest by far.

The MIT Single Particle Impact results also correlated well with the FTIR-DRIFTS data collected by our collaborators Mala Sharma and Tim Eden at Pennsylvania State University. Their work demonstrated that the prominent bayerite Al-OH mode seen in the 95% relative humidity powders essentially disappears when the powders are heated, likely due to water leaving the surface of the particles and the decomposition of the surface hydroxides.

There was not a significant difference in critical impact velocity between the as-received particles and the 50% relative humidity particles. Both had a critical velocity transition in the range of approximately 800 to 830 m/s. However, there was a significant increase in the critical velocity observed for the 95% relative humidity powders. The 95% relative humidity powders displayed a critical velocity between 950 and 1000 m/s. The dramatic increase in critical velocity associated with the 95% relative humidity exposure suggests that the surface chemistry of these powders, which likely incorporates more water in the form of a hydroxide, significantly inhibits bonding.

To further examine the results obtained with the 95% relative humidity powders, a second test was conducted using the same powder after being stored in a desiccator. A small amount of the 95% relative humidity powders was placed in a vacuum desiccator for three days with the goal of removing as much water from the surface of the particles as possible. The impact behavior was tested after drying. The results revealed a decrease in velocity required for adhesion to the substrate with the desiccated 95% relative humidity powders. This served as further evidence that moisture, specifically hydroxide surface chemistry, played a significant role in critical velocity.

The data obtained for the 95% relative humidity powder that was desiccated and dried displayed a critical velocity that was less well defined than the other batches of powders. There was a range of velocities, roughly between 870 and 1000 meters per second, in which a mixture of both adhesion and rebound behavior was observed. This may have been the result of non-uniform drying in the desiccator, as particles at the bottom of the powder vial were less likely to have undergone a change in surface chemistry than particles directly exposed to the desiccator vacuum environment.

5.2.5 Bulk Cold Spray Samples

Bulk samples of material were produced from each of the six powder groups to determine the effects of the surface films produced on the feedstock HP-Al powder on the material properties; including tensile, hardness, and conductivity. The fracture surfaces of the broken tensile specimens were also examined to determine the crack origin, fracture morphology and to discern any important features that may relate to the prior powder treatments and the effects of the surface films.

The conductivity of the block with powder treated under dry conditions showed the highest conductivity levels, about 59%. This result was not surprising as the aluminum particles were partially annealed during this treatment, which was performed at 300°C while the typical annealing temperature for pure aluminum is 343°C. Annealing would increase the ductility of the powder making it more amenable to the cold spray process and increase its deposit efficiency. In contrast, the samples exposed to humid conditions showed the lower conductivity measurements with RH-95% showing the lowest level at 44% which is most likely the direct effect of the amount of oxide/hydroxides in the cold spray bulk material. The similar value of conductivity for As-received and RH-50% samples could be due to the wide range of humidity that the RH-50% samples was exposed to (RH=17-75%).

The micro-hardness measurements had a similar trend to that of conductivity. The set of samples heat treated under dry conditions show the lowest micro-hardness (47 HV) while those exposed to humid conditions showed the higher values, with the highest value for RH-95% (55.6 HV).

Annealed material would exhibit lower hardness and material that contained a higher level of oxides/hydroxides would have higher hardness. Again, the similar value of micro-hardness between As-received and RH-50% samples could be due to the wide range of humidity that RH-50% samples was exposed to (RH=17-75%).

Metallographic examination and chemical analysis of bulk material produced from powder with a thicker surface film revealed higher concentrations of oxygen than that produced from powder having thinner surface layers. The conductivity of aluminum alloys produced by cold spray would generally be inverse to the strength since strength is increased by interstitial elements and other contaminants like iron, which lower conductivity. However, in this study the feedstock powder is high purity aluminum having only trace concentrations of such elements and the only distinguishing factor should be the concentration of oxygen or hydroxides and the strength of the bond between powder particles. Conductivity, strength, and ductility are expected to decrease as the oxygen levels increase, as a result of poor inter-particle bonding from oxides impeding the metallic bond formation.

The results from tensile testing revealed that the RH-95% specimens exhibited higher strength but significantly low ductility than the as-received (AR) powder and the heat treated (HT) powders. This was anticipated because the surface film on the individual powder particles from the RH-95% samples was considerably thicker and would interfere with inter-particle bonding during the cold spray process. The bonding mechanism of the cold spray process is analogous to that of explosive welding, which is another type of solid phase welding process where bonding is also the result of plastic deformation of the metals to be bonded. Bonding occurs when two surfaces under extreme pressure are forced together such that the surface oxide layers are disrupted and bonding takes place between the opposing clean metal surfaces [112]. The high strength values could be attributed to the significant increase of aluminum hydroxides/oxides dispersed throughout the RH-95% cold spray samples whereas the bulk material would act like a metal matrix composite and the oxide particles would contribute to the overall strength of the material.

The HT-Baseline specimens exhibited the highest ductility which is reflective of the extended heat treatment of these powders and the decomposition of the hydroxides. AR1 and AR2 samples showed similar mechanical behavior, but AR3 had a higher yield and ultimate tensile strength with slightly lower ductility.

Fractography was conducted on two sets of tensile samples representing the greatest disparity in ductility as determined by tensile testing, RH-95% and HT-Baseline. The fractures surface of other remaining samples were similar with that of the heat treated baseline and as-received, due to their similar mechanical properties. The heat treated samples experienced fracture in a ductile manner, as substantiated by the dimpled morphology while the RH-95% samples exhibited brittle fracture. The samples showed very little evidence of necking. The fracture surface appears flat relative to the other mini-tensile specimens, which serves as evidence of low plastic deformation and unstable crack growth. The fracture surface can be characterized as wavy, almost as if the fracture occurred along bond-lines of successive cold-spray splats. The intact surface of powder particles were also observed. These results point towards incomplete bonding in the cold-spray deposit.

Energy Dispersive Spectroscopy (EDS) was used to determine the atomic composition of oxygen to aluminum metal and provide a basis of comparison between the HT-Baseline and RH-95% powder samples. There was a significant difference in oxygen concentration between the RH-95% and HT-Baseline samples which was expected and is consistent with the other analytical data generated. The RH-95% samples contained a significantly higher oxygen concentration across the fracture surface.

5.2.6 Single Particle Impact Splats

The results of analyzing numerous cross-sections of individual particles subsequent to impact via the cold spray process revealed that there was significant particle-to particle variation in the morphology of the splats. Additionally, the surface morphology associated with the oxide/hydroxide film was very inconsistent and ‘patches’ were observed on the exterior of these powder particles, which was commensurate with the data obtained by SEM, TEM, XPS and Raman spectroscopy. The RH-95% powder contained a higher concentration and a thicker surface layer that interfered with bonding as evidenced by the delamination between the particle and substrate.

5.3 Summary of Analysis

- This study provided insight and a fundamental understanding of the role of surface oxide/hydroxide layers on particle deformation and bonding during supersonic impact, and the subsequent adverse effect on the cold spray critical impact velocity.
- The data generated from this research clearly revealed that HP-Al powders can hydrolyze at room temperature when exposed to humid conditions and form deleterious hydroxides that in turn, require higher critical impact velocities to adequately consolidate, during the cold spray process. The surface hydroxides formed leads to poor interparticle bonding and subsequently causes inferior material properties of the resultant cold sprayed material.
- It has been well established in published literature that the presence of oxide/hydroxide surface films of powder particles in powder metallurgy (PM) Al alloys can lead to cracking of the compacted material during thermomechanical processing.
- Published literature and industry practices report that gas atomized aluminum powders can have varying degrees of oxide/hydroxide surface films which can increase in thickness as a result of exposure to humid and/or high temperature conditions.

6.0 Conclusions

- The HP-Al powder particles exposed to high humidity (RH-95%) formed a hydroxide film that adversely affected interparticle bonding and had a higher critical impact velocity as compared to the remaining HP-Al powder particle groups.
- Bulk material produced by the cold spray process from powder group (RH-95%) showed significantly lower ductility but slightly higher ultimate tensile strength most likely the result of the incorporation of oxide causing the material to behave like a metal matrix composite, whereas the increase in strength was attributed to the dispersed oxide.

7.0 Recommendations for Future Research

- This study should serve as a basis for the investigation of other aluminum alloy powders to determine the influence of oxide/hydroxide films on the CIV, such as those used extensively in the automotive and aerospace industries (Al2024, Al6061, and Al7075).
- A means to investigate the solidification of single micron sized aluminum particles should be pursued to analyze the formation and growth characteristics of surface oxide/hydroxide films altering the passivation atmosphere by controlling the amount of dry oxygen and/or humid air.
- The effects of air and/or humidity exposure to other metallic powders used for the cold spray process should be explored, as well as ways to mitigate moisture adsorption during gas atomization, packaging, handling, storage and usage of powders for AM processing.
- Post processing techniques should be developed to reclaim powders that have been oxidized and/or hydrolyzed in order to make them viable for cold spray.
- The Critical Impact Velocity needs to be redefined because currently it has little practical use. The CIV refers to the velocity at which particles ‘stick’ to the substrate but the bond strength is not quantified. The CIV makes no distinction between particles with very poor bond strength and those with extremely high bond strength.

8.0 Technology Transfer Plan

Powders produced to date have been engineered for traditional powder metallurgy and thermal spray processes. New Additive Manufacturing (AM) technologies such as Laser Sintering, Industrial 3D printing and Cold Spray are not always conducive to the use of these standard powders, in their current form due to a lack of customized process control. The additive manufacturing industry is, by its very nature, designed to be extremely customizable. As a result, there is limit to the level of commoditization available to the industry. Instead, the growing \$21B (est. by 2025) market is going to be extremely dependent on customized solutions for small-scale production with a few industry giants providing material for large scale production [221]. The powder-based market in particular is poised to see explosive growth, reaching an estimated \$1.1B

market by 2024 [222]. Aluminum based manufacturing in particular is expected to grow 27% in this time period. McKinsey Co. cites high-performing metal powders as one of the biggest opportunities in this sector [223].

In order for AM products to be accepted into the marketplace, they need to be produced through advanced quality control processes, which enable desired performance, in terms of repeatability, reproducibility, reliability and preciseness [224]. Stringent requirements and high precision parts are indicative of many applications associated with the aerospace and automotive industries [225].

However, there is a lack of research and development currently available in open literature, regarding feedstock powders, which are critical for AM processes. There is not a complete fundamental understanding of these powders and their effects on the bulk properties of AM materials. The engineering, production, packaging, storage and handling of AM powders is an open area of research. Quality control is of utmost importance as even slight variations in powder morphology, size and uniformity can have a significant effect on final properties. Cold spray is especially sensitive to these variables because it is a solid state process. Segregation of elements and phase changes, due to differences in cooling rates or heat treatment, as well as, microstructural features such as phases, grain size, dendrites and precipitates can all have an effect.

The results from this research are being used for the development of specialized packaging of AM powders that can be economically transitioned into the industrial base. Specifically, the means to package aluminum cold spray powders that inhibit water adsorption and air infiltration have been developed as a commercial commodity for the powder industry with companies including Valimet, CA and Solvus Global, MA. The concept is to introduce powders that are properly conditioned, classified and packaged in moisture-proof bags filled with an inert gas, that can be subsequently fed into powder feeders during additive manufacturing (i.e. laser or electron beam) and/or industrial coating processes (i.e. thermal and cold spray), without exposure to ambient conditions (Figure 120). Metal containers will be filled with individual bags of powder, along with desiccant as an added protection during shipment and until final use.

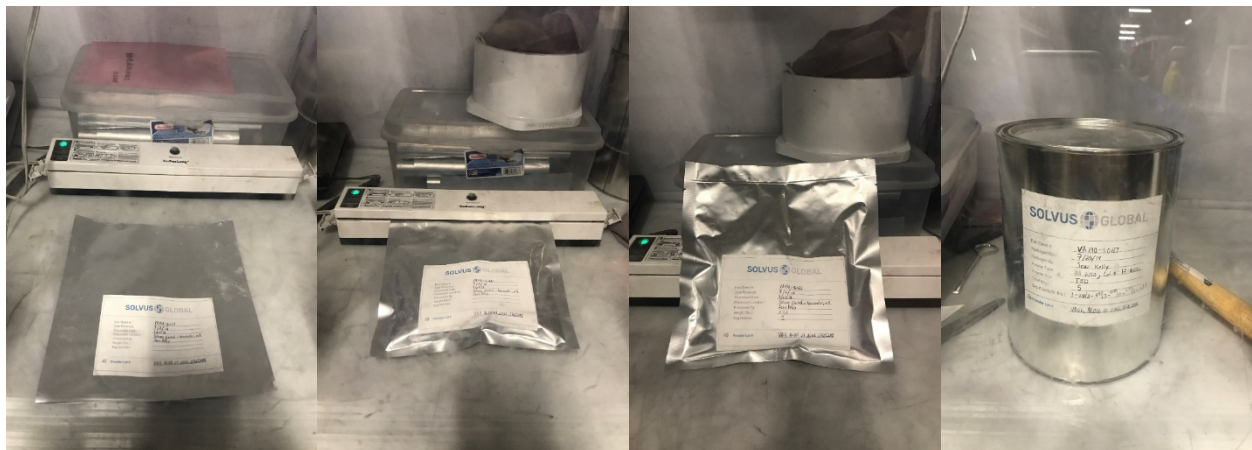


Figure 120. Proposed concept to protect aluminum powder after gas atomization. Bags shown contain 6061 Al provided by Solvus Global.

9.0 References

1. Lee, J.-H., Loya, P., Lou, J. & Thomas, E. L. Dynamic mechanical behavior of multilayer graphene via supersonic projectile penetration. *Science* 346, 1092–1096 (2014).
2. Jae-Hwang Lee, W. Xie, A. A. Dehkharghani, Q. Chen, V. Champagne, et al., “Dynamics and extreme plasticity of metallic microparticles in supersonic collisions”, *Nature Comm.*(2017).
3. Rabin, B.H., Wright, R.N., Flinn, J.E., Adams, J.B., “TEM observations on the microstructure of an atomized high-purity aluminium powder”, *Journal of Materials Science Letters*, Volume 8, Issue 12, December 1989, Pages 1408-1411
4. Pickens, J.R., “Aluminium powder metallurgy technology for high-strength applications”, *Journal of Materials Science* (1981) Vol.16, Issue 6, pp 1437–1457.
5. A.O. Tokarev, “Structure of Aluminum Powder Coatings Prepared by Cold Gas-dynamic Spraying”, *Met. Sci. Heat Treat.*, 1996, 38(3-4), p 136-139
6. T.H. Van Steenkiste, J.R. Smith, and R.E. Teets, “Aluminum Coatings via Kinetic Spray with Relatively Large Powder Particles”, *Surf. Coat. Technol.*, 2002, 154(2-3), p 237-252.
7. S. Yin, X.F. Wang, W.Y. Li, H.L. Liao, and H.E. Jie, Deformation Behavior of the Oxide Film on the Surface of Cold Sprayed Powder Particle, *Appl. Surf. Sci.*, 2012, 259, p 294-300.
8. K.H. Kim, M. Watanabe, and S. Kuroda, “Bonding Mechanisms of Thermally Softened Metallic Powder Particles and Substrates Impacted at High Velocity”, *Surf. Coat. Technol.*, 2010, 204(14), p.2175-2180.
9. M. Fukumoto, M. Mashiko, M. Yamada, and E. Yamaguchi, “Deposition Behavior of Copper Fine Particles onto Flat Substrate Surface in Cold Spraying”, *J. Therm. Spray Technol.*, 2007, 19(1), p.89-94.
10. C.J. Li, H.T. Wang, Q. Zhang, G.J. Yang, W.Y. Li, and H.L. Liao, “Influence of Spray Materials and Their Surface Oxidation on the Critical Velocity in Cold Spraying”, *J. Therm. Spray Technol.*, 2010, 19(1–2), p 95-101.
11. K. Kang, S. Yoon, Y. Ji, and C. Lee, “Oxidation Dependency of Critical Velocity for Aluminum Feedstock Deposition in Kinetic Spraying Process”, *Mater. Sci. Eng., A*, 2008, 486(1–2), p 300-307.
12. ASM Handbook, Volume 7: Powder Metal Technologies and Applications P.W. Lee, Y. Trudel, R. Iacocca, R.M. German, B.L. Ferguson, W.B. Eisen, K. Moyer, D. Madan, and H. Sanderow, editors, (1998) p 834-839.
13. F.R. Billman, J.C. Kuli, Jr., G.J. Hildeman, J.I. Petit, and J.A. Walker, "Processing of

P/M Aluminum Alloys X7090 and X7091," Rapid Solidification Processing: Principles and Technologies III, ed. R. Mehrabian, National Bureau of Standards, Wash.D.C., 1983, pp. 532-546.

14. Dong H, Zhumei S. "Study of the fast reaction characteristics of aluminized PETN explosive powders", Combust Flame. 1996;105:428–30.

15. King MK. "Aluminum combustion in a solid rocket motor environment", Proc Combust Inst. 2009;32(2):2107–14.

16. Ba SH, Jiao QJ, Ren H. "Effect of particle sizes of aluminum powder on radiation intensity of flash pyrotechnic composites", Hanneng Cailiao/Chin J Energ Mater. 2008;16:219–21.

17. Price EW. "Combustion of aluminum in solid propellant flames", AGARD Conf Proc. 1979;14(1–14):15.

18. Price EW. "Combustion of metallized propellants", vol. 90. New York: AIAA; 1984. p. 479–513.

19. Chakravarthy SR, Freeman JM, Price EW, Sigman RK. "Combustion of propellants with ammonium dinitramide", Propellants Explos Pyrotech. 2004;29:220–30.

20. IMARC, "Aluminum Powder Market: Global Industry Trends, Share, Size, Growth, Opportunity and Forecast 2018-2023", <https://www.imarcgroup.com/aluminium-powder-manufacturing-plant>.

21. Flumerfelt, Joel Fredrick, "Aluminum powder metallurgy processing", (1998). Retrospective Theses and Dissertations. 11918. <http://lib.dr.iastate.edu/rtd/11918>.

22. Total Materia , "Sintered Aluminum Powder (SAP)", June 2003, <http://www.totalmateria.com/page.aspx?ID=CheckArticle&site=ktn&NM=76>

23. Jinwang Li, Masaru Nakamura, Takashi Shirai, Koji Matsumaru, Chanel Ishizaki and Kozo Ishizaki , "Advances in Technology of Materials and Materials Processing", 7[1] (2005) 37-42.

24. Metal Nanopowders: Production, Characterization, and Energetic Applications, edited by Alexander A. Gromov, and Ulrich Teipel, John Wiley & Sons, Inc. 2014. "Reaction of Aluminum Powders with Liquid Water and Steam", Larichev M.ikhail Nikolaevich.

25. K.H. Kim, W.Y. Li, and X.P. Guo, "Detection of Oxygen at the Interface and Its Effect on Strain, Stress, and Temperature at the Interface Between Cold Sprayed Aluminum and Steel Substrate", Appl. Surf. Sci., 2015, 357, p 1720-1726

26. W.Y. Li, H.L. Liao, C.J. Li, H.S. Bang, and C. Coddet, "Numerical Simulation of Deformation Behavior of Al Particles Impacting on Al Substrate and Effect of Surface Oxide Films on Interfacial Bonding in Cold Spraying", Appl. Surf. Sci., 2007, 253(11), p 5084-509.

27. JA Slotwinski, EJ Garboczi, PE Stutzman, CF Ferraris, SS Watson, and MA Peltz, "Characterization of Metal Powders Used for Additive Manufacturing", *J Res Natl Inst Stand Technol.* 2014; 119: 460–493.
28. H. Assadi, F. Gärtner, T. Stoltenhoff, and H. Kreye, Bonding Mechanism in Cold Gas Spraying, *Acta Mater.*, 2003, 51(15), p 4379-4394.
29. M. Grujicic, C.L. Zhao, W.S. DeRosset, and D. Helfrich, "Adiabatic Shear Instability Based Mechanism for Particles/Substrate Bonding in the Cold-Gas Dynamic Spray Process", *Materials and Design*, 25 (2004) 681–688.
30. R.C. Dykhuizen, M.F. Smith, D.L. Gilmore, R.A. Neiser, X. Jiang, and S. Sampath, "Impact of High Velocity Cold Spray Particles", *JTTEE5* 8:559-564, 12 May 1999.
31. M. Qian, "Metal Powder for Additive Manufacturing", *The Minerals, Metals & Materials Society, JOM*, Vol. 67, No. 3, Feb. 2015, DOI: 10.1007/s11837-015-1321-z.
32. Jun Hao Tan, Wai Leong Eugene Wong, Kenneth W. Dalgarno, "An overview of powder granulometry on feedstock and part performance in the selective laser melting process", *Additive Manufacturing* 18 (2017) 228–255.
33. J. Dawes, R. Bowerman and R. Trepleton, " Introduction to the Additive Manufacturing Powder Metallurgy Supply Chain", *Johnson Matthey Technol. Rev.*, 2015, **59**, (3), 243–256.
34. D.D. Gu, W. Meiners, K. Wissenbach, R. Poprawe, "Laser additive manufacturing of metallic components: materials, processes and mechanisms", *Int. Mater. Rev.* 57 (2012) 133–164, <http://dx.doi.org/10.1179/1743280411Y.0000000014>.
35. Champagne V, editor. "The Cold Spray Materials Deposition Process: Fundamentals & Applications", Woodhead Publishing Limited, Abington Hall, Cambridge CB21 6AH, England, 2007, p.57 and 132.
36. J.E. Williams, Jr., "Production of Aluminum Powder," *ASM Metals Handbook*", 9th ed.. Vol. 7, American Society for Metals, Metals Park, OH, 1984, pp. 125-130.
37. Zygmunt, Angelika & Gańczyk-Specjalska, Katarzyna & Kasztankiewicz, Anna & Cieślak, Katarzyna & Gołofit, Tomasz. (2017). Application and properties of aluminum in primary and secondary explosives. *Journal of Elementology*. 22. 747-756. 10.5601/jelem.2016.21.3.1073.
- [38] Urbonavicius, Marius, Varnagiris, Sarunas, Milcius, Darius "Generation of Hydrogen through the Reaction between Plasma-Modified Aluminum and Water", *Energy Technology*, 10 Oct 2017, DOI: 10.1002/ente.201700344
39. Valimet Certification of Compliance for HP-Al (9-40 µm dia.)-Batch No. 07-80658.

40. Henan Yuanyang Aluminum Industry Company, Materials Data for HP-Al FLP12, <http://en.hnyyly.com/product/Aluminum-powder-for-pigment.html#S2>
41. V. G. Gopienko, V.P. Kiselev, and N.S. Zobinca, “Methods of Manufacture of Aluminum Powders”, All-Union Scientific-Research and Design Institute of the Aluminum, Magnesium, and Electrode Industry, Translated from Poroshkovaya Metallurgiya, No. 12(264), pgs.32-37 Dec. 1984.
42. J. Davis, editor, “Aluminum and Aluminum Alloys”, ASM International, 1993 - Technology & Engineering, pg. 275.
43. D. Carlson and R. Hoglund, “Particle Drag and Heat Transfer in Rocket Nozzles”, *AIAA Journal*, Vol 2 (No. 11), 1964, pp. 1980 -1984.
44. F.S. Billig, “Shock-Wave Shapes around Spherical and Cylindrical-Nosed Bodies”, *J. Spacecraft*, Vol. 4(No. 5), 1967, pp. 822 - 823.
45. D. Helfritch and V. Champagne, “Optimal Particle Size for the Cold Spray Process”, ITSC 2006, Conference Proceedings.
46. Z.Y. Deng, L.L. Zhu, Y.B. Tang, Y. Sakka, J. Ye, R.J. Xie, Role of particle sizes in hydrogen generation by the reaction of Al with water, *Journal of the American Ceramic Society* 93 (2010) 2998-3001.
47. D.J. Steinberg, S.G. Cochran, and M.W. Guinan, A Constitutive Model for Metals Applicable at High Strain Rate, *J. Appl. Phys.*, Vol 51, 1980, p 1498.
48. E.S. Hertel, R.L. Bell, M.G. Elrick, A.V. Farnsworth, G.I. Kerley, J.M. McGlaun, S.V. Petney, S.A. Silling, and L. Yarrington, Lance CTH: A Software Family for Multi-Dimensional Shock Physics Analysis, *Shock Waves at Marseille*, Vol 1, R. Brun and L.Z. Dumitrescu, Ed., Springer-Verlag, 1995, p 377-382.
49. M. Grujicic, C.L. Zhao, W.S. DeRosset, and D. Helfritch, “Adiabatic Shear Instability Based Mechanism for Particles/Substrate Bonding in the Cold-Gas Dynamic Spray Process”, *Materials and Design*, 25 (2004) 681–688.
50. T. Schmidt, F. Gärtner, H. Assadi, H. Kreye, “Development of a generalized parameter window for cold spray deposition”, *Acta Mater.* 54 (2006) 729–742.
51. W.-Y. Li, H.L. Liao, C.-J. Li, G. Li, C. Coddet, X.F. Wang, *Applied Surface Science*, 253 (2006) 2852–2862.
52. Wen-Ya Li, Hanlin Liao, Chang-Jiu Li, Hee-Seon Bang, and C. Coddet, “Numerical simulation of deformation behavior of Al particles impacting on Al substrate and effect of surface oxide films on interfacial bonding in cold spraying”, *Applied Surface Science* 253 (2007) 5084–5091.

53. M. Gangaraj, D. Veysset, K. Nelson, and C. Schuh, “In-situ observations of single micro-particle impact bonding”, *Scripta Materialia* 145 (2017) 9–13.
54. H. Assadi, F. Gartner, T. Stoltenhoff, and H. Kreye, Bonding Mechanism in Cold Gas Spraying, *Acta Mater.*, 2003, 51(15), p 4379-4394.
55. Alkhimov AP, Kosareve VF, Papyrin AN. Dokl Akad Nauk SSSR 1990;315:1062.
56. McCune RC, Papyrin AN, Hall JN, Riggs II WL, Zajchowski PH. An exploration of the cold-gas-dynamic spray method for several materials systems. In: Berndt CC, Sampath S, editors. *Advances in thermal spray science and technology*. Materials Park (OH): ASM International; 1995. p. 1-1.
57. M. Grujicic, J.R. Saylor, D.E. Beasley, W.S. DeRosset, and D. Helfritsch, Computational Analysis of the Interfacial Bonding Between Feed-Powder Particles and the Substrate in the Cold-Gas Dynamic-Spray Process, *Appl. Surf. Sci.*, 2003, 219(3-4), p 211-227
58. C.-J. Li, W.-Y. Li, H.L. Liao, *J. Thermal Spray Technology* 15 (2006) 212–222.
59. C.-J. Li, H.-T. Wang, Q. Zhang, G.-J. Yang, W.-Y. Li, and H.L. Liao, “Influence of Spray Materials and Their Surface Oxidation on the Critical Velocity in Cold Spraying”, *Journal of Thermal Spray Technology*, Vol.19 (1-2) Jan. 2010, pgs. 95-101.
60. D.L. Gilmore, R.C. Dykhuizen, R.A. Neiser, T.J. Roemer, and M.F. Smith, “Particle Velocity and Deposition Efficiency”, in the *Cold Spray Process*, *J. Therm. Spray Technol.*, 1999, 8(4), p 576-582.
61. T.H. Van Steenkiste, J.R. Smith, R.E. Teets, J.J. Moleski, D.W. Gorkiewicz, R.P. Tison, D.R. Marantz, K.A. Kowalsky, W.L. Riggs, P.H. Zajchowski, B. Pilsner, R.C. McCune, and K.J. Barnett, *Kinetic Spray Coatings, Surf. Coat. Technol.*, 1999, 111(1), p 62-71
62. F. Gartner, T. Stoltenhoff, T. Schmidt, and H. Kreye, *The Cold Spray Process and Its Potential for Industrial Applications*, *Thermal Spray Connects: Explore Its Surfacing Potential*, E. Lugscheider, Ed., May 2-4, 2005 (Basel, Switzerland), DVS Deutscher Verband für Schweißen, 2005, p 158-163.
63. Wen-Ya Li, Chang-Jiu Li, Hanlin Liao, “Significant influence of particle surface oxidation on deposition efficiency, interface microstructure and adhesive strength of cold-sprayed copper coatings,” *Applied Surface Science* 256 (2010) 4953–4958.
64. Shuo Yin, Xiaofang Wang, Wenya Li, Hanlin Liao, Hongen Jie, “Deformation behavior of the oxide film on the surface of cold sprayed powder particle,” *Applied Surface Science* 259 (2012) 294–300.
65. K. Balani, A. Agarwal, S. Seal, J. Karthikeyan, *Scripta Materialia* 53 (2005) 845–850.

66. K. Kim, M. Watanabe, S. Kuroda, *Surface and Coatings Technology* 204 (2010) 2175–2180.
67. R.C. McCunne, W.T. Donlon, O.O. Popoola, E.L. Cartwright, *Journal of Thermal Spray Technology* 9 (2010) 73–82.
68. C. Borchers, F. Gärtner, T. Stoltenhoff, H. Assadi, H. Kreye, *Journal of Applied Physics* 93 (2003) 10064–10070.
69. Kicheol Kang, Sanghoon Yoon, Youlgwun Ji, Changhee Lee, “Oxidation dependency of critical velocity for aluminum feedstock deposition in kinetic spraying process,” *Materials Science and Engineering A* 486 (2008) 300–307.
70. Papyrin A. *Cold Spray Technology. Advanced Materials & Processes*, Sep. 2001, p. 49.
71. Van Steenkiste TH. *Kinetic Spray Coatings. Surface & Coatings Tech.*, 1999, 111, p. 62.
72. Stoltenhoff T, Kreye H, Richter H. *An Analysis of the Cold Spray Process and Its Coatings. Journal of Thermal Spray Technology*, 2002, Vol. 11(4), p. 542.
73. A. Moridi, S. M. Hassani-Gangaraj, M. Guagliano and M. Dao. *Cold Spray Coating: Review of Material Systems and Future Perspectives. Surface Engineering*, March 2014 VOL 36 NO 6, pgs. 369-395.
74. Dillon T, Champagne V, Trexler M, *Consolidation of Magnesium Alloys Using Cold Spray, PowderMet 2012 Conf.*, June 10–13, Nashville, Tennessee.
75. Ajdelsztajn L, *Cold Spray and GE Technology*, <http://www.geglobalresearch.com/blog/cold-spray-ge-technology>, GE Global Research 2013.11.07.
76. Dykhuisen R, Smith M. *Gas Dynamic Principles of Cold Spray. Journal of Thermal Spray Technology*, 1998, 7(2), p. 205.
77. Kosarev VF, Klinkov SV, Alkhimov AP, Papyrin AN. *On Some Aspects of Gas Dynamic Principles of Cold Spray Process. Journal of Thermal Spray Tech.*, 2003, Vol. 12(2), p. 265.
78. Grujicic M, Zhao CL, Tong C, DeRosset WS, Helfritsch D. *Analysis of the Impact Velocity of Powder Particles in the Cold-Gas Dynamic-Spray Process. Materials Science and Engineering A368*, 2004, p. 222.
79. Editors: Rhys Jones A.A. Baker Neil Matthews V K Champagne “*Aircraft Sustainment and Repair*”, Butterworth-Heinemann, December 2017.
80. S.V. Klinkov, V.F. Kosarev, “*Measurements of Cold Spray Deposition Efficiency*”, *Journal of Thermal Spray Technology*, (2006) 364.

81. Champagne V, Helfritch D, Dinavahi S, and Leyman P. Theoretical and Experimental Particle Velocity in Cold Spray, *Journal of Thermal Spray Technology*, August 6, 2010, DOI: 10.1007/s11666-010-9530-z.
82. D. Helfritch and V. Champagne, “Optimal Particle Size for the Cold Spray Process”, *International Thermal Spray Conference Proceedings*, May 15-18, 2006, Seattle, Washington.
83. T. Yukimasa and S. Takemori, “A Review of Metal Powder Production,” *Metallurgical Review of MMIJ*, 6 (2) (1989), pp. 38–53.
84. M. Hohmann et al., “Modern Systems for Ceramic-Free Powder Production,” *Advances in Powder Metallurgy*, 1 (1992), pp. 27–39.
85. Antony, L.V.M. & Reddy, R.G., “Processes for Production of High-Purity Metal Powders”, *JOM* (2003) 55: 14. <https://doi.org/10.1007/s11837-003-0153-4>
86. Georgios Antipas, “Gas Atomization of Aluminum Melts: Comparison of Analytical Models”, *Metals* **2012**, 2, 202-210; doi: 10.3390/met2020202
87. Dumouchel, C.; Cousin, J.; Triballier, K. Experimental analysis of liquid-gas interface at low weber number: Interface length and fractal dimension. *Exp. Fluids* 2005, 39, 651–666.
88. Kim, M.; Jones, H. Effect of process variables in gas-jet atomization and production of multilayer deposits. In *Proceedings of the 4th International Conference on Rapidly Quenched Metal*, Sendi, Japan, 22–24 August 1988.
89. Hiroyasu, H.; Shimizu, M.; Arai, M. The breakup of a high speed jet in a high pressure gaseous atmosphere. In *Proceedings of the 2nd International Conference on Liquid Atomization and Spray Systems*, Madison, WI, USA, 20–24 June 1982.
90. Pai, B.; Nijaguna, B. The charecterization of sprays. In *Proceedings of the 2nd International Conference on Liquid Atomization and Spray Systems*, Madison, WI, USA, 20–24 June 1982.
91. A. Unal, *Material Science. Technol.* **3**, 1029 (1987).
92. C. Roberts, D.Bourell, T.Watt, J. Cohen, “A Novel Processing Approach for Additive Manufacturing of Commercial Aluminum Alloys”, *Physics Procedia*, Volume 83, 2016, Pages 909-917.
93. J. L. Estrada, J. Duszcyk and B. M. Korevaar, *Mater. Sci.* 26 (1991) 1431.
94. S. D. Kirchoff, J. Y. Adkins, W. M. Griffith and A. Martoorell, “Rapidly Solidified Powder Aluminum Alloy”, ASTM STP 890. edited by M. E. Fine and E A. Starke (American Society for Testing and Materials. Philadelphia. PA. 1986) p. 354.

95. L. Kowalski, B. M. Korevaar, J. Duszcyk, "Some new aspects of the theory of oxidation and degassing of aluminum-based alloy powders," *Journal of Materials Science* 27 (1992) 2770-2780.
96. B. E. Hayden, W. W. Yrobisch, W. Opperman, Hachi Cha, P. Hofmann and A. M. Bradshaw, *Surface Science*. 109 (1981) 221.
97. L. Nyborg and I. Ole Qord, "Surface Analysis of Air Exposed Rapidly Solidified Aluminium Powder," *Powder Metallurgy*, Vol. 36, No. 3, 1993, pp. 193-197.
98. T. J. Carney, P. Tsakirooulos, J. F. Watts, and J. E. Castle, *J. Rapid Solid.* 5(1990) 189.
99. A. L. Litvintsev and L.A. Arbuzova, *Poroskhvoaya Mrtallurliya* 49 (1967) I.
100. Hongqi Nie, Mirko Schoenitz, Edward L. Dreizin, "Initial stages of oxidation of aluminum powder in oxygen", *J Therm Anal Calorim* (2016) 125:129–141.
101. L. Ackermann, I. Guillemin, R. Lalauze and Pijolat, *High Strength Powder Metallurgy Aluminum Alloys* Ir. edited by G. J. Hildcman and M. J. Koczak (The Metallurgical Society or AIME Warrendale. PA, 1986) p. 175.
102. S.O zbilen, A.U nal, and T. Sheppard, *Int. Symp. The Physical Chemistry of Powder Metals Production and Processing* (TMSySt. Mary's, Pittsburgh, PA., 1989).
103. P. Kofstad, *High Temperature Oxidation of Metals* (Wiley, New York, 1966), pp. 22–24.
104. C. J. J. Booker, *Corrosion (Metal Environment Reactions)*, L. L. Shreir, ed. (Newnes-Butterworths, London, 1977), p. 1.
105. J. Benard, *ASM Book*, p. 1 (1971).
106. H. H. Uhlig, *Corros. Sci.* 7, 325 (1976).
107. S. Ozbilen, A. Unal, and T. Sheppard, "Influence of Atomizing Gases on the Oxide-Film Morphology and Thickness of Aluminum Powders", *Oxidation of Metals*, Vol. 53, Nos. 1/2, 2000.
108. J V. Champagne Jr, D. Kaplowitz, V. Champagne III, C. Howe, M. West, B. McNally & M. Rokni, "Dissimilar Metal Joining and Structural Repair of ZE41A-T5 Cast Magnesium by the Cold Spray (CS) Process", *Materials and Manufacturing Processes*, 18 November 2016.
109. Th. Stoltenhoff, F. Zimmermann, "LOXPlate® Coatings for Aluminum Aerospace Components Exposed to High Dynamic Stresses", Praxair Surface Technologies GmbH, Ratingen, Germany.
110. Maev, R; Leshchynsky, V; Papyrin, A. Structure Formation of Ni-based Composite Coatings During Low Pressure Gas Dynamic Spraying. *Proceedings of the 2006 ITSC*, ASM , Seattle, WA, 2006.

111. V. K. Champagne, III.; et al. Joining of cast ZE41A-Mg to wrought 6061 Al by the cold spray process and friction stir welding. *Journal of Thermal Spray Technology* **2016** January, 25 (1), 143–159.
112. N. Bay, “Cold welding Part 2 Characteristics, bonding mechanisms, bond strength”, Metal Construction, August 1986.
113. N.W. Buijs, “Explosive welding of metals in a vacuum environment”, Stainless steel World, March 2010, www.stainless-steel-world.net.
114. W.-Y. Li, C. Zhang, X. Guo, C.-J. Li, H. Liao, C. Coddet, “Study on impact fusion at particle interfaces and its effect on coating microstructure in cold spraying”, *Applied Surface Science* 254 (2007) 517–526.
115. G. Bae, S. Kumar, S. Yoon, K. Kang, H. Na, H.-J. Kim, , and C. Lee "Bonding features associated mechanisms in kinetic sprayed titanium coatings," *Acta Materialia*, vol. 57, pp. 5654-5666, 2009.
116. V.K. Champagne, D. Helfritch, P. Leyman, S.G. Ahl, and B.Klotz, Interface Material Mixing Formed by the Deposition of Copper on Aluminum by means of the Cold Spray Process, *Journal of Thermal Spray Technology*, 2005, 14(3), p 330-334.
117. T. Hussain, D.G. McCartney, P.H. Shipway, and D. Zhang, Bonding Mechanisms in Cold Spraying: The Contributions of Metallurgical and Mechanical Components, *Journal of Thermal Spray Technology* 25 Feb. 2009.
118. A.P. Alkhimov, A.I. Gulidov, V.F. Kosarev, and N.I. Nesterovich, Specific Features of Microparticle Deformation Upon Impact on a Rigid Barrier, *Journal of Applied Mechanics and Technical Physics*, **41**(1), 2000, 204–209.
119. S.V. Klinkov, V.F. Kosarev, “Measurements of Cold Spray Deposition Efficiency”, *Journal of Thermal Spray Technology*, (2006) 364.
120. T. Schmidt, F. Gartner, H. Assadi, and H. Kreye, Development of a Generalized Parameter Window for Cold Spray Deposition, *Acta Mater.*, 2006, 54(3), p 729-742
121. A.P. Alkhimov, A.N.Papyrin, V.F. Kosarev, N.I. Nesterovich, and M.M.Shushpanov, U. S. Patent 5 302 414, *Gas Dynamic Spraying Method for Applying a Coating*, April 12, 1994.
122. R.C. Dykhuizen and M.F. Smith, Gas Dynamic Principles of Cold Spray, *Journal of Thermal Spray Technology*, **7**(2), 1998, 205–212.
123. M.F. Smith, J.E. Brockmann, R.C. Dykhuizen, D.L. Gilmore, R.A. Neiser, and T.J. Roemer, Cold Spray Direct Fabrication – High Rate, Solid State, Material Consolidation, *MRS Symposia Proceedings*, Vol. 542, pp. 65–67, Materials Research Society, Pittsburgh, PA, USA, 1999.

124. A.P. Alkhimov, V.F. Kosarev, and A.N. Papyrin, Gas-Dynamic Spraying, Study of Plane Supersonic Two Phase Jet, *Journal of Applied Mechanics and Technical Physics*, **38**(2), 1997, 176–183.
125. A.P. Alkhimov, V.F. Kosarev, and A.N. Papyrin, Gas-Dynamic Spraying. An Experimental Study of the Spray Process, *Journal of Applied Mechanics and Technical Physics*, **39**(2), 1998, 183–188.
126. H. Kreye and T. Stoltenhoff, Cold Spray-Study of Process and Coating Characteristics, *Thermal Spray: Surface Engineering via Applied Research*, C.C. Berndt (Ed.), ASM International, Materials Park, OH, USA, p. 419, 2000.
127. J. Vicek, H. Huber, H. Voggenreiter, A. F. Scher, E. Lugscheider, H. Hallen, and G. Pache, Kinetic Powder Compaction Applying the Cold Spray Process. A Study On Parameters, *Thermal Spray 2001: New Surfaces for a New Millennium*, C.C. Berndt, K. A. Khor, and E. F. Lugscheider (Eds), ASM International, Materials Park, Ohio, USA, 2001.
128. T.H. Van Steenkiste, J.R. Smith, R.E. Teets, J.J. Moleski, and D. W. Gorkiewicz, U. S. Patent 6 139 913, *Kinetic Spray Coating Method and Apparatus*, October 31, 2000.
129. T. Han, Z.B. Zhao, B. Gillispie, and J.R. Smith, A Fundamental Study of Kinetic Spray Process, *Proceedings of the International Thermal Spray Conference, 2004 Thermal Spray Solutions: Advances in Technology and Application*, Osaka, Japan 2004.
130. F. Garetner, C. Borchers, T. Stoltenhoff, and H. Kreye, Numerical and Microstructural Investigations of the Bonding Mechanisms in Cold Spraying, *Proceedings of the International Thermal Spray Conference, 2003*, Orlando, FL, USA, 2003.
131. T. Van Steenkiste and J.R. Smith, Evaluation of Coatings Produced via Kinetic and Cold Spray Processes, *Journal of Thermal Spray Technology*, **13**(2), 2004, 274–282.
132. A. Elmoursi, T. Van Steenkiste, D. Gorkiewicz, and B. Gillispie, Fracture Study of Aluminum Composite Coatings Produced by the Kinetic Spray Method, *Surface and Coatings Technology*, **194**, 2005, 103–110.
133. A. Moridi, et al, “A hybrid approach to determine critical and erosion velocities in the cold spray process” *Applied Surface Science* **273** (2013) 617– 624
134. C.-J. Li, W.-Y. Li, Y.-Y. Wang, G.-J. Yang, and H. Fukunuma, A Theoretical Model for Prediction of Deposition Efficiency in Cold Spraying, *Thin Solid Films*, 2005, 489, p 79-85
135. N. Papyrin, S. V. Klinkov, and V. F. Kosarev, Modeling of Particle-Substrate Adhesive Interaction Under the Cold Spray Process, *Thermal Spray 2003: Advancing the Science and Applying the Technology*, B.R. Marple and C. Moreau, Ed., May 5-8, 2003(Orlando, FL), ASM International, Vol. 1, 2003, p 27-35.

136. ASM Handbook, Vol. 5A, Thermal Spray Technology R.C. Tucker, Jr., editor, 2013, p. 54.
137. H. Mäkinen, J. Lagerbom, and P. Vuoristo, Adhesion of Cold Sprayed Coatings: Effect of Powder, Substrate, and Heat Treatment, Thermal Spray 2007: Global Coating Solutions, B.R. Marple, M.M. Hyland, Y.-C. Lau, C.-J. Li, R.S. Lima, and G. Montavon, Ed., May 14-16, 2007 (Beijing, China), ASM International, 2007, p 31-36.
138. Jae-Hwang Lee, D. Veysset, J. Singer, M. Retsch, G. Saini¹, T. Pezeril, K.Nelson & E. Thomas, “High strain rate deformation of layered nanocomposites”, Nature Comm. 6 Nov. 2012.
139. Hassani-Gangaraj, Mostafa, et al. "Supersonic Impact of Metallic Micro-particles." *arXiv preprint arXiv:1612.08081* (2016).
140. D. Veysset, A.J. Hsieh, S. Kooi, A.A. Maznev, K.A. Masser, K.A. Nelson, “Dynamics of supersonic microparticle impact on elastomers revealed by real-time multi-frame imaging”, Sci Rep 6 (2016),25577.
141. D. Veysset, A.J. Hsieh, S.E. Kooi, K.A. Nelson, “Molecular influence in high-strain-rate microparticle impact response of poly(urethane urea) elastomers”, Polymer (Guildf). 123 (2017) 30–38.
142. Wanting Xie, Arash Alizadeh-Dehkharghani, Qiyong Chen, Victor K. Champagne, Xuemei Wang, Aaron T. Nardi, Steven Kooi , Sinan Müftü & Jae-Hwang Lee, “Dynamics and extreme plasticity of metallic microparticles in supersonic collisions”, Scientific Reports | 7: 5073 | DOI:10.1038/s41598-017-05104-7, www.nature.com/scientificreports.
143. M.V. Vidaller, A. List, F. Gaertner, T. Klassen, S. Dosta, J.M. Guilemany, J. “Single Impact Bonding of Cold Sprayed Ti-6Al-4V Powders on Different Substrates”, Therm. Spray Technology 24 (2015) 644–658.
144. I. Nault, “Matlab Analysis of the Influence of Contact Time and Strain-rate Proportionality on the Critical Velocity using the ,Grujicic One-Dimensional Model”, US Army Research Laboratory, Oct 2017.
145. P.C. King, C. Busch, T. Kittel-Sherri, M. Jahedi, S. Gulizia, “Interface melding in cold spray titanium particle impact”, Surface & Coatings Technology, 239, (2014) 191–199.
146. B. Crossland, Explosive Welding of Metals and Its Application, Clarendon Press, Oxford, 1982.
147. Papyrin, A.N., Cold spray technology 2007: Elsevier.
148. Li, J.F., Agyakwa, P.A., Johnson, C.M., Zhang, D., Hussain, T., and McCartney, D.G., “Characterization and solderability of cold sprayed Sn-Cu coatings on Al and Cu substrates”, Surface and Coatings Technology, 2010. 204 (9-10): p. 1395-1404.

149. T. Hussain, "Cold Spraying of Titanium: A Review of Bonding Mechanisms, Microstructure and Properties", *Key Engineering Materials*, ISSN: 1662-9795, Vol. 533, pp 53-90, 2013 Trans Tech Publications, Switzerland, 27 Dec. 2012.
150. J.E. Field, J.P. Dear, J.E. Ogren, J., "The effects of target compliance on liquid drop impact", *Journal of Applied Physics*, 65 (1989) 533.
151. M. Rein, "Phenomena of liquid drop impact on solid and liquid surfaces", *Fluid Dynamics Research*, 12 (1993) 61–93.
152. H. El-Sobky, "Mechanics of Explosive Welding, Explosive Welding, Forming and Compaction", T.Z. Blazynski, Ed., Applied Science Publishers, London, 1983.
153. Hongqi Nie, Mirko Schoenitz, Edward L. Dreizin, "Initial stages of oxidation of aluminum powder in oxygen", *J Therm Anal Calorim* (2016) 125:129–141.
154. L. Rozic, T. Novakovi, N. Jovanovi, A. Terlecki-Baricevic and Z. Grbavcic, "The Kinetics of the partial dehydration of gibbsite to activated alumina in a reactor for pneumatic transport", *J.Serb. Chem.Soc*, 2001, 66(4), 273-280.
155. S. Engels, U. Bollmann, J. Kobelke, R. Lange, K. Becker, P. Kraak, "Heterogeneous Catalysis", *Proceedings of the 6th International Symposium of Heterogeneous Catalysis*, Publ. House Bulgar.Acad. Sci. Sofia, Part 2 (1987) 351.
156. P. A. Buyanov, O. P. Krivoruchko, B. P. Zolotovskii, *Izv.Acad. Nauk SSSR Ser. Khim.* **11** (1986) 39.
157. LECO Corporation; Saint Joseph, Michigan USA, "Oxygen, Nitrogen, and Hydrogen in Refractory Metals", Form No. 203-821-427 6/18—REV2 © 2018.
158. Dean, John A. (1995). *The Analytical Chemistry Handbook*. New York: McGraw Hill, Inc. pp. 15.1–15.5. *ISBN 0-07-016197-6*.
159. Skoog, Douglas A., F. James Holler and Timothy Nieman (1998). *Principles of Instrumental Analysis* (5 ed.). New York. pp. 805–808. *ISBN 0-03-002078-6*.
160. Sarker, Md Saifur Rahman, et al. "Extraction and characterization of alumina nanopowders from aluminum dross by acid dissolution process." *International Journal of Minerals, Metallurgy, and Materials* 22.4 (2015): 429-436.
161. Baranyai, V. Z., F. Kristály, and I. Szűcs. "Influence of the short time grinding on the thermal decomposition processes of gibbsite produced by the Bayer process." *Materials Science and Engineering* 38.1 (2013).
162. Zhu, Boquan, Binxiang Fang, and Xiangcheng Li. "Dehydration reactions and kinetic parameters of gibbsite." *Ceramics International* 36.8 (2010): 2493-2498.

163. RTI Laboratories, <http://rtilab.com/techniques/ftir-analysis/>, Materials Testing Division 33080 Industrial Road, Livonia, MI 48150.
164. Frost, Ray and Ruan, Huada and Klopogge, Theo (2001) "Comparison of the Raman spectra of Bayerite, Boehmite, Diaspore and Gibbsite", *Journal of Raman Spectroscopy* 32(9):pp. 745-750.
165. Michio Inagaki, Feiyu Kang, Chapter 1 - Introduction, Editor(s): Michio Inagaki, Feiyu Kang, Materials Science and Engineering of Carbon, Butterworth-Heinemann, 2016, Pages 1-6, ISBN 9780128052563.
166. MP Seah, "Summary of ISO/TC 201 Standard: VII ISO 15472 : 2001 — surface chemical analysis — x-ray photoelectron spectrometers — calibration of energy scales", *Surf. Interface Analysis* 31 721-723 (2001).
- [167] Bahr, D. F., Olson, A. L., Morasch, K. R., Kennedy, M. S., Marek, D. R., & Alamr, A. (2003). Fracture in Thin Oxide Films. *MRS Online Proceedings Library Archive*, 795.
- [168] Weppelmann, E., & Swain, M. V. (1996). Investigation of The Stresses and Stress Intensity Factors Responsible for Fracture of Thin Protective Films During Ultra-Micro Indentation Tests with Spherical Indenters. *Thin Solid Films*, 286(1-2), 111-121.
- [169] Minor, A. M., Asif, S. S., Shan, Z., Stach, E. A., Cyrankowski, E., Wyrobek, T. J., & Warren, O. L. (2006). A New View of The Onset of Plasticity During the Nanoindentation Of Aluminium. *Nature Materials*, 5(9), 697.
- [170] Venkataraman, S. K., Kohlstedt, D. L., & Gerberich, W. W. (1993). Continuous Microindentation of Passivating Surfaces. *Journal of Materials Research*, 8(4), 685-688.
- [171] Pharr, George (2018). *Nanoindentation Summer Camp Class Notebook*. Sponsored by Texas A&M University, Nanomechanics, Inc., and the National Science Foundation.
172. Ruslan Zotov, Eugene Meshcheryakov, Alesia Livanova, Tamara Minakova, Oleg Magaev , Lyubov Isupova and Irina Kurzina,* Influence of the Composition, Structure, and Physical and Chemical Properties of Aluminium-Oxide-Based Sorbents on Water Adsorption Ability", *Materials* 2018, 11, 132; doi:10.3390/ma11010132.
173. Alwitt, R. S., The Journal of the Electrochemical Society, Vol. 121 (No. 0), p. 1322, 1974.
174. R.W. Stevenson, "P/M Lightweight Metals," *ASM Metals Handbook*, 9th ed.. Vol. 7, American Society for Metals, Metals Park, OH, 1984, pp. 741-764.
175. Eric N. Coker, "The oxidation of aluminum at high temperature studied by Thermogravimetric Analysis and Differential Scanning Calorimetry", SANDIA REPORT SAND2013-8424 Unlimited Release Printed October 2013.

176. Trunov, M.A., Schoenitz, M. and Dreizin, E.L., **2006**, Effect of polymorphic phase transformations in alumina layer on ignition of aluminium particles. *Combustion Theory and Modelling*, **10(4)**, 603-23
177. Zhang S, Schoenitz M and Dreizin E L 2013 *Combust. Sci. Tech.* **185(9)** 1360-77.
178. Ilyukhina A V, Kravchenko O V and Bulychev B M 2017 *J. Alloy. Comp.* **690** 321-9.
179. Y Liu et al., “Oxidation mechanism of micron-sized aluminum particles in Al-CO₂ gradually heating system”, 2017 IOP Conf. Ser.: Mater. Sci. Eng. **248** 012002.
180. Ingemar Olefjord, Anders Nylund, “Oxidation of aluminium in dry and humid atmosphere studied by ESCA, SEM, SAM and EDX”, Volume 21, Issue 5 May 1994, Pages 290–297.
181. H.B. Peacock, R.L. Sindelar and P.S. Lam, “Temperature and Humidity Effects on the Corrosion of Aluminum-Base Reactor Fuel Cladding Materials during Dry Storage”, Westinghouse Savannah River Co., Aiken, SC (United States). Funding organization: USDOE, Washington, DC (United States), 1995.
182. Milehin J.M., Feldman V.D., Zmanovsky S.V. and etc. Passivation method of fine aluminum powder, RF patent №2407610, 27.12.2010.
183. Sergey V. Zmanovskiy, Alexander M. Gromov, Valentina V. Smirnova, Vadim F. Petrunin, Jin-Chun Kim, “Thermal and Chemical Stability of Micron Aluminum Powders subjected to Gaseous Water”, *Key Engineering Materials*, 2016 *Trans Tech Publications, Switzerland*, ISSN: 1662-9795, Vol. 712, pp 241-24.
184. Cook, Melvin A.; *The Science of High Explosives*; American Chemical Society Monograph No. 139, Van Nostrand Reinhold Co., NY; 1958; pg. 304.
185. Meng Li, De-Gang Xie, Evan Ma, Ju Li, Xi-Xiang Zhang, and Zhi-Wei Shan, “Effect of Hydrogen on the integrity of aluminium–oxide interface at elevated temperatures”, *Nature Communication*, 2017; 8: 14564. 2017 Feb 20. doi: 10.1038/ncomms14564.
186. Toda H. et al., “Growth behavior of hydrogen micropores in aluminum alloys during high-temperature exposure”, *Acta Mater.* **57**, 2277–2290 (2009).
187. Rozenak, P. Hemispherical bubbles growth on electrochemically charged aluminum with hydrogen. *Int. J. Hydrog. Energy* **32**, 2816_2823 (2007).
188. Scamans, G. M. & Rehal, A. S. Electron metallography of the aluminium-water vapour reaction and its relevance to stress-corrosion susceptibility. *J. Mater. Sci.* **14**, 2459_2470 (1979).
189. Degassing behavior of Nanostructured aluminum and its composites, *Metallurgical and Materials Transactions A*, Volume 41A P533, Feb 2012

190. Guido Busca, "The surface of transition aluminas: A critical review", *Catalysis Today*, 2014, 226, 2-13.
191. I. Levin, D. Brandon, *J. Am. Ceram. Soc.* 81 (1998) 1995–2012
192. Cubic to monoclinic phase transformations in alumina, *Acta Mater*, 45, 1997, 9, 3659-3669
193. J. VAN DIJK, "The formation and thermal decomposition of aluminium hydroxide doped with Fe(III) and Cr(III)", PhD Thesis, 1976.
194. K. Wefers and G.M.Bell, "Alcoa Technical Paper No. 19", (1972).
195. <http://www.horiba.com/scientific/products/x-ray-fluorescence-analysis/tutorial/penetration-depths/>
196. Nam-Trung Nguyen, "Micromixers; Fundamentals, Design and Fabrication", William Andrew Publishing, ISBN 9781437735208, 2nd Edition, 2012.
197. ASM Engineered Materials Handbook Desk Edition (Online), Thermal Analysis and Properties of Polymers, Differential Scanning Calorimetry
198. $\text{Al}(\text{OH})_3 \rightarrow \text{Al}_2\text{O}_3 + 3\text{H}_2\text{O}$. The thermal decomposition of aluminum hydroxide to produce aluminum oxide and water. This reaction takes place at a temperature of over 575°C.
199. Takashi Shirai, Hideo Watanabe, Masayoshi Fuji and Minoru Takahashi, "Structural Properties and Surface Characteristics on Aluminum Oxide Powders", Ceramics Research Laboratory, Nagoya Institute of Technology Hon-machi 3-101-1, Tajimi, Gifu 507-0033, JAPAN, セラミックス基盤工学研究センター年報 (2009). Vol. 9, 23-31
200. Du, Xuelian, et al. "Thermal decomposition of grinding activated bayerite." *Materials Research Bulletin* 44.3 (2009): 660-665.
201. Jinwang Li, Masaru Nakamura, Takashi Shirai, Koji Matsumaru, Chanel Ishizaki and Kozo Ishizaki, "Mechanism and Kinetics of Aluminum Nitride Powder Degradation in Moist Air", *Journal of the American Ceramic Society*, Vol.89, Issue 3, March 2006, Pages 937-943.
202. A. Abid, R. Bensalem, and B. J. Sealy, "The Thermal Stability of Aluminum Nitride," *J. Mater. Sci.*, 21, 1301–4 (1986).
203. Y. Kameshima, S. Kuramochi, A. Yasumori, and K. Okada, "Analysis of Surface State and Stability During Storage of AlN Powders by X-Ray Photoelec-tron Spectroscopy," *J. Ceram. Soc. Jpn.*, 106, 749–53 (1998).

- 204 Mathieu Digne, Philippe Sautet, Pascal Raybaud,§ Herve' Toulhoat, and Emilio Artacho, "Structure and Stability of Aluminum Hydroxides: A Theoretical Study", *J. Phys. Chem. B* 2002, 106, 5155-5162.
205. Rothbauer, R.; Zigan, F.; Daniel, H. O. *Z. Kristallogr.* **1967**, 125, 317.
206. Saafeld, H.; Weede, M. *Z. Kristallogr.* "Refinement of the crystal structure of gibbsite, $\text{Al}(\text{OH})_3$ ", 1974, 139, 129. DOI: <https://doi.org/10.1524/zkri.1974.139.1-2.129>
207. Zigan, F.; Joswig, W.; Burger, N. *Z. Kristallogr.* "Advances in Catalysis, Volume 57", 1978, 148, 255.
208. Hill, R. , "Hydrogen Bond Research", *J. Phys. Chem. Miner.*, 1979, 5, 179.
209. Christensen, A. N.; Lehmann, M. S.; Convert, P. "Deuteration of Crystalline Hydroxides. Hydrogen Bonds of $\gamma\text{-AlOO}(\text{H,D})$ and $\gamma\text{-FeOO}(\text{H,D})$ ", *Acta Chem. Scand.* 1982, 36, 303.
210. Corbato', C. E.; Tettenhorst, R. T.; Christoph, G. G. *Clays Clay Miner.* 1985, 33, 71.
211. Farmer, V. *Spectrochim. Acta* 1980, 36A, 585.
212. Kiss, A. B.; Keresztury, G.; Farkas, L. , "Raman and IR spectra and structure of boehmite ($\gamma\text{-AlOOH}$). Evidence for the recently discarded D^{17}_{2h} space group", *Spectrochimica Acta Part A: Molecular Spectroscopy*, Volume 36, Issue 7, 1980, Pages 653-658.
213. Yong Liu, Bo Cheng, Kang-Kai Wang, Guo-Ping Ling, Jun Cai, Chen-Lu Song, and Gao-Rong Han, "Study of Raman spectra for $\gamma\text{-Al}_2\text{O}_3$ models by using first-principles method", *Solid State Communications*, Volume 178, January 2014, Pages 16-22.
214. Slade, R. C. T.; Halstead, T. K. *J. Solid State Chem.* 1980, 32, 119.
215. L.H. Ni, Y. Liu, Z.H. Ren, X. Li, G. Xu, C.L. Song, G.R. Han, *Journal of Applied Physics*, 110 (2011), p. 063506.
216. Yantong Wang, Kaili Xu and Li Li, "Inhibition of the reaction between aluminum dust and water based on the HIM", *RSC Adv.*, 2017, 7, 33327.
217. Z. Y. Deng, J. M. F. Ferreira, Y. Tanaka & J. Ye, *J. Am. Ceram. Soc.*, 2007, 90, 1521–1526.
218. Z. Y. Deng, Y. B. Tang, L. L. Zhu, Y. Sakka and J. Ye, *Int. J. Hydrogen Energy*, 2010, 35, 9561–9568.
219. Z. Y. Deng, J. M. F. Ferreira and Y. Sakka, *J. Am. Ceram. Soc.*, 2008, 91, 3825–3834.
220. W. Z. Gai and Z. Y. Deng, *Int. J. Hydrogen Energy*, 2014, 39, 13491–13497.

221. 360 Research Team, Global Additive Manufacturing Market, Forecast to 2025, 2016.
222. The Market for Additive Manufacturing with Metal Powders to Surpass \$1.1B by 2024, 2018.
223. A. Chalabyan, E. Jansch, T. Niemann, T. Otto, B. Zeumer, K. Zhuravleva, How 3-D printing will transform the metals industry, 2017.
224. Hoejin Kim, Yirong Lin, Tzu-Liang Bill Tseng, (2018) "A review on quality control in additive manufacturing", Rapid Prototyping Journal, Vol. 24 Issue: 3, pp.645-669, <https://doi.org/10.1108/RPJ-03-2017-0048>
225. Wong, K.V. and Hernandez, A. (2012), "A review of additive manufacturing", ISRN Mechanical Engineering, Vol. 2012, No. 2012.

10.0 Relevant Papers and Presentations

10.1 Published Papers (refereed journals)

1. Mostafa Hassani-Gangaraj, David Veysset, Victor K. Champagne, Keith A. Nelson, Christopher A. Schuh, “*Adiabatic shear instability is not necessary for adhesion in cold spray*”, *Acta Materialia*, 158 (2018) 430e439, 30 July 2018.
2. S Suresh, S-W Lee, M. Aindow, HD Brody, VK Champagne and AM Dongare, “*Unraveling the Mesoscale Evolution of Microstructure during Supersonic Impact of Aluminum Powder Particles*”, *NATURE Sci Rep.* **8**: 10075 (2018). [doi: 10.1038/s41598-018-28437-3]
3. V Champagne Jr, D Kaplowitz, VK Champagne III, C Howe, MK West, “*Dissimilar metal joining and structural repair of ZE41A-T5 cast magnesium by the cold spray process*”, *Materials and Manufacturing Processes* 33, 130-139, 2018.
4. Jafarlou, D.M., Champagne, V.K., Krishnamurty, S., and Grosse., I.R. (2018). *Influence of Cold Sprayed CrC-Ni Coating on Fracture Characteristics of Additively Manufactured 15Cr-5Ni Stainless Steel*, *Materials and Design*, 155: 134-147, doi: [10.1016/j.matdes.2018.05.063](https://doi.org/10.1016/j.matdes.2018.05.063)
5. T.B. Bush, Z. Khalkhali, V.K. Champagne, D.P. Schmidt, J.P. Rothstein, *Optimization of cold spray deposition of high-density polyethylene powders*, *J. Therm. Spray Technol.*, 26 (2017) 1548-1564.
6. C. Walde, D. Cote, V. Champagne, R. Sisson, “*Characterizing the Effect of Thermal Processing on Powder Al Alloys for Additive Manufacturing Applications*”, *Journal of Materials Engineering and Performance*, July 2018.
7. MR Rokni, AT Nardi, VK Champagne, SR Nutt, “*Effects of Preprocessing on Multi-Direction Properties of Aluminum Alloy Cold-Spray Deposits*”, *Journal of Thermal Spray Technology*, 27, 818-826, 2018
8. Zahra Khalkhali, Wanting Xie, Victor Champagne, Jae-HwangLee, Jonathan Rothstein, “*A comparison of cold spray technique to single particle micro-ballistic impacts for the deposition of polymer particles on polymer substrates*” *Surface and Coating Technology* 351, pp 99-107 (2018)
9. Anastasios G. Gavrasa, Diana A. Lados, Victor K. Champagne, Robert J. Warren, “*Effects of processing on microstructure evolution and fatigue crack growth mechanisms in cold-spray 6061 aluminum alloy*”, *International Journal of Fatigue* 110 (2018) 49–62.
10. Qiyong Chen, Arash Alizadeh, Wanting Xie, Xuemei Wang, Victor Champagne, Andrew Gouldstone, Jae-Hwang Lee, Sinan Mu, “*High-Strain-Rate Material Behavior and Adiabatic Material Instability in Impact of Micron-Scale Al-6061 Particle*”, *J Thermal Spray Technology*, 5 Jan 2018, pp 641-653, <https://doi.org/10.1007/s11666-018-0712-4>
11. C. Widener, M. Alabi, B. Jasthi, M. Carter, V. Champagne, “*Repair and Corrosion Protection Using High Pressure Cold Spray*,” 2017 DoD Allied Nations Technical Corrosion Conference, Paper 2017-0000, 7-10 August 2017.

12. W. Xie, A. Alizadeh-Dehkharghani, Q. Chen, V. Champagne, X. Wang, A. Nardi, S. Kooi, . Müftü & Jae-Hwang Lee, “*Dynamics and extreme plasticity of metallic microparticles in supersonic collisions,*” NATURE Scientific Reports, 11 July 2017. | 7: 5073 | DOI:10.1038/s41598-017-05104-7.
13. M. R. Rokni, S. R. Nutt, C. A. Widener, V. K. Champagne, R. H. Hrabe, “*Review of Relationship Between Particle Deformation, Coating Microstructure, and Properties in High-Pressure Cold Spray*”, Journal of Thermal Spray Technology, 11 May 2017, DOI 10.1007/s11666-017-0575-0.
14. Davoud M. Jafarlou, Caitlin Walde, Victor K. Champagne, Sundar Krishnamurty, Ian R. Grosse, “*Influence of Cold Sprayed CrC-Ni Coating on Fracture Characteristics of Additively Manufactured 15Cr-5Ni Stainless Steel*”, Materials & Design (IF 4.525) Pub Date : 2018-05-29, DOI: [10.1016/j.matdes.2018.05.063](https://doi.org/10.1016/j.matdes.2018.05.063).

10.2 Publications (other)

1. E. Lin, Q. Chen, O.C. Ozdemir, V.K. Champagne, Jr. and S. Muftu, “*Effects of Interface Bonding on the Residual Stresses in Cold Sprayed Al-6061: A Numerical Investigation*”, Proceedings of the International Thermal Spray Conference. 2018 May 7-10; Orlando, FL. Materials Park: ASM International.
2. M. Hassani-Gangaraj*, D. Veysset, V.K. Champagne, C.A. Schuh “*In-situ Observations of the Bonding Moment in Cold Spray*” International Thermal Spray Conference & Exposition, Orlando FL, USA, May 2018.
3. Pranjal Nautiyal, Cheng Zhang, Victor Champagne, Benjamin Boesl, Arvind Agarwal, In situ Mechanical Investigation of Splat Sliding in Cold Sprayed 6061Al Coatings, Symposium: Characterization and Testing: Mechanical Properties, International Thermal Spray Conference (ITSC 2018), Orlando, FL, May 7-10, 2018.
4. Widener C.A., Champagne, V.K., Jasthi, B.K., Carter, M., and Alabi, M. “Repair and Corrosion Protection Using High Pressure Cold Spray,” DoD Corrosion Conference Proceedings.
5. Champagne, V.K. and Widener, C.A. Invited Keynote: “Emerging Capabilities in High Pressure Cold Spray,” Thermec 2018 and the European Cold Spray Symposium, Paris, FRANCE, July 2018.
6. Jafarlou, D.M., Champagne, V.K. and Grosse, I.R., 2018, March. “*Evaluation of the Mechanical Properties of 15Cr-5Ni Stainless Steel Produced by Direct Metal Laser Sintering*”. In TMS Annual Meeting & Exhibition (pp. 75-84). Springer, Cham. Bioinspired Photocatalytic Shark-Skin Surfaces with Antibacterial and Antifouling Activity via Nanoimprint Lithography-CONFERENCE PROCEEDINGS
7. Lindsay Bjerregaard (V. Champagne interview), “*Cold Is Hot-Cold spray techniques are seeing increased adoption for aircraft structural repairs*”, Aviationweek & Space Technology, July 2018.

8. V. Champagne, “*Cold Spray for Chrome Plating Replacement*,” Products Finishing Magazine, Featured Article, August 2017.
9. BA Bedard, T Flanagan, AT Ernst, A Nardi, AM Dongare, HD Brody, VK Champagne Jr., S-W Lee, and M Aindow, “*Microstructure and Micromechanical Response in Gas-Atomized Al 6061 Alloy Powder and Cold-Sprayed Splats*”, Submitted to: J Therm Spray Technol. 7/2/18-CONFERENCE PROCEEDINGS

10.3 Technical Briefings and Conference Presentations

1. V. Champagne, A. Nardi, “*Cold Spray Coatings for Cr and Ni Replacement*”, ASETS Defense Workshop 2018, Sustainable Surface Engineering for Aerospace and Defense, Denver, CO, 21-23 August 2018.
2. Enqiang Lin, Qiyong Chen, O. Ozdemir, Sinan Müftü, V. Champagne, “*Effects of Interface Bonding on the Residual Stresses in Cold Sprayed Al-6061*”, ITSC2018 Orlando, Florida, 7-10 May 2018.
3. C. Taglienti, Wanting Xie, Victor K. Champagne, Aaron Nardi, Sinan Müftü, and JaeHwang Lee, “*Temperature-dependent Laser-induced Projectile Impact Test of Aluminum 6061 Microspheres for Cold Spray Additive Manufacturing*”, Society of Engineering Science (SES) Annual Meeting / ASME-AMD Joint Conference, Boston, MA (7/25/2017)
4. C. Walde, D.B. Cote, R.D. Sisson, Jr., V. Champagne, Jr., “*Optimization of Solution Treatment Parameters for Aluminum Alloy Powders through the use of Thermal Analysis*,” North American Thermal Analysis Society Conference 2017, Newark, DE, August 7-10, 2017.
5. V. Champagne, “*Advancements in Cold Spray Materials*,” SURFIN, 19-21 June 2017, GA.
6. D. Tsaknopoulos, D.B. Cote, V. Champagne, Jr., R.D. Sisson, Jr., “*Application of Computational Modeling to Trial and Error Minimization for Alloy Optimization*,” Materials Science & Technology Conference, Pittsburgh, October 8-12, 2017.
7. K. Fitzpatrick-Schmidt, D.B. Cote, R.D. Sisson, Jr., V. Champagne, Jr., “*Dissolution of Secondary Phases in Al Alloys Using DICTRA Simulations*,” Materials Science & Technology Conference, Pittsburgh, October 8-12, 2017.
8. C. Walde, D.B. Cote, R.D. Sisson, Jr., V. Champagne, Jr., “*Characterizing the Effect of Thermal Processing on Powder Al Alloys for Additive Manufacturing Applications*,” Materials Science and Technology 2017, Pittsburgh, PA, October 8-12, 2017.

10.4 Book Chapters

1. Publisher: Springer Nature
 Editor: Prof. Dr. Pasquale Cavaliere
 Title of Book: Cold-Spray Coatings - Recent trends and future perspectives
 Title of Chapter: Cold Spray Applications

Authors: Victor K. Champagne, Jr., Victor K. Champagne, III, Dr. Christian Widener
Publication Date: 8 November 2017

2. Publisher: Springer

Editor: Prof. Dr. Pasquale Cavaliere

Title of Book: Cold-Spray Coatings - Recent trends and future perspectives

Title of Chapter: Structure-Properties Relations in High Pressure Cold Spray Deposits

Authors: R. Rokni, S. Nutt, C. Widener, R. Hrabe, C. Crawford, V. Champagne

Publication Date: 8 November 2017

10.5 Books

1. Publisher: Elsevier

Editors: R. Jones, N. Mathews, R. Baker, V. Champagne

Title of Book: Aircraft Sustainment and Repair

Publication Date: 5 December 2017

2. Publisher: Springer

Editors: V. Champagne, D. Helfritsch and O. Ozdimir

Title of Book: Practical Handbook of the Cold Spray Process

Publication Date: Submitting final book chapters September 2018-December 2018

3. Publisher: Taylor & Francis/CRC Press

Editor: Victor Champagne

Title of Book: THESIS: Cold Spray Feedstock Powders for Additive Manufacturing:
Fundamentals and Applications

Publication Date: Submitting final Thesis and supporting chapters Dec. 2018-Jan. 2020

10.6 Patents

1. Title: Reactive Particles for Coating Technologies Christian Widener, Vic Champagne, Matthew Trexler, Dennis Helfritsch, Rob Hrabe, Patent No. CA 2862459 “Cold Spray System and Device”, 8/28/2018 (Patent Granted)
2. Vic Champagne, Jr and Vic Champagne, III, “Method to Join Dissimilar Metals by the Cold Spray Process”, Application No. 14499282, 8/28/2018 (Patent Application).
3. Christian Widener, Vic Champagne, et al., “Method for Cold Spray Repair”, Application No. 14/066,443, 5/3/2018 (Patent Granted).
4. Jim Watkins, David Schmidt, Jacobo Morere Rodriguez, Victor Champagne, “Active Cooling of Cold-Spray Nozzles by Compressed Gas Expansion” (joint w/ Army Research Laboratory) USSN 62/660,368 filed 4/20/2018. (Patent Application)
5. Schiffman, J.D., Klier, J., Champagne, V.K., Yang, G., Huang, M., “Reactive particles for coating technologies.” Application No. PCT/US18/26693, 4/9/2018. (Patent Application)
6. Butler, T., Alberts D., Champagne, V., “Method and Apparatus for Liquid Jet Assisted Cold Spraying”, Attorney Docket No. 86151-003PR4, (Invention Disclosure)

11.0 Acknowledgements

I wish to thank the many colleagues of mine across the country, especially all those at WPI, Bucknell, Penn State, UCONN, UMASS, MIT and UCI who were involved in helping to generate data and those who had taken the time to discuss various aspects of the topic with me at great length. These include but not limited to the following individuals; Dr. Dennis Helfritch, Dr. Isaac Nault and Dr. Jeremy Schreiber for providing information regarding the derivation of the J-C and PTW models and Dr. Nault for performing a MatLab simulation to test the validity of the CIV data reported by Grujicic. Aaron Nardi, Dr. Tim Eden, Dr. Mala Sharma, Dr. Gangaraj, Dr. Jae-Hwang Lee, Derek Tsaknopoulos, Dr. Mark Aindow and Dr. Christian Widener, for debating various topics pertinent to the thesis. Dr. Diran Apelian, Dr. Aaron Birt, Dr. Danielle Cote and Dr. Baillie McNally for their insightful discussions and helpful commentary. Dr. Rick Sisson, my advisor, for guiding and directing me toward the study of the cold spray bonding mechanism. The US Army Research Laboratory for supporting my pursuit of higher education, especially Dr. Jeffery Zabinski and Dr. Mark VanLandingham. Finally, I wish to thank my son who is also pursuing his PhD, for his support and competitiveness, my daughter who is setting the bar by getting straight A's in college, to my wife, who was without a husband during the countless hours of study and composition, particularly during all of the weekends and to the rest of my family who had to endure my temperament and motivation to achieve this goal.

Additional researchers and students who should be recognized for their contributions are: Bryer C. Sousa and Christopher J. Massar from WPI, who performed Dynamic Nanoindentation; Matt Siopis, Anais Espinal, Kerisha Williams and Daniel Goberman from UTRC, who conducted Auger Electron Spectroscopy, X-ray Photoelectron Spectroscopy, heat treatment and exposure tests of the HP-Al powder, cold spray of bulk samples and metallography; Mark Cloutier of L&M Machine, for his precision in machining micro-tensile samples; Swetaparna Mohanty and Wanting Xie of UMASS and Jasper Zebulon Lienhard from MIT, for performing single particle impact experiments; Cameron Crook, Lorenzo Valdevit, Maryam Zahiri Azar, Daniel Mumm, Baolong Zheng, Darryl Mack and Enriquer Lavernia for characterization of the surface films on the powders; Tyler Flanagan, Ben Bedard, and Seok-Woo Lee of UCONN for conducting micro-tensile tests and fractography of the bulk cold spray samples and finally Matthew Dunstan and Clara Hofmeister Mock for performing Inert Gas Fusion to detect hydrogen within the powder.

12.0 Appendix A: List of Tables

Table 1. Summary of Project Goals.....	8
Table 2. Chemical Composition of High Purity Al Powder-Valimet (9-40 μm dia.) [39].....	10
Table 3. Chemical Composition of High Purity Al Powder- FLPG12 (5-25 μm dia.) [40].....	10
Table 4. Stages of the Explosive Welding Process [113].....	26
Table 5. Critical Impact Velocity for Three Pure Metals (Empirical vs. Theoretical).....	32
Table 6. Critical Impact Velocity for Various Metals (Empirical vs. Theoretical) [54].....	33
Table 7. Cold spray process parameters used to generate Figure 20.....	33
Table 8. Heat Treatment of Aluminum HP Powder under dry conditions.....	39
Table 9. Exposure of Aluminum HP Powder under humid conditions.....	39
Table 10. Dehydration of Gibbsite Al (OH) ₃ to alumina [154].....	40
Table 11. Particle Size Distribution.....	47
Table 12. Inert Gas Fusion Measurements of Oxygen of All Seven Groups of Powders.....	49
Table 13. Graphical representation of the measurements from Table 12 for ease in comparison. Bar representing sample RH95% has been truncated to allow the remaining groups to be plotted.	49
Table 14. Summary of Inert Gas Fusion (IGF) Test Apparatus, Methods and Standards.....	50
Table 15. Inert Gas Fusion (IGF) of Calibration Standards.....	50
Table 16. LECO ONH836 Inert Gas Fusion Measurements of Powder AR.....	51
Table 17. LECO ONH836 Inert Gas Fusion Measurements of Powder RH95.....	51
Table 18. Comparison of Inert Gas Fusion Measurements of Powder AR and RH95.....	51
Table 19. Concentration of Elements Detected (in atom%)......	59
Table 20. Nanohardness Measurements of Single Powder Particles Representing all Groups....	75
Table 21. Lowest Speed Bonded Particle vs Highest Speed Rebounding Particle.....	81
Table 22. Lowest Speed Bonded Particle vs Highest Speed Rebounding Particle.....	82
Table 23. Critical velocity ranges for the As-received powder, RH-50% and RH-95%.....	86
Table 24. Critical velocity ranges for the HT-baseline, HT-30, HT-60 and HT-240.....	87
Table 25. Cold Spray Parameters for Producing Bulk Samples from HP-Al Powder.....	89
Table 26. Summary of Conductivity and Hardness of the Cold Spray Bulk Samples.....	91
Table 27. Summary of Mechanical Properties of Bulk Cold Spray HP-Al.....	92
Table 28. Mechanical Test Data of all HP-Al Powder Groups.....	93
Table 29. Particle Diameter and Impact Velocity of bonded HP-Al Powder Particles.....	104
Table 30. Description of the 12 TEM Lift Out Samples Made from Bulk Material.....	105
Table 31. Decomposition of Aluminum Hydroxides [193].....	120

13.0 Appendix B: List of Figures

Figure 1. The morphology of aluminum powders produced by different processes.	11
Figure 2. Cross-section of gas atomized aluminum powder showing spheroidal shape.	11
Figure 3. Deformation characteristics of a spheroidal shaped particle (a) as compared to an acicular shaped particle (b).	12
Figure 4. Effect of oxygen content on CIV of 316L stainless steel powder [59].	15
Figure 5. Schematic of the cold spray bonding process showing the break-up and entrapment of surface oxides and the formation of jetting [63].	16
Figure 6. Simulation of the break-up of the surface oxide layer during cold spray, of an Al 6061-T6 particle, at an impact velocity of 700 m/s.	16
Figure 7. Flattening ratio of deposited aluminum particles with different oxygen content for the same process condition [69].	17
Figure 8. Schematic of the cold spray process.	18
Figure 9. Cold spray model developed by Helfritch et al. [59] to calculate the temperature of the gas as it expands from the nozzle as a function of inlet temperature and pressure.	19
Figure 10. CS is capable of depositing various engineering materials with near theoretical density.	20
Figure 11. Schematic of the gas atomization process for production of AM powders (Courtesy of LPW Technology, UK). [33]	21
Figure 12. Time evolution for aluminum powder oxidation during helium gas atomization with 2.0 volume percent oxygen in the atomization gas [21].	23
Figure 13. Graph of oxygen content of the oxide layer on CP-Al powder as a function of particle diameter and oxide film thickness [21].	24
Figure 14. UFG structures at interface due to high strain rate deformation [108].	25
Figure 15. Types and transitions resulting from explosion welding: (a) laminar, (b) wavy, (c) turbulent.	26
Figure 16. Mechanical interlocking of a Cu coating applied by cold spray onto 6061 AL-T6.	27
Figure 17a. Particle impact and bonding. Figure 17b. Particle impact and rebound.	28
Figure 18. Single particle impact apparatus with micron-scale and nanosecond-level resolution [53].	30
Figure 19. Multi-frame sequences with 5 ns exposure times showing 45- μ m Al particle impacts on Al substrate at 605 m/s (a) and 805 m/s (b), respectively below and above critical velocity. Material jetting is indicated with white arrows [53].	31
Figure 20. Graphical representation of velocity of particles with varying diameters keeping the cold spray parameters constant [144, 82].	34
Figure 21. Schematic showing the major stages of the proposed research.	36
Figure 22. Measured isothermal TG traces of pure aluminum and theoretical calculations using kinetics by Hongqi Nie et al., for respective temperatures [153].	37
Figure 23. Aluminum oxide thickness as a function of temperature for constant heating rates. Thin lines represent measurements; bold lines show calculations. Calculations are based on kinetics derived from isothermal measurements and b constant heating rate measurements [153].	38
Figure 24. Apparatus to perform elevated temperature exposure tests on powder.	40
Figure 25. Apparatus to perform humidity exposure tests on powder.	41

Figure 26. Apparatus to perform short duration temperature exposure test on powder.	42
Figure 27. Appearance of powder after exposure to humid conditions.....	43
Figure 28. Mini-tensile specimen for characterization of bulk cold spray material.	46
Figure 29. Inspection Certificate for High Purity Aluminum Powder from Valimet Inc.....	48
Figure 30. DSC scans of As-received, 50% humidity, and 95% humidity samples. 20°C to 550°C with 10°C/min ramp.....	52
Figure 31. Comparison between oxygen content and associated enthalpies of reaction of the main endothermic peak near 290°C.....	53
Figure 32. DSC scans of RH 95% sample. 20°C to 550°C with 10°C/min ramp.	53
Figure 33. DSC thermogram of aluminum hydroxide taken from published literature [160].....	54
Figure 34. DSC scans of the heat-treated samples (HT). 20°C to 550°C with 10°C/min ramp. Graphs were shifted vertically for easier viewing and comparison.....	55
Figure 35. DSC scans of all runs for comparison purposes. 20°C to 550°C with 10°C/min ramp. Graphs were shifted vertically for easier viewing and comparison.....	56
Figure 36. TGA curves of As-received, 50% humidity, and 95% humidity samples run in nitrogen.	56
Figure 37. “TG and DTG curves of unground or ground and previously not heat treated aluminum hydroxide samples, in the function of temperature. Above: TG, %; below: DTG, mg/min” [161].....	57
Figure 38. FTIR-DRIFTS: Spectra collected under Argon purge at ~30C.....	58
Figure 39. High resolution Al 2p spectra curve fit into Al ⁰ and Al ³⁺	60
Figure 40. TEM of as-received (AR) powder showing surface layer.	61
Figures 41a and b. Higher magnification TEM of as-received powder showing surface film.	61
Figures 42a and b. STEM and EDS mapping of the as-received (AR) powder.	62
Figure 43. TEM of powder sample HT-Baseline showing surface layer.	62
Figures 44a and b. Higher magnification TEM of HT-Baseline powder showing surface film... ..	63
Figures 45a and b. STEM and EDS mapping of the HT-Baseline powder.	63
Figures 46a and b. TEM high resolution (HRTEM) of HT-240 layer approximately 5 nm although much less uniform as compared to AR and remaining HT samples.....	64
Figures 47a and b. HAADF-STEM and EDS mapping of RH50% powder sample.	64
Figure 48. TEM of RH50% showing spikes protruding from the surface layer.....	65
Figure 49. TEM high resolution (HRTEM) of RH95% showing the surface layer to be approximately 6 nm although much less uniform as compared to RH50% and HT-240.	65
Figures 50a and b. STEM and EDS mapping of the RH95% powder sample.....	66
Figure 51. Representative SEM images of all the powder groups except for RH95%.....	66
Figure 52. SEM image of a powder particle from RH95%.	67
Figure 53. Raman spectrum obtained from powder sample RH-95%.	68
Figure 54. Raman spectroscopy micron map (CLS fit) of RH-95%.....	68
Figure 55. Al hydroxide polymorphs from sample RH-95% identified by Raman spectroscopy.....	69
Figure 56. Raman spectrum obtained from powder sample HT-Baseline.....	69
Figure 57. Taken from [167]. On the left, “Surface (through thickness) cracks surrounding the residual impression from a nanoindentation into an anodically grown oxide film on Ti.” On the right, “Schematic of cracking development during nanoindentation of a hard film on soft substrate.”.....	70
Figure 58. A load-displacement curve for an RH 95% HP Al powder particle. Note the initial excursion in the load via the enlarged area of the graph as indicated by the left most arrow.	71

Figure 59. A hardness vs. load curve in direct relation to the sample defined in Figure 58.....	72
Figure 60. (a) Enlargement of area identified by arrow and blue circle of Al powder was placed onto carbon paste. (b) Shows the residual imprint left on the powder particle after testing.	73
Figure 61. Fused Si data that demonstrated that the system was well calibrated and consistent with the known Elastic modulus and hardness values of reference materials.	74
Figure 62. Comparison of indentation hardness vs. depth curves for three particles of AR HP Al powder. Arrows indicate the depth used in calculating the native oxide film thickness.	74
Figure 63. A load-displacement curve for an RH 50% HP Al powder particle.....	76
Figure 64. Plot of two hardness-load curves for two RH 95% HP Al powder particles.	76
Figure 65. Plots of two load-displacement curves for two RH 95% HP Al powder particles.....	77
Figure 66. Categorical comparison of each of the three samples studied herein in terms of indentation hardness and average thickness for each.	77
Figure 67. Apparatus used by UMASS to electro-polish the substrates prior to SPI testing.	78
Figure 68. Comparison of polishing results of the two grades of pure aluminum.....	79
Figures 69a and b. Single particle experiment using the UMass LIPIT system. (a) Schematic illustration of SPI. (b) An ultrafast photograph shows a collision/rebound motion of an aluminum particle with an interframe time of 603 ns.	80
Figure 70. Rebound speeds of “As-received”, “RH-50”, and “RH-95” powders. The symbol color represents the impacting particle’s diameter.	81
Figure 71. Trend of rebound speeds of “As-received”, “RH-50”, and “RH-95” powders. The symbol color represents impacting particle’s diameters.	82
Figure 72. Rebound speeds of “HT-baseline”, “HT-30”, “HT-60”, and “HT-240” powders. The symbol color represents the diameter of the impacting particle.	83
Figure 73. Trend of rebound speeds of “HT-baseline”, “HT-30”, “HT-60”, and “HT-240” powders. The symbol color represents the diameters of the impacting particles.	84
Figure 74. Coefficient of restitution as a function of CIV for AR, RH-50% and RH-95%.	85
Figure 75. Coefficient of restitution as a function of impact velocity for the 95% relative humidity particles and desiccated 95% relative humidity particles.....	87
Figure 76. Coefficient of restitution as a function of CIV for HT-baseline, HT-30, and HT-240	88
Figure 77. Images of Cold Sprayed deposits of heat treated powders under dry conditions.....	89
Figure 78. Images of Cold Sprayed deposits of heat treated powders under humid conditions...	90
Figure 79. Video measurement of ductility.	92
Figure 80. Stress-strain Curves of Cold Spray Bulk Samples of HP-Al.	94
Figure 81. (a) Fracture surface of HT-Baseline specimen; (b) The magnified view of fracture surface. Dimpled morphology support the ductile fracture of HT-Baseline specimen.	95
Figure 82. (a) Fracture surface of RH-95% specimen. The fracture surface is much flatter than other groups; (b) Magnified view of fracture surface.....	96
Figure 83. (a) Fracture surface of RH-95% specimen; (b) Magnified view of fracture surface...	96
Figure 84. Fracture surface of RH-95% specimen. The fracture surface contains evidence of particle impact sites not completely bonded and ‘half-moon’ features denoted by the red arrows.	96
Figure 85. Magnified view of fracture surface of Figure 84, showing a featureless fracture morphology associated with decohesion of splats. Note some SEM charging indicative of oxides.	97
Figure 86. (a) SEM and BSE (b) of RH-95% tensile fracture showing decohesion of splats.	97

Figure 87. (a) Fractured tensile bar representing HT-Baseline and (b) fractured tensile bar representing RH-95%. Note the differences in necking and the brittle nature of RH-95%. Arrows denotes cracks in grip section. Red circled regions are enlarged in Figure 83.	99
Figure 88. (a) Circled area on Figure 83a enlarged showing elongated grains and (b) Circled area on Figure 83b showing abrupt fracture with little evidence of ductility before final fracture.	99
Figure 89. (a) SEM of tensile fracture surface from HT-Baseline and (b) corresponding X-ray map.	100
Figure 90. Spectrum obtained from X-ray mapping obtained from Figure 85.	100
Figure 91. (a) SEM of tensile fracture surface from RH-95% and (b) corresponding X-ray map.	101
Figure 92. Spectrum obtained from X-ray mapping obtained from Figure 86. Note the high oxygen concentration of RH-95% as compared to that of HT-Baseline.	101
Figure 93. Visible light microscopy images indicating where each of the different powder splats are located on each substrate. A) As-received powders. B) Heat treated baseline powders. C) HT-240 powders. D) RH-95% relative humidity powders.	103
Figure 94. Example of FIB lift-out procedure to extract a cross-section of a splat for analysis.	105
Figure 95. SE SEM image from each of the RH-95% splats that were sectioned for analysis. .	106
Figure 96. STEM and EDX analysis of Particle 3 from splat sample RH-95%.	107
Figure 97. Enlargement of high oxide area from Figure 88 denoted by blue circle and arrow.	107
Figure 98. Line scan (1) of interface between substrate and splat of Particle 3 from splat RH-95%.	108
Figure 99. Line scan (2) of interface between substrate and splat of Particle 3 from splat RH-95%.	109
Figure 100. Line scan (3) of interface between substrate and splat of Particle 3 from splat RH-95%.	109
Figure 101. Line scan (4) of interface between substrate and splat of Particle 3 from splat RH-95%.	110
Figure 102. Line scan (5) of interface between substrate and splat of Particle 3 from splat RH-95%.	110
Figure 103. Line scan (6) of interface between substrate and splat of Particle 3 from splat RH-95%.	111
Figure 104. Line scan (7) of interface between substrate and splat of Particle 3 from splat RH-95%.	111
Figure 105. Line scan (8) of interface between substrate and splat of Particle 3 from splat RH-95%.	112
Figure 106. STEM and EDXS of the bottom splat/substrate interface from RH-95% Particle 3.	112
Figure 107. Enlargement of STEM and EDXS image shown in Figure 98 of the bottom splat/substrate interface from RH-95% Particle 3.	113
Figure 108. Line scan (10) of the bottom splat/substrate interface of RH-95% Particle 3.	113
Figure 109. STEM and EDX analysis of Particle 2 from splat sample RH-95%.	114
Figure 110. STEM and EDX analysis of Particle 6 from splat sample RH-95%.	115
Figure 111. STEM and EDX analysis of Particle 2 from splat sample As-Received.	115
.Figure 112. STEM and EDX analysis of Particle 32 from splat sample HT-Baseline.	115

Figure 113. Stages of oxidation occurring on aluminum metal in relation to temperature, superimposed on a typical TGA plot [157,158].	117
Figure 114. Hydrogen blisters in 6061 Al cold spray bulk material after solution heat treat.	118
Figure 115. Degassing behavior of aluminum and its composites [189].	118
Figure 116. Schematic of the primary solid state transformations of alumina [190-192].	119
Figure 117. Thermal dehydration sequence of aluminum hydroxide [193,194].	120
Figure 118. (a) TG and DSC curves of unground bayerite and (b) bayerite ground for 2h. [200]	124
Figure 119. (a) Schematic illustrating the hydrolysis of an Al particle [216] and (b) real-life. SEM image in the center is of the morphology of a powder particle from group RH-95% for comparison.	126
Figure 120. Proposed concept to protect aluminum powder after gas atomization. Bags shown contain 6061 Al provided by Solvus Global.	133